Measurement of the Production Cross-Section of Single Top Quarks in Association with W Bosons at ATLAS

D I S S E R T A T I O N

zur Erlangung des akademischen Grades

doctor rerum naturalium (Dr. rer. nat.)
im Fach Physik

eingereicht an der
Mathematisch-Naturwissenschaftlichen Fakultät
Humboldt-Universität zu Berlin

von

Francesco Michelangelo Giorgi

Präsident der Humboldt-Universität zu Berlin:
Prof. Dr. Jan-Hendrik Olbertz

Dekan der Mathematisch-Naturwissenschaftlichen Fakultät:
Prof. Elmar Kulke

Gutachter:
1. Prof. Dr. rer. nat. habil. Thomas Lohse
2. Herr Prof. Dr. Heiko Lacker
3. Prof. Andrea Giammanco

Tag der mündlichen Prüfung: 22.11.2016

Abstract

The work reported in this thesis is aimed at measuring the cross section of electroweak single top quark production in association with a W boson, a process also referred to as Wt-channel. The interest in this production mechanism relies in the confirmation of the Standard Model predictions together with the possibility of identifying new physics phenomena when comparing its cross section with the one of the other single top production modes (the t- and s-channel.) After providing a general introduction on the physics of the top quark and a description of the experimental setup employed for the detection and the reconstruction of the physics objects, the analysis of 4.7 femtobarn of proton-proton collision data at a centre-of-mass energy of 7 TeV, recorded by the ATLAS detector at the Large Hadron Collider in the year 2011, is presented. The selected events contain one highly energetic lepton (an electron or a muon), three highly energetic jets, of which one is identified as originating from a beauty quark, and an amount of missing energy reconstructed in the transverse plane that is compatible with the presence of a highly energetic neutrino. Since the Wt channel production rate at the LHC is considerably smaller than its main background, a chi-squared based kinematic fit has been developed to help the identification of the signal events allowing the use of simultaneous mass constraints from the W boson and the top quark populating the final states. The chi-squared value in each event is then used as a parameter to rank the event in terms of its probability to match or not the signal hypothesis and a cut on its value is used to implement a first tight event selection. The final selection step consists of requiring that the system composed by the top quark and the W boson reconstructed by the fit is balanced in the transverse plane. The extraction of the cross section is done by means of a maximum likelihood fit using the count of the events which pass the selection. The measurement is found to be dominated by the systematic uncertainties which affect it by an amount close to 100 % of the cross section value. The observed (expected) upper limit on the Wt production cross section is set to 32.51 TeV (30.03 TeV) at 95 % confidence level.

Zusammenfassung

Das Ziel der vorgelegten Arbeit ist die Messung des Wirkungsquerschnittes der elektroschwach vermittelten Produktion einzelner Top Quarks in Assoziation mit einem W-Boson. Dieser Prozess wird auch abkürzend als Wt-Kanal bezeichnet. Die Vermessung dieses Produktionskanals stellt einen Test der Standardmodell-Vorhersage dar und bietet gleichzeitig die Möglichkeit durch einen Vergleich mit anderen Produktionskanälen für einzelne Top Quarks (t- und s-Kanal) Rückschlüsse auf neue Physik jenseits des Standardmodells zu ziehen. Nach einer allgemeinen Einführung zur Physik des Top Quarks folgt eine Beschreibung der für die Detektion und Rekonstruktion physikalischer Objekte wichtigen Systeme des ATLAS-Detektors. Anschließend wird die Analyse der Proton-Proton-Kollisions Daten die im Jahr 2011 vom ATLAS Detektor am Large Hadron Collider (LHC) augzeichnet wurden präsentiert. Diese Daten wurden bei einer Schwerpunktsenergie von 7 TeV aufgezeichnet und haben einen Umfang von 4.7 inverse femtobarn. Die Signalereignisse sind definiert durch das Vorhandensein eines hochenergetischen Leptons (Elektron oder Muon), drei hochenergetischen Jets, von denen einer als von einem Beauty-Quark stammend identifiziert wurde, sowie eines mit dem Vorhandensein eines hochenergetischen Neutrinos kompatiblen fehlendem Transversalimpulses. Da die Produktionsrate des Wt-Kanals am LHC sehr klein im Vergleich zu seinem Hauptuntergrund ist, wurde ein Chi-Quadrat-basierter kinematischer Fit entwickelt um die Identifikation der Signalereignisse zu begünstigen. Hierbei werden W-Boson und Top-Quark aus den Endzustandsteilchen rekonstruiert und durch Bedingungen hinsichtlich der W-Boson und Top Quark Masse evaluiert. Der errechnete Chi-Quadrat-Wert gibt die Wahrscheinlichkeit an, mit der das einzelne Ereignis mit der Signal-Hypothese übereinstimmt und kann als Schnittvariable verwendet werden um eine striktere Ereignisselektion zu erhalten. Im finalen Selektionsschritt wird verlangt, dass das durch den Fit rekonstruierte System aus W-Boson und Top-Quark in der Transversalen Ebene ausbalanciert ist. Die Messung ist von systematischen Unsicherheiten dominiert, die fast 100 % des gemessenen Wirkungsquerschnitts betragen. Die beobachtete (erwartete) obere Schranke auf den Wirkungsquerschnitt der Wt-Produktion beträgt 32.51 TeV (30.03 TeV) bei einem Konfidenzintervall von 95 %.

Contents

1. Introduction

A new age started for the world of particle physics in the early spring of 2010, when proton beams at the Large Hadron Collider (LHC) at CERN collided at the centre-of-mass energy of 7 TeV for the first time. The construction of this unique and advanced machine is, simply in itself, an impressive success of the technological advancement of humanity. The need for this tool lies ultimately in the fact that the higher the energy transferred to a system is, the smaller is the spatial scale that can be probed. The LHC collisions have then provided access to an energy regime unexplored before, and are studied at the two multi-purpose detectors ATLAS and CMS and the more specific experimental setups LHCb and ALICE.

The current reach of our knowledge of the fundamental laws of nature is condensed in the theoretical framework developed during the 1960s and 1970s, the Standard Model of the elementary particle physics. The Standard Model relies on the same mathematical infrastructure that provides the basis to Quantum Electrodynamics (QED), which so well incorporates and unifies the principles of Special Relativity and Quantum Mechanics into a finite, predictive and extremely precise theory of the electromagnetic interaction. Extending the gauge principle to the symmetries that rule the weak and strong interactions, the Standard Model constitutes today a complete theory of all known forces and particles, with the exception of the Gravitational force. The recent discovery of its last cornerstone, the Higgs boson, is only the most recent of its successes in predicting all the known phenomena. Yet this description covers a bare 5 % fraction of what exists in the universe, which appears, from the astrophysical measurements and cosmological models, mostly composed of *dark matter* (25 %) and *dark energy* (70 %). A unified description of the Standard Model with the Gravitation theory provided by the General Relativity has not been found yet, even though all known interactions are expected to merge, through the unification of their running coupling constants, at very small distances few orders of magnitude above the Planck scale and thus far beyond the reach of both the current and foreseen LHC collisions.

A wide variety of theoretical models exist to extend or incorporate the Standard Model and solve some or all of its problems. In order to succeed in that, the existence of new particles is necessarily predicted, whose discovery or exclusion is needed to either accept or dismiss them. Until now, however, the trail for new physics beyond the Standard Model has not been detected in the data that was taken and analysed by the LHC experiments. In this perspective, the ability to detect and measure precisely all the processes predicted by the Standard Model is vital in order to calibrate the detector and fully understand its performance, to improve the detail of the simulation and the reach of the analysis techniques thus being able to spot possible anomalous effects connected to new physics.

This analysis is aimed at the study of the a specific production mode of the top quark fermion, whose existence was predicted by Makoto Kobayashi and Toshihide Maskawa in 1973 to be finally discovered at the Tevatron in 1995. Two properties grant the top quark a unique position in the fermionic zoology. Its mass of 172.9 GeV [Nakon] is very close to the electroweak scale of 246 GeV, taken to be the *vacuum expectation value* of the Higgs field, a fact which has opened for several years a small backdoor access to the study of the Higgs sector of the Standard Model before the discovery of the boson in 2012. Furthermore, the top quark mass is huge with respect to the mass scale of the remaining quarks, creating a theoretically unjustified hierarchy among the mass parameters of the Standard Model. The Standard Model predicts the top quark lifetime to be as short as 10^{-25} s which, being about a factor of twenty times smaller than the strong interaction timescale, prevents it from hadronising and passing its quantum number onto its decay products.

This work focuses on the measurement of the cross section of the electroweak production of a single top quark in association with a W boson, a process often referred to as Wt-channel. This process is the second most important contribute to the production of single top quarks at the LHC, with a SM prediction of 15.7 pb^{-1} for its cross section at a centre-of-mass energy of 7 TeV. The production rate of the Wt events is sensitive to specific new physics effects which can not occur in the other single top production modes, and it therefore constitutes an exclusive framework to test a unique set of theories beyond the Standard Model. Furthermore, it constitutes one of the backgrounds when searching for both neutral and charged Higgs boson signal, and for several new physics models. The Wt-channel has escaped the detection at the Tevatron, since the cross section is negligible at 1.96 TeV where its signal is the lowest among the single top production channels, but it is predicted to be visible at the energies of the LHC. In this context, the level of precision required in the quest for the Wt-channel is similar to that necessary for the search of new physics. The discovery of the existence of the Wt associated production has been recently achieved at the LHC, where both ATLAS and CMS have indipendently measured its production cross section at the centre-of-mass energy of both 7 and 8 TeV reaching a sensitivity level of 3.4 and 4.0 (7 TeV), and 7.7 and 6.1 standard deviations (8 TeV) [A$^+$12c, Cha13, C$^+$14b, A$^+$16]. These measurements are set to explore the final state configuration where both the top quark and the associated W boson decay leptonically, and no univocal reconstruction of the top quark state is allowed. This analysis is thus devoted to identify and measure the signal from the associated Wt production at the center-of-mass energy of 7 TeV in the semileptonic search channel, where only one of the real W bosons – either the associated one or that produced by the top quark decay – decays leptonically, while the other decays into a quark pair. Despite the clear experimental signature, several challenges are met in the process of isolation of a statistically significant set of Wt events, and a dedicated analysis procedure relying on a χ^2-based kinematic fit with invariant masses constraints has been set into place.
This thesis is organised as follows. In Chap. 2 a brief description of the Standard Model is presented, with a focus on the physics of the top quark. Here its properties and production

modes are described, and a review of the most important results from the analyses performed at Tevatron and the LHC is outlined. Also, the phenomenology of the Wt events is presented in the chapter together with the expected background processes. In Chap. 3 the experimental setup at the Large Hadron Collider and the ATLAS experiment is presented. Chap. 4 describes in detail the standard criteria and corrections commonly developed by the ATLAS Top Working Group for the selection of events containing top quarks. The implementation of the kinematic fitting procedure employed for the identification of top quarks is described in Chap. 5, while its application aimed at the reconstruction and the selection of Wt events is contained in Chap. 6. The extraction of the cross section result and the statistical treatment of the systematic uncertainties is described in Chap. 7, and the thesis is concluded in Chap. 8, where the final result is compared against the previous measurements and an outlook is given with respect to the performance upgrades expected at the LHC.

2. Top Physics at the LHC

This chapter presents a basic overview of the Standard Model that describes the current understanding of fundamental matter particles and their interactions with the gauge boson fields. The basic themes of the Standard Model are presented in Sec. 2.1, focusing the attention on those aspects that are relevant for the study of the physics of the top quark; the features of the top quark sector are therefore displayed in Sec. 2.3. The production modes of the top quarks at the hadron colliders through the strong and electroweak interaction presented in Sec. 2.3.1 and 2.3.2 and the latest experimental results are shown; a detailed overview of the production of single top quarks in association with a real W boson is given, and the aspects and intricacies that accompany the full theoretical treatment of the process beyond the leading order are also discussed. Eventually, the physical properties of the top quark are reviewed in Sec. 2.2.

2.1. The Standard Model

Our current working knowledge of the fundamental laws obeyed by nature is condensed in the theoretical framework developed during the 1960's and 1970's, the Standard Model of the elementary particle physics. The Standard Model (SM) is built on the twin pillars of group theory and relativistic quantum field theory (QFT), the latter being the result of the unification of the Einsteinian description of relativistic motion with the quantum mechanics; the arch stone of the system, that connects the two mathematical domains and provides a simple and natural origin to the existence of interactions, is the *gauge principle*. In this framework, the elementary particles that constitute the matter are described by fermionic fields and their fundamental interactions are modelled through bosonic fields originated by the gauge symmetries which the Standard Model relies upon. In the following sections the existing particles and their interactions are described, and the spontaneous breaking of the symmetry mechanism and the necessity of the Higgs field are briefly introduced. Throughout this thesis, the $\hbar = c = 1$ convention is employed.

2.1.1. Fundamental Particles and their Interactions

A gauge theory, as the Standard Model is, involves two kinds of particles; this classification does not strictly depend on the spin of the particles, but divides them between those which carry a 'charge' and those which mediate interactions between currents by coupling directly

to the charge. The particles of the first kind are the fermions and the nonabelian gauge bosons, while in the second class is composed only by gauge bosons (both abelian and nonabelian); the actual (physical) type of charge depends on the theory. The fundamental fermions are listed in Tab. 2.1; there are in total six particles for both the quark and the lepton sector, coupled in terms of the weak isospin, organised in terms of three generations, growing in mass. Within the particle sector, each member of these doublets can transform into its partner when coupling to a *charged current* interaction.

Gen.	Quarks			Leptons		
	Flavour	charge	mass [GeV]	Flavour	charge	mass [GeV]
1	up	+2/3	0.00015 - 0.004	ν_e	0	$< 3 \times 10^{-9}$
	down	-1/3	0.004 - 0.008	e	-1	0.511×10^{-3}
2	charm	+2/3	1.15 - 1.35	ν_μ	0	$< 0.17 \times 10^{-3}$
	strange	-1/3	0.08 - 0.13	μ	-1	0.106
3	top	+2/3	172.5 ± 1.4	ν_τ	0	< 0.0155
	beauty	-1/3	4.1 - 4.4	τ	-1	1.78

Table 2.1.: The fundamental fermions, [Nakon].

Lagrangian of the Standard Model

Once the generators of the local gauge symmetries are established and the matter fields have their (gauge) quantum numbers defined, the Lagrangian of the model is fixed by requiring it to be simultaneously *local*, *renormalisable* and *gauge invariant*. It is divided in four pieces as follows:

$$\mathcal{L}_{SM} = \mathcal{L}_{Gauge} + \mathcal{L}_{Matter} + \mathcal{L}_{Yukawa} + \mathcal{L}_{Higgs}. \tag{2.1}$$

The first item in Eq. (2.1) contains the kinetic term of the gauge fields and their self-interactions:

$$\mathcal{L}_{Gauge} = \frac{1}{2g_S^2} \operatorname{Tr} G^{\mu\nu} G_{\mu\nu} + \frac{1}{2g^2} \operatorname{Tr} W^{\mu\nu} W_{\mu\nu} + \frac{1}{2g'^2} \operatorname{Tr} B^{\mu\nu} B_{\mu\nu}\,, \tag{2.2}$$

where $G^{\mu\nu,i}$,$W^{\mu\nu,i}$ and $B^{\mu\nu}$ are respectively the gluon, the weak isospin and the hypercharge field tensors. The second item contains the kinetic energy for the matter fields and their interactions with the gauge fields:

$$\mathcal{L}_{Matter} = i\bar{Q}_L^i \not{D}\, Q_L^i + i\bar{u}_R^i \not{D}\, u_R^i + i\bar{d}_R^i \not{D}\, d_R^i + i\bar{L}_L^i \not{D}\, L_L^i + i\bar{e}_R^i \not{D}\, e_R^i\,, \tag{2.3}$$

where the i suffix stands for the sum over all the fermion generations, and the interactions are expressed in terms of the covariant derivatives. For example in the left-handed quark

sector we define

$$\not{D}\, Q_L = \gamma^\mu \left(\partial_\mu \, + \, i\, g_S\, G_\mu \, + \, i\, g\, W_\mu \, + i\, \frac{1}{6}\, g'\, B_\mu\right). \tag{2.4}$$

The information regarding the strength of the interactions is contained in the gauge (running) couplings g,g_S,g'. The third element of Eq. (2.1) contains the mass terms of the fermion fields. The insertion of explicit mass terms of the gauge bosons are forbidden in this simple model, due to the requirement for the theory to be renormalisable. On the other hand, the parity violation of the coupling to the W fields would introduce a breaking of the gauge symmetry when the fermion mass terms are inserted "by hand". For these reasons the introduction of an additional weak-isospin doublet with non-vanishing vacuum expectation value – the Higgs field – is proposed. The Higgs field is now expected to couple to the fermions through the Yukawa interaction described in Eq. (2.5).

$$\mathcal{L}_{\text{Yukawa}} = -\Gamma_u^{ij}\, \bar{Q}_L\, \epsilon \phi^*\, u_R^i \, - \Gamma_d^{ij}\, \bar{Q}_L\, \phi\, d_R^i \, - \Gamma_e^{ij}\, \bar{L}_L\, \phi\, e_R^i \tag{2.5}$$

Here $\epsilon = i\sigma_2$ is the two-dimensional totally antisymmetric tensor, which ensures the charge neutrality of each term of the Lagrangian. The Γ_u,Γ_d,Γ_e are the 3×3 complex matrices in the space of the fermion generations. They do not need to be simultaneously diagonal in both the interaction and the mass space, thus allowing the mixing between different generations. The last item in Eq. (2.1) is given by

$$\mathcal{L}_{\text{Higgs}} = (D^\mu \phi)^\dagger D_\mu \phi \, - \, \mu^2 \phi^\dagger \phi \, + \, \lambda (\phi^\dagger \phi)^2 \, . \tag{2.6}$$

It contains the most general renormalisable potential for a boson field (the Higgs field), and the μ, λ couplings are chosen such that the field can assume a non-vanishing vacuum expectation value. In this formalism, the masses of the gauge bosons arise naturally from the covariant derivatives, brought up by their interaction with the Higgs doublet. Choosing an appropriate phase for the two electrically neutral $W^{\mu\nu,3}$ and $B^{\mu\nu}$ generators in terms of the weak (Weinberg) angle θ_W is possible to retrieve the vanishing mass of the photon, and predict the mass of the neutral Z boson in terms of the mass of the charged W bosons by means of the g,g' couplings and the Higgs vacuum expectation value v [Gol61, GSW62]:

$$m_W = \frac{1}{2} g v, \;\; m_Z = \frac{1}{2}\sqrt{g^2 + g'^2}\, v \, = \frac{g v}{2 cos\theta_W} \tag{2.7}$$

The experimental evidence of the validity of the model was confirmed analysing the collisions performed at the Sp$\bar{\text{p}}$S collider at CERN in the early 1980's, where the weak bosons were first found and and their mass and properties measured [A$^+$83, B$^+$83].

More recently, in 2012, a new particle of bosonic nature with a mass of about 126 GeV was observed by ATLAS [ATL12] and CMS [Cha12]. consistent with the excitation of this field, known as the "Higgs particle". The value of the mass lies exactly in the region predicted for the Higgs mass by electroweak precision fits of the Standard Model in its minimal expression

[FGH+09]. Furthermore, the zero spin and the coupling of this new bosonic particle to W and Z bosons is found to be in agreement with the Standard Model expectation [A+13d, A+13a].

For the fermion sector, the mass term form is given by

$$m_f = \Gamma_f \frac{v}{\sqrt{2}}\,, \tag{2.8}$$

where the Γ_t are the Yukawa couplings. The diagonalisation of the mass matrices – the change of basis from the eigenstates of the weak interaction to the mass eigenstates – leads to the Cabibbo-Kobayashi-Maskawa (CKM) matrix [Cab63, KM73]:

$$\begin{pmatrix} d' \\ s' \\ b' \end{pmatrix} = \begin{pmatrix} V_{ud} & V_{us} & V_{ub} \\ V_{cd} & V_{cs} & V_{cb} \\ V_{td} & V_{ts} & V_{tb} \end{pmatrix} \begin{pmatrix} d \\ s \\ b \end{pmatrix}. \tag{2.9}$$

whose values are regarded as *free parameters* in the SM, and therefore have to be measured in experiments and set by hand in the calculations. Equation 2.9 connects the weak eigenstates of the quarks to the mass ones, thus consenting, within the kinematic restrictions, to up- or down-like quarks the decay into any of their weak isospin partners, when coupled to a W boson. The squared amplitudes of the CKM matrix set the probability of each flavour transition. The assumption of the unitarity of the CKM matrix does not fully constrain the number of generations, allowing the existence of a fourth one. The measurement of $|V_{tb}|$ is still needed. As shown later on in Sec. 2.2, the top quark has a lifetime shorter than required to form bound states such as the *toponium*, the direct result being that only two contexts are left to the experimentalists to investigate directly the W-t-b vertex structure: the decay of the top quark (in top-pairs produced in QCD interactions) and the electroweak production of *single* top quarks. Preliminary results of the $|V_{tb}|$ measurements within both contexts have been done already by the experiments at the LHC, yet no significant deviation from the SM expectations has been found. The structure of the electroweak interaction – *i.* e. the coupling of weak isospin doublets to the tensor fields of the gauge bosons – is such that the flavour change through *neutral currents* – *e.* g. the coupling to an electrically neutral particle, like a photon or a Z – is forbidden at the tree level of the calculations. As a result, the existence of the top quark could be inferred long before its discovery at the Tevatron in 1995, evaluating the loop contributions in the radiative decays of B mesons [Lan89, Hol90].

2.2. Properties of the Top quark

The existence of the top quark is one of the striking predictions of the Standard Model; the renormalisability of the electroweak theory was maintained at the cost of postulating the presence of a weak-isospin partner to the beauty quark. The measured values of the quantum numbers of the b quark [Nakon] constrain the spin, the weak-isospin and the

charge of the top quark, a set of predictions that is expected to be fully confirmed at the LHC. In the framework of the Standard Model, the top quark transforms as a colour triplet under the $SU(3)_C$ group of the Quantum Chromodynamics and as the weak isospin partner of the beauty quark, undergoing all the fundamental interactions that are currently known. All the properties of the top quark are predicted by the Standard model, with the only exception of its mass and decay width. The indirect measurements at LEP [BEM+00] and following direct measurements performed at the Tevatron [TEW11] first and at the LHC [A+12i, C+12b, C+12c] put the world average of the top quark mass to $172.9 \pm 0.6 \pm 0.9$ GeV [Nakon]. This value is surprisingly close to the electroweak scale $v = (G_F\sqrt{2})^{-1/2} = 246\,\text{GeV}$, taken to be the *vacuum expectation value* of the Higgs field (where G_F is the Fermi constant), and huge with respect to the mass scale of the remaining quarks, establishing a yet unexplained and still puzzling hierarchy. The properties and peculiarities of the top quark are briefly reviewed in the following sections.

Mass

Even though the top quark is the last of its kind to have been discovered, its mass m_t is known more accurately than any other quark. This turns out to be of the utmost importance, given the role that the top quark mass value assumes in the SM precision fits, due to it being close to the electroweak energy scale. Like the other parameters of the SM, the mass of the top quark depends on the convention used. In contrast to the rest of the quark family, the top quark does not live long enough to hadronise (see Sec. 2.2), and it is then possible to treat it like a quasi-free fermion, and use the concept of the *pole mass*, which is defined to be the real part of the complex pole of the quark propagator. Yet this is not an observable in strict sense, but a simple "perturbative" concept, as due to the *colour confinement* the quark propagator does not have a pole. As for any other quark, the top quark mass defined as the propagator pole has an intrinsic theoretical uncertainty of $\mathcal{O}(\Lambda_{\text{QCD}}) \sim 200\,\text{MeV}$, which is smaller than the experimental precision that either the Tevatron or LHC experiment can reach. The most recent combinations of the top quark mass measurements from the analyses performed at the Tevatron are shown in Fig. 2.1.

Decay and lifetime

Thanks to the huge mass (see Sec. 2.2 the top quark is kinematically allowed to decay into an on-shell (real) W boson and a down-like quark, and according to the unitarity constraints on the CKM matrix the following branching ratios are predicted:

$$B(\text{t} \to \text{bW}^+) = 0.998 \qquad B(\text{t} \to \text{sW}^+) \simeq 1.9 \times 10^{-3} \qquad B(\text{t} \to \text{bW}^+) \simeq 10^{-4}\,. \quad (2.10)$$

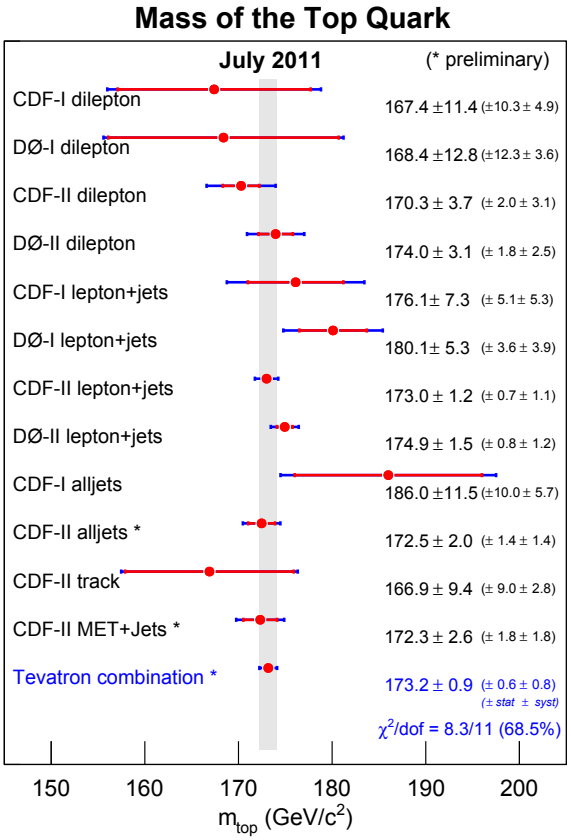

Figure 2.1.: Summary of the input measurements and resulting Tevatron average mass of the top quark [TEW11]. Given the experimental technique used to extract the top mass, these mass values should be taken as representing the top pole mass.

In the SM, when including the first order QCD corrections, the top quark decay rate is given by

$$\Gamma_t = \frac{G_F m_t^3}{8\pi\sqrt{2}} \left(|V_{td}|^2 + |V_{ts}|^2 + |V_{tb}|^2\right) \left(1 - \frac{m_W^2}{m_t^2}\right)^2 \left(1 + 2\frac{m_W^2}{m_t^2}\right) \left[1 - \frac{2\alpha_s}{3\pi} \cdot f(y)\right], \qquad (2.11)$$

where $y = (m_W/m_t)^2$ and $f(y)$ is a polynomial function. The net contribution of the QCD corrections to the top decay rate diminishes the tree level result by 10%. By means of the latest m_t results one finds

$$\Gamma_t \simeq 1.3\,\text{GeV}. \qquad (2.12)$$

This value is significantly lower than the experimental resolution both at the Tevatron and the LHC; at the present day, the direct measurement of the top quark width is not possible at hadron colliders, but an indirect determination can be performed taking into account the

measurements of the $t\bar{t}$ and single top production cross sections. The lifetime of the top quark is then very short:

$$\tau_t := \frac{1}{\Gamma_t} \simeq 10^{-25}\,\mathrm{s}\,; \tag{2.13}$$

this value is about ten times smaller than the hadronisation time $\tau_{had} \simeq 1/\Lambda_{QCD} \approx 10^{-24}\,s$ which defines the time necessary for a quark to connect to other (anti)quarks in the final state to form a colour-neutral bound state due to the confinement. In other words, the top quark decays weakly *before* being able to form any kind of mesonic $t\bar{q}$ or baryonic tqq' matter in the final state; for this reason the information regarding the spin quantum number of the top quark is conserved and passed on to its decay products before being lost by the hadronisation process, as happens for all the other flavours.[1] The discussion above applies only to hadronisation processes. The top quark is produced as a free particle with a defined colour quantum number, and due to the confinement of the colour charge it has to connect to the other products in the final state of its production process. This causes the phenomenon of colour reconnection with the initial and final states of the hard process and with the beam remnants [WS08]. According to the SM the decay of the top quark has a $V-A$ structure and the composition of the helicity states of the outcoming W boson is completely predicted up to $\mathcal{O}(\alpha_s)$ and $\mathcal{O}(\alpha_W)$ level, taking into account gluon-strahlung, $m_b > 0$ and finite width of the W boson. The angular distributions of the decay products are therefore fixed in the SM, and a deviation from the theoretical expectations would be a signal of physics beyond the Standard Model. The first ATLAS results [A+12j] fully confirm the predictions.

Spin

From the angular distributions in the observed $t \to bW$ decay, the known spins of the products and the helicity conservation it follows that the top quark is a spin 1/2 fermion, even though a dedicated measurement of this observable has not been realised yet. In fact, from the measurement of the $t\bar{t}$ production cross section at the Tevatron and the LHC it is only possible to exclude the possibility of top quarks to be $S = 3/2$ fermions. Direct experimental evidence for the top quark having spin 1/2 can arise from the observation of the polarisation of the particles in the final state, and spin-correlation effects. These measurements are part of the physics menu of the experiments at the LHC. A more detailed treatment of the top quark spin topic is given in [CKR03].

Colour and electric charge

Like the other quarks, top quarks carry a colour charge, which means that they transform as colour triplets under the $SU(3)_C$ gauge group of the strong interactions. The phenomenon of colour confinement, caused by the negative sign of the β-function resulting from the

[1] For comparison, the mean lifetime of b hadrons, which contain the next heaviest quark, is about 13 orders of magnitude larger, $\tau_{b\,\mathrm{hadron}} \simeq 1.5 \times 10^{-12} s$.

QCD structure, makes this quantum number inaccessible to any experimental technique; the results from $t\bar{t}$ production cross section are consistent with the SM predictions for a colour triplet and anti-triplet quark-antiquark pair. The top quark is the $I_3 = 1/2$ weak-isospin partner of the b-quark. The doublet structure of the weak current leads to the prediction for the top quark charge to be $Q = +2/3$, in units of the positron charge $e > 0$. This value was not measured in experiments for a long time, leaving an open possibility for the existence of some exotic top-like quarks to exist having a charge $Q = -4/3$. The top quark charge has been measured at the LHC studying the (rare) events where a top quark radiates off a photon *before* its standard decay; such events would have a additional photon in the final state, and the top quark charge can be extracted by the $\sigma(t\bar{t}\gamma)/\sigma(t\bar{t})$ ratio. Studying these events, the possibility for the top quark to have the aforementioned negative charge was ruled out with a significance higher than 8 standard deviations [A$^+$13c].

2.3. Top Quark Production

There are two principal processes that can produce top quarks in hadronic collisions. The first one is the production of pairs of top quarks by the strong interaction, and constitutes the main contribution both at the Tevatron and the LHC. The second one, characterised by a sensibly smaller cross section, is the production of single quarks by means of the electroweak interaction; both types of the production are described in the following sections. The main ingredients needed to calculate the cross sections in proton-(anti)proton collisions are the *quark-parton model* and the *factorisation theorem*. In the context of the quark parton model a highly energetic hadron A – *i.* e. a proton at the LHC – is seen as composed of quasi-free partons (quarks and gluons) which share the longitudinal momentum P_A of the hadron they belong to the fraction of momentum carried by each parton i can be expressed as

$$x_i = p_i / P_A. \tag{2.14}$$

The factorisation theorem states that the total hadronic cross section, expressed in Eq. 2.15 is given by the convolution of the partonic density functions (PDFs) $q_i(x, \mu_R^2)$ in the colliding hadrons A and B, and the partonic cross section. The PDFs are defined as the probability density of a given parton inside a hadron A to carry a fraction x of its longitudinal momentum, measured at a given scale Q^2 of transferred momentum in deep inelastic scattering experiments, which is assumed to be equivalent to the energy scale $\mu_F^2 2$ at which the cross hadronic section is factorised.

$$\sigma(s, \mu) = \sum_{i,j=q,q',g} \int dx_i dx_j \, q_{i,\mu_R^2}(x_i, \mu_F^2) \, q_{j,B}(x_j, \mu_F^2) \, \sigma_{AB}(x_i x_j s, \mu_R^2) \tag{2.15}$$

In Eq. 2.15 s is the squared energy in the centre-of-mass of the hadronic collision – which is used to define $\hat{s} \equiv (x_i P_A + x_j P_B)^2 \approx x_i x_j s$, the centre-of-mass energy for the partonic

system – and μ_R^2 is the scale of renormalisation of the divergent diagrams – usually set at the level of the heaviest mass involved in the process. It is here important to note that the renormalisation scale μ_R^2 and the factorisation scale μ_F^2 are in principle distinguishable. The dependence on the renormalisation procedure is expected to vanish in the complete perturbation series. Nevertheless,since the theoretical calculations can only be performed at finite orders, a dependence on the μ_R^2 is still present and a choice must be made. For physics processes where the production of top quark occurs, both scales μ_F^2 and μ_R^2 are commonly set to the momentum scale of the hard scattering process $\mu_F^2 = \mu_R^2 = m_t^2$. By varying the renormalisation scale the stability of the perturbation series is tested, and the theoretical uncertainty estimated. In order for the production of a top quark to occur, the squared centre-of-mass energy of the partonic system $\hat{s}$ has to exceed the threshold value of m_t^2, while a value higher than $4m_t^2$ is needed for the production of a pair of top quarks. It is therefore possible to obtain an estimate of the average threshold of the momentum fraction carried by the parton for the production of top quarks at the LHC:

$$x_{1,2}^{\text{threshold}} \approx \sqrt{\frac{\hat{s}}{s}} = \begin{cases} \frac{m_t}{\sqrt{s}} & \approx 0.025 \quad \text{single top} \\ \frac{m_W + m_t}{\sqrt{s}} & \approx 0.036 \quad \text{Wt production} \\ \frac{2m_t}{\sqrt{s}} & \approx 0.050 \quad t\bar{t} \end{cases} \tag{2.16}$$

The average production thresholds at the LHC lie at x-values where the gluon density is sensibly dominant over the quark density, as can be seen in Fig. 2.2. For this reason the difference in performance of a pp collision machine with respect to a $p\bar{p}$ one is strongly reduced: the loss of the cross section enhancement from valence quarks in a $p\bar{p}$ collider is negligible, but it is a small price to pay when taking into account the much easier techniques of production and storage of high energy proton beams compared to antiprotons.

2.3.1. Strong Production of Top Quark Pairs

The production of $t\bar{t}$ pairs production at 7 TeV happens by the strong force. The leading order (LO) Feynman diagrams of the process are shown in Fig. 2.3. The amplitude for the "gluon-gluon fusion" sub-processes (Feynman diagrams in Fig. 2.3b, 2.3c, 2.3d) is responsible for almost 90% of the production rate at the LHC; the quark-quark annihilation from the sub-process depicted in Fig. 2.3a, which is the main contribution to $t\bar{t}$ pair production at the Tevatron, is suppressed by the large contribution from sea in the PDFs. The full next-to-leading order (NLO) corrections of $\mathcal{O}(\alpha_S^3)$ to the *tree level* include processes like gluon bremstrahlung ($q\bar{q} \to t\bar{t}+g$ and $gg \to t\bar{t}+g$) and the emission of real quark radiation from the initial and final states, such as $qg \to t\bar{t} + q$. The NLO calculations have been performed by different authors (*cf.* Ref. [ALL+11] and the references therein). The latest and most precise results are obtained by the HATHOR program, where the top pair production cross section is computed including the soft gluon resummation at next-to-next-to-leading logarithmic-order

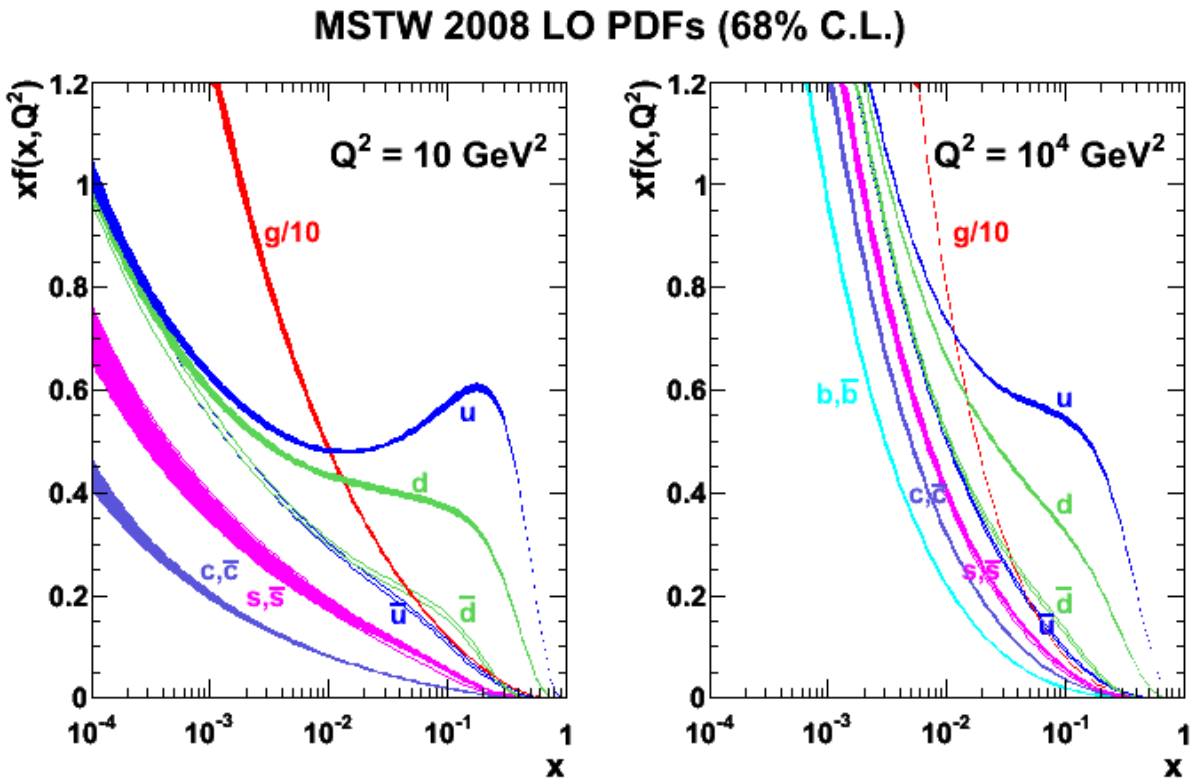

Figure 2.2.: The leading-order PDFs of the MSTW 2008 set are shown. The values are measured at a transferred momentum scale of $Q^2 = 10\,\mathrm{GeV}^2$ (left) and $Q^2 = 10^4\,\mathrm{GeV}^2$ (right) at 68% confidence level [MSTW09].

(NNLL) accuracy:

$$\sigma(pp \to t\bar{t}) \;=\; 166.78^{+4.68}_{-9.26}\,(\mathrm{scale})\,^{+5.12}_{-4.93}(m_t)\,^{+15.80}_{-15.09}(\mathrm{PDFs}{+}\alpha_s)\ \mathrm{pb}. \tag{2.17}$$

It is important to remark that the cross section for top quark production has a strong dependence on the mass of the quark; a simultaneous measurement of the $t\bar{t}$ production cross section and the top mass constitutes a (another) severe test of the validity and predictivity of the Standard Model. Given the presence of pairs of top quarks, and their production cross section being considerably bigger, $t\bar{t}$ events constitute the main source of background for an analysis aimed at investigating the single top signal. The $t\bar{t}$ production cross section at centre-of-mass energy of 7 TeV has been measured independently by the two collaborations combining results from the analyses focused on final states containing both one and two high energy leptons, and in the all-hadronic final state. The latest published results published by the ATLAS and CMS collaborations are shown in Fig. 2.4.

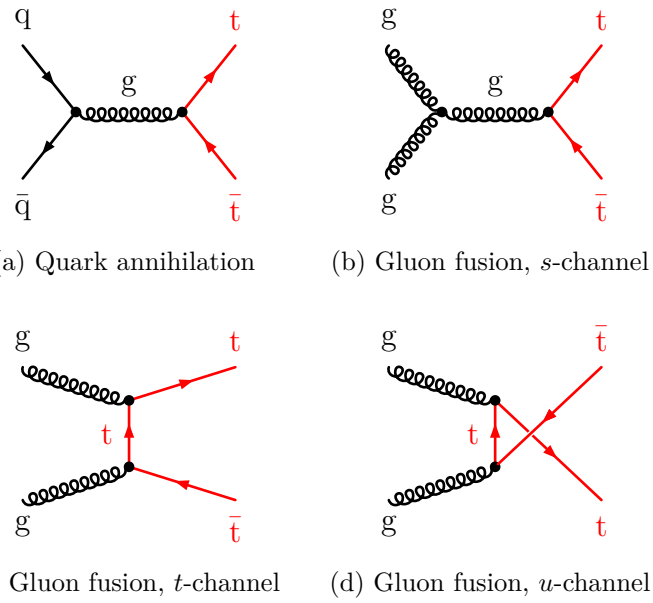

(a) Quark annihilation (b) Gluon fusion, s-channel

(c) Gluon fusion, t-channel (d) Gluon fusion, u-channel

Figure 2.3.: The four partonic diagrams responsible for the two main modes of strong $t\bar{t}$ production: quark annihilation (a), gluon annihilation (b) and gluon scattering (c,d).

2.3.2. Electroweak Production of Single Top Quarks

In contrast to the $t\bar{t}$ pair production, the production of single top quarks in hadronic collisions can be only mediated by the charged currents of the electroweak force, as it can be generally seen as the process of *flavour-changing* of either one of the quarks in the incoming protons. Depending on the sign of the momentum transferred by the W boson in the event, single top quarks can be produced as the result of a scattering process (t-channel) or annihilation and subsequent production of a pair of weak isospin partners (s-channel). A third way of production of single top quarks is in association with a W boson (Wt associated production), the mediator of the process being a virtual b quark. The three production modes are described in the following sections; a special care is devoted to the Wt associated production description and the theoretical issues involved in the calculation of its cross section at NLO level, since it is the main focus of this analysis. The CDF and D0 experiments at the Tevatron provided in 2009 the first evidence of the electroweak production of single top quarks [A$^+$09b, A$^+$09c]. Both results, which exploit principally the t-channel signature, were obtained combining several analyses based on boosted decision trees, Bayesian neural networks and matrix elements.

The cross section for all single top quark production modes has been calculated beyond the NLO level, by including higher-order corrections from next-to-leading-logarithm (NLL) soft gluon resummation. Furthermore, recent advances in two-loop calculation with massless

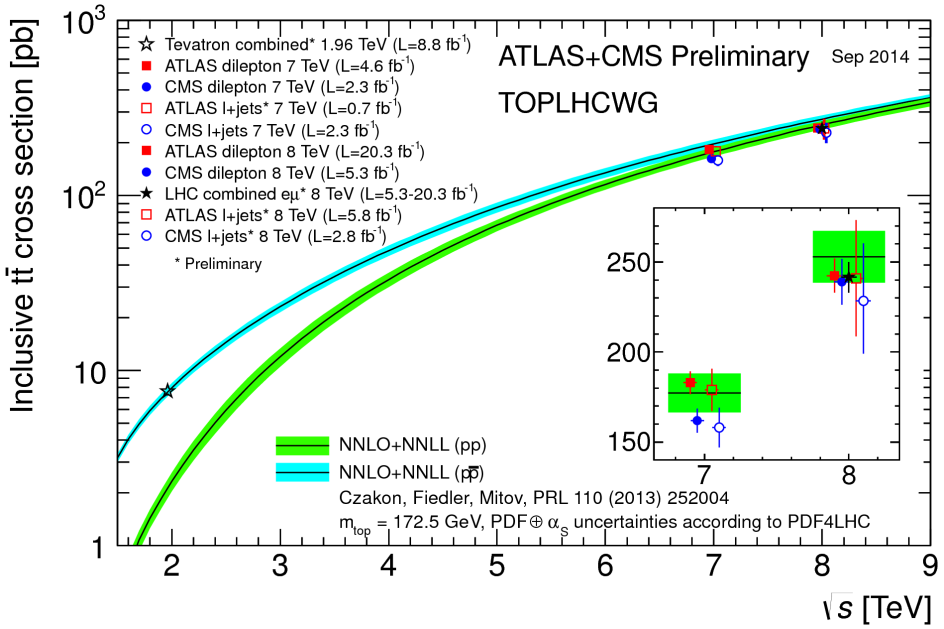

Figure 2.4.: Summary of LHC and Tevatron measurements of the top-pair production cross-section as a function of the centre-of-mass energy compared to the NNLO QCD calculation complemented with NNLL resummation (top++2.0). The theory band represents uncertainties due to renormalisation and factorisation scale, parton density functions and the strong coupling. The measurements and the theory calculation is quoted at $m_{top} = 172.5\,\text{GeV}$. Measurements made at the same centre-of-mass energy are slightly offset for clarity. [Top14b]

and massive quarks allowed calculations at next-to-next-to-leading-logarithm (NNLL) order. The current predictions of the cross section of the production of single top quarks at centre-of-mass energy of 7 TeV, for reference values of the top quark mass $m_t = 172\,\text{GeV}$ and using MSTW2008 NNLO parton density functions, are reported in Tab. 2.2, and will be used as reference value throughout this work. The cross sections have been measured by the ATLAS and CMS experiments and confirmed the predictions of Tab. 2.2, as shown in Fig. 2.6. The appearance of single top quarks in the final states is due to the flavour change induced by the coupling to a W boson with a b-quark from one of the protons. This can happen either due to sea pairs, or subsequent $b\bar{b}$ splitting of gluons. It is therefore important to distinguish the production amplitudes between $2 \to 2$ and $2 \to 3$ particles processes, the second case involving a gluon in the initial state in stead of the b quark, and an additional – mostly collinear with the beam axis – $b(\bar{b})$ quark in the final state. The $2 \to 3$ particles partonic reaction needs to be included in the NLO calculation, raising the problems of quantum interference with other processes that involve identical initial and final states, that can in principle affect the autonomy of the single top production modes as "distinct" from each other. As shown in the following sections, the absence of quantum interference between the amplitudes of the t- and s-channel is straightforward, and the production modes can

be immediately classified as distinct processes. This is not the case of the associated Wt production, where the interference with the $t\bar{t}$ production is safely removed only after a careful choice of the phase space under investigation, as shown in Sec. 2.3.2.

t-channel

The main source of single top quark at the LHC are processes where a b-quark from the sea of one of the colliding protons undergoes a scattering reaction with a light quark from the opposite side via the exchange of a virtual W boson, as shown in the LO and NLO diagrams in Fig. 2.5. The *t*-channel production mode takes place by means of a space-like W boson,

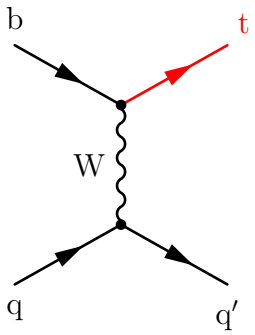

(a) *t*-channel $2 \to 2$ process

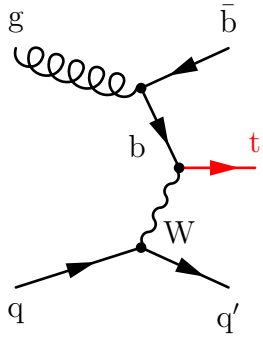

(b) *t*-channel $2 \to 3$ process

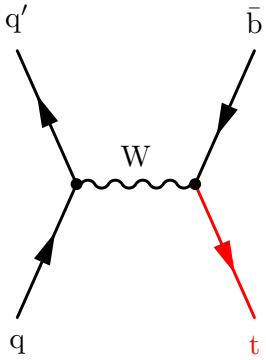

(c) *s*-channel $2 \to 2$ process

Figure 2.5.: Production of single top quarks in the *t*-channel for the 2→2 particles (a) and 2→3 (b) processes. In (c) the *s*-channel mode is shown for the 2→2 process only.

and the partonic process has the following form:

$$\begin{cases} 2 \to 2: & q\,b \to q'\,t \\ 2 \to 3: & q\,g \to q'\,b\,t. \end{cases} \tag{2.18}$$

The production via the t-channel is the main source of single top quarks both at the LHC and at the Tevatron, where the first evidence of single top production was registered. Originally known as *W-gluon fusion*, this process was predicted in the mid 1980s as principal source of heavy quarks (assuming $m_U - m_D$ is large) produced through the electroweak interactions, expecting that, at some high energy, the production rate of processes that scale like $1/M_W^2$ would eventually overcome those which typically scale like $1/\hat{s}$ [WD86]. The production rate in the t-channel is predicted to be charge-asymmetric, meaning that the production rate of single top and single anti-top quarks are expected to differ. The production cross section is directly sensitive to the charge of the light quark from only one of the incoming protons, since it takes the initial state partner from the sea of the second proton, in both the processes with only 2 or 3 particles final states, as shown in Eq. 2.18. As a direct result, top quarks produced from valence quarks entering the reaction in Eq. 2.18 are expected to be exactly twice more abundant than their anti-particles. This effect, modulated by effects from NLO contributions and light flavoured sea quarks, leads to the two separate predictions for (anti)top quark production rates that are shown in the first column of Tab. 2.2, and makes the t-channel available for a further test of the SM and the provide insights on the use of parton density functions at hadronic colliders.

By the time of the redaction of the work at hand, the cross section for the production of single top quarks in t-channel has been measured by ATLAS and CMS at both the centre-of-mass energies of 7 and 8 TeV – *cf.* [A$^+$14a, C$^+$12a] and [A$^+$14b, C$^+$14a, Top13] respectively. A first measurement of the t-channel cross section ratio has been done by ATLAS (*cf.* [A$^+$14b]) and provides a preliminary confirmation of the SM predictions. The main signature, besides the kinematic observables related to the presence of a top quark in the event, is the direction of the remaining light flavour quark, often referred to as "spectator" quark. Moreover, the t-channel events have the feature that the top quark in its rest frame is polarised along the direction of the spectator d ($\bar{\mathrm{d}}$) quark (reconstructed as the forward light flavoured jet). The t-channel production mode constitutes one of the main backgrounds to the identification of Wt-channel events, due to the presence of one real top quark and to its production cross section being twice as large.

s-channel

The production of single top quarks mediated by a time-like W boson is usually referred to as s-channel, and its tree level Feynman diagram is shown in Fig. 2.5. It is easy to note that the investigation of s-channel production events can probe the *crossing symmetry* of the charged weak current [PS95] at leading order level, with respect to the t-channel mode. The s-channel represents the second leading production mode of single top at the Tevatron, where its production rate contributed to assess the evidence of single top quarks production and its cross section as a "distinct" process has been measured by the CDF and D0 collaborations [A$^+$11g, A$^+$11h]. On the contrary, the predicted s-channel production rate at the LHC is the smallest of the single top production modes, as shown in Tab. 2.2, and only an

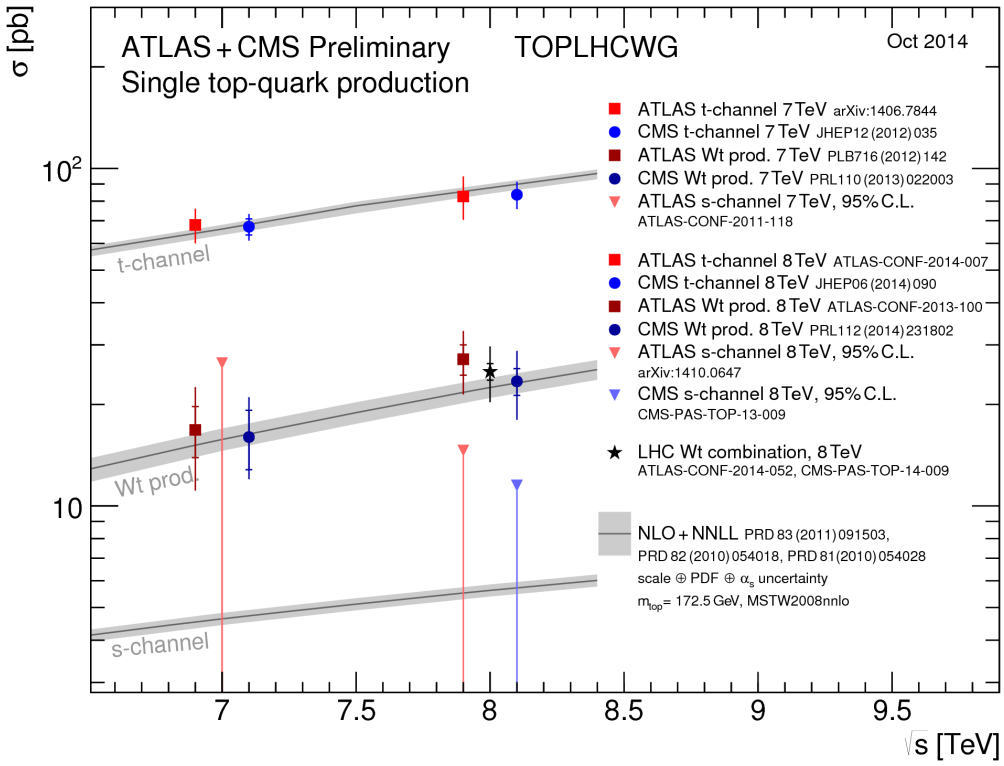

Figure 2.6.: The results from the single top production cross section in the *t*-channel, Wt-channel and *s*-channel are shown as a function of the centre-of-mass energy. For the *s*-channel only an upper limit is shown. The measurements realised by both the ATLAS and CMS experiments at the centre-of-mass energy of 7 and 8 TeV show a perfect agreement with the predictions provided by a theoretical calculation based on NLO QCD complemented with NNLL resummation [Kid11, Kid10a, Kid10b]. The measurements of the Wt-channel production cross section shown in the plot were performed in the dileptonic channel exclusively, while the analysis reported in the document at hand is focused on the lepton+jets channel.

exclusion limit on the production cross section has been obtained by the ATLAS collaboration at both centre-of-mass energies of 7 and 8 TeV [A$^+$11f, A$^+$14c].[2] It is important to remark here that no quantum interference with NLO amplitudes from the *t*-channel production mode occur when dealing with $\mathcal{O}(\alpha_s)$ corrections, even though there is a complete overlap of initial and final states, due to a different colour structure of the quantum amplitudes. As is easily seen, the $t\bar{b}$ pair in the *s*-channel final state is represented by a colour *singlet* since it participates in a pure W-t-b vertex, while it belongs to an colour octet in the *t*-channel,

[2]The measurement of the single top production cross section in the *s*-channel suffers of the same class of systematic uncertainties that affect this work, shown later on in Sec. 7.1.

since the $\bar{b}$ is originated by a gluon.

$$\begin{cases} 2 \to 2: & q\,\bar{q}' \to \bar{b}\,t \\ 2 \to 3: & q\,g \to q'\,\bar{b}\,t. \end{cases} \tag{2.19}$$

Wt-channel

Single top quarks can be produced in association with a W boson, as depicted by the Feynman diagram shown in Fig. 2.7. This production involves a b quark in the initial state, like the t-channel process. Similarly to the t and s-channel, the top quark is produced in a pure W-t-b vertex; in contrast to these processes though, the main propagator of the reaction belongs to a b quark rather than a W boson, which then appears to be *on shell* in the final state of the process. The first calculation of the cross section for the $2 \to 2$ particles reaction has been done by Tait [Tai00] including higher order corrections of $\mathcal{O}(1/ln(m_t^2/m_b^2))$, but it was not a full NLO prediction. Originally thought for $p\bar{p}$ collisions at 2 TeV and pp collisions at 14 TeV, it was able to show that the Wt production cross section would be negligible at the Tevatron and significant at the LHC, where it exceeds the s-channel rate. Like the t and s-channel modes, the cross section of the associated production has been calculated at NNLL accuracy by Kidonakis [Kid10b]. The corrections due to the approximate NNLO computation of the logarithmic resummation are found to enhance the NLO prediction by 8%.[3] The predicted value of the approximate NNLO cross section for the Wt production at the centre-of-mass energy of 7 TeV is reported in Tab. 2.2.

In the following the hard process reactions that bring to the appearance of a single top quark in association with a W boson in the final state are shown, both at tree level and first order correction.

$$\begin{cases} 2 \to 2: & b\,g \to W\,t, \\ 2 \to 3: & g\,g \to W\,t\,\bar{b}. \end{cases} \tag{2.20}$$

The production of two heavy particles reduces the overall phase space of momentum fraction from the incoming partons which provide the centre-of-mass energy available to the particle production, thus diminishing the production rate of Wt events. Moreover, unlike the t-channel, the process scales like $1/\hat{s}$; these two features lead to a cross section for the associated production which is a factor five smaller than the t-channel mode, despite the fact that it is of order $\alpha_s\alpha_W$ rather than α_W^2. The Wt production at the LHC accounts for 20% of the total single top cross section, and it is sensitive to new physics effects which can modify the W-t-b vertex structure, but *not* to 4-fermions interactions which can in principle affect the t-channel and its cross-symmetric twin. The presence of a real W boson accompanying the top quark in the final state prevents such vertices to interfere, thus allowing the

[3] This behaviour is in contrast with the correction given by the approximate NNLO computation for the t-channel cross section, which adds a negative contribution of about 1% to the NLO prediction [Kid11]. For the s-channel production the NNLL corrections enhance the cross section by 15% [Kid10a].

experiment to test different sets of BSM theories. In fact, the Wt production rate provides complementary information on the W-t-b vertex and test the existence of a fourth generation of weak isospin doublets [A$^+$07b, KP$^+$07, S$^+$10, Cha09, HH$^+$09]. Thirdly, it constitutes one of the backgrounds when searching for both neutral and charged Higgs boson signal.

A first evidence of the process occurrence has been established in dileptonic final state searches by both the ATLAS and CMS collaborations [A$^+$12c, C$^+$13]. The measurements, shown in the global picture presented in Fig. 2.6, used 2.0 and 4.9 fb^{-1} of collisions data at the centre-of-mass energy of 7 TeV respectively, and obtained an incompatibility of 3.3 and 4.0 standard deviations with the background-only hypothesis, including systematic effects. Later, during the period 2012-2013, proton-proton collisions at the centre-of-mass energy of 8 TeV were performed. With 20.3 and 12.2 fb^{-1} of data respectively collected by ATLAS and CMS, an excess consistent with the signal hypothesis was observed in the dilepton channel. These measurements [A$^+$13b, C$^+$14c], later combined in [Top14a], show a significance corresponding to to 4.2 and 6.1 standard deviations above a background-only hypothesis, respectively.

Wt+$\mathrm{t\bar{t}}$ Quantum Interference

The reaction in the second line of Eq. 2.20 is identical to the gluon fusion reaction ($gg \to t\bar{t}$) depicted by the diagrams in Fig. 2.3b and 2.3c, when considering the intermediate decay of either one of the top quarks ($t \to Wb$). In fact the W$\bar{\mathrm{b}}$ pair in Eq. 2.20 can be due to an off shell top quark propagator when considering all the possible NLO corrections to the Wt production. It follows that the two processes are virtually indistinct beyond the leading order; therefore, from a rigorous theoretical approach, one should conclude that Wt production does not exist, and that its status as independent process is an accident of perturbation theory at leading order. Once the sum of the quantum amplitudes is made explicit, most of the interferences are cancelled by a different colour structure of the vertices as in the case of the t-channel and s-channel interference. The treatment of the remaining interference terms is shortly discussed here, while for a complete treatment of the topic the reader is addressed to [WFLM09], where a full and satisfactory solution is given.

The reasoning used to restore the Wt production as a distinct process is based on the kinematics of the additional $\bar{\mathrm{b}}$ quark in Eq. 2.20. It is easy to expect that, yet being on shell, the quarks coming from the splitting of the partonic gluon are mostly collinear, and are not expected to carry an amount of transverse momentum significant enough to escape the beam pipes and the LHC and undergo the detection. The situation is different for the decay products from the production of $\mathrm{t\bar{t}}$ pairs, which are produced mainly back-to-back in the plane transverse to the collision axis. It is then expected that the collinear $\bar{\mathrm{b}}$ quark from the NLO correction to the Wt production and either one of the b($\bar{\mathrm{b}}$) quarks in $\mathrm{t\bar{t}}$ events belong to different regions of the phase space. It is demonstrated in [WFLM09] that the interference between the two classes of processes vanish when applying the kinematic cuts necessary to reconstruct the physical objects in the context of the experimental setup,

and the single top production in association with a W boson is a well distinct process in quantum sense. The practical dealing with the interfering diagrams while producing NLO computations in the context of parton shower approach, which will be treated in more detail in Sec. 3.3, is described in [Zhu02, CT05, FLM+08, FW08]. Depending on the treatment of the interference, the following two working definitions of Wt production can be given:

- *diagram removal*: removal of resonant $t\bar{t}$ effects from Wt at the *amplitude level* by not including the gluon-fusion diagrams in Fig. 2.3b.
- *diagram subtraction*: subtraction of resonant $t\bar{t}$ effects from the *squared amplitude* of the Wt production cross section.

The difference, either in the diagram removal or the diagram subtraction framework scheme, provides a measure of the interference between Wt and $t\bar{t}$ production; by comparing the analysis results from Monte Carlo samples produced with both codes, one is able to test whether interference effects represent a problem for a given set of analysis cuts or not. If the interference is small, it is proved that the two WWbb final states belong to two *distinct* observables in quantum sense, which one is then allowed to flag as Wt-like and $t\bar{t}$-like signatures. The comparison between the two removal schemes of total cross section prediction and kinematic distributions shows an agreement at the 3% level. An ultimate test is given by demonstrating that the isolation of Wt-like events is possible *above* the uncertainty of the $t\bar{t}$ production rate due to renormalisation scale variation, in both the removal schemes.

$\sqrt{s}$ (TeV)	Process	σ_{sgtop} (pb)	Scale Unc. (pb)	PDF Unc. (pb)
7	t-channel	65.9	+2.1/-0.7	+1.5/-1.7
	s-channel	4.63	+0.20/-0.18	
	Wt-channel	15.74	+1.17/-1.21	

Table 2.2.: Predicted cross sections at approximate NNLO of the single top production processes at centre-of-mass energy of $\sqrt{s} = 7\,\text{TeV}$. The values are computed assuming $m_t = 173\,\text{GeV}$ for the t-channel, and $m_t = 172.5\,\text{GeV}$ for the s and Wt channel respectively [Kid11, Kid10a, Kid10b]. For the t-channel case, the PDF error of the calculation includes the additional contribution of the α_S uncertainty.

2.4. Topology of Wt events and backgrounds

The top quark decays principally into a beauty quark and a real W boson, following well known kinematics , as described in Sec. 2.2; the signature of the top quark decay inside a detector is therefore defined by the decay of the W boson, and its branching ratios (BR).

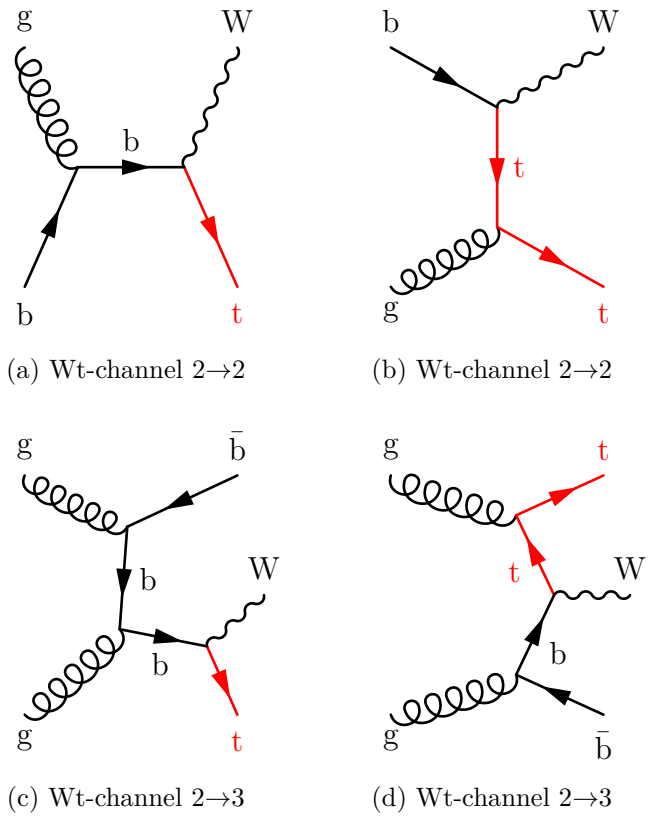

(a) Wt-channel 2→2 (b) Wt-channel 2→2

(c) Wt-channel 2→3 (d) Wt-channel 2→3

Figure 2.7.: Production of single top quarks in the Wt-channel. In diagrams (a) and (b) the 2→2 particles processes are shown. Diagrams (c) and (d) represent the contribution from the 2→3 processes due to gluon-splitting, which lead to the interference with the $t\bar{t}$ production shown in Fig. 2.3.

Before discussing the experimental signature of the Wt events and its backgrounds, it is important to focus on the fact that the number of jets in a hard process is not fixed. Any process where partons are involved has a probability proportional to α_s to occur with the presence of an extra parton (either a quark or a gluon) in the final state, and it has been shown that recursive scaling laws exist of the form:

$$\frac{\sigma(\text{X+(n+1)partons})}{\sigma(\text{X+n partons})} = \alpha_s, \tag{2.21}$$

where X represents any existing final state. Processes such as single top and $t\bar{t}$ pairs production follow a similar behaviour.[4] As a direct effect, the number of partons in the final

[4]Precise measurements of α_s at hadron colliders are based on Eq. 2.21.

states of the processes at the LHC is not limited to the LO predictions. For this reason events containing Ws in the final state, that are characterised by a huge LO production cross section, can acquire extra jets maintaining a production rate that is larger than the signal, thus mimicking a signature with a high number of jets and entering the final yields in a significant amount.

2.4.1. Experimental Signature of Wt Events

The identification of Wt events is determined by the composition of its final states, which are defined by the decay of the W bosons originated in the intermediate process:

$$\mathrm{tW} \rightarrow \mathrm{bW} + \mathrm{W}. \tag{2.22}$$

The situation is then identical to the final state of the $\mathrm{t\bar{t}}$ decay explained later on in Sec. 2.4.3, with the difference that there is a b-jet less. Depending on whether both or only one W boson in Eq. 2.22 decay leptonically, the search channels are named *fully leptonic* and *semi-leptonic*. [5] A summary of the main decay fractions of two W bosons is depicted in Fig. 2.9. The production rate of Wt events is very small when compared to those SM processes with experimentally similar final states, as can be seen from the production cross sections listed in Tab. 2.3. For this reason the presence of at least one lepton in the event is a necessary request to isolate the signal above the huge QCD background processes which is completely constituted of hadrons and appears as only populated of jets; the *fully hadronic* final states are therefore not taken into account for the signal extraction and not discussed any further. Since the τ lepton is a particle of difficult identification with an intrinsic background formed by jets faking its signature, only the electron and the muon are left in order to mark the decay, and the experimentally available branching fraction of the dilepton final state is therefore reduced to 4%, while it raises to 30% in the single lepton case. The lepton+jets search mode, is then a fair compromise between the need of statistical precision and the discrimination against the background. The partonic reaction expected is then the following:

$$\mathrm{tW} \rightarrow \mathrm{bW} + \mathrm{W} \rightarrow \mathrm{b}\,\ell\,\nu_\ell\,\mathrm{q}\,\bar{\mathrm{q}}' \tag{2.23}$$

where one W boson in the intermediate state decays hadronically and the other one decays leptonically.

Since the lifetime of both the top quark and the W bosons are way too short to allow for the reconstruction of their decay vertices, an intrinsic ambiguity is raised, being impossible to establish univocally the decay mode of the W boson emitted by the top quark the W boson produced in association in Eq. 2.23. Due to the confinement, free quarks are not directly observable but can be reconstructed as jets of hadrons. The topology of the Wt events is the shown in Fig.2.8. In order to identify the Wt events, the following reconstructed objects

[5] These two search modes are also addressed, in the current literature, as *dileptonic* and *lepton+jets*.

are expected in the final state:

- Exactly one high-p_t isolated lepton (e, μ).
- One neutrino (appearing in as an high amount of energy missing in the transverse plane).
- One high energy b-jet originating from the b-quark of the top quark decay.
- Two high energy jets resulting from the hadronic decay of one of the two W bosons in the event. These jets have mostly light flavours.

The objects listed above are likely to have high-p_t values and populate the central region of the detector. As previously discussed in Sec. 2.3.2 for the NLO correction, the additional b-quark produced in Fig. 2.7d coming from the splitting of the gluon in the initial state is mostly collinear with respect to the partonic gluon and therefore emitted close to the beam direction, thus escaping the detection.

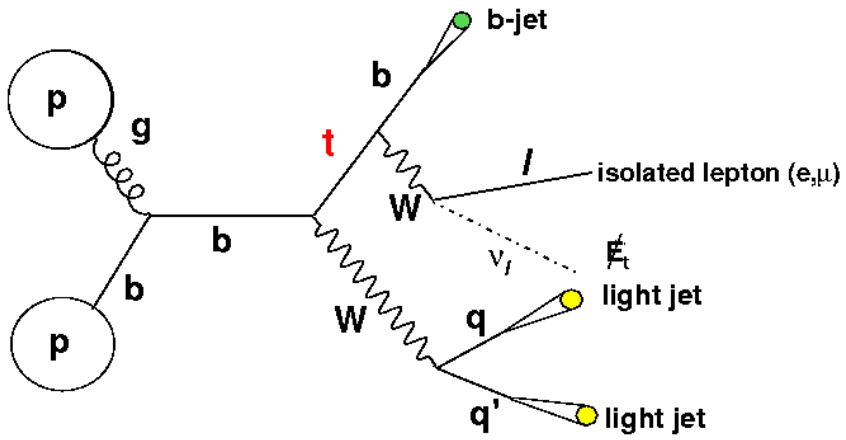

Figure 2.8.: Event topology of a Wt production event. Here, W boson from the top quark decays leptonically. Exactly one b-jet is required in the selection to identify the decay of the top quark. The transverse component of the momentum of the neutrino from the W boson decay is attributed to the missing transverse energy measured in the event.

.

2.4.2. Other Single Top Processes

The two other single top production modes, t-channel and s-channel enter the selection defined above, due to the presence of a real top quark accompanied by at least one jet in the final state, and to the NLO effects discussed in the beginning of this section.

t-channel

As seen in Sec. 2.3.2 the single top events produced in the t-channel are characterised by the presence of a highly energetic jet in the very forward region of the detector. This different feature, along with a comparable production rate (*cf.* Tab. 2.3), result in a minor contribution from t-channel events in the final yield, since the occurrence of additional highly energetic jets is suppressed according to the scaling law shown in Eq. 2.21.

s-channel

The single top quarks produced in the s-channel have a very small production rate (*cf.*Tab. 2.3), as shown in Sec. 2.3.2. By applying the set of kinematic cuts shown above, the contribution to the final yield is expected to be negligible. The fraction of these events in the final count is diminished further by requiring exactly one b-quark in the final state, a cut principally aimed at reducing the $t\bar{t}$ background.

2.4.3. Top Pair Production

Pairs of real top anti-top quarks are produced with a rate that is approximately ten times bigger than events containing a single top quark (*cf.* Tab. 2.3), which renders the $t\bar{t}$ production the main background to single top events. The decay modes of $t\bar{t}$ pairs are classified in the exact same way described above for the production of Wt associated events, due to the presence of two real W bosons from the decay of the top quarks, whose branching fractions are summarised in Fig. 2.9. In the following reaction the semi-leptonic decay of a $t\bar{t}$ pair is shown:

$$t\bar{t} \rightarrow bW^{+}\ \bar{b}W^{-} \rightarrow bq\bar{q}'\ \bar{b}\ell^{-}\nu_{\ell}\ + \text{c.c.} \tag{2.24}$$

The final states populating Eq. 2.24 are very similar to those of the Wt associated production events shown in Eq. 2.23, since the only difference is represented by the presence of one additional b quark. [6] As for the associated Wt events, the decay products of the $t\bar{t}$ pairs are mainly produced centrally in the detector.

[6] It is important to note here that the tagging of jets containing b quarks is a challenging task in itself and prone to systematic errors (described in detail in Chap. 4 dedicated to the reconstruction of physical objects in ATLAS).

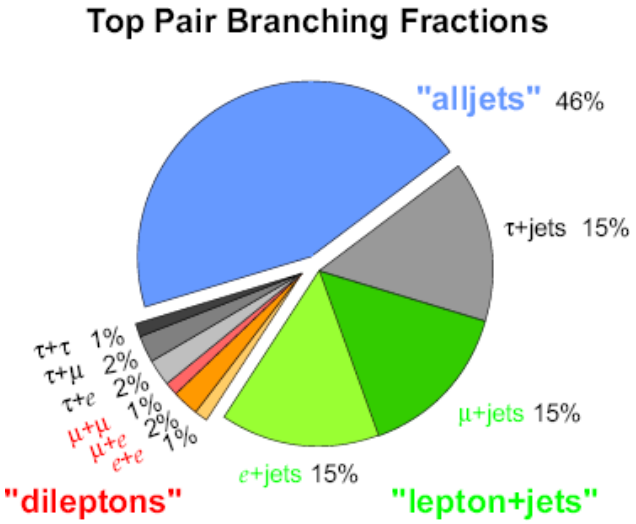

Figure 2.9.: Branching ratios of the W pair produced in $t\bar{t}$ and Wt production. The leptonic flavour breakdown shows that a 30% fraction is accessible to a single lepton selection limited to electronic and muonic final states.

2.4.4. W+Jets Production

The W bosons are produced at the LHC mainly via the annihilation of quark-antiquark pairs of different flavour. Bosons produced by leading order interactions are produced at rest with respect to the transverse plane, but can gain momentum when perturbations occur, with the appearance of one or more additional partons in the final state. Examples of production of W bosons at hadron colliders are depicted in Fig. 2.10. The leading production is shown in Fig. 2.10a with the subsequent leptonic decay of the on-shell W boson. Following the scaling law of Eq. 2.21 events of the kind depicted in Fig. 2.10b and 2.10d can occur, so that extra partons enter the final state of the process entering the selection according to the jet multiplicity. Without a selection based on the physical properties of a top quark events with a leptonically decaying W boson and three additional partons in the final state are virtually identical to the Wt production. When a gluon is emitted from an initial quark with a high transverse energy, it can further split into a pair of heavy flavour quarks as in Fig. 2.10d, thus contributing to the b-tagged signal. Single heavy flavour quark can also be produced through electroweak charged currents in association with a W boson, as shown in Fig. 2.10c. The production rates of W bosons with respect to a varying number of additional partons at the LHC are computed in [A$^+$10f], and reported in Tab. 2.3. The uncertainty on the cross section prediction for the W+jets production has been evaluated in Ref. [A$^+$10b] and follows the α_s scaling law of Eq. 2.21, yielding an iterative 24% uncertainty for the increasing number of partons in the final states. The resulting overall uncertainty on the cross section normalisation for the W+jets production is about 60%. To overcome the effect of this uncertainty on the final result the data-driven model based on charge asymmetry

described in Sec. 4.3.2 has been developed.

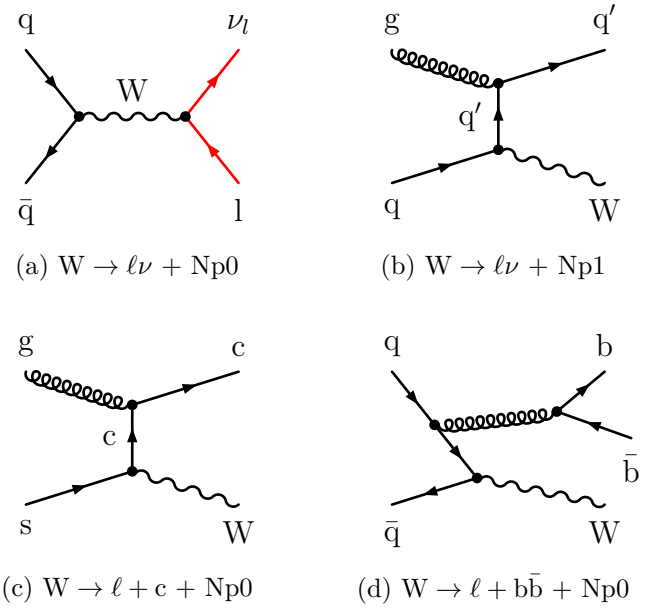

(a) W $\to \ell\nu$ + Np0 (b) W $\to \ell\nu$ + Np1

(c) W $\to \ell$ + c + Np0 (d) W $\to \ell + b\bar{b}$ + Np0

Figure 2.10.: Some exemplary W+Jets production modes. The production modes of a W boson with and without an additional light flavour parton are shown in (a)and (b). The production of a W boson in association with only one charmed quark without additional partons is shown in (c). In (d) the production of a $b\bar{b}$ pair in the final states is shown.

2.4.5. Z+Jets Production

The production of Z bosons in association with a varying number of partons in the final state is quite similar to the W+jets case discussed in Sec. 2.4.4, but happens with a total cross section which is about 10 times smaller, which is the result of two combined effects; on one hand the leptonic branching ratio W $\to \ell\nu$ is about 3 times larger than its equivalent Z $\to \ell\ell$, while on the other hand a further factor of order 3 is given by the difference in total cross sections, due to the boson mass difference. The background is formed by those events where a Z boson decays into leptons and where additional partons populate the final state, as shown in Fig. 2.11a and 2.11b. A misreconstructed object (a lepton or a jet) in such events can result in a big amount of missing transverse energy, that can fake the presence of a neutrino. Z+jets events are usually rejected by requiring the presence of only one high energy lepton in the final state. The theoretical cross sections for the production of Z+jets as a function of the number of additional partons is provided in Tab. 2.3. The overall uncertainty on the predicted cross section is evaluated according to the same procedure described in Sec. 2.4.4,

assuming a 60% variation from the central value. No data-driven method is employed in this case, due to the small impact of Z+jets events on the final selection.

2.4.6. Diboson

Events with a pair of any weak bosons in the final state have a rather small production rate when compared to the other processes treated in the above sections. The small size of the production rate is due to the fact that (at leading order) only a $q\bar{q}$ pair can ignite the electroweak reaction. Two exemplary Feynman diagrams that contribute to the production of diboson events at the leading order are drawn in Fig. 2.11c and 2.11d. The weak coupling occurs twice, thus further suppressing the production rate. A high energy lepton can arise from the decay of either one of the two boson produced, allowing the other to decay into a $q\bar{q}$ ($q\bar{q}'$) pair. The leading contribution is given by WZ events that enter the final count from the selection given in Sec. 2.4.1, when the W boson decays into a lepton and a neutrino, and the Z boson decays hadronically and one additional parton is produced via QCD interactions with a quark from the initial or final state. The theoretical cross sections for the inclusive diboson production are provided in Tab. 2.3.

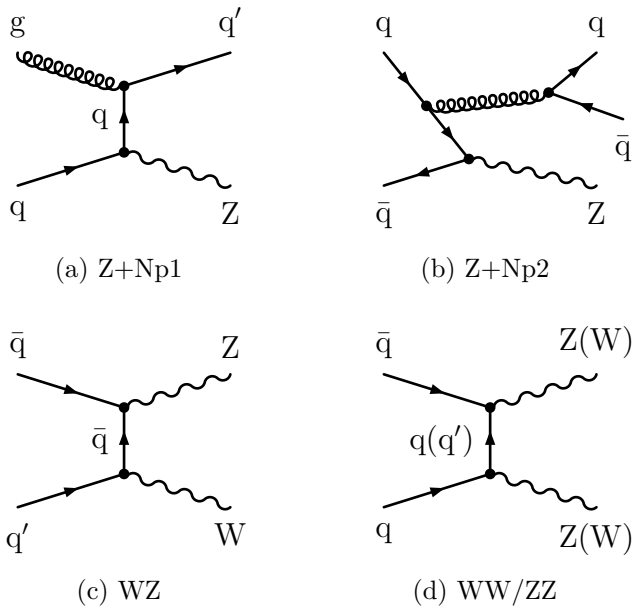

(a) Z+Np1 (b) Z+Np2

(c) WZ (d) WW/ZZ

Figure 2.11.: Some exemplary Z+Jets and dibosons production modes. The production of a Z produced in association with one and two additional partons is shown in diagram (a) and (b) respectively. The production of dibosonic final states is shown in (c) and (d).

2.4.7. QCD Multi-Jet Events

The production of high energy jets through pure QCD interactions is the process occurring with the highest rate during LHC collisions, as shown in the production cross section comparison plot in Fig. 3.9. The magnitude of the cross section for the inclusive production of jets [7] events is of $\mathcal{O}(10^{10}\,\text{pb})$, which is about eight orders of magnitude larger than the typical top quark production rates. After the standard lepton selection cuts recommended by the top quark physics performance groups (*cf.* Sec. 4.1 and Ref. [A+12k]) particle jets with low transverse momentum constitute the main source of background for the electron and muon reconstruction algorithms. The combination of reconstruction algorithms with necessarily finite rejection power with the high jet multiplicity in QCD events leads to the fact that the probability that a jet is reconstructed as a lepton is statistically non zero. At the same time, algorithms mistaking a jet for a lepton or one simple jet escaping detection, added to inevitable object energy resolution effects, can lead to a total amount of energy reconstructed in the event (*cf.* Sec. 3.5.8), that is significantly different from zero. As a result, the total energy produced in the event is unbalanced in the transverse plane, appearing as if a energetic neutrino has been produced, allowing a small fraction of events to pass the selection cuts. After the standard selection criteria, the QCD-induced *lepton fake* events contribute to about 10 to 1 % of the final event yield, with the exact figures depending on the jet multiplicity and on the presence of a b-jet in the reconstructed final state. The *data-driven* technique presented in Sec. 4.3.1 has been adopted to estimate the QCD contribution to the total background in the analysis.

[7] More specifically the production of events containing at least one jet, emitted in the ID acceptance region, carrying a minimum transverse momentum $p_{\text{t}} > 20\,\text{GeV}$, *cf.* Ref. [A+12f].

Process	Final States	σ (pb)	MC Generator
Single Top	Wt-channel (incl. semi-/dileptonic)	15.7426	MC@NLO+JIMMY
	t-channel eν	6.971	ACERMC+PYTHIA
	t-channel $\mu\nu$	6.971	ACERMC+PYTHIA
	t-channel $\tau\nu$	6.971	ACERMC+PYTHIA
	s-channel eν	0.348	MC@NLO+JIMMY
	s-channel $\mu\nu$	0.348	MC@NLO+JIMMY
	s-channel $\tau\nu$	0.348	MC@NLO+JIMMY
$t\bar{t}$	(incl. semi-/dileptonic)	90.5455	MC@NLO+JIMMY
W+LF jets	W $\to \ell\nu$ + Np0	8306	ALPGEN+JIMMY
	W $\to \ell\nu$ + Np1	1566	ALPGEN+JIMMY
	W $\to \ell\nu$ + Np2	455	ALPGEN+JIMMY
	W $\to \ell\nu$ + Np3	122	ALPGEN+JIMMY
	W $\to \ell\nu$ + Np4	31	ALPGEN+JIMMY
	W $\to \ell\nu$ + Np5	8.4	ALPGEN+JIMMY
W+HF jets	W $\to \ell$ + c + Np0	979	ALPGEN+JIMMY
	W $\to \ell$ + c + Np1	312	ALPGEN+JIMMY
	W $\to \ell$ + c + Np2	77.2	ALPGEN+JIMMY
	W $\to \ell$ + c + Np3	17.3	ALPGEN+JIMMY
	W $\to \ell$ + c + Np4	4.26	ALPGEN+JIMMY
	W $\to \ell + c\bar{c}$ + Np0	153	ALPGEN+JIMMY
	W $\to \ell + c\bar{c}$ + Np1	126	ALPGEN+JIMMY
	W $\to \ell + c\bar{c}$ + Np2	62.5	ALPGEN+JIMMY
	W $\to \ell + c\bar{c}$ + Np3	20.4	ALPGEN+JIMMY
	W $\to \ell + b\bar{b}$ + Np0	56.8	ALPGEN+JIMMY
	W $\to \ell + b\bar{b}$ + Np1	42.9	ALPGEN+JIMMY
	W $\to \ell + b\bar{b}$ + Np2	20.8	ALPGEN+JIMMY
	W $\to \ell + b\bar{b}$ + Np3	7.96	ALPGEN+JIMMY
Z+jets	Z $\to \ell\ell$ + Np0	835	ALPGEN+JIMMY
	Z $\to \ell\ell$ + Np1	168	ALPGEN+JIMMY
	Z $\to \ell\ell$ + Np2	50.7	ALPGEN+JIMMY
	Z $\to \ell\ell$ + Np3	13.9	ALPGEN+JIMMY
	Z $\to \ell\ell$ + Np4	3.6	ALPGEN+JIMMY
	Z $\to \ell\ell$ + Np5	1.04	ALPGEN+JIMMY
Diboson	WW (incl. semi-/dileptonic)	17.02	HERWIG
	WZ (incl. semi-/dileptonic)	5.54	HERWIG
	ZZ (incl. semi-/dileptonic)	1.26	HERWIG

Table 2.3.: MC simulation samples used in the analyses.

3. Experimental Setup

In this chapter the experimental complex that has been used for the analysis is presented together with the Monte Carlo techniques employed for the data simulation and the algorithms developed for the reconstruction of the physical objects. The LHC machine and the ATLAS detector are described respectively in Sec. 3.1 and 3.2; all the subdetectors are outlined, with special emphasis on those systems that are most related to this analysis. The description of the experimental complex throughout this chapter is mainly based on [A+08].

3.1. The Large Hadron Collider

The Large Hadron Collider (LHC) is a proton-proton collider situated at the European Centre for Nuclear Research (CERN) near Geneva, at the border between France and Switzerland. The LHC is placed in the same tunnel where the LEP, the previous e^+e^- collider, was situated, about 100 m under the ground level with a circumference of 27 km. The choice to build a hadron collider is due to the fact that the particles that in reality take part to the fundamental interactions are the partons inside the accelerated hadrons, which at the energies needed to conduct frontier physics experiments can be seen as mere wrappings of substantially free quarks and gluons. These constitute the partons inside the proton, and carry a fraction x of its momentum (as explained in Sec. 2.14). As a direct result, a broad centre-of-mass energy range becomes available for hard processes to occur, and therefore an hadronic collider is the most suitable choice for a machine aimed at the discovery of new physical phenomena when the energy scale of their occurrence is unknown. New physics effects linked to the electroweak symmetry breaking are expected to show up at the TeV energy scale. When hadronic beams reach these scales of energy, the valence quarks contribution in the PDFs (see Sec. 2.3) becomes small and the most of the hadron composition is accounted by gluons and quark pairs from the QCD sea. For this reason a proton-proton machine was chosen in stead of a proton-antiproton one; the intensity of the beams is therefore highly increased, by avoiding the technical complexities of the production, accumulation, storage and acceleration of intense anti-proton beams.

The protons are pre-accelerated by the systems depicted in Fig. 3.1 from LINAC 2 to the SPS, where they are stored at the energy of 450 GeV, and injected in the LHC where they are accelerated until they reach the designated energy. In the very first phase of the operations the beams were not accelerated but test analyses of collisions at the centre-of-mass energy of 900 GeV and 1.38 TeV were performed, in order to ensure the correct behaviour of the collider

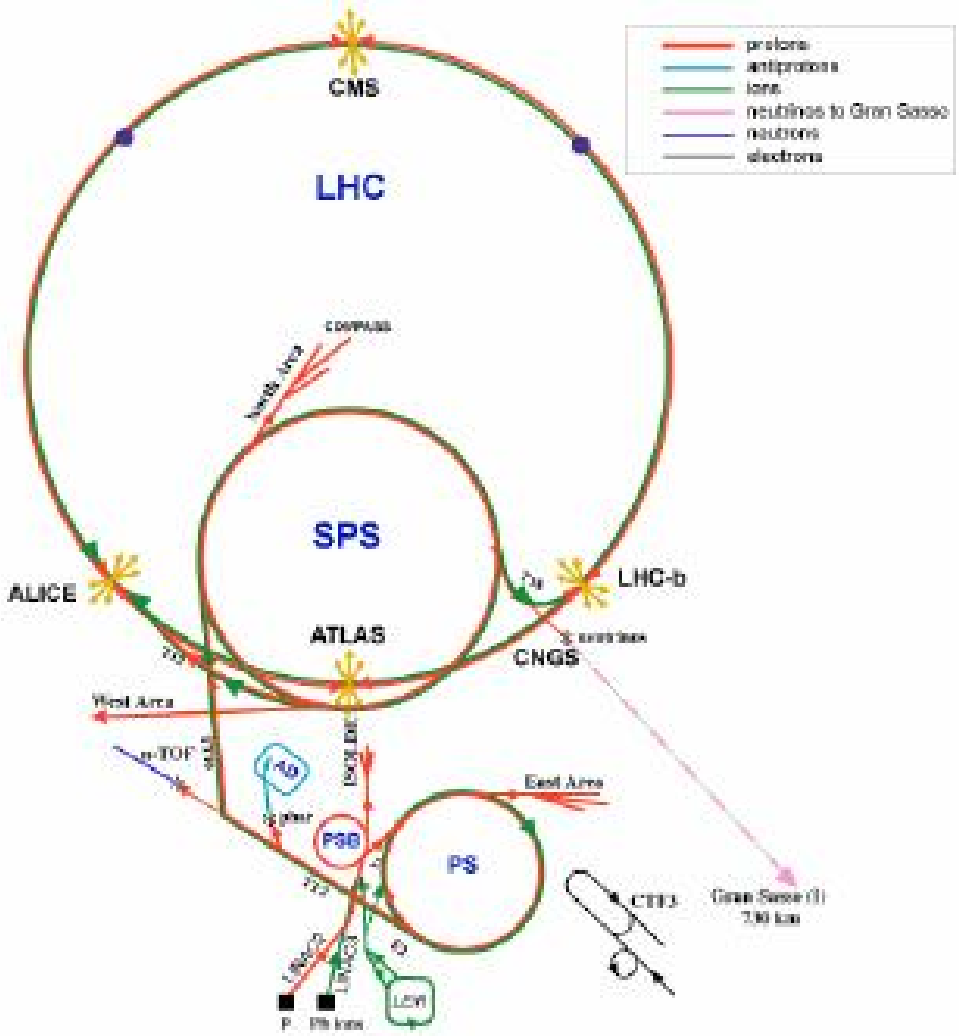

Figure 3.1.: The CERN accelerator complex showing the Large Hadron Collider, the experiments and the existing accelerator facilities. Protons are accelerated in sequence in the LINAC 2, the Booster and the PS to be bundled and stored in the SPS where they reach the energy of 450 GeV before being injected into the LHC.

and the four detectors within a physics domain already known since the Sp$\bar{p}$S operations. After the September 2008 incident, the working point energy of 3.5 TeV for stable beams used for collisions was chosen and an overall integrated luminosity of $5\,\text{fb}^{-1}$ was delivered in the years 2009-2011. In 2012, the last year of operations before a two years long shutdown, the LHC beam energy was raised to 4 TeV. For the purposes of this analysis, the full dataset of proton-proton collisions recorded at the centre-of-mass energy of 7 TeV will be used. During the last month of operations of the each year of activity, the LHC was set to work as a heavy ions collider, accelerating Pb nuclei instead of protons.

In order to accelerate protons up the 3.5 TeV a 8.4 T transverse magnetic field is generated by a current of about 11.7 kA in superconducting magnets of NbTi operating in pressurised superfluid helium at the absolute temperature of 1.9 K. The LHC is constituted of 1232 dipoles for beam bending purposes; in addition, 392 quadrupoles, 688 sextupoles and 168 octupoles are employed for the beam squeezing and focusing. The final beams are composed of a number of bunches that increased from 2009 to the end of 2011 to a maximum value of 1392 bunches per fill, where each bunch contains $\mathcal{O}(10^{11})$ protons. The beams circulating in the LHC are crossed in four points, where the collisions take place inside each of the four "4π"-coverage experiments respectively conducted by the ATLAS, CMS, ALICE and LHCb collaborations.

In Fig. 3.11 the integrated luminosity delivered by the LHC and the fraction recorded by ATLAS are put into comparison for the whole data taken in 2011 at 7 TeV of centre-of-mass energy that is used in this work. The delivered luminosity (green) accounts for the luminosity delivered from the start of stable beams until the LHC requests ATLAS to turn the sensitive detector off to allow a beam dump or beam studies. Given is the luminosity as determined from counting rates measured by the luminosity detectors.

3.2. The ATLAS Detector

ATLAS is a general-purpose detector, designed to explore physics phenomena that can happen on a broad energy scale, ranging from 100 GeV – about the lower limit for the mass of the SM Higgs boson at the time of the design – up to 1 TeV where a whole new world of particles might lie waiting for detection, as predicted by several New Physics models, and which is the upper constraint on the Higgs boson mass prediction from the unitarity of the theory. In order to fully exploit the opportunities given by the LHC, the ATLAS needs to meet the challenges imposed by the experimental environment. The ATLAS detector, of which a visualisation is provided in Fig. 3.2, includes:

- High-precision trackers for the accurate measurement of momenta of charged particles in a high-occupancy environment, for the measurement of the position of the primary interaction vertex and for the identification of secondary vertices coming from the decay of long-lived particles (B-mesons, τs),

- Electromagnetic and hadronic calorimeters for the identification and energy measurements of electrons, pions, photons and hadronic jets and for the reconstruction of missing energy in the transverse plane,
- A muon spectrometer for the precise reconstruction of high-p_{t} muons,
- A multi-level trigger system, able to discern interesting physics events from the overwhelming background (*cf.* Fig. 3.9).

The ATLAS detector is built in the typical configuration of experiments at symmetric particle colliders: subdetectors are positioned in concentric layers around the beam axis (the barrel section) and in wheels (the end-caps) that close the ends of the cylinder. ATLAS is 40 m long with a diameter of 22 m. The first barrel layer, located next to the interaction point, is the Inner Detector (ID); this apparatus is composed of three sub-detectors: (from inside to outside) the Pixel Detector, the Semi-Conductor Tracker (SCT) and the Transition Radiation Tracker (TRT). A brief summary of the ID subsystems is given in Sec. 3.2.3. The hits recorded by the Inner Detector allow to reconstruct the trajectories of the charged particles, to distinguish between primary and secondary vertices and to measure the momenta of the tracked particles. The reconstruction of secondary vertices is crucial for the identification of jets initiated by b-quarks (*cf.* Sec. 3.5.7). The Inner Detector is surrounded by a large cryostat, which contains the Central Solenoid and the Liquid Argon (LAr) calorimeter. The Central Solenoid is constituted of a superconducting coil and generates a magnetic field oriented along the beam axis, that serves to measure the momenta and the sign of the tracks. The liquid argon calorimeter is responsible for the measurement of the energy of electromagnetic showers initiated by electrons and photons. The ATLAS calorimetry in the barrel region is completed by the Tile calorimeter (TileCal), which measures the energy deposited by showers not contained within the liquid argon calorimeter, principally caused by hadrons. The steel structure of the TileCal is used as yoke for the return flux of the solenoid. A more detailed description of the ATLAS calorimetry systems is given in Sec. 3.2.4. The outermost ATLAS barrel layer is the Muon Spectrometer (MS), which uses a separate magnetic field, generated by eight superconducting coils deployed radially around the beam axis. The coils create a toroidal magnetic field that surrounds the whole ATLAS barrel. The Muon Spectrometer, described in Sec. 3.2.5, uses two types of chambers in the barrel region: Monitored Drift Tube (MDT) chambers for precision measurements, and Resistive Plate Chambers (RPC) for triggering. Inside the Muon System barrel, two cryostats seal the calorimeters and the inner detector. Behind each cryostat a wheel of Cathode Strip Chambers (CSC) is located. The end-caps have their own dedicated toroidal magnetic fields, generated by two eight-coil toroids contained by the cryostats that plug into the ATLAS barrel. The Muon Spectrometer in the end-cap region consists of MDT chambers and Thin Gap Chambers (TGC), which complete the muon trigger. The MDTs and TGCs are mounted on wheels placed between the ATLAS end-caps and the walls of the underground experimental area. Two high-density Forward Calorimeters cover the very forward

region of ATLAS and enhance the hermeticity of the detector. Two beam shields connect the ATLAS to the LHC accelerator and protect the end-cap instrumentation from beam radiation and radio-frequency fields. The nominal performance of the ATLAS components is summarised in Tab. 3.1.

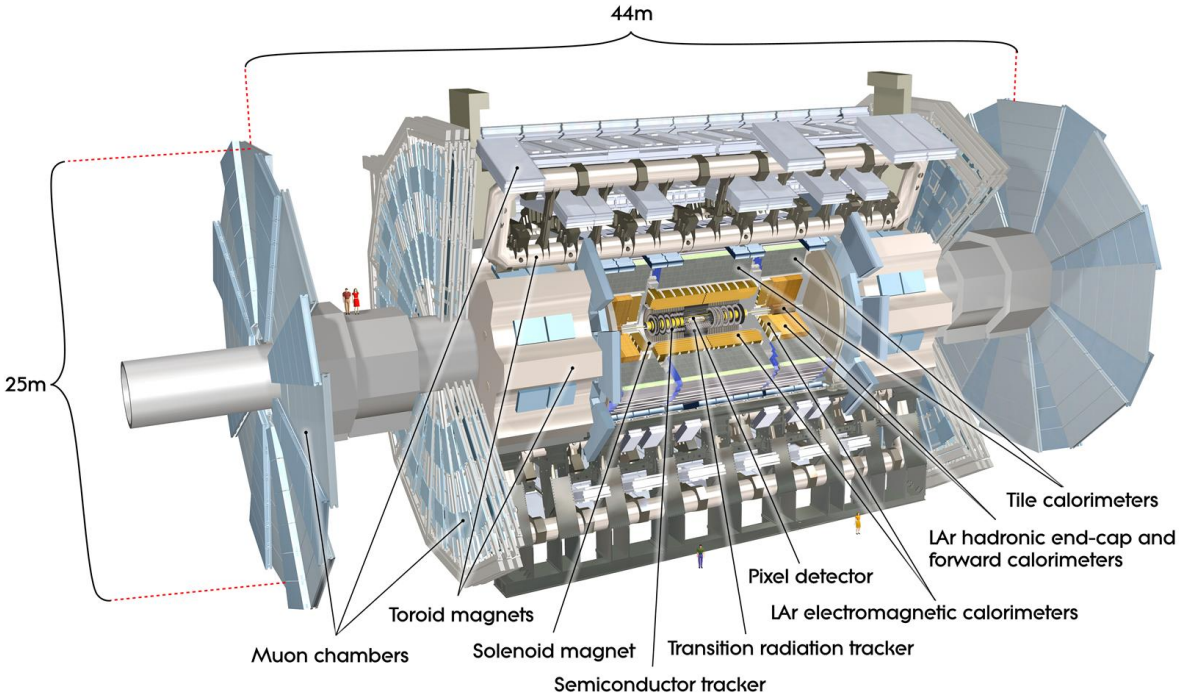

Figure 3.2.: View of the ATLAS detector. From inside out the Inner Detector, the calorimeters and the Muon System are visible. The solenoid and toroid magnets are embedded in the structure [A+08].

3.2.1. The ATLAS Coordinate System

The system of coordinates and the nomenclature employed for the detector description are shortly summarised here, as they are used repeatedly throughout this thesis. The origin of the coordinate axes system is taken in the nominal interaction point, while the beam direction defines the z axis and the xy plane is transverse to it. The positive x and y axes are respectively defined as pointing inside the LHC ring and in the upward direction, while the anti-clockwise verse of the collider is adopted as positive z-axis.

As it is shown in figure 3.2 the ATLAS detector has a cylindrical geometry; a set of polar coordinate system (R, η, ϕ) is then assumed for the analysis. For the detector geometry, a set of Cartesian Oxyz is assumed, where z is the position in the direction along the beam

Detector component	Required resolution		η coverage
Inner Detector	$\sigma_{p_t}/_{p_t} = 0.05\,\% \cdot p_t$	$\bigoplus 1\,\%$	$\pm$ 2.5
EM Calorimeter	$\sigma_E/_E = \frac{10\,\%}{\sqrt{E[\mathrm{GeV}]}}$	$\bigoplus 0.7\,\%$	$\pm$ 3.2
Hadronic Calorimeter:			
Barrel & End-Caps	$\sigma_E/_E = \frac{50\,\%}{\sqrt{E[\mathrm{GeV}]}}$	$\bigoplus 3\,\%$	$\pm$ 3.2
Forward	$\sigma_E/_E = \frac{100\,\%}{\sqrt{E[\mathrm{GeV}]}}$	$\bigoplus 10\,\%$	$3.1 \leq \lvert\eta\rvert \leq 4.9$
Muon System	$\sigma_{p_t}/_{p_t} = 10\,\%$	at $p_t = 1\,\mathrm{TeV}$	$\pm$ 2.7

Table 3.1.: General performance of the ATLAS detector [A+08]

.

axis, and a radius R is taken as the radius in xy plane centred in the nominal interaction point. The angle ϕ is the azimuthal angle around the beam axis. It is customary at hadron colliders to employ the pseudorapidity η as polar variable, which in terms of θ it is expressed as

$$\eta = -\ln\left(\tan\frac{\theta}{2}\right). \tag{3.1}$$

The advantage of this particular definition is that differences in pseudorapidity are invariant under boosts along the z axis. In this sense, the angular difference between two reconstructed objects is therefore defined as

$$\Delta R = \sqrt{\Delta\eta^2 + \Delta\phi^2}. \tag{3.2}$$

ATLAS Nomenclature

The detector can be roughly divided in three pseudorapidity sections:

- Barrel: $|\eta| < 1.05$,
- Extended Barrel: $1.05 \leq |\eta| < 1.4$,
- End-Caps: $|\eta| > 1.4$.

According to their position the side A of the detector is defined as the side with positive z and the side C is the side with $z < 0$. Side B is the beam-transverse plane at z = 0.

3.2.2. Magnet System

A model of the ATLAS magnet system complex is shown in Fig. 3.3. It consists of four principal components: a central solenoid (CS) that provides the magnetic field in the Inner

Detector and three large air-core toroids that generate the magnetic field in the end-caps (ECTs) and barrel (BT) regions of the Muon System. The CS creates a magnetic field in the vicinity of the interaction point with a nominal strength of 2 Tesla, that rapidly degrades in both the z and transverse direction. Its position between the Inner Detector and the calorimetric system was chosen to ensure a better performance of the track reconstruction and a simpler calibration of the cluster energy measurement. The position inside the calorimeter has then required an attentive minimisation of the material distribution, in order to avoid the showering of the particles before entering the detection zone. The two end-cap toroids are tightly inserted at each end of the central solenoid, and completely contained inside the barrel toroid. A stable and predictable magnetic field is produced in the central region ($|\eta| \leq 1.0$) by the BT and in the forward region ($1.4 \leq |\eta| \leq 2.7$) by the ECTs, while in the transition region ($1.0 \leq |\eta| \leq 1.4$) it is produced by a combination of the two.

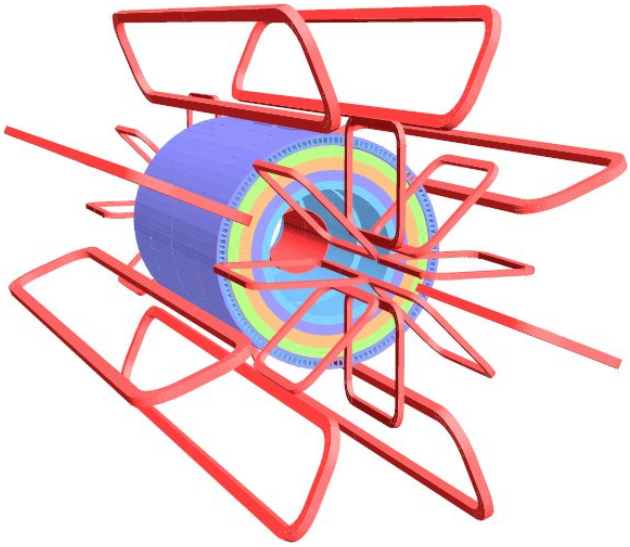

Figure 3.3: ATLAS magnet system. The eight barrel toroid coils, with the end-cap coils interleaved are visible. The solenoid is contained inside the calorimeter barrel cylinder [A+08].

3.2.3. Inner Detector

The ATLAS Inner Detector, shown in Fig. 3.4, is the result of the difficult task of addressing four simultaneous necessities dictated by the rarity and the complexity of the events investigated in the LHC physics menu. The first of ATLAS' needs is to have a reliable system able to track in fine detail the charged particles produced in the pp collisions, that is robust against both the increasing pile-up conditions and the high multiplicity environment created by the LHC beams. Secondly, the fine granularity of the tracking systems must be achieved by minimising the amount of passive (dead) material transversed by the particles, in order to not degrade the energy resolution of the calorimeters in the outer layers. Thirdly, a good identification of the charged particles is needed in the tracking region, before the absorption in the calorimeters occurs. Last but not least, budget limits have to be taken into account.

The result of such needs is an Inner Detector composed of three sub-detectors (Pixel Detector, SCT and TRT) each of them characterised by the barrel/end-cap double structure, as dictated by the cylindrical symmetry.The Inner Detector has been designed to fulfill the following major performance requirements:

- Tracks reconstruction in the region defined by $|\eta| < 2.5$,
- Transverse momentum resolution up to $\frac{\Delta p_t}{p_t} < 30\,\%$, for $p_t = 500\,\text{GeV}$ and $|\eta| < 2$,
- Efficiency about 95 % for the reconstruction of isolated tracks carrying a transverse momentum $p_t > 5\,\text{GeV}$,
- Good 3-dim vertex reconstruction and resolution of the impact parameter in order to tag jets of particles originated by prompt b quarks and τ leptons via secondary vertex identification.

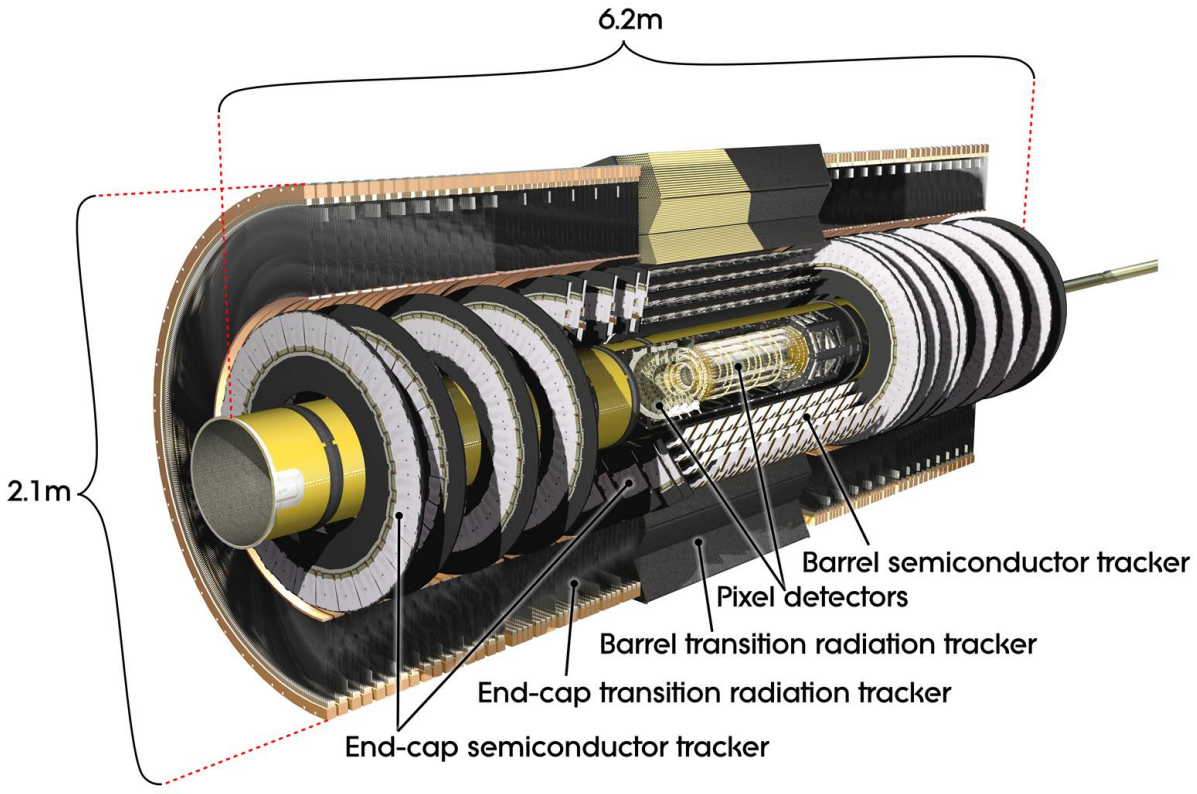

Figure 3.4.: The ATLAS Inner Detector. The sub-detector components are visible in the structure. A cross section of the barrel region and of part of the end-cap disks is shown [A+08].

Typically, three pixel layers and eight strip layers are crossed by each track, providing at least four space points precisely measured. In addition, an average of 36 hits per track is provided by the straw-tube tracker (TRT), which allows for a continuous tracking by means of a limited amount of dead material and at a sensibly lower cost. The combination of the two techniques ensures robustness and uniformity of the overall recognition and precision performance. The lower absolute precision per point achieved in the outer region of the Inner Detector – compared to the innermost semiconductor components – is balanced by the considerably larger number of measurements and the higher average radius, allowing to reach a relative precision uniform across the components. The granularity of the ATLAS Inner Detector is such that photon conversions and heavy meson decays are safely recognised. The overall particle identification performance is enhanced by the detecting the transition radiation in the TRT. The momentum resolution of the Inner Detector system is given in Tab. 3.1.

Globally, the outer radius of the Inner Detector cylinder is 115 cm, while the height is 7 m, limited by the inner size of the solenoid cryostat and the EM calorimeter end-caps respectively.

Pixel Detector

The ATLAS Pixel Detector is the innermost sub-detector of the entire complex and is therefore required to combine the highest and most feasible granularity with an excellent robustness against hardware damaging radiation expected at the LHC. Preliminary studies have shown that at least three pixel points with good efficiency are necessary to meet the performance requirements that listed in Tab. 3.1. Subsequently the following design choices and constraints are met:

- three pixel hits over the full rapidity range covered by the Inner detector, which requires a combination of barrel and disk elements;
- the smallest practical pixel size, which is set by the electronics design to 50 µm × 300 µm;
- minimum radius for the B-layer [1], which is set by practical requirements to implement the beam pipe vacuum system;
- minimum material in all elements of the system, consistent with a realistic assembly yield and safe operation.

[1] The name B-layer is given to the innermost layer of the Pixel Detector, that is mainly responsible for the determination of the impact parameter with respect to the primary vertex. The impact parameter of a track is a source of information on the lifetime of the tracked particle, and therefore the presence of B-quarks in the event can be assessed. The first of the pixel layers has a lifetime that is limited by the rate of damaging impinging radiation, and will need replacement after few years of operations. The mechanical design of the system allows the possibility of replacing the B-layer (this is referred to as "Insertable B-Layer").

The two-dimensional (pixel) segmentation of the semiconductor modules is chosen to allow for a unique determination of space points bypassing the ambiguities connected to a crossed strip geometry, thus requiring the use of advanced bonding techniques. The readout chips have a large area, with one circuit dedicated to each pixel element, and a buffering circuit is included to store the data while the Level-1 trigger decision is taken (*cf.* Sec. 3.2.7). The whole readout system is radiation hardened, in order to be able to maintain the desired performance for the designed ten years of operations, during which more than 300 kGy of ionising radiation and 5×10^{14} neutrons/cm^2 are expected.

The Pixel Detector consists of a total of 140 million silicon pixels that are identical in the barrel and end-cap disks, each one of size $50 \times 300\,\mu m^2$. The pixels are then placed on modular plates that are, also, designed identical in the barrel and the end-cap disks. Each module is 62.4 mm long and 21.4 mm wide and contains 61,440 pixel elements read out by 16 chips. The modules are distributed over three coaxial barrels – 1,500 in total, at average radii of 4 cm, 10 cm and 13 cm – and five disks perpendicular to the beam axis on each side – 700 in total, placed between radii of 11 cm and 20 cm – which cover the solid angle around the nominal interaction point up to $\eta \leq 2.5$. In order to obtain a hermetic azimuthal coverage the modules are overlapped in the support structure. The nominal thickness of each layer amounts to 1.7 % of a radiation length at perpendicular incidence. The spatial resolution $\sigma(r)$ of the Pixel Detector is of 130 µm over the entire pseudorapidity coverage.

Semiconductor Tracker

The SCT contributes to the measurement of the transverse momentum, the vertex and the impact parameter of each track. The system is constituted of independent modules, each one composed by four panels of silicon microstrip detectors. These are organised in two pairs wired together, where the two paired detector panels are glued back to back. The modules assembly allows the measurement of precision space points in the Rϕ and z coordinates per track in the intermediate radial range. The Rϕ coordinate is given by the position of the single strip crossed by the track, while the z coordinate is obtained by the design of a 40 mrad stereo angle with respect to the silicon microstrips that are glued back to back on two consecutive sides of each module, thus providing information about the crossing point. Each silicon detector is $6.36 \times 6.40\,cm^2$ and is composed by 768 readout strips 80 µm thick. The detector contains a total active area of 61 m^2 covered by silicon detectors, read out by 6.2 million channels. The system has a resolution of 17 μm in Rϕ and 580 μm in z, and can resolve 2 parallel tracks separated by 200 μm or more; this permits to resolve ambiguities in the pattern recognition, assigning each hit to a single track against the dense tracking environment. The ageing tests show that the modules containing both detectors and front-end electronics are able to resist and maintain the nominal performance throughout the expected ten years of LHC operations.

In order to provide precision space measurements, both the Pixel and the SCT systems rely heavily on high dimensional stability; for this reason the structures are realised with ma-

terials characterised by as low a thermal expansion coefficient as possible, and heat removal techniques are set into place inside the Inner Detector.

Transition Radiation Tracker

The TRT constitutes the outermost part of the Inner Detector. It consists of 36 layers of 4 mm diameter straw tubes filled with a gas mixture of 70% Xe, 20% CO_2 and 10% CF_4, needed for ionising, quenching and stabilising purposes, respectively. They are interspaced with a radiator that causes the emission of transition radiation (TR). The emission rates of transition radiation are inversely proportional to the mass of the charged particle, thus helping the particle identification. The track density is relatively low at large radii giving a number of 36 points per track. This ensures good pattern recognition performance against the large occupancy and the high counting rates sourced by the LHC. Each straw is 2 mm in radius and contains a 30 µm thick gold-plated Tungsten wire, for a maximum straw length of 144 cm. The barrel contains 50,000 straws read out at both ends, while the 320,000 radial end-caps straws have the readout chips placed at the outer radius, for a total number of 420,000 electronic channels. Each readout channel is able to measure the drift-time, that is translated into a spacial resolution of 170 µm per straw; the detection makes use of two independent thresholds connected to whether or not transition radiation above a certain threshold is generated before the hit, providing additional information to the electron identification algorithms. The straws are distributed across modular units in the barrel and end-caps; these units are positioned following a pattern that ensures that both the number of straws and the material crossed are constant. A good pattern recognition is then assured by the continuous tracking supported by 36 TRT hits per track, leading to a spatial resolution of about 10 µm in the radial direction and 115 µm in the z direction.

3.2.4. Calorimetry

The ATLAS calorimetry is represented in Fig. 3.5. The system is composed by an internal electromagnetic (EM) calorimeter and an external hadronic calorimeter, both covering the pseudorapidity region $|\eta| < 3.2$. Both systems follow the same main layout of the other ATLAS subdetectors, being divided into a barrel and two end-caps covering the central and forward region respectively. In order to analyse the collision products emitted in the most forward region, forward calorimeters are plugged in the endcaps, to cover the $3.1 < |\eta| < 4.9$ pseudorapidity range.

The barrel EM calorimeter is contained in a barrel cryostat, where the 2 T central solenoid is located, around the Inner Detector described in Sec. 3.2.3. Two end-cap cryostat host the remaining end-cap and forward calorimeters. The barrel part of the hadronic calorimeter supports the cryostats and provides the magnetic field flux return. In the $|\eta| < 1.8$ pseudorapidity range, a presampler detector is installed between the outer wall of the cryostat

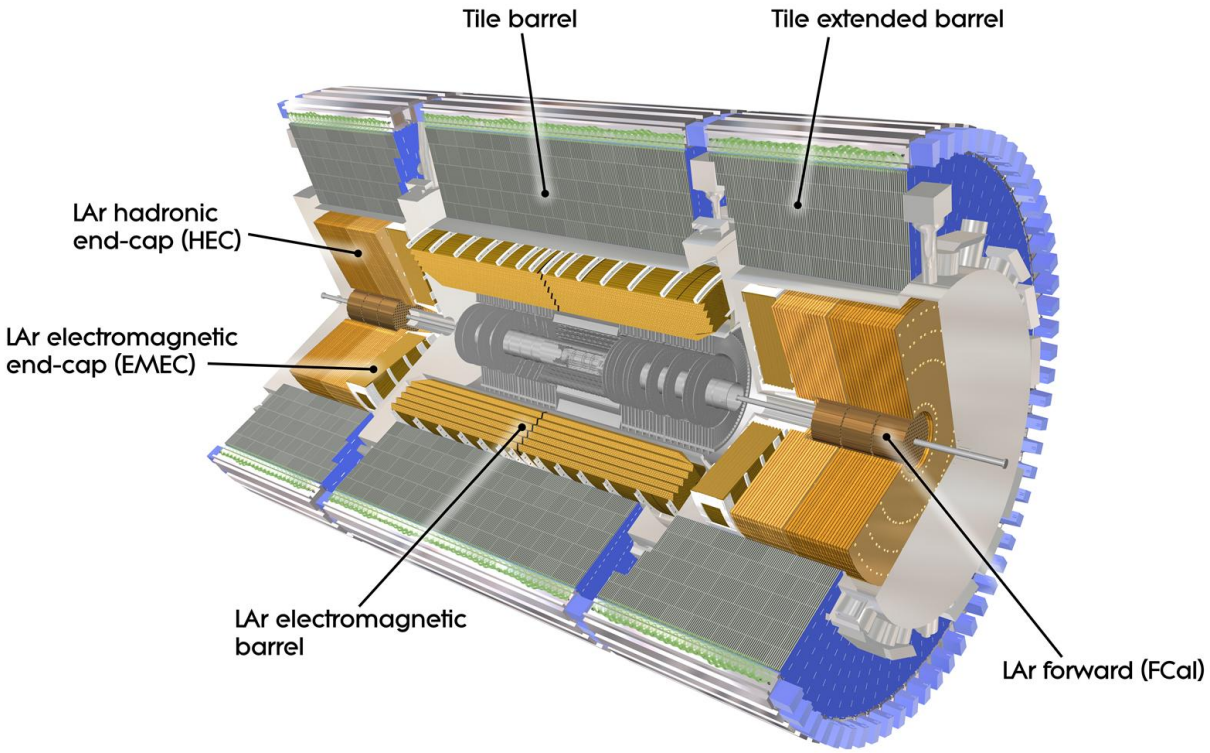

Figure 3.5.: Cross section view of the ATLAS Calorimeters. From inside out the electromagnetic and hadronic calorimeter components are shown in the barrel and end-cap regions. The Inner Detector (in grey) is visible in the centre [A+08].

that contains the solenoid and the EM calorimeter. The presampler is used to correct for the energy loss due to the dead material upstream the calorimeter (ID, cryostats, coil).

The ATLAS calorimeters guarantees a precise measurement of the missing transverse energy, $E_{\mathrm{T}}^{\mathrm{miss}}$, and in combination with the Inner Detector and the Muon System, they are able to provide a robust particle identification, exploiting the fine design granularity both in the lateral and the longitudinal direction. The energy resolution of the ATLAS calorimeters is reported in Tab. 3.1.

Electromagnetic Calorimeter

The Electromagnetic Calorimeter is a highly granular lead/liquid-argon (LAr) sampling calorimeter with accordion-shaped lead absorbers and Kapton electrodes both in the barrel and in the end-cap region. The barrel calorimeter covers the region defined by $|\eta| < 1.475$ and consists of two identical half barrels, separated by a small 6 mm gap at $z = 0$. The end-

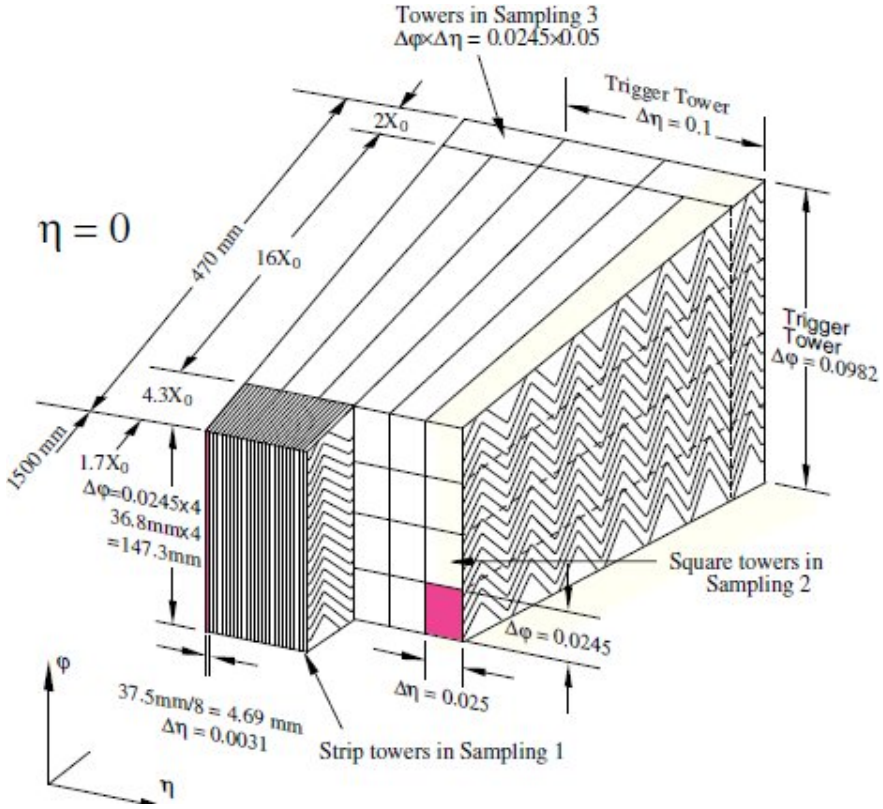

Figure 3.6.: Illustration of an Electromagnetic Calorimeter barrel section at $\eta = 0$. Here the particles enter from the left side and travel outwards in the right direction. The tower granularity in η and ϕ and the accordion folding shape across the three different longitudinal layers is shown [A+08].

caps are divided into two coaxial wheels, covering the $1.375 < |\eta| < 2.5$ and $2.5 < |\eta| < 3.2$ regions. Thanks to this geometry there are no azimuthal cracks, thus enabling the detector to have a fully hermetic coverage over the transverse plane. Also, inside the accordion folding shape the calorimeter cells are designed such to point towards the interaction region over the entire η-coverage. The LAr gap has a constant thickness of about 2 mm in the barrel, and variable with the complicated accordion geometry in the end-caps. The total thickness of the EM calorimeter is greater than 24 radiation lengths, X_0, in the barrel and greater than $26\,X_0$ in the end-caps, including the upstream material. The EM calorimeter is segmented into three longitudinal sections. The first section acts as 'preshower' and provides a good particle identification in terms of γ/π^0 and e/π separation. A precise space measurement is possible thanks to the fine $\Delta\eta \times \Delta\phi$ granularity, that spans between $0.003{\times}0.1$ to $0.006{\times}0.1$ for the $|\eta| < 2.5$ region. The middle section has a total thickness reaching $24\,X_0$ and adsorbs the most of the EM shower; it has a constant transverse granularity of 0.025×0.025 for the $|\eta| < 2.5$ region, i.e. $4 \times 4\,\mathrm{cm}^2$ at $z = 0$. The third and outermost sampling layer has a granularity of 0.05×0.1. A graphical visualisation of the accordion structure across the

cells of the three sampling layers is shown in Fig. 3.6.

A maximum of $7\,X_0$ of dead material upstream the EM calorimeter is reached at the boundary between the barrel and the end-cap components of the EM calorimeter, therefore the $1.37 < |\eta| < 1.52$ pseudorapidity regions are not used for precision physics measurements.

The EM calorimeter has a total number of about 190,000 readout channels. The signals are extracted at the inner and outer faces of the calorimeter and transported to preamplifiers located outside the cryostats.

Hadronic Calorimeter

The hadronic calorimeters cover the pseudorapidity region $|\eta| < 4.9$. Because of the wide spectrum of physics requirements and differing radiation environments as a function of the pseudorapidity, the design of the ATLAS hadronic calorimetry consists of four subsystems exploiting two different detection techniques. Over the $|\eta| < 1.7$ region, a consecutive sandwich structure of iron and plastic scintillating tiles is used in the barrel and extended barrel sections. Over the $1.5 < |\eta| < 4.9$ range, liquid Argon calorimeters are chosen instead for the intrinsic radiation-hardness of such a technique. Copper and tungsten-reinforced copper are chosen as absorber materials in the hadronic end-caps and the forward calorimeter respectively. These techniques offer a very good performance combined with a simple and low cost construction. In combination with the EMcal, the hadronic calorimeters are required to identify and measure the energy and direction of jets as well as the total $E_{\mathrm{T}}^{\mathrm{miss}}$. This is achieved by a longitudinal segmentation into three and four sampling layers in the hadronic tile and LAr systems respectively. The nominal performance in terms of energy resolution of the ATLAS hadronic calorimeters is shown in Tab. 3.1. The angular resolution is given by the cell granularity of the sampling layers. The size of the hadronic tile cells varies from $\Delta\eta \times \Delta\phi = 0.1 \times 0.1$ in the first sampling layer to 0.2×0.1 in the second and third layer. The cells of the hadronic LAr end-caps are $\Delta\eta \times \Delta\phi = 0.1 \times 0.1$ large in the $1.5 < |\eta| < 2.5$ region and 0.2×0.2 for the remaining $2.5 < |\eta| < 3.2$. A total hermeticity amounting to $10\,\lambda$ (nuclear interaction length) is realised over the whole pseudorapidity range, ensuring the hadron punch-through rate to fall well below the irreducible level of prompt or decay muons.

3.2.5. Muon System

A complete view of the ATLAS muon spectrometer is provided in Fig. 3.7. The driving design principle, as for the Inner Detector, is the magnetic deflection of the tracks, which is carried out by the air-core toroid magnets that encompass the hadronic calorimetry cylinder. The toroidal windings of the outer magnetic system are intertwined with the trigger instrumentation and the high precision tracking chambers both in the barrel and in the end-caps; the triggering and detection techniques differ in the two section, due to the pseudorapidity dependence of the particle fluxes. The magnet field configuration with respect to the po-

sitioning of the muon chambers ensures that the detected tracks are mostly orthogonal to the bending field, as it is seen in Fig. 3.8, where one quadrant of the Muon System in the Rz plane is shown. At the same time the configuration is such that the multiple scattering occurrence is minimised, guaranteeing that the momentum resolution is least degraded. The muon spectrometer is composed of independent trigger and precision measurement chambers. Over the whole $|\eta| < 2.7$ pseudorapidity region, the tracks are measured in chambers organised in three subsequent parallel layers, called *stations*. The muon stations are arranged on coaxial cylinders in the barrel and on disks orthogonal to the beam axis in the end-caps. For triggering purposes, the thin gap and the resistive plate techniques have been adopted in the end-caps and the barrel respectively where, in turn, the TGC and RPC chambers are installed. Over most of the pseudorapidity range ($|\eta| < 2$), the precision measurement of the track space points is provided by the Monitored Drift Tubes, operated with a gas mixture of 93% Ar and 7% CO_2 at 3 bar absolute pressure for a total volume of 800 m^3. The tubes are cylinders of 30 mm diameter and length variable between 70 and 630 cm, with a central 50 µm thick W-Re wire. At the chosen working point the resolution of the single wire is about 80 µm. In the remaining large pseudorapidity region $2 < |\eta| < 2.7$ Cathode Strip Chambers are used instead, which allow for a higher granularity and can then resolve the tough demands of the forward activity at the LHC collision rates. The CSCs consist of four layers of consecutive multiwire proportional chambers, operated with a gas mixture of 30% Ar, 50% CO_2 and 20% CF_4. The signal is read out with cathode strips arranged orthogonally with respect to the anode wires. The anode-cathode spacing is equal to the anode wire pitch, and the precision coordinate is obtained by measuring the charge induced on the cathode by the avalanche sourced in the vicinity of the anode wire. A spacial resolution of about 60 µm is reached by the segmented design of the readout cathode, and by interpolation of the charge between the consecutive strips.

3.2.6. Luminosity Detectors

Beam Conditions Monitor

The Beam Conditions Monitor (BCM) consists of four small diamond sensors, placed on each side of the interaction point, at a distance of $z = \pm 184$ cm. The sensors are approximately 1 cm^2 in cross section and are arranged around the beam pipe in a cross pattern. The BCM is a fast device originally designed to monitor background levels and issue beam-abort requests when beam losses start to risk damaging the Inner Detector. The fast readout of the BCM also provides a bunch-by-bunch luminosity signal at $|\eta| = 4.2$ with a time resolution of 0.7 ns. Even though the overall response of the two devices is expected to be very similar, the acceptances, thresholds, and data paths show small differences between BCMH and BCMV, therefore these two measurements are treated as being independent for calibration and monitoring purposes.

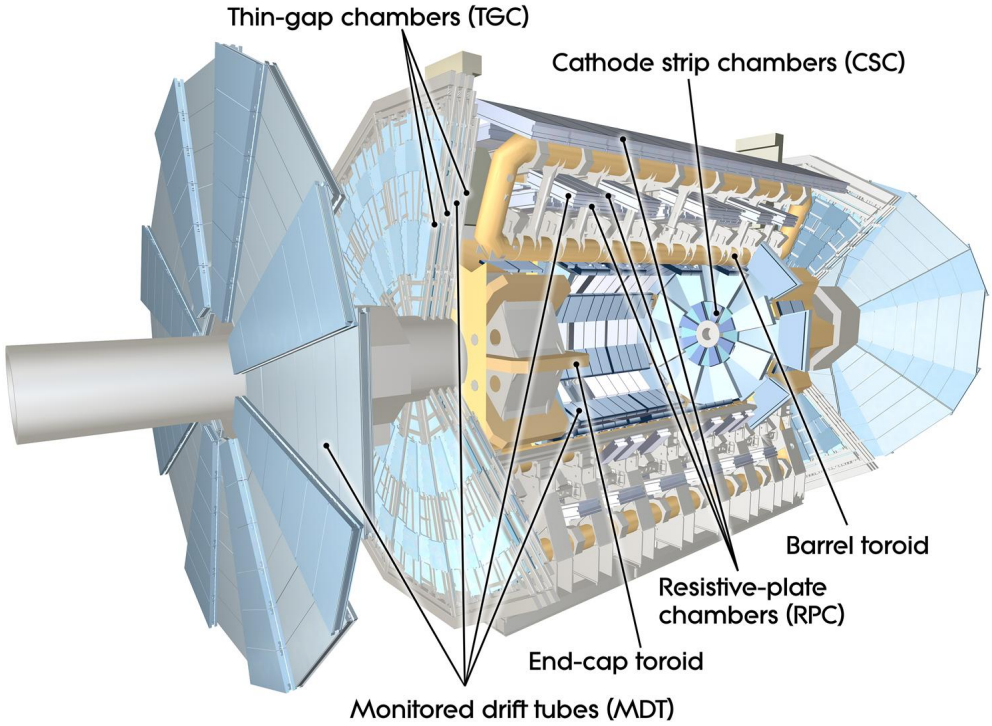

Figure 3.7.: The ATLAS Muon System. In the cross section view the sub-systems dedicated to muon triggering (TGCs, RPCs) and position measurements (CSCs, MDTs) are shown. The barrel and end-cap magnet toroids are visible in the structure [A+08].

LUCID

LUCID is a Cherenkov detector specifically designed for measuring the luminosity in ATLAS. Sixteen aluminium tubes filled with C_4F_{10} gas surround the beam pipe on each side of the IP at a distance of 17 m covering the pseudorapidity range $5.6 < |\eta| < 6.0$. The Cherenkov photons created by charged particles in the gas are reflected by the tube walls until they reach the photomultiplier tubes (PMTs) situated at the back end of the tubes. Additional Cherenkov photons are produced in the quartz window separating the aluminium tubes from the PMTs. The Cherenkov light created in the gas typically produces 60-70 photoelectrons per incident charged particle, while the quartz window adds another 40 photoelectrons to the signal. A "hit" is recorded for a certain tube during a given bunch crossing if one of the LUCID PMTs produces a signal over a preset threshold equivalent to 15 photoelectrons. The LUCID hit pattern is processed by a custom-built electronics card based on Field Programmable Gate Arrays (FPGAs). The arrays can be tuned to different luminosity algorithms, and provide separate luminosity measurements for each LHC bunch crossing.

Both BCM and LUCID are fast detectors with electronics capable of making statistically

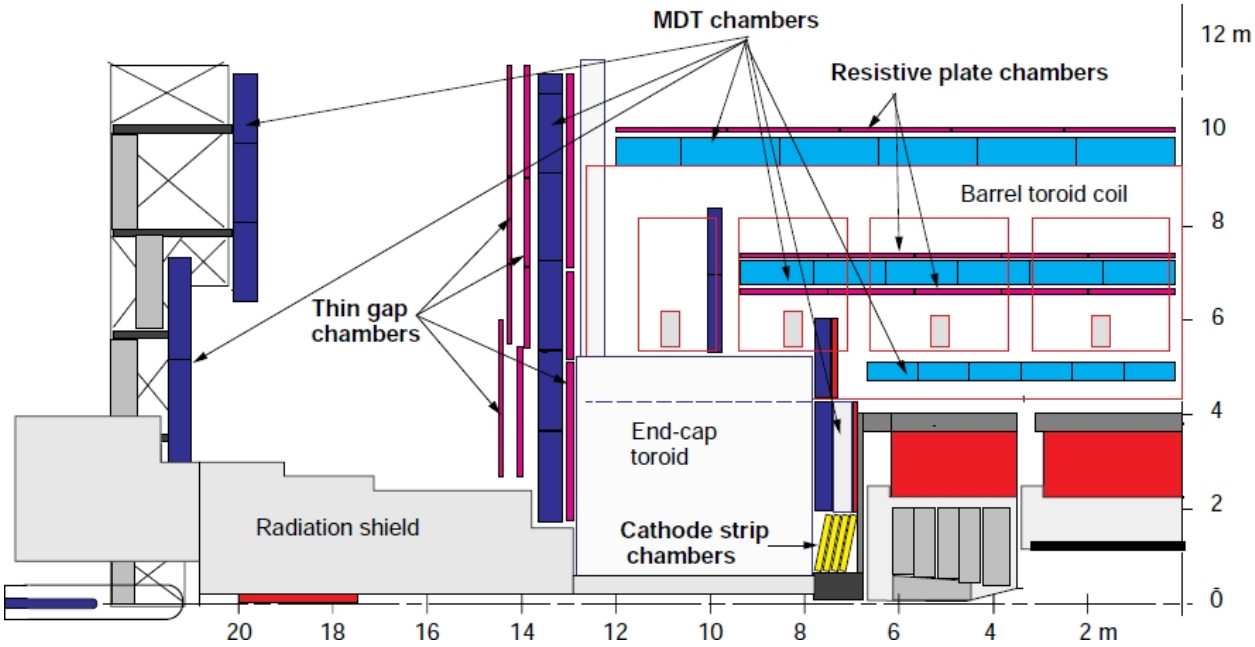

Figure 3.8.: R-z view of one quadrant of the muon spectrometer. High energy muons typically traverse at least three stations [A+08].

precise luminosity measurements separately for each bunch crossing within the LHC fill pattern with no deadtime. These FPGA-based front-end electronics run autonomously from the main ATLAS data acquisition system, and in particular are not affected by any deadtime imposed by the ATLAS Central Trigger Processor.

3.2.7. Trigger and Data Acquisition

As shown in Fig. 3.9, the rate of interesting physics events occurring at the LHC design luminosity ($\mathcal{L} = 10^{34}\,\mathrm{cm}^{-2}s^{-1}$) is many orders of magnitude lower than the 40 MHz design collision rate. The extraction of interesting physics events by the ATLAS trigger and data-acquisition (TDAQ) system relies on three subsequent decision levels where the selection quality is refined after each step. The decision system design of the TDAQ is such that the rate of collision events stored permanently amounts to about 400 Hz, that must be selected from the initial collision rate. A block-diagram visualisation of the ATLAS trigger system is given in Fig. 3.10. The three layers of the event selection are Level-1 (L1), Level-2 (L2), and event filter (EF). The L2 and event filter together form the High-Level Trigger (HLT).

Level 1

The L1 trigger acts at hardware level, exploiting ATLAS customised electronics, while the HLT is almost entirely software based, and exploits the networking hardware systems. The

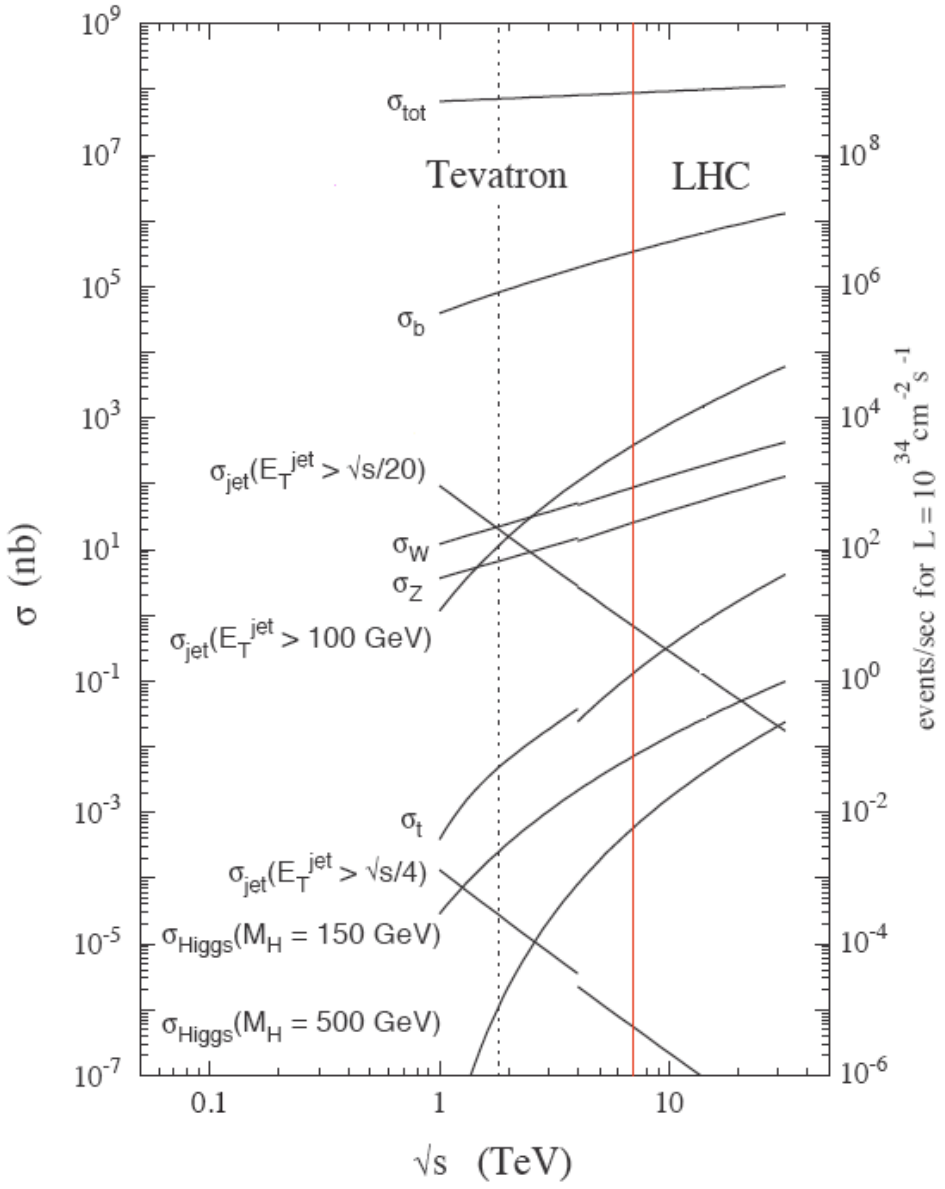

Figure 3.9.: The predicted cross sections for typical SM known processes and exemplary Higgs productions as a function of the pp centre-of-mass energy. The LHC centre-of-mass energy working point of 7 TeV is drawn as solid line. The expected event rate for the design luminosity value is shown on the scale of the right side of the plot. At the centre-of-mass energy of 7 TeV the production rate of top quarks (σ_t) is visible, below the overwhelming production of W andZ bosons and high-energy jets events. [Cat00]

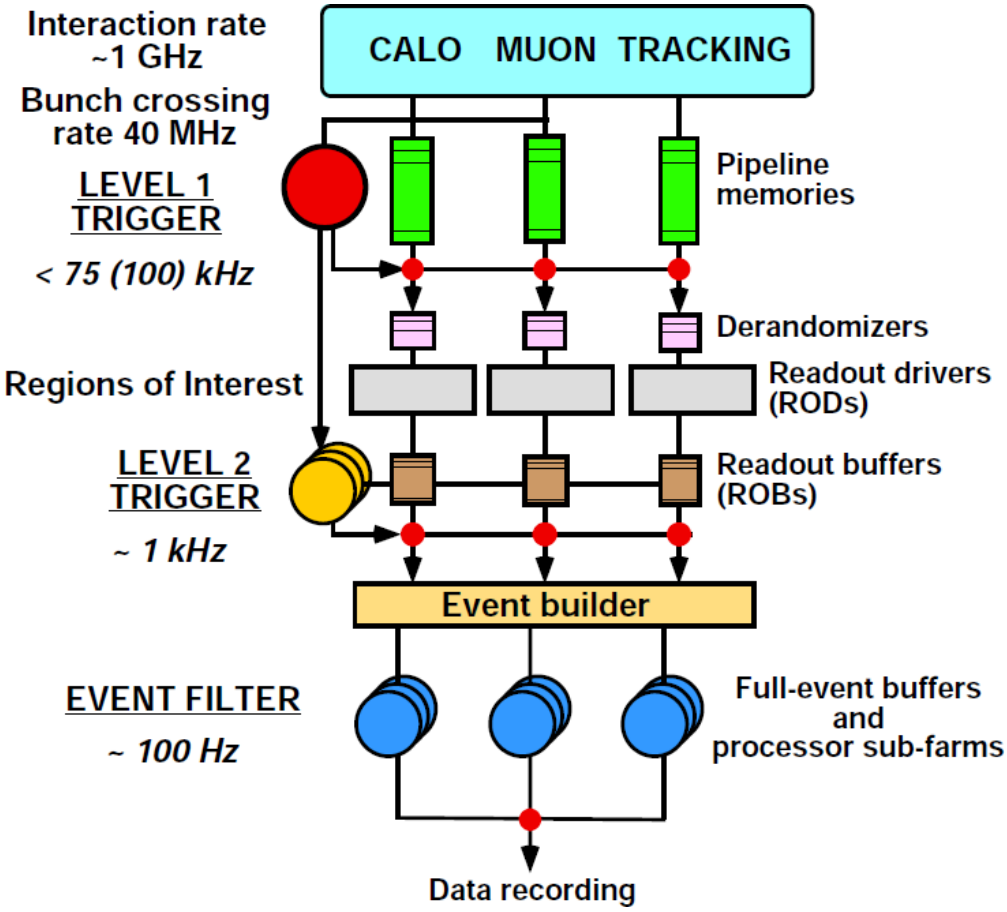

Figure 3.10.: Block diagram of the Trigger/DAQ system. The orders of magnitude at the different trigger levels are shown, starting from an interaction rate of about 1 GHz in which an average value μ of multiple interactions per bunch crossing is considered. The average size of the events accepted by the trigger amounts to about 1.3 MB. The actual rate of accepted events is about 400 Hz, leading at a rate of about 550 MB/s saved on disk [A+08].

L1 trigger uses reduced-granularity information from the RPCs and TGCs searching for high-p_t muon signatures, and the from the calorimeter sub-systems to identify events with important electromagnetic clusters, jets, τ-leptons, E_T^{miss} and large total transverse energy. If accepted by the L1 trigger the event data is moved through the Readout Driver (ROD) into the Readout Buffer (ROB) for temporary storage. The detector readout systems can withstand a maximum L1 output rate of 75 kHz, , upgradeable to 100 kHz; the L1 decision must be taken within 2.5 µs after the associated bunch crossing.

Level 2

For each event passing the L1 decision, Regions-of-Interest (RoI) are created, that are regions of the detector where the L1 trigger has identified possible trigger objects within the event. The RoI information, which includes energy, position and signature type, is used by the L2 trigger. At this level the full granularity in the RoI can be exploited. The typical size of a RoI amounts to about 2% of the event data, and the average event processing time of approximately 40 ms. At this point the event rate is reduced to less than 3.5 kHz, which is passed over to the EF. The selection criteria of both L1 and L2 are primarily inclusive, such as high-E_{t} objects above defined thresholds.

Event Filter

The event filter acts offline on fully-built events processed by the event builder (EB) to further select events down to a rate at which they can be recorded for subsequent offline analysis. At the end of the trigger chain, the event rate is reduced to approximately 400 Hz, with an average event processing time of about four seconds, which is realised by a parallel processing of the events. The average size of the accepted events is about 1.3 MB. The HLT algorithms use the full granularity and precision of calorimeter and muon chamber data, as well as the tracking information from the inner detector, that help to refine the trigger selections. Typically the same algorithms of the later offline reconstruction are used. Better information on energy deposition improves the threshold cuts, while track reconstruction in the inner detector significantly enhances the particle identification (for example distinguishing between electrons and photons).

According to the EF trigger items associated, recorded events are written into datasets that are named after the trigger stream they belong to (*e.* g.. "Muons", "Egamma", "TauJetEtMiss"). Under such general assumptions, events containing two or more objects of different physical nature that have simultaneously fired their dedicated trigger can be duplicated by being stored in more than one stream dataset[2].

Data Acquisition

The DAQ system collects and buffers the event data from the detector-specific readout electronics at the L1 trigger rate. It transmits to the L2 trigger any data requested by the trigger (typically the data corresponding to RoI's) and, for those events fulfilling the L2 selection criteria, event-building is performed. The assembled events are then moved by the data acquisition system to the event filter, and the events selected are moved to permanent event storage. In addition to controlling movement of data down the trigger selection chain, the data acquisition system is responsible for the configuration, control and monitoring of

[2]For example an event where both an electron and a muon have fired the trigger can be stored in the "Egamma" and in the "Muons" trigger stream simultaneously.

the ATLAS detector during data-taking. Supervision of the detector hardware (gas systems, power-supply voltages, etc.) is provided by the Detector Control System (DCS).

3.3. Monte Carlo Simulation

Given the complexity of the experimental setup, precise event simulations play an essential role in understanding the data collected by ATLAS. The simulation is carried out by means of Monte Carlo (MC) techniques, where the entire available knowledge of the physics processes involved as well as the experiment components and its geometry are taken into account. The purpose of the simulation is to reproduce the recorded outcome of proton proton collisions in the most possibly realistic way. Such detailed prediction is necessary in order to determine the selection efficiencies and assess the discovery potential of ATLAS in terms of the most important physics signatures, design the most suitable trigger system and optimise the algorithms for the offline reconstruction of physics events. The common ATLAS framework called Athena [A+05] is used, among many purposes, to embed in a shared and centrally controlled fashion the canonical three steps of the event simulation procedure: Event Generation, Detector Simulation and Event Reconstruction.

A brief description of the simulation steps is given in the following, while the reconstruction of physics objects in the events is described in detail in Sec. 3.5. In order to assess the impact of systematic effects related to the choice of the PDF set used for the generation of events, the technique of PDF re-weighting described in Sec. 7.1.1 is used.

3.3.1. Event Generation

The first phase of the event generation process is performed using physics event generators. The generators simulate the collisions of protons at the centre-of-mass energy of 7 TeV. The input needed by the generator generally contains the design beam energy, the PDFs set that fixes the proton composition, the tables of decay probabilities for all known particles that enter the simulation, the specific particle interaction models and eventually the particle composition of the desired final state.

Generators are able to produce lists of simulated particles emerging from the interaction region for any desired physics interaction model provided to the program. The output is a collection of events which serve as input to the following simulation step. For each particle object generated in the event it is then possible to retrieve the particle-type, the electric charge, the initial vertex position, as well as the four-momentum vectors. To simulate high energy physics processes, several Monte Carlo packages are available that implement either leading or next-to-leading order terms of the matrix elements. The optimal choice of the specific generator to be used for the production of each physics process is driven by their ability to describe the data. For this reason several MC packages with different generating procedures are used to produce the simulations, in accor-

dance with the studies performed inside the entire ATLAS collaboration. Monte Carlo packages used for this analysis that simulate physics interactions at leading order precision are AcerMC [KRW04] and Alpgen [MMP+03], Pythia [SMS06, A+11b] and Herwig [C+01], while for next-to-leading order precision simulations the processes are generated with Mc@NLO [Nas04, LGH+10, FW02] and PowHeg [FNO07]. The final states generated with MC generators include the effect of QCD corrections at perturbative level only. This is done by fixing the QCD renormalisation scale cutoff parameter, Λ_{QCD}. Its setting is crucial since it affects directly the hard parton composition of the *initial* and *final state radiation* (I/FSR) in the event.

Event generators of short distance processes do not reproduce the effects of hadronisation and formation of the underlying event (UE), for which no unique model based on first principles is available. Hadronisation and UE formation are non-perturbative QCD phenomena that occur on a timescale that is longer than the high energy process and much shorter than the time needed for the final state particles to reach detection. For this reason the event generation is carried out in a modular way, and the final states of the fundamental interaction simulation of the above must be interfaced with further packages, dedicated to correctly simulate the parton fragmentation and their hadronisation. The lists of physics objects resulting at the end of the event generation process are stored in the HepMC event record.

Hadronisation Models

Hadronisation models are used to reproduce the population of particle jets and their stable hadrons composition that is seen in real data. This simulation step involves the physics of the so called *parton showering* (PS) processes. Two main algorithms were developed in the latest years to reproduce the parton fragmentation and are interfaced with the event generators used to simulate ATLAS data. These are the Lund string and the Cluster, which are implemented in the Pythia and Herwig event generators respectively. [3] The two models, which differ in the parametrisation of the form factors of the radiation emission are equally reliable and developed independently from each other. For this reason a comparison between the two is used later to assess the systematic effects arising from the approximations and the assumptions of the chosen hadronisation model.

After the generation of leading order hard processes, higher order effects are added in the form of a parton shower, where simulated parton objects are allowed to subsequently split into pairs of other partons, until a cut-off energy threshold is reached. The shower components are then grouped into colour-singlets to form the hadrons. By means of the decay tables short-lived hadrons are allowed to decay according to the known rates. To

[3] The Pythia and Herwig tools are software packages. These can be interfaced with the other generators in order to simulate the parton shower, but they also include private matrix event generators, which are often used for the simulation of Multijet events.

reproduce as closely as possible the experimental results, the hadronisation models and their parameters are tuned to ATLAS data that were collected at the beginning of the collisions phase and in beam conditions that were as similar as possible to the periods when physics data was being recorded.

Underlying Event

In a last step the underlying event structure is adjusted with the aid of dedicated tools such as the JIMMY [BFS96]. Objects that are not produced either in the "hard" event or in the hadronisation phase are added to the event. These can be originated in the interactions undergone by beam remnants and as a result of additional interactions between the partons that do not represent initial states to the "hard" event.

Pile-up

To describe the effect of pile-up events in the simulated samples, minimum bias events generated with PYTHIA are added to the initial events at the digitisation step before the reconstruction.

3.3.2. Detector Simulation And Digitisation

For each generated event, the HEPMC particle lists are passed through the ATLAS detector simulation. At this step, the interaction of each particle with the traversed material is simulated within the GEANT4 [A+03b] framework. For simulating the particle propagation, detailed information on the detector geometry, matter composition across the subdetectors layers and the most precise map of the embedded magnetic field are used. During this step, the decay of long lived particles is taken into account. As a very last step, the simulated events are digitised simulating the subdetectors response and readout. The simulated events are recorded in raw data objects (RDO) format.

The lengthy full simulation (FS) chain described so far is applied to all samples necessary to the main physics analyses inside ATLAS. For assessing the impact of systematics arising from the uncertainties related to the intrinsic limits of physics modelling, a comparison between samples simulated with different packages is carried out. In order to reduce the usage of computing resources, the alternative and faster simulation chain available within the Athena framework ATLFASTII [Luk12], is used for the production for the comparison samples. These tools make use of simplified parametrisations and smearing routines, and adopt detailed look-up tables of average detector response that reduce very sensibly the size and the computation time of the samples. The data description provided by the ATLFASTII simulation has been shown to be in very good agreement with the one provided by the full simulation package [A+12l, Bil12].

3.4. Luminosity Determination

The rate of inelastic interactions in the collision of the proton bunches in ATLAS is of essential importance to be able to perform an analysis of the data which is able to resolve the detailed predictions of the Standard Model.

The luminosity of a pp collider can be expressed as

$$\mathcal{L} = \frac{R_{\text{inel}}}{\sigma_{\text{inel}}} \tag{3.3}$$

where R_{inel} is the rate of inelastic collisions and σ_{inel} is the pp inelastic cross section. For a storage ring, operating at a revolution frequency f_{r} and with n_{b} bunch pairs colliding per revolution, this expression can be rewritten in terms of the measured (visible) cross section $\sigma_{\text{vis}} = \epsilon\,\sigma_{\text{inel}}$ and the average number of pp interactions per bunch crossing (BC) $\mu_{\text{vis}} = \epsilon\,\mu_{\text{inel}}$. Here, the measured cross section σ_{vis} is intended as a calibration constant, while ϵ is an efficiency factor for the detectors and the reconstruction algorithms involved in the measurement. The luminosity formulated in Eq. 3.3 can be then re-expressed as

$$\mathcal{L} = \frac{\mu_{\text{vis}} n_{\text{b}} f_{\text{r}}}{\sigma_{\text{vis}}}\,. \tag{3.4}$$

The design setup of the LHC combined with the overall performance of the ATLAS experiment are such that the μ_{vis} value can not be approximated by a linear relation to the number of detected bunch crossings[4], since more than one pp collision per BC can occur, a condition referred to as *in-time pile-up*. To restore the linearity of μ_{vis} in terms of detected bunch crossing the *hit counting* algorithms are implemented. These algorithms rely on the count of readout channels of the LUCID and BCM detectors (*cf.* Sec. 3.2.6) firing above a pre-determined threshold, thus enhancing the probability to find an event where highly energetic particles have been produced. The algorithms share the common assumption that the number of hits during a pp collision and the number of interactions per BC follow the binomial and Poisson statistics respectively, thus providing a mathematical relation that links the average number of interactions per pp collision to the count of hits and the number of available channels N_{CH} (*cf.* Ref. [A+12d]). In order to achieve a temporal control, the formula for the instantaneous luminosity Eq. 3.4 is defined in terms of certain luminosity block (LB). The luminosity is then assumed to remain constant within the duration of the block, which is tipically a few minutes long.

As described in more detail in [vdM68], the calibration constant σ^{vis} is extracted using a procedure based on dedicated beam separation scans, also known as van der Meer scans. The absolute luminosity can be directly computed from the measurements of the beam parameters [Rub77]. The luminosity delivered by the LHC can be written in terms of the

[4] More specifically, the approximation reduces μ_{vis} to the ratio between the number of detected crossings and the number of expected bunch crossings N_{BC}.

accelerator parameters as

$$\mathcal{L} = \frac{n_b f_r n_1 n_2}{2\pi \Sigma_x \Sigma_y}, \tag{3.5}$$

where n_1 and n_2 are the bunch populations (protons per bunch) in beam 1 and beam 2 respectively (together forming the bunch population product), and Σ_x and Σ_y characterise the horizontal and vertical beam widths. During a van der Meer scan, the distance that separates the beam is known in detail, which allows a direct measurement of Σ_x and Σ_y. This measurement is combined with an external measurement of the bunch population product $n_1 \cdot n_2$, providing a direct determination of the luminosity when the beams are unseparated. In order to reduce the uncertainty on the luminosity measurement a comparison is performed of the output of the hit counting algorithms coupled to the offline vertexing procedure in the Inner Detector (see Sec. 3.5.3) and the forward hadronic calorimeter. The accumulation plot of the instantaneous luminosity, usually referred to as "integrated luminosity" - recorded by the ATLAS detector in the year 2011 are shown in Fig. 3.11.

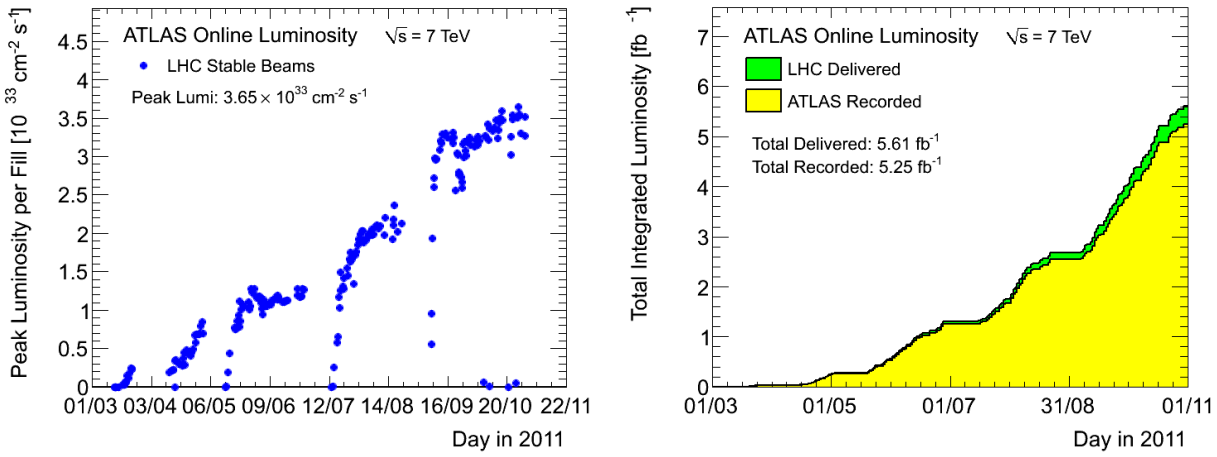

Figure 3.11.: Peak instantaneous luminosity of ATLAS by LHC fill (a) and accumulation of the integrated luminosity (b) delivered to (green) and recorded by ATLAS (yellow) during stable beams for pp collisions at 7 TeV centre-of-mass energy in year 2011 [A+12d].

3.4.1. Pile-up

The number of proton-proton interactions per bunch crossing can be described by a Poisson distribution with mean value μ. During a fill, such a quantity reaches its peak at the start of the stable beams collision run, and decreases monotonically with the beam intensity. Since the number of interactions per bunch crossing varies between the bunches, its estimate needs

to be averaged over all the bunch crossings and the data analysed. The value of μ is calculated inverting the relation in Eq. 3.4. The uncertainty on μ depends on the uncertainties of the luminosity measurement and of the total inelastic cross section. Depending on the time resolution and the length of the read-out temporal window of a sub-detector, signals from neighbouring bunch crossings can leak into the following collision and leave noisy remnants when the detector is read out. The impact of the interactions from the neighbouring bunch crossings is referred to as *out-of-time pile-up*, as opposed to in-time pile-up which results from additional interactions in the same bunch crossing. Given the read-out window of the Inner Detector, the out-of-time pile-up has a much smaller impact than the in-time pile-up. It slightly increases the occupancy in the TRT, which has a read-out window of 75 ns, in contrast to the silicon detectors which have read-out windows of 25 ns. The 75 ns read-out window for the TRT is needed to read out the full signal that spans a range of about 50 ns. A veto rejecting out-of-time hits in the TRT minimises the impact of out-of-time pile-up.Given the steady increase of the instantaneous luminosity delivered by the LHC (reported in Fig. 3.11), monitoring the average number of pp interaction per bunch crossing in data is of the utmost importance in order to provide a correct parametrisation for modelling the in-time pile-up conditions in the MC simulation. The procedure to reweigh the simulated samples to mirror the pile-up effects in data is described in more detail in Sec. 4.2.2.

3.5. Physics Reconstruction

The possible final states of top quark production reactions are populated by quarks and leptons. In this section the algorithms used by ATLAS for the reconstruction of top quark decay products that enter the final analysis are presented. As shown in Sec. 2.4.1, only final state objects like electrons, muons, jets and neutrinos are treated in the present work. A basic description of the reconstruction algorithms is provided in the following sections along with considerations regarding their general performance.

3.5.1. Event Reconstruction

The event reconstruction procedure is divided in two subsequent steps. As a first step, complex pattern recognition methods are used to reconstruct tracks and calorimeter clusters that have been produced in the event. At this pre-analysis step, only information relative to specific subdetectors is used for reconstruction. As a second step, the subdetector-specific physics objects information is combined across the subsystems, in order to identify and reconstruct physics objects used for detailed event analysis. After this step objects such as muons, electrons, jets and missing transverse energy are added to the event record. In the processing chain that connects recorded RDO to the quality level needed for physics analysis, the events are stored in various formats with different amount of information and event size. In the Event Summary Data (ESD) the complete event information after the first

step are contained, besides the reconstructed objects. At this storage level, the information about the calorimeter cells energy deposits and about the reconstructed tracks and clusters is included. In contrast, the Analysis Object Data (AOD) contain only the result of the full reconstruction procedure. Following a general agreement among the ATLAS physics working groups, the Derived Physics Data (DPD) format is used for analysis; such data format is constituted of flat ROOT [A+09d] ntuples files, where only information that is strictly necessary for detailed physics analysis is contained.

3.5.2. Tracking

Inner Detector Tracks

Tracks are reconstructed in the acceptance region of the Inner Detector ($|\eta| < 2.5$) using a sequence of χ^2-based fitting algorithms [A+12n, Str12].

At a first stage, an *inside-out* algorithm starting from 3-point seeds in the precision trackers is employed. This algorithm uses a combinatorial Kalman filter [Gav97] to add hits in the outwards direction with respect to the interaction point, resolving the ambiguities in the silicon detectors[5] and extending the track to the TRT. The inside-out algorithm is designed for the identification of *primary* charged particles, *i.* e. particles produced either in the pp collision vertex or in the decay of particles with a lifetime shorter than 3×10^{-11} s. A transverse momentum of $p_t > 400$ MeV is required for primary particles reconstructed with the inside-out algorithm.

In a second stage, an *outside-in* algorithm is used instead to search for TRT segments and extend them adding hits in the silicon trackers[6]. This back-tracking procedure is used to reconstruct *secondary* particles that are produced in the decay of the primary collision products.

In the 2011 dataset analysis, the tracks used as input by the subsequent object reconstruction algorithms[7] is required to have the following characteristics:

- At least 9 hits in the silicon detector (pixel+SCT),
- No holes[8] in the pixel layers where a hit is expected.

These requirements ensure that the performance is not sensitive to in-time pile-up. The reconstruction efficiency of primary (secondary) particles is found to have 1(2) % variations

[5] The ambiguity involves hits shared by multiple tracks, incomplete tracks or fake track candidates. It is solved by means of a complex rating procedure that ranks the track likelihood to describe a real trajectory. More details on the ranking procedure are given in Sec. 4.1.3 of Ref. [A+07a].

[6] The TRT segments for which no extension in the precision trackers has been found are referred to as TRT-standalone tracks.

[7] It is important to remark that these requirements are *not* directly applied to the track reconstruction, but rather by the object reconstruction algorithms themselves.

[8] A hole is a missing (expected but not found) space point measurement in a given trajectory. In case the silicon module was recorded as inactive, it is not accounted for as a hole.

across the whole 2011 data taking. Comparisons between the data/MC distributions of the invariant masses of reconstructed K_s^0 mesons as a function of the azimuthal angle show that the resolution of the tracking system meets the goal requirements shown in Tab. 3.1.

Muon System Tracks

Using the information recorded by the Muon System the so called *stand-alone* tracks are reconstructed. At first step, the MS hits are used to form local straight segments[9] in the MDT or CSC modules, that are then combined to form a curved track. For each segment, the η and ϕ coordinates are independently provided by the tracking module (MDT, CSC) and by the trigger chamber (RPC, TGC) respectively. The fit includes a treatment of the inert material by allocating scattering centres along the tracks, so that energy loss and multiple Coulomb scattering are correctly taken into account. The performance of the MS tracking system is studied in terms of chamber alignment and *sagitta* resolution using cosmic-rays whose tracks are collected by switching off the magnetic field in the toroids. The sagitta is defined as the distance from the Middle-station segment to the straight line connecting the segments in the Inner and Outer stations. The sigma of a double Gaussian curve is used to fit the sagitta distribution, parametrising the multiple scattering and the intrinsic resolution. The two Gaussian components represent the multiple scattering and intrinsic resolution, respectively dominating at high and low momenta. Using the solenoidal magnetic field of the Inner Detector to determine the momentum of the muon tracks, the intrinsic component of the sagitta resolution is found to be between 80 and 100 µm, which, in terms of p_{t} resolution, is close to the design requirements listed in Tab. 3.1. An average efficiency of 95 % is found for the reconstruction of MS-standalone tracks.

3.5.3. Vertexing

The primary vertices in particle collisions are the space points where a hard scatter interaction takes place. Vertices are reconstructed at ATLAS using an iterative finding algorithm [A+10e]. In a χ^2 minimisation procedure that uses the beamspot position as a constraint, seeds are taken from the z-position of the reconstructed tracks at the beam line and for each track a weight is computed as a measure of the compatibility with the fitted vertex. Tracks that are displaced by more than $7\,\sigma$ from the fitted vertex are used to seed a new iteration, and the procedure is repeated until no additional vertices are found. The resolution is evaluated from data by means of a split vertex technique (*cf.* [A+12n]), and it is found be about 23 µm in the transverse plane and 40 µm in the longitudinal axis, for vertices of 70 tracks. The efficiency of reconstructing a primary vertex with at least two primary charged particles (defined in Sec. 3.5.2) with $p_{\mathrm{t}} > 400\,\mathrm{MeV}$ within $|\eta| < 2.5$ is about 90 %,

[9] The local segment reconstructed by a MS module is "straight" in the xy plane, since the tracks are bent in the Rz plane by the toroid.

for a single interaction ($\mu = 1$), and decreases to about 50 % at $\mu = 41$, when multiple interactions occur too closely and can not be resolved.

Fake vertices are possible in high pile-up conditions, due to the increased number of fake tracks, and a rate of 7 % is found in MC simulation samples for $\mu = 41$. The fake rate is suppressed by the track robust quality requirements (*cf.* Sec. 3.5.2).

3.5.4. Muons

The muon object selection follows the general prescriptions released by the ATLAS muon performance group for the analysis of the full 2011 collision dataset. Such prescriptions are based on the MUID algorithm [A+03a], which combines the tracks reconstructed by the inner detector and the muon spectrometer using a global refit of the two tracks. The result is a collection of all the information available, along the muon trajectory, recorded by the inner detector, the calorimeters and the muon system. The objects provided by the subdetectors (*cf.* Sec. 3.5.1) are used to compute two muon cone isolation variables $E_t^{0.2}$ and $p_{\mathrm{t}}^{0.3}$. These are defined as the vectorial sum of the energy and momentum belonging to EM objects (tracks) inside cones of given ΔR sizes around the main muon track. The size of the isolation cone is usually indicated on the right apex of the isolation quantity considered. For example $E_t^{0.2}$ indicates the transverse energy deposited in a cone of $\Delta R \leq 0.2$ around the muon barycentre. The isolation variables are of the utmost importance to improve the purity of the selection of *prompt* muons. The muon candidates are reconstructed in four quality varieties: *very loose*, *loose*,*medium* and *tight*, where each tighter selection level is built as a subset of the looser. For the purposes of the analysis only tight muons are considered that fulfill the following basic conditions:

- Muons are required to be combined.
- Muons are required to be within the Inner Detector acceptance, $|\eta| < 2.5$.
- Muons are required to have $p_{\mathrm{t}} > 25\,\mathrm{GeV}$ to be on the plateau of the single muon trigger efficiency.
- Transverse energy isolation cone $E_t^{0.2} < 4\,\mathrm{GeV}$.
- Transverse momentum isolation cone $p_t^{0.3} < 2.5\,\mathrm{GeV}$.
- The z coordinate of the muon track is required to lie within 2 mm from the primary vertex.
- Muons are required to pass additional track quality cuts optimised by the ATLAS ID Tracking group in liaison with the Muon Combined Performance Group (*cf.* *e.* g. [A+11a]).

Furthermore, scale factors are applied on a event basis when a muon is found in the Monte Carlo simulation. These event weights are introduced in order to correct for the discrepancies, in terms of trigger and reconstruction efficiencies, between data and MC. The efficiencies in data need to be extracted with a tag & probe method applied in the Z mass peak, since the truth information is obviously not available, while a simple matching algorithm can be used to compute the efficiencies in the MC. These event scale factors are distributed around unity, and provided as a function of η and p_{t} of the reconstructed muon. Procedures to adjust the energy scale and resolution smearing in the MC simulation are performed as final refinement, and are treated in more detail in Sec. 4.2.4.

3.5.5. Electrons

The electron reconstruction procedure in ATLAS is based on clusters reconstructed in the EM calorimeter, which are associated to tracks of charged particles reconstructed in the Inner Detector [A$^+$12b, A$^+$12q]. The several algorithms used to provide an optimal reconstruction of the momentum vector of isolated electrons from a few GeV to a few TeV over the full pseudorapidity range covered by the ID tracker, excluding the crack region of the overlapping calorimeter components at $1.37 < \eta_{\mathrm{cluster}} < 1.52$. The electron reconstruction is based on a sliding window algorithm operating on seed clusters carrying a minimum energy of 2.5 GeV in a 3×5 η/ϕ-cell. In a first procedural step, reconstructed tracks are extrapolated from their last hit point to the second layer of the EM calorimeter. At this point each extrapolated track is matched to the nearest cluster. An electron is found if the difference of η and ϕ coordinates between the extrapolated track and the cluster seed is below a certain threshold. In case of multiple tracks pointing to the same energy cluster, the track with the smallest ΔR distance is chosen as the best electron candidate. As a refining step, the cluster energy is computed again, increasing the cluster window size to $3 \times 7\,(5 \times 5\,)$ in middle layer cell units in the barrel (end-caps). In the final result the electron transverse energy E_{t} is taken combining the information of the calorimeter and the ID, computing it as:

$$E_{\mathrm{t}}^{\mathrm{electron}} = \frac{E_{\mathrm{cluster}}}{\cosh \eta_{\mathrm{track}}}\,. \tag{3.6}$$

When building the reconstructed electron object, the η and ϕ directions are taken from track, while the absolute energy is the one from the calorimeter cluster. In order to provide a complete reconstruction of the energy deposited in the calorimeter, the following contributions are added to the measured cluster energy:

- The estimated energy deposition in the material upstream from the EMCAL,
- The estimated lateral leakage outside the cluster (within the EMCAL),
- The estimated longitudinal leakage into downstream material (mainly HCAL).

Once the electron object is created, further quality requirements are applied to select them from the background, that divide the reconstructed electrons in three categories, referred to as *loose(++)*, *medium(++)* and *tight(++)*, where each set of looser requirements includes the tighter[10] ones. To avoid the selection of jets misreconstructed as electrons, the electron candidates have to fulfill two isolation criteria analogous to the muon case: the energy deposited and the vectorial sum of track p_{t} inside a cone of $\Delta R = 0.2$ and $\Delta R = 0.3$ around the electron ($E_t^{0.2}$, $p_t^{0.3}$ respectively) must be compatible with a detector efficiency of 90%[11]. As in the muon case, the z coordinate of the designated electron track is required to lie within 2 mm from the primary vertex. Furthermore, like for the muon events, scale factors are applied on a event basis to electron candidates in MC to correct for the mismodelling of the actual η and p_{t} dependent trigger, identification and reconstruction efficiencies in data. Also, the electromagnetic cluster energies need to be rescaled in MC. The complete set of corrections applied to the event that are due to the electron reconstruction are discussed in Sec. 4.2.4.

3.5.6. Jets

A wide variety of procedures and algorithms has been developed inside the ATLAS collaboration with the purpose to identify jets of hadrons. For this analysis, in agreement with the majority of the studies focussed on the top quark, the jets are reconstructed using the anti-kt algorithm [CSS08]. The reason for adopting this specific jet-finding algorithm, for which a distance parameter R of 0.4 is chosen, lies in the fact that it is one of the very few ones which is able to combine two crucial properties. Firstly, it is proved to be safe with respect to infrared and collinear perturbations. Secondly, it is built in such a way that the jet boundary is resilient with respect to soft radiation, but flexible with respect to hard radiation. In other words, the shape of the jet is not influenced by soft radiation, which might originate from underlying event effects. To find the jets in the ATLAS data, the FastJet software [CS06, CSS12] is used. In this software, the anti-kt algorithm is implemented and developed by the original authors. To a certain extent, the algorithm is independent on the inner nature of its inputs, and is then able to reconstruct jets constituted of both truth particles produced by the MC generator (*cf.* Sec. 3.3.1) and detector-specific objects. Stable simulated particles are therefore used to identify "truth" jets, while reconstructed tracks in the inner detector and energy deposits in the calorimeter are used to reconstruct track jets and calorimeter jets respectively. In the definition adopted by the present work, the energy deposits used are the topological calorimeter clusters (*topo-clusters*) with positive energy. Such topo-clusters are constituted by topologically connected calorimeter cells that contain a significant signal. The signal is regarded as significant if it exceeds a 4σ threshold, and a

[10] The '++' notation stands for the upgraded requirements which present an improvement, in terms of reconstruction performance, with respect to the corresponding loose/medium/tight categories.

[11] The requirement of compatibility of the electron with the 90% efficiency working point is provided by the EIsoTool developed by the ATLAS Egamma performance group.

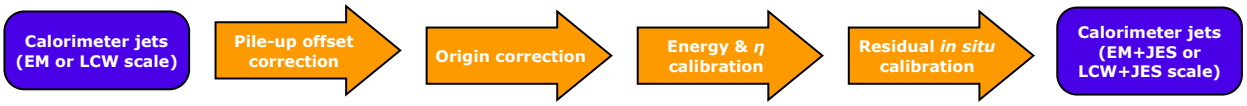

Figure 3.12.: The scheme of the jet calibration scheme commonly adopted for ATLAS data analyses. The calibration takes into account corrections of the energy scale and the direction. [A+12e].

neighbour cell is considered topologically connected if it registered a signal above 2σ. The σ is here defined as the standard deviation due to electronic and pile-up noise[12]. After a jet is found, its uncalibrated four-momentum vector is defined as the sum of the four-momenta of the constituents. At this point, the topo-clusters are reconstructed at the electromagnetic scale (EM), which measures the energy deposited in the calorimeter by particles produced in electromagnetic showers [A+12e]. As it can be seen in Fig. 3.12, the procedure for the calibration of the jet momentum is constituted by several consecutive steps:.

- The cluster energy of the uncalibrated jet is corrected for the effect associated to the expected energy offset due to pile-up interactions. This calibration depends on the average number of proton-proton interactions per bunch crossing, μ, (*cf.* Sec. 3.4.1 and 3.4) and the number of primary vertices N_{PV} in the event.
- A geometrical shift is applied to the jet origin, modifying the calorimeter jet in order to point to the event's reconstructed primary vertex.
- A second topo-cluster correction is built calibrating the calorimeter cells such that the response of the calorimeter to hadrons is correctly reconstructed. At this point, the energy scale (JES) and pseudorapidity of the jet are calibrated to the those of the particle jet.

The first and third points of the scheme above are derived with the help of the MC simulation. Jets to which this calibration is applied are referred to as jets at EM+JES energy scale.

At this point, a last refinement procedure, referred to as jet energy resolution (JER), is applied. This is a residual *in situ* correction derived from Minimum Bias data and MC samples of QCD events, which exploits two different cases where the transverse momentum of the jet is assumed to be balanced with a reference system. The two techniques are described in [A+12e].

Analogously to the electron and muon case, depending on the requirements applied, reconstructed jets can be classified as *tight(er)*, *medium* or *loose(r)* [A+12p]. Such selection

[12] For the 2011 dataset analysis,the overall noise threshold is defined as the squared sum of the electronic and pile-up contributions: $\sigma_{\mathrm{noise}} = \sqrt{(\sigma_{\mathrm{noise}}^{\mathrm{electronic}})^2 + (\sigma_{\mathrm{noise}}^{\mathrm{pile\text{-}up}})^2}$. The pile-up contribution has been determined with MC simulation and corresponds to an average of eight additional proton-proton interactions per bunch crossing ($\mu = 8$) in 2011. It is found to be negligible with respect to the electronic noise, with exception of the forward calorimeters, where $\sigma_{\mathrm{noise}}^{\mathrm{electronic}} \ll \sigma_{\mathrm{noise}}^{\mathrm{pile\text{-}up}}$

criteria are necessary to reject event containing jets whose reconstruction is due to noise sources such as cosmic-ray induced showers, LHC beam-gas interactions or hardware problems in the calorimeter. Over the whole pseudorapidity region accepted by the analysis ($|\eta| < 2.5$), the reconstruction efficiency calibration curve for the tight selection (adopted by the analysis) amounts to 85 % for values of transverse momentum of 25 GeV and reaches a 98 % plateau for values higher than 50 GeV [A+12e].

Jet Vertex Fraction

To further reduce the in-time pile-up contribution, the *jet vertex fraction* (JVF) quantity is designed [A+09a]. Such quantity classifies the jets in terms of their probability to originate from any primary vertex:

$$\mathrm{JVF}(\mathrm{jet}_i, \mathrm{vtx}_j) = \frac{\sum_k p_\mathrm{t}(\mathrm{trk}_k^{\mathrm{jet}_i}, \mathrm{vtx}_j)}{\sum_n \sum_l p_\mathrm{t}(\mathrm{trk}_l^{\mathrm{jet}_i}, \mathrm{vtx}_n)} \,. \tag{3.7}$$

The index k runs over all the tracks associated to vertex vtx_j, while index l runs over the tracks belonging to the n-th vertex reconstructed in the event. Since jets originated from non-primary vertices are naturally rejected, only the JVF associated to the *primary* vertex is considered. [13] A set of scale factors in the form of multiplicative event weights are provided for by the ATLAS Jet/$E_\mathrm{T}^\mathrm{miss}$ Performance Group, for the optimised JVF cut value. In data, a tag&probe method needs to be used to evaluate the performance of the JVF cut, since the truth jet information is not available. Events where one high-p_t Z boson and one jet were produced back-to-back are used to calculate the efficiencies.

3.5.7. B-Tagging

In order to select events where top quarks have been produced, the identification of jets that originate from the b-quarks is important. The b-tagging algorithms exploit the space resolution of the ID and the performance of the tracking and vertexing algorithms shown in Sec. 3.5.2 and 3.5.3. to interpret the jet sub-structure and identify those signatures that are unique of b-jets only. Due to the unitarity of the CKM matrix (see Sec. 2.9), not only V_{tb} is constrained to about unity, but also V_{ub} and V_{cb} are bound to be small, thus allowing the b-hadrons to have an average lifetime of about 1.6 ps [Nakon]. Together with the Lorentz boost in the laboratory frame, this directly translates into an average flight path of the b-hadrons of about 4.5 mm length, which is within the resolution of the vertexing and tracking algorithms (*cf.* Sec. 3.5.3).

[13] A value JVF $= -1$ is assigned to those jet objects for which not enough tracking information is stored for the quality standards required by the JVF construction. Jets found outside the tracking region, or mainly consisting of neutral particles belong to such group.

The b-tagging algorithms (*b-taggers*) exploit the spatial position of secondary vertices and the quality of tracks pointing to such vertices[14]. In turn, the tracks identified as stemming from a secondary vertex are used to compute the *impact parameter* with respect to the primary vertex. The b-taggers provide a weight associated to each jet that embodies the tagger result of the analysis of vertices and impact parameters. The distribution of the so called *tag weight* is built to have different behaviours depending on whether b-jets, charmed jets or light-flavoured jets data is used, falling off rather steeply in the latter case. The tag weight distribution is used to plot algorithm-specific calibration curves, where the background rejection power as a function of the signal efficiency is drawn and the tagger performances are compared.

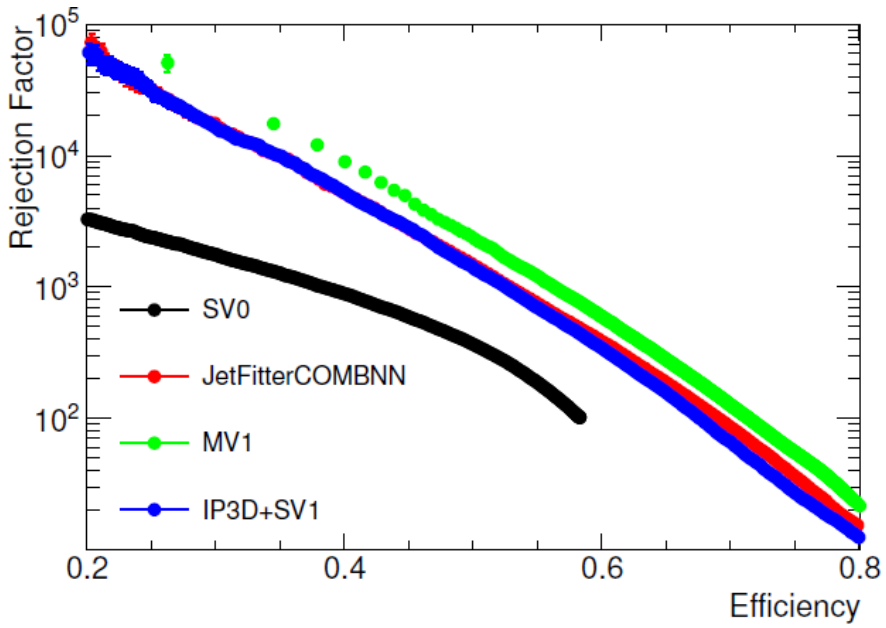

Figure 3.13.: The rejection factors as a function of the tagging efficiency for some of the b-jet taggers available at ATLAS. As can be seen, the MV1 tagger shows the best rejection power for light-flavoured jets and is therefore highly recommended to be used [A+12k].

B-Tagging Algorithms

The MV1 b-tagger has been used in this analysis. The algorithm belongs to a class of *combined* algorithms that simultaneously employ more than one *base* algorithm at the time. The MV1 tagger consists of a neural network that combines the output of three simpler likelihood ratio-based taggers:

[14] Given the fine quality needed by the b-tagging task, maximum care is devoted to the choice of the tracks involved. Tracks compatible with light-mesons decay and potential photon conversions are discarded as well as tracks that do not have at minimum of seven hits in the precision trackers.

- **IP3D** exploits the significance of the reconstructed 3-dimensional impact parameter. A two dimensional histogram of the signed transverse impact parameter significance $d_0/\sigma(d_0)$ and longitudinal impact parameter significance $z_0/\sigma(z_0)$ is used to build a *probability density function* that exploits its correlations in simulated events containing b- and light-flavoured jets.

- **SV1** is based on the presence of secondary vertices inside the jet cone. Vertices compatible with photon conversions are rejected/ The tagger uses a log-likelihood ratio which is based on three vertex properties: the number of two-track vertices, the invariant mass of all tracks associated to the secondary vertex and the ratio of the sum of the energies of the tracks from the vertex with respect to the sum of the energies of all tracks in the jet.

- **JetFitter** exploits the topological structure of weak b- and c-hadron decays inside the jet. A Kalman filter [Gav97] is used to find a common line on which the primary vertex and the b- and c-vertices lie, and their position on this line. This line is assumed to approximate the flight path for the b-hadron. With this approach, the b- and c-hadron vertices are not necessarily merged, even when only a single track is attached to each of them. The fitter information, together with additional variables such as the flight length significances of the vertices, are used to build the likelihoods.

For a detailed description of the b-tagging algorithms see [A+11d]. The rejection power as a function of the b-tagging efficiency of the MV1 tagger is shown in Fig. 3.13 and put into comparison with its other taggers. Due to its performance in terms of signal efficiency and background rejection power the employment of the MV1 tagger has been strongly recommended for all kind of top-physics analyses [A+12k]. To correct for different reconstruction efficiencies in data and MC simulated samples, event scale factors are provided for each jet as a function of its kinematic variables and of the tag weight *cut* used to select b-jets in the analysis. Jets containing long-living D mesons (*i.* e. charm-flavoured) and, for purely statistical reasons, light-flavoured jets can be selected by the b-tag algorithm. To account for the uncertainty of the background efficiency, additional scale factors are provided.

3.5.8. Missing Transverse Energy

Proton-proton collision events are by construction fully balanced with respect to the projection on the xy plane of the vectorial sum of the energies of its products. A considerable amount of *missing transverse energy* in the event, $E_{\mathrm{T}}^{\mathrm{miss}}$, is therefore considered as the experimental signature of the production of non-interacting particles such as neutrinos, and is then of crucial importance for the identification of leptonic W decays. At a preliminary stage (*e.* g. at trigger level) an approximate definition of the $E_{\mathrm{T}}^{\mathrm{miss}}$ vector components can be outlined as:

$$E_{\mathrm{x,y}}^{\mathrm{miss}} = E_{\mathrm{x,y,Calo}}^{\mathrm{miss}} + E_{\mathrm{x,y,MS}}^{\mathrm{miss}} + E_{\mathrm{x,y,Cryo}}^{\mathrm{miss}} \,. \tag{3.8}$$

The formula above represents the balancing of the transverse components of the sum of the energy measured in the calorimeters and the muon spectrometer, accounting for the expected energy loss in the cryostats. The resolution of the $E_{\mathrm{T}}^{\mathrm{miss}}$ measurement is obviously entangled with the reconstruction performance for all the physical objects (electrons, muons, jets) in the event and their four-momentum resolution. At this stage the $E_{\mathrm{x,y,Calo}}^{\mathrm{miss}}$ term in Eq. 3.8 doesn't carry sufficient information about the energy scale of reconstructed objects for which a dedicated calibration is needed, *i.* e. electrons and jets; a *refined* version [A+12m], sensitive to the objects definition must be used instead for the analysis. Such refined formulation takes the following form:

$$\begin{aligned} -E_{\mathrm{x,y,Ref}}^{\mathrm{miss}} = & E_{\mathrm{x,y}}^{\mathrm{RefEle}} + E_{\mathrm{x,y}}^{\mathrm{RefJets}} + E_{\mathrm{x,y}}^{\mathrm{RefSoftJets}} + \\ & E_{\mathrm{x,y}}^{\mathrm{RefMuon}} + E_{\mathrm{x,y}}^{\mathrm{RefCellOut}}. \end{aligned} \tag{3.9}$$

For consistency, the terms entering Eq. 3.9 must reflect the object definitions chosen for the analysis. The electron term $E_{\mathrm{x,y}}^{\mathrm{RefEle}}$ uses electrons of tight++ quality (*cf.* Sec. 3.5.5) with $p_{\mathrm{t}} > 10\,\mathrm{GeV}$, where all the energy scale corrections have been applied. Analogously, the muon term $E_{\mathrm{x,y}}^{\mathrm{RefMuon}}$ includes all the reconstructed combined muons that survive the overlap removal procedure presented in detail in Sec. 4.2.1; a treatment of the overlap between the isolated muon tracks and the energy deposited by these muons in the calorimeter cells (populating the Cell Out term) is *not* implemented. Further reference on the muon term can be found in Ref. [A+10c]. The main jet term $E_{\mathrm{x,y}}^{\mathrm{RefJets}}$ includes jets that do not overlap with electrons in the sense specified in Sec. 4.2.1 and have $p_{\mathrm{t}} > 20\,\mathrm{GeV}$. These jets are calibrated to the EM+JES energy scale described in Sec. 3.5.6, in contrast to those entering the $E_{\mathrm{x,y}}^{\mathrm{RefSoftJets}}$ term, that are chosen in the $7\,\mathrm{GeV} < p_{\mathrm{t}} < 20\,\mathrm{GeV}$ transverse momentum range and are calibrated at the EM level only. The sum order of Eq. 3.9 is of the utmost importance, since the energy clusters in the calorimeters must enter the computation only once, and the order has to be globally consistent with the overlap removal procedure. As a final correction, the $E_{\mathrm{x,y}}^{\mathrm{RefCellOut}}$ term accounts for all the reconstructed energy clusters that were not assigned to any reconstructed object. Events containing reconstructed τs and γs are not considered in the analysis, therefore their contribution doesn't need a dedicated $E_{\mathrm{x,y,Ref}}^{\mathrm{miss}}$ term but is expected to be negligible and counted for in the $E_{\mathrm{x,y}}^{\mathrm{RefCellOut}}$ term as well.

4. Event Preselection and Background Modelling

Before computing the event kinematic quantities necessary for the analysis and the subsequent signal extraction, several corrections must be applied to the reconstructed objects in both data and Monte Carlo. Such corrections are needed in order to properly take into account the intrinsic difference between the recorded data – where the truth event is unknown – and its simulation, whose precision is limited from the side of the theoretical and computational approximations needed by the physics models. The guidelines that have been issued by the ATLAS top physics reconstruction group aimed at a pre-selection of events compatible with the top quark experimental signature are then presented in Sec. 4.1, and a full overview of the event refinement procedures applied in accordance with the physics performance recommendations is presented in Sec. 4.2, in terms of physics reconstruction, pile-up modelling and flavour composition. The background composition is presented in Sec. 4.3. A special emphasis is dedicated to the description of the data-driven techniques adopted for the estimate of the QCD multi-jet and W+jets contributions, in Sec. 4.3.1 and 4.3.2, respectively.

4.1. Selection of Single Lepton Events

The following event preselection cuts are applied:

- **Trigger** An event is required to be selected by the smallest unprescaled high-p_{t} electron or muon event filter (EF) trigger. The involved exact p_{t}-threshold is dependent on the run-period (*cf.* Tab. 4.1).
- **LAr Quality** The event is discarded if it contains a noise burst in the EMCal.
- **Primary Vertex** The primary vertex must have at least 5 associated tracks.
- **Overlap Removal** Reconstructed electron, muons and jets presenting a geometric overlap are rejected, according to the procedure described in Sec. 4.2.1.
- **Lepton Selection** Exactly one signal lepton (as defined in sections 3.5.4 and 3.5.5 for muons and electrons respectively) is required. The lepton must be found in the ID active region ($|\eta| < 2.47$) and fulfill the following transverse momentum requirements,

Run Periods	Luminosity [pb^{-1}]	Electron Trigger	Muon Trigger
B-D	178.388	e_20_medium	mu_18
E-H	948.666	e_20_medium	mu_18
I	337.543	e_20_medium	mu_18
J	226.392	e_20_medium	mu_18_medium
K	590.363	e_22_medium	mu_18_medium
L-M	2431.74	e_22vh_medium1	mu_18_medium

Table 4.1.: Run-period dependent trigger requirements (e_X_Y and mu_X_Y denote electron and muon trigger items with p_t thresholds of X GeV and lepton identification quality Y).

according to the lepton type:
e: $p_t > 30\,\text{GeV}$,
$\boldsymbol{\mu}$: $p_t > 25\,\text{GeV}$.

- **Lepton Veto** No second lepton of signal quality must be present in the event.

- **Lepton Trigger Compatibility** The selected signal lepton must be matched to the above trigger object within $\Delta R < 0.15$.

- **Neutrino Event** A cut on the missing transverse energy, E_T^miss, is applied, in order to select events containing a neutrino from the leptonic decay of a on-shell W boson; according to the lepton type, events are *accepted* if:
e: $E_\text{T}^\text{miss} > 30\,\text{GeV}$
$\boldsymbol{\mu}$: $E_\text{T}^\text{miss} > 25\,\text{GeV}$.

- **QCD Rejection** In order to suppress the QCD background, a cut is applied on the reconstructed transverse mass of the W boson in the event, m_T^W; according to the lepton type, the events are *accepted* if:
e: $m_\text{T}^W > 30\,\text{GeV}$
$\boldsymbol{\mu}$: $E_\text{T}^\text{miss} + m_\text{T}^W > 60\,\text{GeV}$.

- **Jet Selection (PreTag)** There must be exactly three or four good jets with $p_t > 25\,\text{GeV}$ found in the $|\eta| < 2.5$ region (as defined in Sec. 3.5.6).
If there is a jet not fulfilling the quality requirements with $p_t > 20\,\text{GeV}$, the event is rejected.

- **b-Tag Selection** Exactly one of these jets must yield a b-tag weight compatible with an efficiency of 70 % of the MV1 algorithm (*cf.* Sec. 3.5.7).

4.2. Corrections

4.2.1. Physics Objects Overlap Removal

After the selection operated by the EF trigger decision, the kinematic cuts listed in Sec. 4.1 are applied to enrich the yield of events containing top quarks and additional jets in the final states. Since the reconstruction algorithms operate independently from each other, some corrections are necessary to prevent the selection of physics objects that have been reconstructed by more than one algorithm, or to drop events where two reconstructed objects are spatially too close to ensure a correct resolution performance. The full procedure follows the prescriptions described in the following, in the order that is given.

Electron-Jet Overlap

Energy clusters in the calorimeter that have been deposited by electrons are also used by the jet reconstruction algorithms, therefore it is frequent that highly energetic electrons presenting a minor leak in the HCal are also identified as low energy jets. To clean the, a prescription to keep the event and remove from it all jets found within $\Delta R = 0.2$ is applied, *after* the kinematic cuts on jets and electrons. As a further refinement, if a second (selected) jet is found within a $\Delta R = 0.4$ distance from the electron cone, the electron is discarded.

Electron-Muon Overlap

This procedure is implemented to prevent the bias from events where a (real o noise-induced) MS track segment is associated to an electron track, and reconstructed as a prompt muon. For this purpose, if the ID track is shared between an electron and a muon both satisfying the selection criteria, the whole *event* is *rejected*.

Jet-Muon Overlap

To avoid the selection of punch-through muons that have not been rejected by the muon quality selection cuts, muons that are found within $\Delta R = 0.4$ from any of the selected jet axis are removed from the event. As mentioned in Sec. 3.5.8, the computation of the muon contribution to the missing transverse energy takes this procedure into account.

4.2.2. Pile-up Reweighting

During the 2011 data taking period, the conditions of the pile-up phenomenon described in Sec. 3.4.1 have not been stable, but have rather increased linearly with the instantaneous luminosity, as it is visualised in Fig. 3.11. As it can be seen, the number of hard interactions per bunch crossing moved from an average of $\mu = 5$ at the beginning of the 7 TeV operations to a maximum of about 40 in the final phase. Also, in practice, the variations of the average

number μ of pile-up interactions in real data occur not only in different runs but also, within a given run, between the elementary recorded intervals of luminosity blocks, as it is described in Sec. 3.4. As a result, a detailed simulation of the pile-up varying with the data period beam conditions turns out to not be feasible from a mere computational point of view, since the MC production campaigns are lengthy and therefore need to be launched long before the end of a data taking period. A pile-up model adherent to the data is then imposed *a posteriori* on the simulation samples. The model consists of an event reweighting procedure that corrects each event by a factor computed from the average pile-up distribution used for the Monte Carlo production and the one that is measured in the dataset used for the analysis [A+11e].

4.2.3. Heavy Flavour Overlap Removal

As shown in Tab. 2.3 the ALPGEN [MMP+03] software is used to produce separated datasets of W+jets samples with respect to the flavour composition of the final states. Within the ALPGEN setup, no attempt is made to match explicitly the flavour content, which is normally done in generators based on matrix elements interfaced with a parton shower model. This means that there are cases where the same heavy flavour final states arise in multiple samples, being produced by either the event generator or the parton shower algorithm, and such classes of events need therefore to be vetoed, in order to avoid double-counting.

Several methods have been made available to perform the heavy flavour overlap removal (HFOR) procedure [A+10d]. The HFOR procedure used in this analysis follows the prescriptions which the ATLAS collaboration agreed upon that exploits the different strengths of the matrix element and of the parton shower algorithm, that are more apt to describe the quark pair production at wide angles and the collinear gluon splitting respectively. The procedure used consists of applying a selection based on the distance ΔR between quark pairs, where the value 0.4 is chosen in accordance with the cone size of the jet algorithm. In detail, the following selection are applied to all the samples listed in Tab. 2.3:

- W+Np:
  Remove all events where the presence of heavy flavour is due to the matrix element. Remove all events in which the heavy-flavour quark-pairs are not matched to one reconstructed jet.
- W + c+Np:
  Remove all events in which the heavy-flavour quark-pairs are not matched to one reconstructed jet.
- W + $c\bar{c}$+Np:
  Remove all events in which $c\bar{c}$ pairs are matched to one reconstructed jet.
- W + $b\bar{b}$+Np:
  Remove all events in which $b\bar{b}$ pairs are matched to one reconstructed jet

When the official ATLAS HFOR tool is applied, events are labelled as light, c, $c\bar{c}$ or $b\bar{b}$ according to the truth flavour content. These labels are necessary since the cross section values provided for the background normalisation are computed with respect to the truth flavour content of the complete W+jets MC dataset, rather than the nominal one. When these labels are correctly assigned, a reshuffling of the events occurs. Events originally contained in the light-flavour W+jets datasets can be identified as heavy-flavoured (and vice versa) and grouped into datasets that are named according to their correct label. When this occurs, their contribution inside the new datasets needs to be weighted according to the production cross section of their provenance datasets. This is necessary in order to be able to implement the data-driven techniques that provide the scale factors for the normalisation of these reshuffled W+jets datasets.

4.2.4. Object Corrections

In order to compensate the effect of different reconstruction performance in terms of efficiency and 4-momentum resolution that occur in simulated and real data, the following corrections are applied to the physical objects in all the simulated events. All the corrections described hereafter follow the common prescriptions from [A+12k].

Leptons

- The lepton energy is smeared in the MC samples, using additive correction factors that exploit the precise knowledge of the Z mass.
- The event is weighted by a *lepton scale factor*, computed by means of tag&probe techniques[1] applied on $Z \to \ell\ell$ events, which corrects for the different trigger efficiency measured in data and MC.
- The electron energy is corrected in the MC according to the available *in situ* calibration measurements in the calorimeter. No energy calibration is found to be necessary in the muon case, since the momentum is computed from the track parameters in the ID.

Jets

- The jet energy is scaled by a factor that carries the effect of the *in situ* calibration, which is done analysing events where one jet is produced together with a second object

[1] The tag&probe method integrates over all relevant kinematical variables to obtain a global trigger efficiency, or a differential one – when the available statistics allows a detailed modelling – as a function of the pseudorapidity and the transverse momentum. Two samples are defined: a *diagnostic* sample, constituted of events where at least one electron passes the trigger (the "tag"), and a *control* sample, constituted of events where at least two electrons pass the trigger (the "probe"). The two are determined by counting in the absence of background (more generally, by sideband subtraction or a mass peak fit).

that has a better 4-momentum resolution. The calibrations used in this analysis are based on the reconstruction of the electronic decay of Z bosons in $Z + 1$ jet events and the subsequent measurement of exactly one recoiling jet.

- No energy smearing is found to be necessary, due to an overall good agreement between the kinematic distributions in data and MC [A+12k].
- A multiplicative scale factor is applied to the event weight to correct for the different efficiency of the Jet Vertex Fraction cut on data and MC.
- A multiplicative scale factor is applied to the event weight, accounting for the discrepancies of the jet reconstruction efficiency between the data and the simulation. Analogously to the the case of the lepton factors, these efficiencies are extracted with a "tag" and "probe" method, using minimum bias data and QCD multi-jet MC samples[Gho12].
- To account for the discrepancies between data and MC of the JVF > 0.75 cut efficiency, four multiplicative scale factors are combined in a single one and then applied to the event weight. Each of these factors represent the table of confusion[2] of the four combinations of (in)efficiency effects of selecting (rejecting) the hard scatter jets (pile up).
- Multiplicative event scale factors are applied to offset the data/MC discrepancies related to the b-tag weight cut. The b-tagging scale factors are provided as function of the momentum and pseudorapidity of the tagged jet, and for each optimised working point (*cf.* Sec. 3.5.7).

It is important to remark that the corrections listed above are associated to each jet in the event; therefore, the final weight of the selected MC events is built necessarily from the product of the scale factors assigned to all the jets passing the selection cuts.

4.3. Background Modelling

As it is described in Sec. 2.4, the main background processes for the single top Wt-channel are, in order of decreasing production rate: QCD multi-jet production, W+jets (light and heavy flavour jets), Z+jets, top-pair production and the two other single top production channels, t- and s-channel production.

As noted in Sec. 2.4.7, the appearance of multi-jet events in the lepton selection is due to the huge order of magnitude of the QCD cross section which can not be totally vetoed by the

[2] In the field of predictive analytics, a table of confusion (also referred to as confusion matrix) is a table with two rows and two columns that reports the rates of false positives, false negatives, true positives, and true negatives.

necessarily finite background rejection power of the lepton reconstruction algorithms. Since too many QCD events would need to be simulated to obtain a statistically significant sample of multi-jet background in the final selection, alternative methods based on data itself must be employed to provide the background model.

Also, as shown in Sec. 2.4.4, the overall theoretical uncertainty of the W+jets component of the background amounts to about 60% when all the additional partons are included in the final state of the simulated samples. Data-driven methods are then needed to assess its correct absolute normalisation, for both the light an heavy flavoured final state composition.

The QCD and the W+jets backgrounds are estimated with the data-driven methods described in the following sections, while for modelling the remaining background processes, both the kinematic distributions and the luminosity normalisations adopted are taken from the MC simulation samples listed in Tab. 2.3. The

4.3.1. QCD Multi-Jet Events

The QCD multi-jet background is modelled by a data-driven method, the so-called *jet-electron* model, described in [A$^+$12k] and already used for the ATLAS measurement of the single top production cross section in the t-channel [A$^+$12h]. The jet-electron method derives a shape for the QCD multi-jet background by selecting events in data that display similar kinematic features as the signal selection but the signal electron is replaced by a jet, whose set of reconstruction parameters is very similar to the lepton. The normalisation of the model is performed by a template fit to the $E_{\mathrm{T}}^{\mathrm{miss}}$ distribution in the sideband region $E_{\mathrm{T}}^{\mathrm{miss}} \leq 25\,\mathrm{GeV}$. In Fig. 4.1 the concept sketch of the extrapolation from the low energy sideband region in the jet-electron model is visualised. For these events the refined computation of the transverse missing energy shown in Eq. 3.9 needs a further adjustment, and the jet used in place of the electron is removed from the $E_{\mathrm{x,y}}^{\mathrm{RefJets}}$ term and added to $E_{\mathrm{x,y}}^{\mathrm{RefEle}}$. This approach turned out to also yield good results when the procedure is applied in the same manner to model the background to the muon reconstruction. It is therefore used in this analysis to model the QCD multi-jet background in both lepton channels. In order to ensure an optimal performance of the jet-electron model, the electron channel sample was split into events with a central signal electron and events with a forward signal electron. The corresponding weight factors to scale this QCD estimate to data luminosity on the b-tagged sample are collected in Tab. 4.2.

Jet Bin	n_{QCD} (e, central)	n_{QCD} (e, forward)	n_{QCD} (μ)
$N_{\mathrm{jets}} = 3$	0.0858	0.0858	0.0821
$N_{\mathrm{jets}} = 4$	0.0661	0.0661	0.0282

Table 4.2.: Jet bin and signal lepton flavour dependent normalisation factors for the data-driven QCD contributions (the QCD yield after the b-tag selection is computed as $\mathcal{N}_{\mathrm{QCD}}^{Tag} = n_{\mathrm{QCD}} \cdot \mathcal{N}_{\mathrm{DATA}}^{Tag}$).

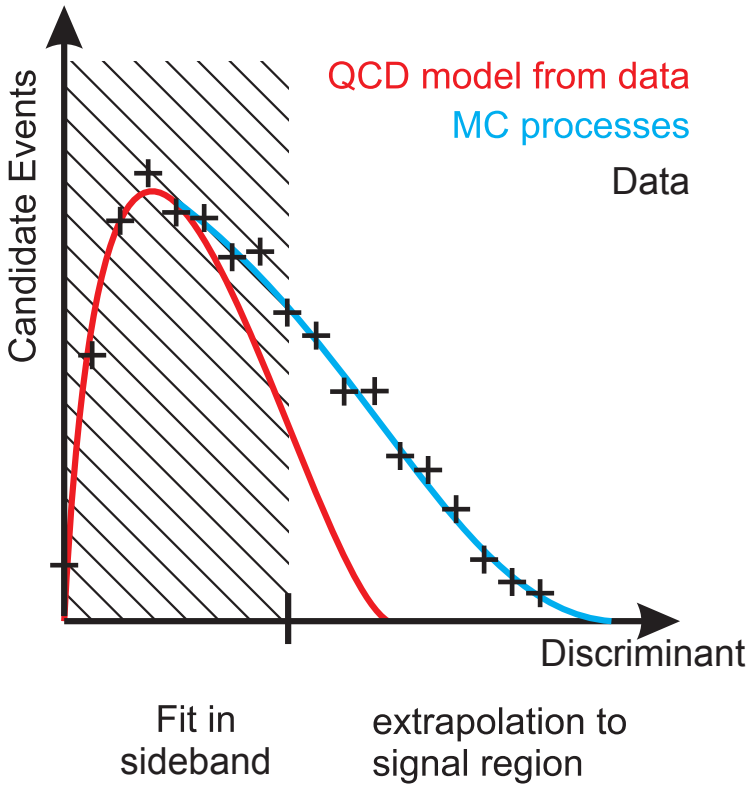

Figure 4.1.: Concept of a sideband extrapolation in the jet-electron model [A+12k]. In the model's assumptions, a selection cut is applied on a given observable quantity, which is expected to discriminate the signal-enriched fraction of the data from a region essentially populated with background events of a determined component of the background. The number of events collected in the sideband region is expected to provide a robust support to the fit, allowing for a statistically more reliable alternative to the MC. The normalisation factor of the model is extracted from the fit parameters in the sideband region, and extrapolated to the signal region. In the jet-electron model, the physical observable used as discriminant is the missing transverse energy, while the model itself consists of events where the standard lepton is replaced by a fictitious one, fabricated from a jet whose reconstruction parameters are very similar to the lepton.

In Fig. 4.3 the $E_{\mathrm{T}}^{\mathrm{miss}}$ and m_{T}^{W} distributions are shown after applying the normalisation factors shown in Tab. 4.2 to the jet-electron sample, for the three jets selection after the b-tag requirement. The correct modelling of the m_{T}^{W} distribution after the selection operated on data and MC shows a substantial agreement, confirming the goodness of the $E_{\mathrm{T}}^{\mathrm{miss}}$ sideband fit results.

4.3.2. Flavour Composition and Normalisation of W+jets

The W+jets background consists of processes in which leptonically decaying W bosons are produced in association with jets originating from light or heavy flavour quarks (*cf.* Tab. 2.3). The heavy flavour final states considered are W+c, W+c$\bar{\mathrm{c}}$ and W+b$\bar{\mathrm{b}}$. All other final states are denoted by W+light flavour. The estimation of this background contribution is also estimated using a mixed approach that exploits both Monte Carlo and data-driven techniques. The analysis selection is performed on the MC samples of W+jets and subsequently the contributions of the four different HFOR types (W+light flavour, W+c, W+c$\bar{\mathrm{c}}$ and W+b$\bar{\mathrm{b}}$) are reweighted with respect to each other according to scale factors derived from data. The scale factors related to the flavour fractions are extracted counting the events surviving the standard pre-tag and b-tag preselection defined in Sec. 4.1. For reducing the statistical uncertainty, the estimate of the scale factors is performed in the two jet bin, where W+jets events constitute the dominant contribution, and extrapolating the result to the higher jet bin case.

Overall W+jets Normalisation

A scale factor K_N, accounting for the overall W+jets normalisation, is estimated from data. The extraction overall normalisation is accomplished by the charge-asymmetry method (*cf.* [A$^+$12k]). This method makes use of the fact that W+jets is the main background process which displays a charge asymmetrical production rate, and relies on the data yield as well as on the MC yields of all non-W+jets background processes. In general, the ratio

$$r_{MC} \equiv \frac{\sigma(\mathrm{pp} \to \mathrm{W}^+)}{\sigma(\mathrm{pp} \to \mathrm{W}^-)} \tag{4.1}$$

between the pure theoretical cross sections of the production of $W^{+/-}$ bosons is a quantity that is known with a very small associated uncertainty. This knowledge is used in the general formula leading to the data-driven estimate of the W+jets events is given in Eq. 4.2, to express the total number of W bosons that is measured in the experiment:

$$N_{W^+} + N_{W^-} = \left(\frac{r_{MC}+1}{r_{MC}-1}\right)\left(D^+ - D^-\right). \tag{4.2}$$

In equation 4.2 the quantity $D^+(D^-)$ represents the number of selected events containing positively (negatively) charged leptons. Using Eq. 4.2 in Eq. 4.3 as follows, the number $W^n_{\geq 1tag}$ is found of total W+jets events surviving the tag selection for the bin containing n good jets as defined in Sec. 3.5.6:

$$N^n_{Tag} = N^n_{PreTag} \cdot f^2_{Tag} \cdot f^{2\to n}_{Tag}. \tag{4.3}$$

Following this prescription the overall W+jets normalisation factor is found by means of:

- N^n_{PreTag}: the data-driven estimate of events found in the pretag region when analysing the n jet bin;
- f^2_{Tag}: the b-tag fraction in the 2 jet bin; this quantity is measured from data after subtracting the number of all the contributions from non-W expected events (i.e. the number of QCD events estimated with the data-driven method and the MC yields for all other channels) in the W+jets control region.
- $f^{2\to n}_{Tag}$: the ratio between the b-tagged fraction in the n and 2 jet bin, using the pure Monte Carlo model.

The overall normalisation scale factor for the W+jets yield can be defined as

$$W_N = \frac{N^{\mathrm{W}}_{\mathrm{data}}}{N^{\mathrm{W}}_{\mathrm{MC}}}. \tag{4.4}$$

The scale factor values obtained in this analysis by applying the procedure are listed in Tab. 4.3.

Flavour Composition Determination

After determining the total number of W+jets events in the collected data, the four real compositions of the flavour (HFOR labels) fractions are estimated using as an input:

- the flavour fractions in the 2 jet bin computed from the MC: $F_{\mathrm{LF},2}$, $F_{\mathrm{c},2}$, $F_{\mathrm{cc},2}$ and $F_{\mathrm{bb},2}$, defined as
$$F_{xx,2} = \frac{N^{\mathrm{W,PreTag}}_{xx,2}}{N^{\mathrm{W,PreTag}}_{2}}, \quad xx \in \{\mathrm{LF},\, \mathrm{c},\, \mathrm{cc},\, \mathrm{bb}\}\,. \tag{4.5}$$
- the total number of W+jets events after the *Tag* selection, expressed in terms of the number of *PreTag* events:
$$N^{\mathrm{W,Tag}}_{2} = N^{\mathrm{W,PreTag}}_{2}(F_{\mathrm{LF},2}P_{\mathrm{LF},2} + F_{\mathrm{c},2}P_{\mathrm{c},2} + F_{\mathrm{cc},2}P_{\mathrm{cc},2} + F_{\mathrm{bb},2}P_{\mathrm{bb},2}) \tag{4.6}$$
which is obtained by means of the probabilities $P_{xx,2}$ to find a b-jet in each of the xx flavour type MC sample.

- A unitarity condition on the flavour fractions:

$$F_{\mathrm{LF},2} + F_{\mathrm{c},2} + F_{\mathrm{cc},2} + F_{\mathrm{bb},2} = 1\,. \tag{4.7}$$

At this point, one additional condition is imposed, that the ratio in data of the fractions of W+cc and W+bb events is identical to its MC estimate $k_{\mathrm{cc}\to\mathrm{bb}}$, thus reducing the number of unknown quantities to three. Finally, in order to gain the third independent equation necessary to solve the system, the condition in Eq. 4.6 is split according to the lepton charge, assuming that the dependence involves only the quantities $N_2^{\mathrm{W,Tag}\pm}$ and $N_2^{\mathrm{W,PreTag}\pm}$, and not the $F_{\mathrm{xx},2}$ and $P_{\mathrm{xx},2}$ [Her14, Vre13].

The flavour fractions in the 2 jet bin are then used to extrapolate the values in the 3 jet bin used in the present work, imposing again that the respective flavour fractions add up to unity [Her14, A$^+$12k]. The flavour composition scale factors obtained, K_{LF}, K_{c}, K_{cc} and K_{bb}, are shown in Tab. 4.3 and used during the further steps of this analysis. The values found in this work are in agreement with the current W+jets scaling settings obtained independently by other groups involved in top physics analyses at ATLAS [A$^+$12k].

4.3.3. Control Distributions

In order to verify the goodness of the data model components, the effects of the event preselection and MC corrections are visualised using control distributions of physical observables. In this work, following the common prescriptions adopted in the ATLAS top quark working group, two levels of the pre-processing are considered: the *PreTag* and the *Tag* sample, corresponding to the selection levels before and after the b-tag requirement, respectively. Exemplary plots of the reconstructed $E_{\mathrm{T}}^{\mathrm{miss}}$ and m_{T}^{W} distributions before and after the b-tag requirement selection in the three-jet bin are shown in Fig. 4.2 and 4.3.

Normalisation of MC Histograms and Treatment of Statistical Errors

In order for the Monte Carlo distributions to represent the data faithfully, the histograms of all the simulated processes are normalised to the total integrated luminosity $\mathscr{L}_{\mathrm{data}}$ of the data sample which they are compared to. In practice, the number of entries $N_{\mathrm{MC},i}$ of each distribution of each MC process is replaced by a normalised quantity:

$$N_{\mathrm{MC},i}^{\mathrm{norm}} = N_{\mathrm{MC},i}\frac{\sigma_{\mathrm{MC},i}\cdot\mathscr{L}_{\mathrm{data}}}{N_{\mathrm{MC},i}^{\mathrm{sample}}}. \tag{4.8}$$

Here $\sigma_{\mathrm{MC},i}$ is the Monte Carlo cross section associated to the i-th process (listed in Tab. 2.3) and $N_{\mathrm{MC},i}^{\mathrm{sample}}$ is the total number of events that was initially generated for the i-th MC sample. Inserting in the original number of generated events has the effect of including the selection acceptance in the normalisation factor. The sum $\sum N_{\mathrm{MC},i}^{\mathrm{norm}}$ of all MC histograms is then

compared to the data histogram. In this sense, in each distribution the top of the simulation stack represents the sum of the MC histograms of all the considered processes. Together with the number of expected events, the uncertainties of each bin entries, $\Delta N_{\mathrm{MC},i}$, are scaled according to Eq. (4.8) for each process. The definition of the statistical error depends on the number of entries populating the single bin of each of the distributions. After the selection, if the number of bin entries is large enough, the uncertainty is the width of the Poisson distribution, $\Delta N_{\mathrm{MC}} = \sqrt{N_{\mathrm{MC}}}$. In this case the error definition adopted is symmetrical around the central value. On the contrary, when the number of entries in the bin is low, the uncertainties follow the definition given by the Feldman-Cousins method [FC98]. Using asymmetrical definitions for central values close to zero, the unphysical intervals which exceed the domain of the variable are avoided; in this work, 33 bin entries were chosen as a suitable threshold for the error regime transition. The total uncertainty of the stacked MC histograms in each bin then follows from simple error propagation:

$$\Delta N_{\mathrm{MC}}^{\mathrm{total}} = \sqrt{\sum_{i} (\Delta N_{\mathrm{MC},i}^{\mathrm{norm}})^2} \tag{4.9}$$

Throughout this study, the error $\Delta N_{\mathrm{MC}}^{\mathrm{total}}$ is drawn with a pink hatched area above the stacked histograms of all MC samples. The same treatment of the statistical uncertainties, depending on the number of entries populating each bin on the MC histograms and using also a threshold of 33 entries to define the error definition transition, is used in a study performed in parallel to this work, where the kinematic fit technique is used to identify single top events in the t-channel [Her14].

PreTag Control Distributions

The *PreTag* control distributions of $E_{\mathrm{T}}^{\mathrm{miss}}$ and m_{T}^{W} are shown in Fig. 4.2 for both the electron and muon channels in the 3 jet bin. The distributions of the missing transverse energy and the transverse mass of the reconstructed W boson are used to verify the goodness of the W+jets scale factor estimation described in Sec. 4.3.2. The signal and background MC samples, including W+jets, are normalised to the theoretical cross sections, reported in Tab. 2.3. The QCD multi-jet part is normalised using the factors extracted by the Jet-Electron fit for the *PreTag* selection. Since the scale factors for the W+jets samples can not be extracted for the *PreTag* selection level, it is here chosen to display the simulation data after a further scaling of the simulation stack with a common factor, to best fit the collision data. As can be seen from the figures, the W+jets background component dominates the *PreTag* level of the selection.

Tag Control Distributions

All the simulation samples after the *Tag* selection level are normalised to the data luminosity, according to the cross sections shown in Tab. 2.3. At this stage, the QCD multi-jet background component obtained from the Jet-Electron method is normalised by means of the scale factors presented in Tab. 4.2. The W+jets components are normalised using the W+jets scale factors, given in Tab. 4.3, as they are found with the data-driven method.

	Jet Bin	$K_{bb/cc}$	K_c	K_{ll}	W_N
e	3	1.153525	0.939875	0.981052	0.854447
	4	1.145241	0.933125	0.974007	0.909405
μ	3	1.229149	0.974645	0.956930	0.898860
	4	1.215753	0.964022	0.946500	1.004964

Table 4.3.: Jet-bin dependent W+jets normalisation factors for each flavour fraction used in the analysis. The figures in the table have been obtained from the tag counting method. The statistical uncertainty on $K_{bb/cc}$,K_c and K_{ll} is $X_{bb/cc}$%,X_c%,and X_{ll}% respectively. The scale factors K_Ns are used for the overall normalisation of the W+jets contribution. The remaining flavour factors, K_is, are used for the normalisation of the differently flavoured components of the W+jets spectrum. The values found by us are in agreement with the current W+jets scaling settings obtained independently by other groups involved in top physics analyses at ATLAS [A$^+$12k].

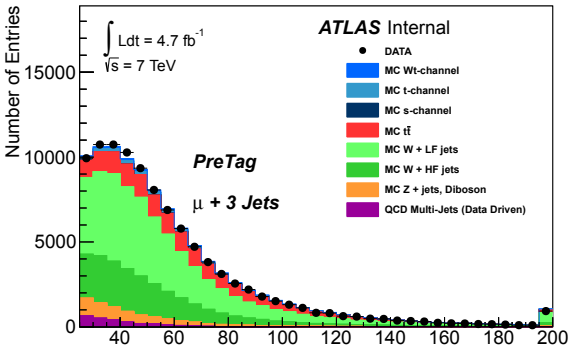

(a) Missing transverse energy. μ+3 jets, pre-tag.

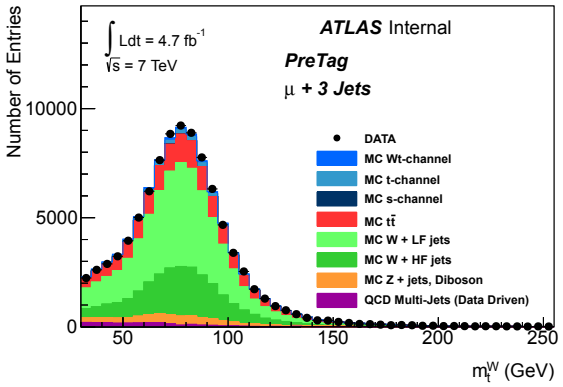

(b) Transverse W mass. μ+3 jets, pre-tag.

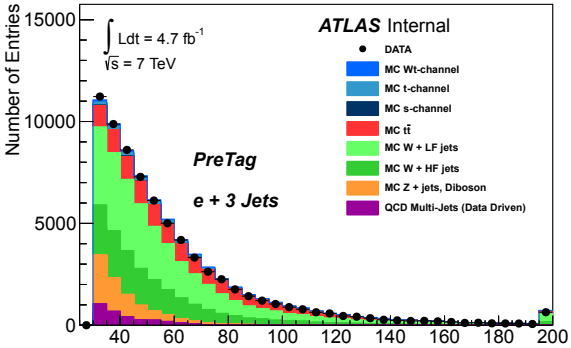

(c) Missing transverse energy, e+3 jets pre-tag.

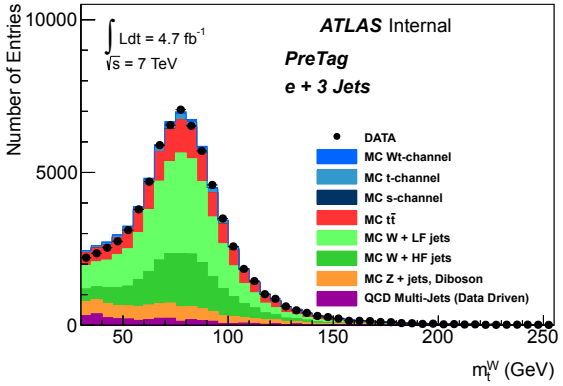

(d) Transverse W mass. e+3 jets, pre-tag.

Figure 4.2.: Distribution of the missing transverse energy and the transverse W mass, requiring the presence of exactly one lepton and three jets without b-tagging requirements, for the muon ((a), (b)) and electron ((c), (d)) selection. The jet-electron model described in Sec. 4.3.1 for modelling the multi-jet background contribution, using the normalisation factors of Tab. 4.2. For the W+jets fraction the kinematic distribution are taken from the MC simulation, while the data-driven factors in Tab 4.3 extracted from the charge asymmetry event yield are used for the normalisation. The remaining samples are normalised according to the theory. The full MC stack plot is scaled by an overall 1.08 factor. After this final normalisation step a good shape agreement between the data and the MC is seen. The last bin contains the sum of the events in that bin or higher.

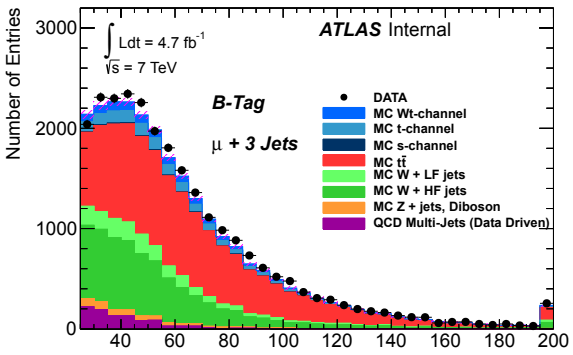

Missing transverse energy, μ+3 jets selection.

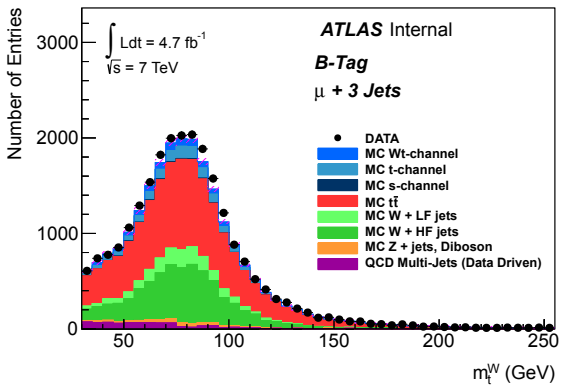

Transverse W mass, μ+3 jets selection.

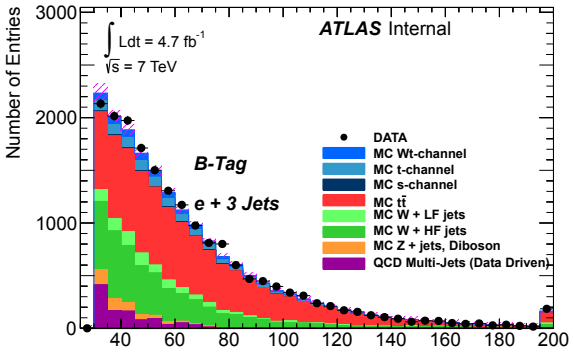

Missing transverse energy, e+3 jets selection.

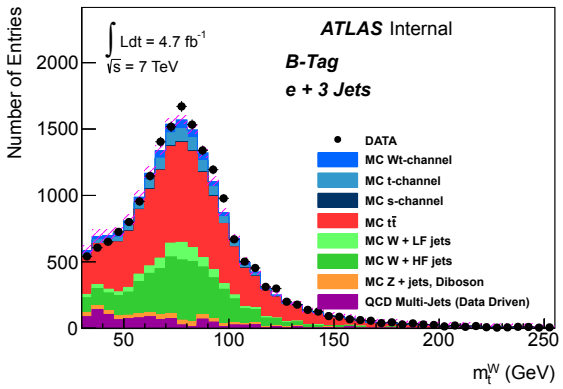

Transverse W mass, e+3 jets selection.

Figure 4.3.: Distribution of the missing transverse energy and the transverse W mass, requiring the presence of exactly one lepton and three jets of which exactly one is b-tagged, for the muon ((a), (b)) and electron ((c), (d)) selection. The jet-electron model described in Sec. 4.3.1 for modelling the multi-jet background contribution, using the normalisation factors of Tab. 4.2. For the W+jets fraction the kinematic distribution are taken from the MC simulation, while the data-driven factors in Tab 4.3 extracted from the charge asymmetry event yield are used for the normalisation. The remaining samples are normalised according to the theory. The last bin contains the sum of the events in that bin or higher.

5. Kinematic Fit of Single Top Events

In this chapter the basic principles of the kinematic fitting of high energy physics events are presented along with its implementation in the analysis framework. This serves as a manual for the application of the fitter to the reconstruction of events where a single top quark is produced in association with a W boson, described in Chap. 6.

5.1. The Kinematic Fitter

The main idea of the kinematic fit is to test a certain hypothesis of a final state or a decay chain by means of the measured particle momenta in the final state. One assumes invariant masses of the decaying particles as well as of the final state particles. The hypotheses of the particle identities determine the kinetic energies of the outgoing particles. Further constraints, like momentum conservation, are possible. The final decision to accept or decline the hypothesis is based on the minimal χ^2 value returned.

A prominent application of a kinematic fit is the reconstruction of particle decays or decay chains. Aside from the removal of physical background originating from similar looking processes, the kinematic fitter is also able to substantially reduce combinatorial background by testing the fit hypothesis for all possible combinations, allowing for a subsequent comparison of the resulting χ^2 values. Beside the assignment of particle tracks, the fitter also corrects the momenta of the final state particles individually, which in turn will reduce systematic errors. The fitter is also able to extend the measurement. Not all momentum components of the final state particles need to be known, provided that the number of constraints in the fit surpasses the number of unknown parameters.

This is used in the kinematic reconstruction of single top events since here the neutrino coming from the leptonic W decay does not interact with the detector. Only the missing transverse energy contains information about the neutrino, and thus its polar angle is an un-measured input parameter for the fit. As will be shown, the fit is able to reconstruct the unknown variable properly. A fully detailed reference including the validation and the performance studies that led to the application of the kinematic fit technique to ATLAS data is found in [BBG+12].

5.1.1. Least Squares and Non-linear Constraints

The fit method used here was first discussed in [BL98]. The fit relies on n unbiased measurements $\{y_i\}_{i=1,2,\ldots,n}$ and p un-measured parameters $\{a_j\}_{j=1,2,\ldots,p}$. The covariance matrix of the measurements is denoted as $C_{\mathbf{y}}$.

Based upon a given model the fitter tries to find statistical estimators for the measurements $\mathbf{y}$ and solutions for the un-measured parameters $\mathbf{a}$, respectively. The estimators are supposed to be closer to the true values $\bar{\mathbf{y}}$ which are the expectation values of the measurements $\mathbf{y}$. Let $\bar{\mathbf{a}}$ be the true parameter values which are restricted by the constrains given by the model

$$f_k(\bar{\mathbf{a}}, \bar{\mathbf{y}}) = 0 \ , \quad k = 1, 2, \ldots, m \, . \tag{5.1}$$

In general, the measurements deviate from $\bar{\mathbf{y}}$, its variances are given by $C_{\mathbf{y}}$. Corrections $\mathbf{\Delta y}$ are needed for which the sum $\mathbf{y}+\mathbf{\Delta y}$ fulfills the given constraints. At the same time the deviations from the measurements should be small. For the simple case of uncorrelated measurements $C = \mathrm{diag}(\sigma_1^2, \ldots, \sigma_n^2)$ the following minimisation is needed:

$$\chi^2 = \sum_{i=1}^{n} \frac{(\Delta y_i)^2}{\sigma_i^2} = \mathbf{\Delta y}^T C_{\mathbf{y}}^{-1} \mathbf{\Delta y} \, . \tag{5.2}$$

For the general case the last term must be extended. If the measurements are correlated, *i.* e. the matrix $C_{\mathbf{y}}^{-1}$ is not diagonal, a linear transformation of the $\mathbf{y}$ in combination with the respective error propagation would be sufficient to diagonalise the matrix $C_{\mathbf{y}}$. One can easily show that the so transformed χ^2 is identical to that in Eq. 5.2.

In case of constraints the minimisation is more difficult. One approach is the use of Lagrangian multipliers, λ_k:

$$L = \chi^2(\mathbf{y}) + 2 \cdot \sum_{k=1}^{m} \lambda_k f_k(\mathbf{a}, \mathbf{y}) \, . \tag{5.3}$$

Here, the Lagrange function L is the sum of the χ^2 function to be minimised, and the constraints which are multiplied by the factors λ_k.[1] The minimisation of the χ^2 requires the partial derivatives of L with respect to all y_i and λ_k to vanish. In addition, χ^2 depends implicitly on the un-measured parameters $\mathbf{a}$. Therefore the requirement $\partial L / \partial a_j = 0 \, \forall j$ is needed as well.[2]

In case of linear constraints this approach solves the problem directly. In case of non-linear constraints a numerical solution must be used. For this the constraints are linearised and their solutions are iterated until certain convergence criteria are fulfilled, or the procedure is terminated without success after too many iterations.

[1] The factor 2 is by convention.

[2] An equivalent approach is to minimise by using $\partial L / \partial y_i = \partial L / \partial \lambda_j = 0 \, \forall i, j$ as usual and afterwards minimise $\chi^2[\mathbf{y}(\mathbf{a})]$ with respect to $\mathbf{a}$.

Let $\mathbf{y}_0$ and $\mathbf{a}_0$ denote start values for the corrected measurements and the un-measured parameters. For $\mathbf{y}_0$ the measurements themselves offer good start values. For the un-measured parameters $\mathbf{a}_0$ meaningful start values have to be found depending on the problem.

The values after the last iteration are indicated by $\mathbf{y}^*$ and $\mathbf{a}^*$, while $\boldsymbol{\Delta}\mathbf{y}^* = \mathbf{y}^* - \mathbf{y}_0$ and $\boldsymbol{\Delta}\mathbf{a}^* = \mathbf{a}^* - \mathbf{a}_0$ denote the respective corrections. For the first iteration the corrections are $\boldsymbol{\Delta}\mathbf{y}^* = 0$ and $\boldsymbol{\Delta}\mathbf{a}^* = 0$. Furthermore $\mathbf{y}$ and $\mathbf{a}$ are the wanted values of the next iteration. The respective corrections are given by $\boldsymbol{\Delta}\mathbf{y} = \mathbf{y} - \mathbf{y}_0$ and $\boldsymbol{\Delta}\mathbf{a} = \mathbf{a} - \mathbf{a}_0$. The linearised constraints are then

$$\begin{aligned} f_k(\mathbf{a},\mathbf{y}) &\approx f_k(\mathbf{a}^*,\mathbf{y}^*) + \sum_{i=1}^{p} \frac{\partial f_k}{\partial a_i}(a_i - a_i^*) + \sum_{i=1}^{n} \frac{\partial f_k}{\partial y_i}(y_i - y_i^*) \\ &= f_k(\mathbf{a}^*,\mathbf{y}^*) + \sum_{i=1}^{p} \frac{\partial f_k}{\partial a_i}(\Delta a_i - \Delta a_i^*) + \sum_{i=1}^{n} \frac{\partial f_k}{\partial y_i}(\Delta y_i - \Delta y_i^*) \\ &= f^* + A(\boldsymbol{\Delta}\mathbf{a} - \boldsymbol{\Delta}\mathbf{a}^*) + B(\boldsymbol{\Delta}\mathbf{y} - \boldsymbol{\Delta}\mathbf{y}^*) \stackrel{!}{=} 0 \quad \forall k\,. \end{aligned}$$

Here, the matrices $A \in \mathbb{R}^{m\times p}$, $B \in \mathbb{R}^{m\times n}$ and the vector $\mathbf{f}^* \in \mathbb{R}^n$ are defined as:

$$A_{ij} = \frac{\partial f_i}{\partial a_j}(\mathbf{a}^*,\mathbf{y}^*)\,, \quad B_{ij} = \frac{\partial f_i}{\partial y_j}(\mathbf{a}^*,\mathbf{y}^*)\,, \quad f_i^* = f_i(\mathbf{a}^*,\mathbf{y}^*)\,.$$

The vector $\mathbf{c}^* \in \mathbb{R}^n$ is

$$\mathbf{c} := A\boldsymbol{\Delta}\mathbf{a}^* + B\boldsymbol{\Delta}\mathbf{y}^* - f^*\,,$$

leading to a Lagrange function

$$L = \boldsymbol{\Delta}\mathbf{y}^T C_{\mathbf{y}}^{-1} \boldsymbol{\Delta}\mathbf{y} + 2\lambda^T(A\boldsymbol{\Delta}\mathbf{a} + B\boldsymbol{\Delta}\mathbf{y} - \mathbf{c})\,. \tag{5.4}$$

with the multipliers λ. The requirements $\partial L/\partial y_i = \partial L/\partial \Delta y_i = 0$, $\partial L/\partial a_j = \partial L/\partial \Delta a_j = 0$, $\partial L/\partial \lambda_k = 0\ \forall\, i,j,k$ lead to a linear system of $m+n+p$ equations from which the corrections $\boldsymbol{\Delta}\mathbf{a}$, $\boldsymbol{\Delta}\mathbf{y}$ and λ can be obtained by using

$$\begin{pmatrix} C_{\mathbf{y}}^{-1} & 0 & B^T \\ 0 & 0 & A^T \\ B & A & 0 \end{pmatrix} \begin{pmatrix} \boldsymbol{\Delta}\mathbf{y} \\ \boldsymbol{\Delta}\mathbf{a} \\ \lambda \end{pmatrix} = \begin{pmatrix} 0 \\ 0 \\ \mathbf{c} \end{pmatrix}.$$

For a better comprehension the following matrices are defined

$$\begin{aligned} C_B &= (BC_{\mathbf{y}}B^T)^{-1}\,, \\ C_A &= (A^T C_B A)\,. \end{aligned}$$

The solution is then given by

$$\begin{aligned} \mathbf{\Delta y} &= C_{\mathbf{y}} B^T C_B (1 - A C_A^{-1} A^T C_B)\mathbf{c}\,, \\ \mathbf{\Delta a} &= C_A^{-1} A^T C_B \mathbf{c}\,, \\ \lambda &= C_B (A C_A^{-1} A^T C_B - 1)\mathbf{c}\,. \end{aligned}$$

In order to compute the variances and correlations the following matrices are helpful

$$\begin{aligned} C_{11} &= C_{\mathbf{y}}(1 - B^T C_B B C_{\mathbf{y}} + B^T C_B A C_A^{-1} A^T C_B B C_{\mathbf{y}})\,, \\ C_{21} &= -C_A^{-1} A^T C_B B C_{\mathbf{y}}\,, \\ C_{22} &= C_A^{-1}\,. \end{aligned}$$

Error propagation leads to the covariance matrix for the vector $(\mathbf{y}, \mathbf{a})$

$$C_{(\mathbf{y},\mathbf{a})} = \begin{pmatrix} C_{11} & C_{21}^T \\ C_{21} & C_{22} \end{pmatrix}.$$

To ensure that the global minimum of the χ^2 function is reached, convergence criteria must be defined. The χ^2 function should vary only by a small amount ε_{χ^2} between consecutive iterations. At the same time the constraints $f_k = 0$ must be fulfilled. Therefore the sum of its different parts should not exceed a small value ε_f. Thus the complete convergence criteria are

$$|\chi^2(\mathbf{y}) - \chi^2(\mathbf{y}^*)| < \varepsilon_{\chi^2}\,, \tag{5.5}$$

$$\sum_{k=1}^{m} |f_k(\mathbf{a}, \mathbf{y})| < \varepsilon_f\,. \tag{5.6}$$

The procedure described above is the most general form of least squares. It is a transparent method and can be used in many applications. The interpretation of the results is done by using the χ^2 value computed by $\mathbf{\Delta y}^T C_{\mathbf{y}}^{-1} \mathbf{\Delta y}$. For Gaussian distributed errors and linear constraints this variable follows a χ^2 distribution with $m-p$ degrees of freedom.[3]

In reality the measurements used for the fit are likely to be biased by systematic effects. In addition, the underlying model could be wrong. In order to check the consistency of the fit results a look at the pull distributions of the input variables is needed which are defined by the normalised corrections

$$p_i := \frac{\Delta y_i}{\sigma_i}\,. \tag{5.7}$$

[3] The measurements do not increase the number of degrees of freedom since all of their components are allowed to vary within their resolutions. The constraints however provide additional information and thus give additional degrees of freedom while those are taken away by the un-measured parameters.

The standard deviations σ_i of the corrections Δy_i are easily obtained by using $\sigma_i = \sqrt{(C_{\mathbf{y}} - C_{\mathbf{y_0}})_{ii}}$. For an ideal fit the mean values of the pull distributions are expected to be at zero with a standard deviation of one.

5.1.2. The KinFitter Package

The fit procedure described above is implemented in the KinFitter library [SG09] which has been written in C++ based upon the RooT [A+09d] libraries. It is part of the ATLAS software framework ATHENA but can be run independently also.[4] The fitter library offers several predefined constraints and particle parametrisations. This makes the fitter applicable for a vast number of event and decay topologies. The user only needs to enter the associated particles and their constraints. The basic scheme of the fitter library is depicted in Fig. 5.1. In order to compute the corrections $\mathbf{\Delta y}$ and the parameters $\mathbf{a}$, the fitter needs in every iteration step the latest values of the constraints $\mathbf{f}(\mathbf{a}^*, \mathbf{y}^*)$, as well as the matrices A and B. The partial derivatives of the constraints are obtained most easily in Cartesian coordinates $\{P_i\}_{i=1,\ldots,n}$. Since the particles might be parametrised in a different way $\{y_i\}_{i=1,\ldots,n}$, the following transformation must be applied

$$\frac{\partial f_k}{\partial y_i} = \sum_{j=1}^{n} \frac{\partial f_k}{\partial P_j} \cdot \frac{\partial P_j}{\partial y_i} \,.$$

Now it is possible to compute $\partial f_k / \partial P_j$ from the constraints alone, while $\partial P_j / \partial y_i$ follows from the parametrisations of the particles only. This leads to a certain structure of the fitter library in order to have code which is both compact and flexible. In the beginning, objects describing the particles and their constraints are constructed. These are used to compute the derivatives and to transfer those and other needed information to a fit object which in turn provides the final results. In detail, the procedure works as follows:

Step 1: The actual values of the constraints $\mathbf{f}(\mathbf{a}^*, \mathbf{y}^*)$ are transferred to the fitter.

Step 2: The derivatives $\partial f_k / \partial P_j$ of the constraints and the derivatives $\partial P_j / \partial y_i$, $\partial P_j / \partial a_i$ of the particles are calculated and given to the fitter as well.

Step 3: The deviates of the matrices A and B are computed using the proper transformation.

Step 4: The fitter evaluates the corrections $\mathbf{\Delta y}$ and $\mathbf{\Delta a}$. For this the covariance matrix $C_{\mathbf{y}}$ is needed which was loaded into the memory already. The new corrections are applied to the particles and the constraints.

[4] The version of the KinFitter library used here contains some improvements which are not yet part of the version included in ATHENA.

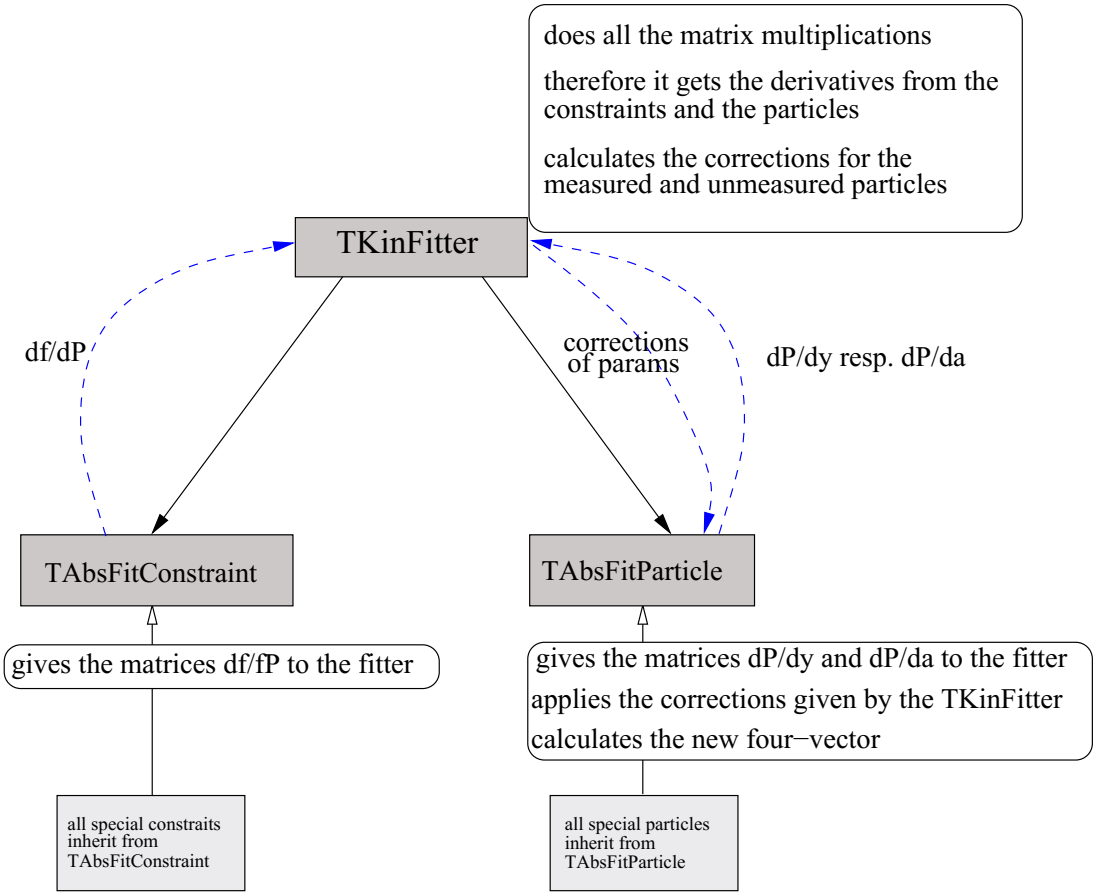

Figure 5.1.: Scheme of the KinFitter software [SG09]. Constraints (class TAbsFitConstraint) and particles (class TAbsFitParticle) are realised as individual objects and connected to the central fit object (class TKinFitter) which performs the actual fit. The usage of abstract base classes and virtuality ensures a high flexibility and its usage for a wide range of event and decay topologies.

Step 5: The fitter checks the convergence criteria. If they are not fulfilled the procedure will start again at step 1.

The particles can be parametrised *e.* g. in coordinates $(p_\mathrm{t}, \eta, \varphi)$ or $(p_\mathrm{t}, \vartheta, \varphi)$. The fitter ensures that the variable p_t is always positive.[5]

For the mass constraints either a fixed mass or a mass distribution with finite width can be used for the fit. This is implemented by an additional variable which is used like a measurement during the fit process. Its starting value is set to the most probable mass. For

[5] If a correction leads to negative p_t value then the magnitude of the respective correction vector will be divided by two until p_t gets positive again.

Gaussian distributions the constraint is given by

$$f_M(\mathbf{a},\mathbf{y}) \;=\; \|\sum_i p_i(\mathbf{a},\mathbf{y})\,\| - \alpha M \;\stackrel{!}{=}\; 0\,. \tag{5.8}$$

Here the p_i denote the particle momenta while $\|\cdot\|$ indicates its invariant mass and M is the most probable mass. The variable α is added quadratically to the χ^2 function weighted with the relative mass width Γ/M

$$\chi^2 \;=\; \ldots + \frac{(\alpha-1)^2}{(\Gamma/M)^2}\,.$$

The fitter therefore tries to bring α close to one which is equivalent to the pole mass of the particle in question.

In order to evaluate the results of the kinematic fits presented below, instead of the χ^2 distribution f_{ndf}, which depends on the number of degrees of freedom, the χ^2 probability, often referred to as p-value, will be used:

$$\mathcal{P}(\chi^2) = \int_{\chi^2}^{\infty} f_{\mathrm{ndf}}(x)\mathrm{d}x\,. \tag{5.9}$$

Being a probability, the p-value is equally distributed given the reconstructed decays fulfill the fit hypothesis and the employed covariance matrices are correct.

5.2. Reconstruction of Single Top Events

The simplest topology of a single top event consists of a top quark and a spectator particle[6] in the final state (see Fig. 2.5 or 2.7). Within the standard model, the top quark decays almost exclusively into a W-boson and a b-quark.

In order to employ the method of kinematic fitting for the reconstruction of single top events the physical objects entering the fit need to be defined and their covariance matrices need to be provided. Furthermore, the fit constraints carrying the information about the hypothesis to be tested must be formulated.

The covariance matrices are discussed in more detail in Sec. 5.2.2 for leptons and in Sec. 5.2.3 for jets and the missing transverse energy.

For exemplary purposes the reconstruction procedure of a single leptonically decaying top quark is described in the following. The general idea is then applied in Chap. 6 to the specific case of the Wt-channel signature, and extended to include both the leptonic and hadronic decay channels of the W-bosons.

[6] The spectator is a light quark emitted in the forward direction, a real W or a B-quark in the t, Wt and s channel respectively (*cf.* Sec. 2.4.2).

5.2.1. An Example: "Leptonic" Top Quark Fit

At the detector level, the final state objects are a charged lepton and transverse missing energy from the neutrino, both associated to the W decay that in combination with a b-jet originates from the top quark decay. The momenta for the lepton, the b-quark and the neutrino are used as input to the fitter. For the latter, the component ϑ_ν is un-measured:

$$\text{Lepton: } \vec{p}_\mathrm{l} = \begin{pmatrix} p_{\mathrm{t,l}} \cos\varphi_\mathrm{l} \\ p_{\mathrm{t,l}} \sin\varphi_\mathrm{l} \\ p_{\mathrm{t,l}} \sinh\eta_\mathrm{l} \end{pmatrix}, \qquad b\text{-quark: } \vec{p}_\mathrm{b} = \begin{pmatrix} p_{\mathrm{t,\,b}} \cos\varphi_\mathrm{b} \\ p_{\mathrm{t,\,b}} \sin\varphi_\mathrm{b} \\ p_{\mathrm{t,\,b}} \sinh\eta_\mathrm{b} \end{pmatrix},$$

$$\text{Neutrino: } \vec{p}_\nu = \begin{pmatrix} p_{\mathrm{t,}\,\nu} \cos\varphi_\nu \\ p_{\mathrm{t,}\,\nu} \sin\varphi_\nu \\ p_{\mathrm{t,}\,\nu} / \tan\vartheta_\nu \end{pmatrix}, \quad \vartheta_\nu \text{ un-measured}.$$

The procedure therefore consists of fitting a top quark four-momentum with these three objects respecting the invariant mass constraints for the W-boson and top quark as indicated in Fig. 5.2. In the following, the χ^2 function is formulated, in its dependence on the particle momenta, their covariance matrices and the transformed masses μ for the corresponding mass constraints as described in Sec. 5.1.2:

$$\begin{aligned} \chi^2 = {} & (\vec{p}_\mathrm{l,fit} - \vec{p}_\mathrm{l,start})^T \, C_\mathrm{l}^{-1} \, (\vec{p}_\mathrm{l,fit} - \vec{p}_\mathrm{l,start}) \\ & + (\vec{p}_\mathrm{b,fit} - \vec{p}_\mathrm{b,start})^T \, C_\mathrm{b}^{-1} \, (\vec{p}_\mathrm{b,fit} - \vec{p}_\mathrm{b,start}) \\ & + \left(\vec{p}_{\nu_\mathrm{x,y},\mathrm{fit}} - p_{\nu_\mathrm{x,y},\mathrm{start}}\right)^T \, C_{\nu_\mathrm{x,y}}^{-1} \left(\vec{p}_{\nu_\mathrm{x,y},\mathrm{fit}} - p_{\nu_\mathrm{x,y},\mathrm{start}}\right) \\ & + \mu_\mathrm{Top}^2 + \mu_\mathrm{W}^2 \\ \overset{!}{=} {} & \text{minimal} \end{aligned}$$

The μ_Top^2 and μ_W^2 represent the mass constraints for the t-quark and the W boson:

$$\begin{aligned} \text{t quark mass constraint:} \quad & f_{\mathrm{M_{Top}}}(\vec{p}_\mathrm{l}, \vec{p}_\nu, \vec{p}_\mathrm{b}, \mu_\mathrm{Top}) = 0\,, \\ \text{W boson mass constraint:} \quad & f_{\mathrm{M_W}}(\vec{p}_\mathrm{l}, \vec{p}_\nu, \mu_\mathrm{W}) = 0\,. \end{aligned}$$

Here, Gaussian mass constraints are employed. Assuming that the charged lepton with the highest transverse momentum of the selected ones is almost always the actual signal lepton, the remaining combinatorial freedom is in choosing a b-jet from the list of all selected b-jets. This freedom of choice is exploited to ensure that the correct b-jet from the top-decay is used: For each combination of the signal lepton and the transverse missing energy with a b-jet, the top quark fit determines a total χ^2. The best combination is the one with the smallest value of the χ^2 and is chosen as the top quark candidate. By requiring the χ^2 to be below a certain threshold which correspond to a minimum p-value (*cf.* Eq. 5.9), signal-like events can be enriched in the final selection. Since the kinematic fit determines the full four-momenta of the fit objects, the neutrino p_z component can be recovered by this method.

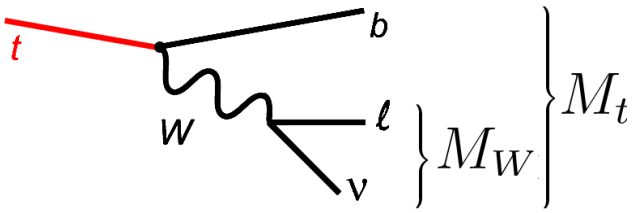

Figure 5.2: Reconstruction of the top quark by a kinematic fit with constraints on the invariant masses of the leptonically decaying W-boson and the top quark.

5.2.2. Covariances of Track Helices

As described in Sec. 3.5.2, at ATLAS the tracks are obtained from a fit in the ID and MS. In the final result, the tracks and their covariances are described by the helix parameters (d_0, z_0, θ, ϕ, q/p). For each track the helix parameters and their covariance matrix can be retrieved from its track summary.[7] The kinematic fitter then needs different parametrisations, e.g. (p_t, η, ϕ). With the help of the transformations

$$\begin{aligned} \eta &= -\ln(\tan(\theta/2))\,, \\ p_\mathrm{t} &= \tfrac{q}{\pi}\sin\theta\,, \\ \phi &= \phi \end{aligned} \tag{5.10}$$

with $\pi = q/p$. and by a propagation of the errors by using the transformation

$$C_{(\eta,p_\mathrm{t},\phi)} = TC_{(\theta,\pi,\phi)}T^T\,, \qquad T = \begin{pmatrix} -\frac{q}{\pi^2}\sin\theta & \frac{q}{\pi}\cos\theta & 0 \\ 0 & -\frac{1}{\sin\theta} & 0 \\ 0 & 0 & 1 \end{pmatrix} \tag{5.11}$$

the parameters needed for the kinematic fitter can be computed for each input track. Note that this approach is valid for electrons and muons only. For other reconstructed objects like jets and missing transverse energy no covariance matrices are provided and must be determined on a statistical basis (*cf.* Sec. 5.2.3).

5.2.3. Covariances for Jets and $E_\mathrm{T}^\mathrm{miss}$

For jets and the missing transverse energy the covariance matrices do not exist for each individual object as in the case of the leptons. Instead, they have to be obtained on a statistical basis by comparing the reconstructed objects with their true counterparts in simulated events. One should note that this comparison is the only dependence of the kinematic from simulation; apart from that the KinFitter is completely data-driven. Because the fitter is to be used for the reconstruction of single top or $\mathrm{t\bar{t}}$ events here, the covariances are determined

[7] One should keep in mind that the helix parameters are given with respect to a certain reference point. For vertex-fitted tracks this is either the primary or secondary vertex, for tracks without a vertex constraint this is usually the point of closest approach to the beam-line.

from the cross section weighted sum of Monte Carlo samples for top-pair and single top production.

In order to let the fit operate within the exact phase space model adopted by the analysis, the extraction of the covariances is performed using reconstructed events and physics objects that fulfill the preselection requirements and the corrections described in Chapter 4. Events containing at least one good reconstructed jet are used, without applying a b-tag weight selection (PreTag).

To determine the covariance matrices for the reconstructed missing transverse energy, its magnitude and azimuth are compared to that of the neutrino originating from the W boson of the semi-leptonic top quark decay. For the jets such an unique assignment to their true counterparts does not exist. Here, the jets reconstructed at the hadron level are taken for comparison. The matching between the jets at the detector level (dl) and the hadron level (hl) is done by using the parameter

$$d^2 = (\eta_{\mathrm{dl}} - \eta_{\mathrm{hl}})^2 + (\varphi_{\mathrm{dl}} - \varphi_{\mathrm{hl}})^2 + (p_{\mathrm{t,\,dl}} - p_{\mathrm{t,\,hl}})^2 / p^2_{\mathrm{t,\,hl}}\,. \tag{5.12}$$

The parameter d is computed for each combination of a detector level jet with a hadron level jet and the combination with the smallest value of d is taken as match. This procedure turned out to be robust and reliable.

Since the detector resolutions are strongly dependent on the transverse momentum and the pseudo-rapidity of the reconstructed objects, the covariance matrices are determined in bins of p_{t} and η of the object in question. The binning is chosen such that sufficient statistics is collected in every bin for a precise determination of each matrix element. The procedure to obtain the average for a matrix element in a certain bin differs for diagonal elements and off-diagonal elements.

For the diagonal elements the residual distributions $X_{\mathrm{rec}} - X_{\mathrm{true}}$ of a variable X – which might be p_{t}, η, φ for the jets, or $E_{\mathrm{T}}^{\mathrm{miss}}$, φ for the missing transverse energy – are fitted with a Gaussian. The square of the resulting width of the residuals gives the average of the wanted variance. An example for this is shown in Fig. 5.3a. To determine the off-diagonal elements, the products of the residuals $(X_{\mathrm{rec}} - X_{\mathrm{true}}) \cdot (Y_{\mathrm{rec}} - Y_{\mathrm{true}})$ of the pair of variables X and Y in question are histogrammed (see Fig. 5.3b). The mean value of the final histogram is a good estimator for the wanted off-diagonal element. The resulting covariance matrix elements in bins of p_{t} an η are collected in Fig. 5.4 for the jets and in Fig. 5.5 for the missing transverse energy [PP12].

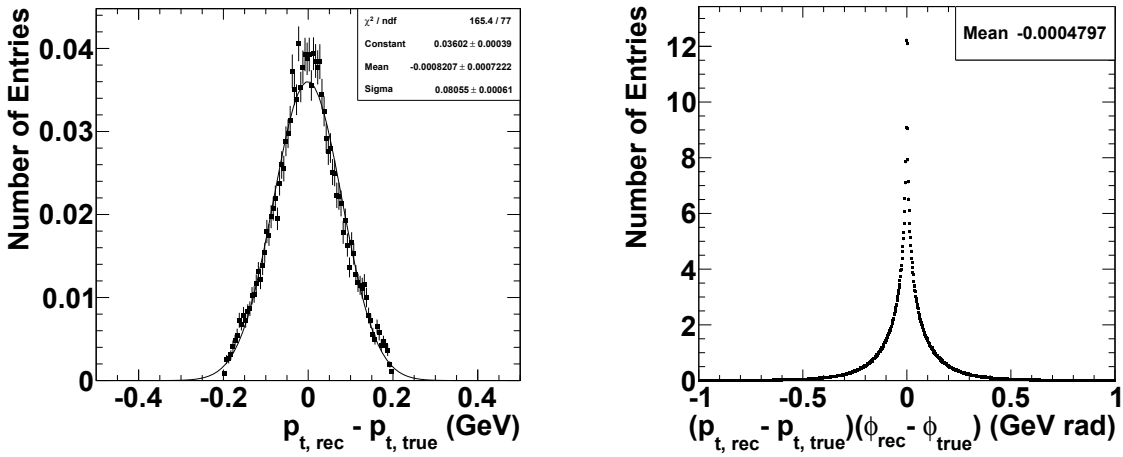

(a) Determination of jet $(\Delta p_\mathrm{t})^2$

(b) Determination of jet $\Delta p_\mathrm{t} \Delta \phi$

Figure 5.3.: Examples for the determination of the covariance matrix elements. In (a) the determination of a diagonal element is shown. A Gaussian is fitted to the residual distribution of the element in question (here p_t for jets) and the resulting width squared is taken. For the off-diagonal elements (b) the products of the residuals of both variables (here p_t and ϕ) are histogrammed. The mean value of the histogram gives the wanted off-diagonal element.

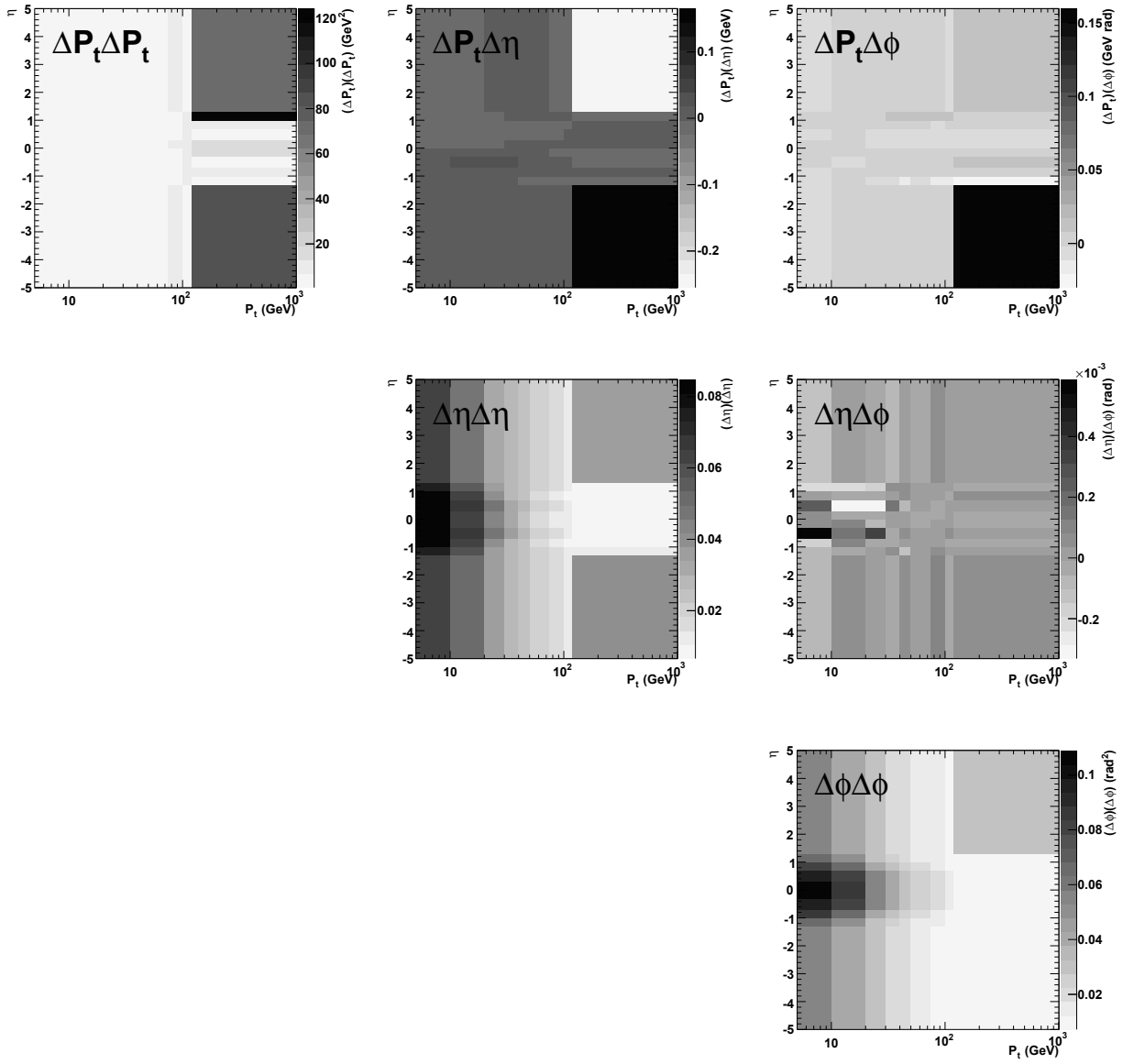

Figure 5.4.: The histograms show the six covariance matrix elements for the three-momentum vectors of all jets in $(p_\mathrm{t}, \eta, \varphi)$ representation obtained by the statistical method in bins of p_t and η of the jets as described in the text.

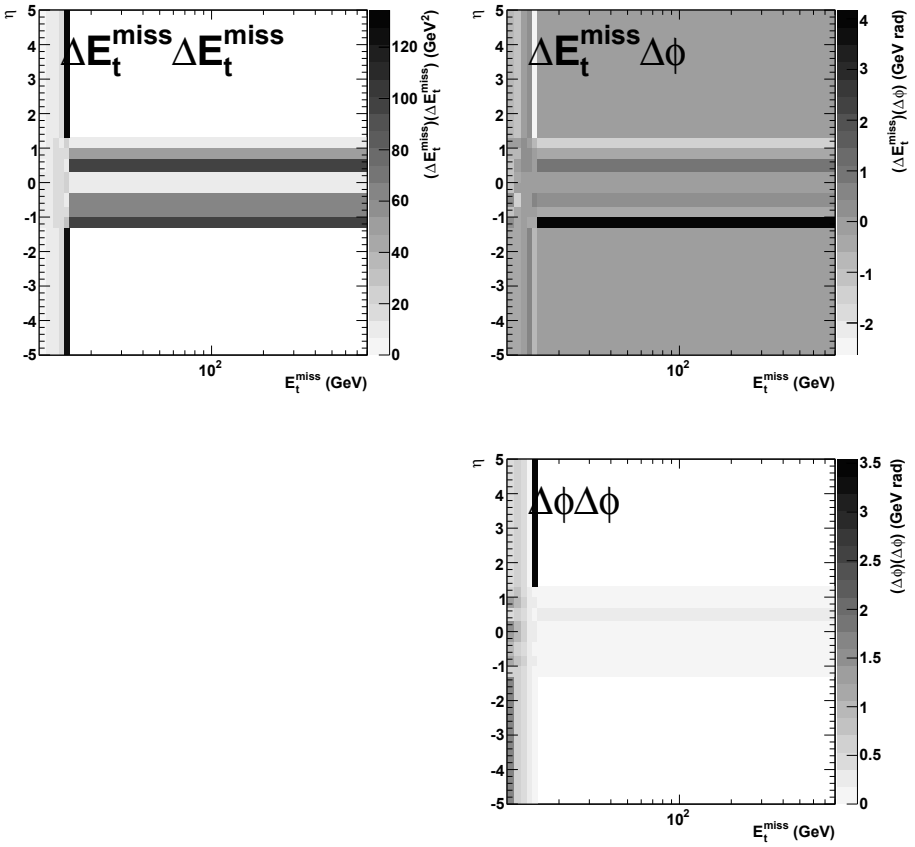

Figure 5.5.: The three covariance matrix elements for the missing transverse energy obtained by the statistical method described in the text are histogrammed in bins of p_{t} and η.

6. Fit and Selection of Single Top Wt Events

In this analysis the selection of semi-leptonic Wt events containing a high-p_t lepton and jets in the final state is performed with the aid of the kinematic fit technique described in Chap. 5. The top quark decays into a W boson and a quark, therefore the presence of the associated W boson leads to an ambiguity in the event reconstruction since it is not known which of the W bosons decays leptonically into the high-p_t lepton and the neutrino, while the other W decays hadronically into two jets, as depicted in Fig. 6.6 and 6.7. To solve this ambiguity the kinematic fit is run twice for every event: once for testing the hypothesis of the associated W boson decaying hadronically (Sec. 6.3), and a second time for the hypothesis of a leptonic decay of the associated W (Sec. 6.4). The fit with the best χ^2 value is chosen. In order to enrich signal-like events a minimum cut on the χ^2-probability of the selected fit is imposed. For events containing at least four jets, an additional kinematic fit is performed to test the hypothesis of top-pair production (see Sec. 6.6.1). If the χ^2-probability of this fit exceeds a certain threshold, the event will be marked as background and rejected. The final selection criteria are presented in Sec. 6.7, and an immediate visualisation of the analysis workflow is presented in Fig. 6.1.

6.1. Fitter Analysis Setup

Given the W decay ambiguity in the final states, two fitting procedures are put in place, where the only physical contrants are the W boson and top quark mass, as shown in Fig. 6.6 and 6.7. For this work, mass constraints with Gaussian distributions defined in Eq. (5.8) are employed, following the work of [Rie10]. In Tab. 6.1, the values used for the W and top quark masses and decay widths fit constraints are displayed. Each global fit (hadronic top, leptonic top associated to hadronic W) returns a χ^2 value, which is iteratively tested until the convergence criteria referred in Eq. (5.5) are fulfilled. The values in Tab. 6.2 are the optimised thresholds chosen for the convergence criteria [Rie10]. These threshold ensure at the same time that the global minimum is found, and that not too many iterations are performed when the test hypothesis can not be fulfilled. At the end of the fit, the event is accepted if either one of the iterative fitting procedures have converged. The complete procedure for the selection of Wt events, is summarised in Fig. 6.1.

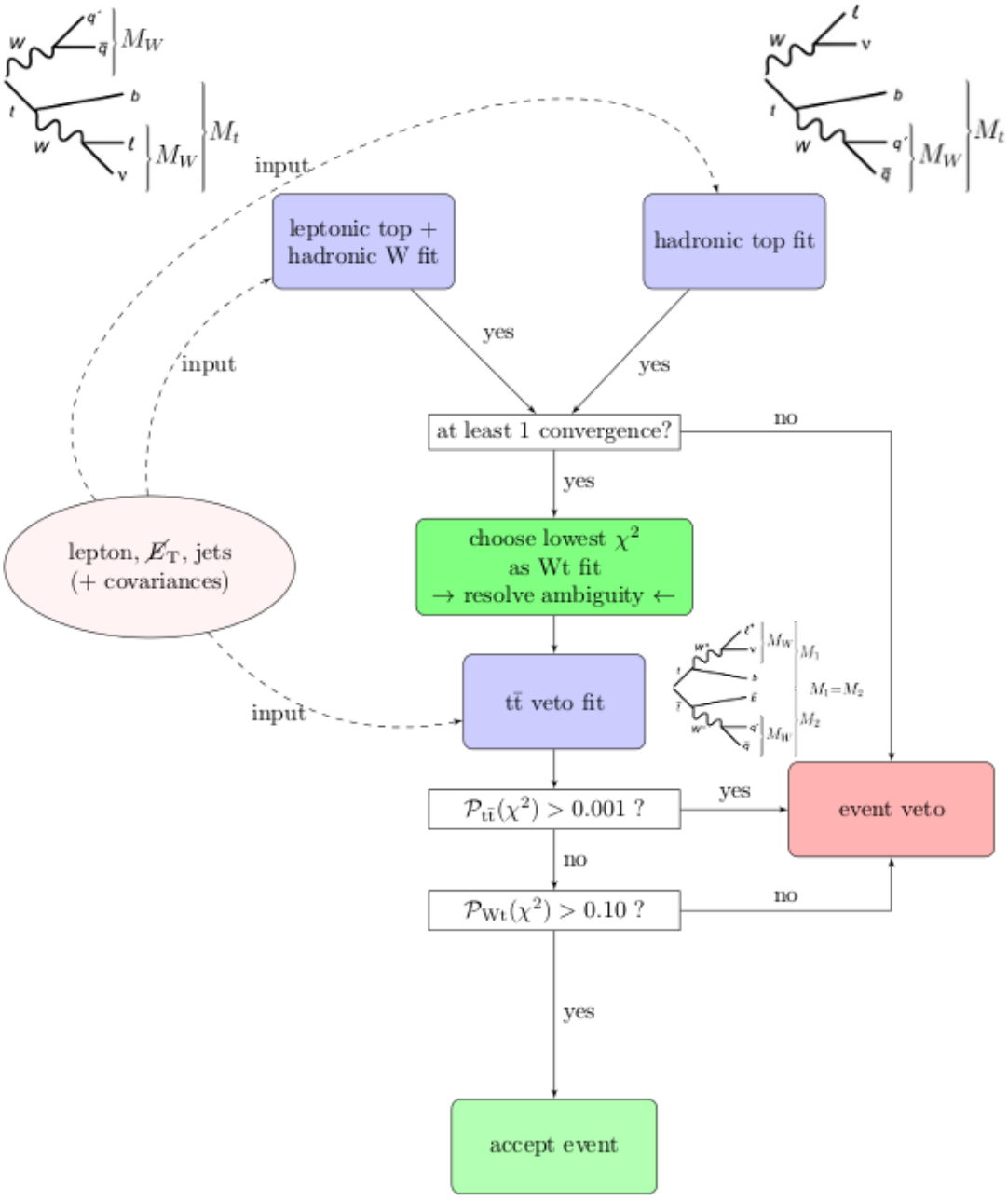

Figure 6.1.: Flow-chart of the full kinematic fitting procedure for single top production Wt-channel events including the veto fit on $t\bar{t}$ events.

Particle	Mass (GeV)	Width (GeV)
W	80.399	2.085
t	172.9	1.99

Table 6.1.: Masses and decay widths of the W boson and the top quark used as constraints in the kinematic fit. The values used in the fit correspond to those available at the time when this work was developed [Nakon].

Parameter	Value
$N_{\text{iter}}^{\text{max}}$	100
ε_{χ^2}	$5 \cdot 10^{-5}$
ε_f	$1 \cdot 10^{-4}$

Table 6.2.: Detailed settings of the KinFitter used for this analysis. $N_{\text{iter}}^{\text{max}}$ denotes the maximum number of iterations in a fit, ε_{χ^2} is the maximum deviation of the minimum function for successive iterations and ε_f is the maximum value of the constraints (cp. Equations (5.5)). The values are the same ones as used in [Rie10].

6.2. Input Objects

From all the events surviving the preselection described in Sec. 4.1, the following objects fulfilling the previously stated quality requirements are used as an input for the fit:

1. The b-tagged jet in the event, expected in the production of the b-quark from the top decay. [1]

2. Exactly two or three light-flavoured jets, from which one pair is expected to be originated in the hadronic decay of one of the W bosons in the event.

3. The isolated high-p_{t} electron or muon originating from one of the two W boson decays in the event.

4. The missing transverse energy indicating the neutrino from the leptonic W boson decay.

In Fig. 6.3, 6.2 and 6.4 the kinematic variables of the input objects are shown. A good agreement between the simulated distributions and real data can be seen, after the application of the data-driven normalisation procedures.

[1] The kinematic fit can in principle deal with more than one b-jet by testing all possible combinations and choosing the one with the best χ^2. For the sake of a better comparison with other analyses the allowed number of b-jets per event is restricted to one.

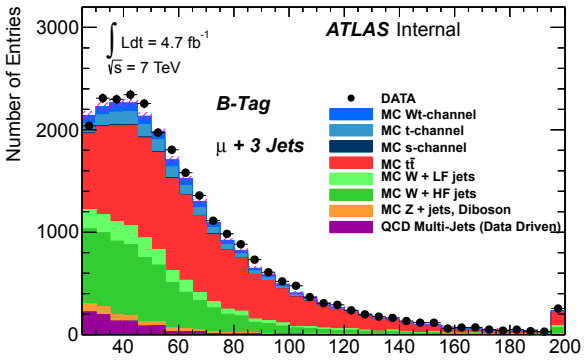

(a) Missing Transverse Energy

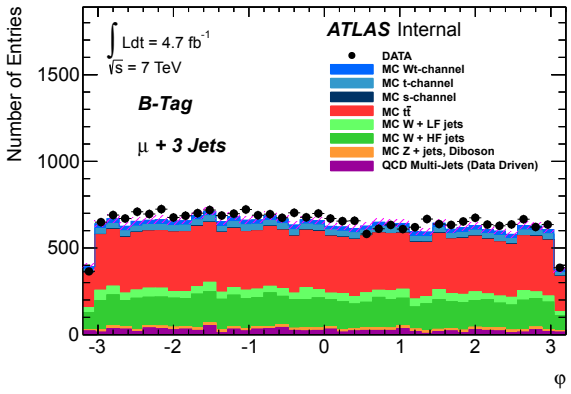

(b) Azimuth of the Missing Transverse Energy

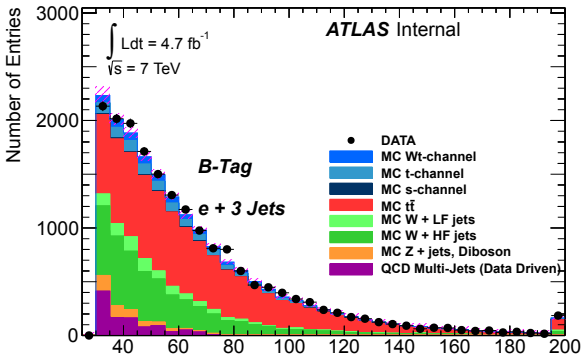

(c) Missing Transverse Energy

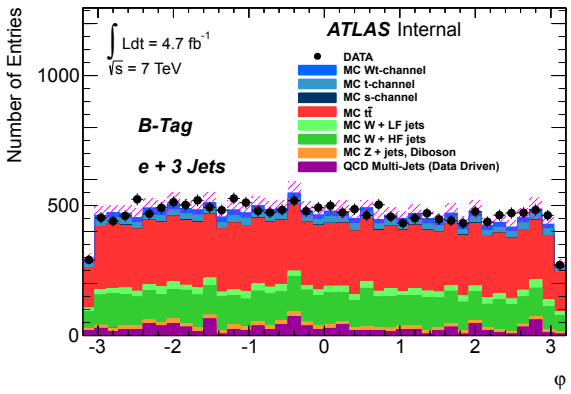

(d) Azimuth of the Missing Transverse Energy

Figure 6.2.: The magnitude of the missing transverse energy (a),(c), and the azimuth angle φ of the corresponding missing transverse momentum vector (b),(d). The distributions shown here are the ones used as input for the main kinematic fit of the top quark (*i.* e. after the b-tag requirement) and for the muon (left) and electron (right) channel in the $N_{\text{jet}} = 3$ bin. The single top Wt, t, s-channel, $t\bar{t}$, Z+jets and diboson samples are normalised to their theory predictions; the W+jets and QCD multi-jet components of the background are normalised by means of data-driven techniques. The rightmost bin contains the sum of the events in that bin or higher.

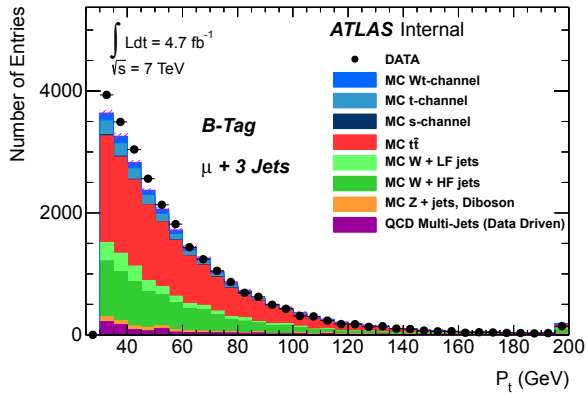

(a) Muon Transverse Momentum

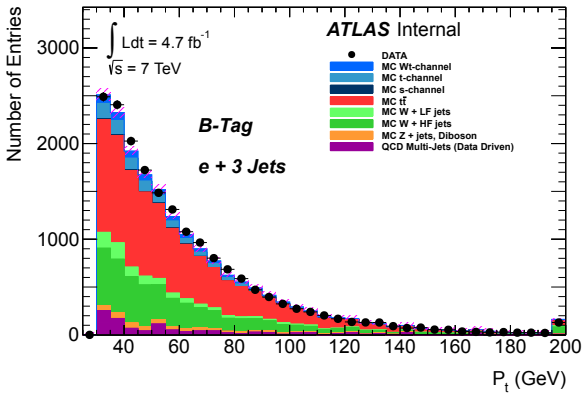

(b) Electron Transverse Momentum

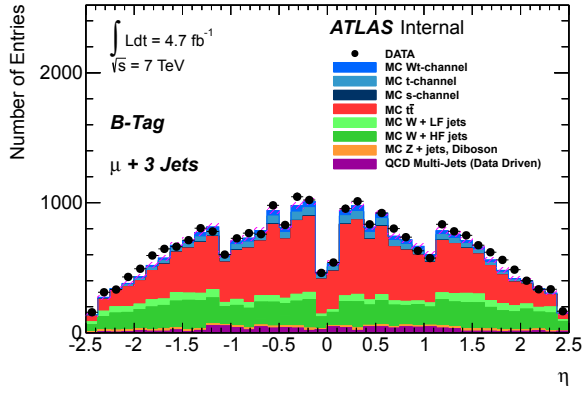

(c) Muon Pseudorapidity

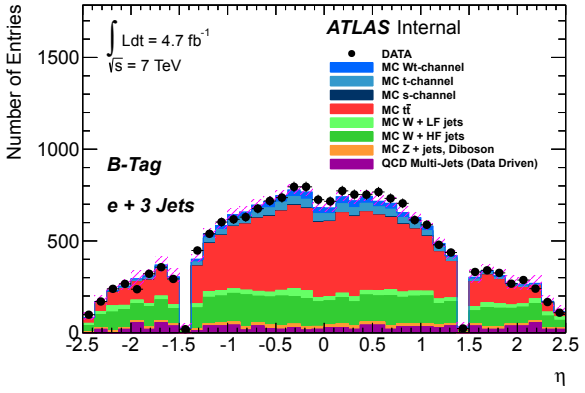

(d) Electron Pseudorapidity

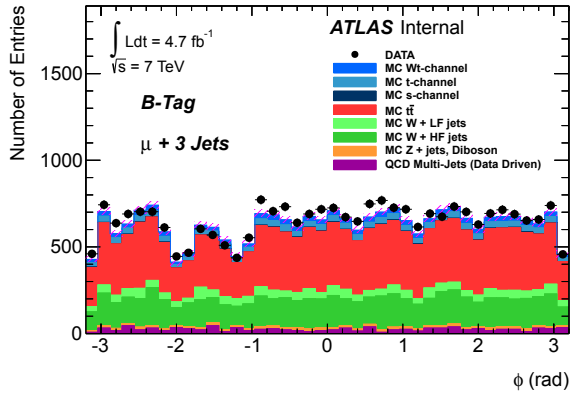

(e) Muon Azimuth

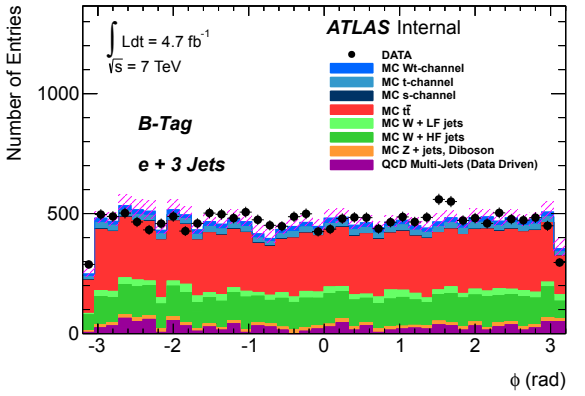

(f) Electron Azimuth

Figure 6.3.:]
Kinematic distributions of the muon (a),(c),(e) and the electron (b),(d),(f) entering the main kinematic fit (after the b-tag selection) in events with $N_{\text{jet}} = 3$. The single top Wt, t, s-channel, $t\bar{t}$, Z+jets and diboson samples are normalised to their theory predictions; the W+jets and QCD multi-jet components of the background are normalised by means of data-driven techniques. The rightmost bin contains the sum of the events in that bin and higher.

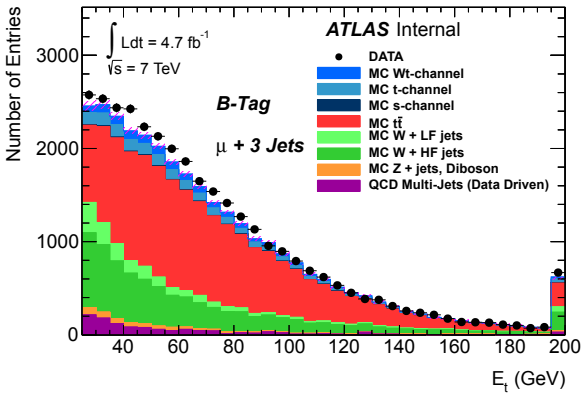

(a) b-Jet Transverse Momentum

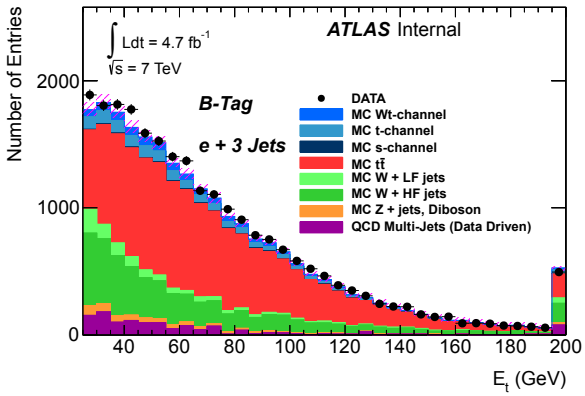

(b) b-Jet Transverse Momentum

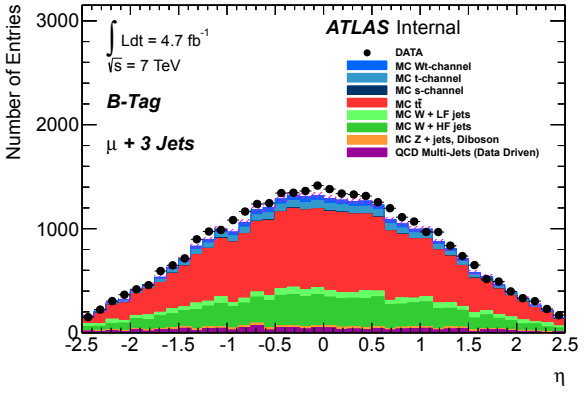

(c) b-Jet Pseudorapidity

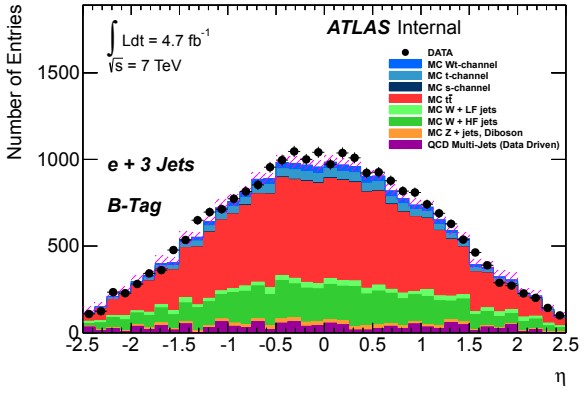

(d) b-Jet Pseudorapidity

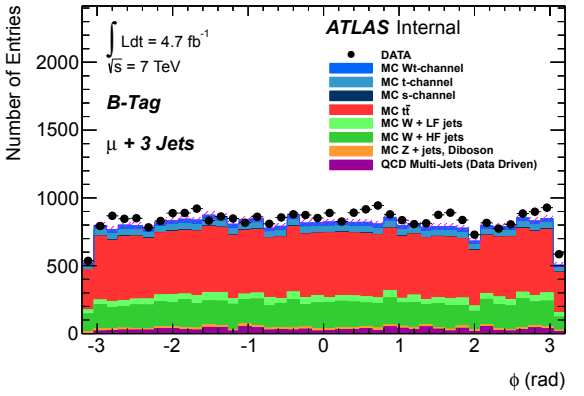

(e) b-Jet Azimuth

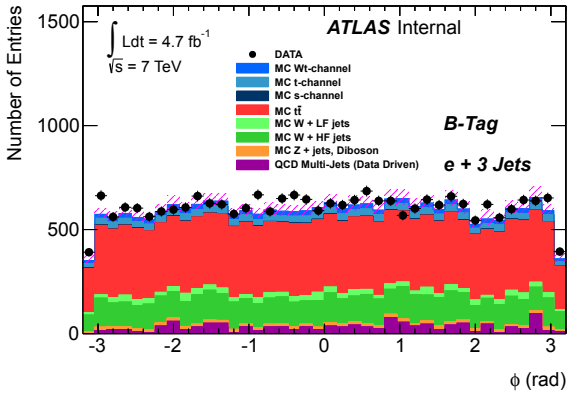

(f) b-Jet Azimuth

Figure 6.4.: Transverse momentum (a),(b), pseudorapidity (c),(d) and azimuth (e),(f), of the b-jets used for the main kinematic fit of the top quark for the $N_{\text{jet}} = 3$ channel. The single top Wt, t, s-channel, $t\bar{t}$, Z+jets and diboson samples are normalised to their theory predictions; the W+jets and QCD multi-jet components of the background are normalised by means of data-driven techniques. The rightmost bin contains the sum of the events in that bin or higher.

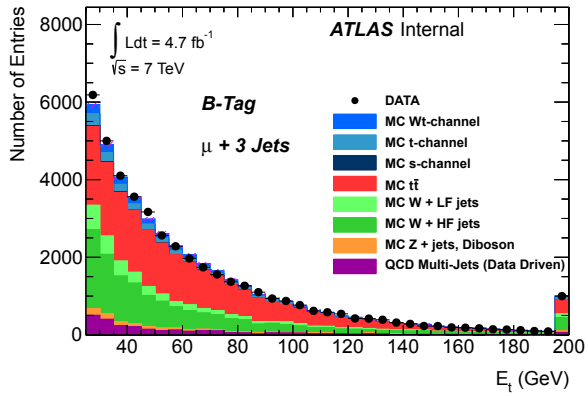

(a) light-Jet Transverse Momentum

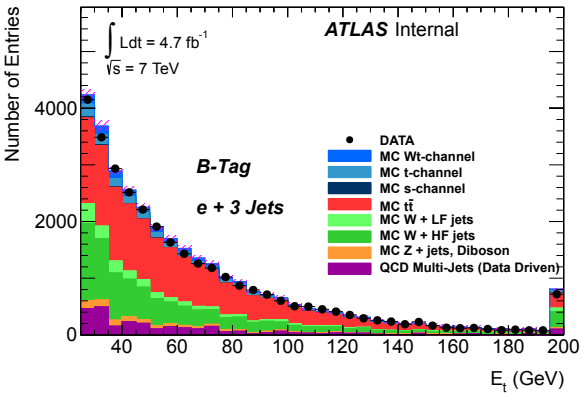

(b) light-Jet Transverse Momentum

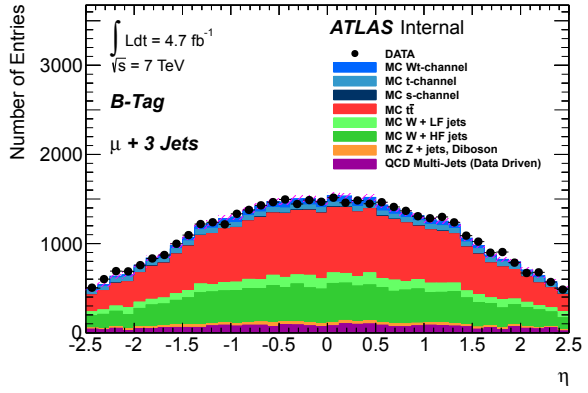

(c) light-Jet Pseudorapidity

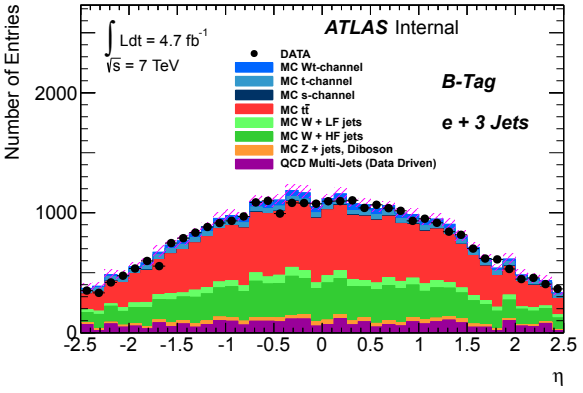

(d) light-Jet Pseudorapidity

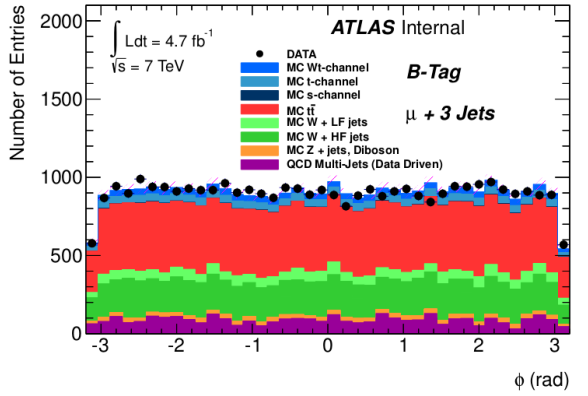

(e) light-Jet Azimuth

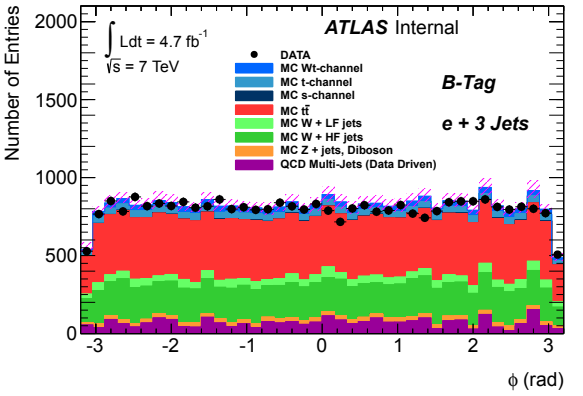

(f) light-Jet Azimuth

Figure 6.5.: Transverse momentum (a),(b), pseudorapidity (c),(d) and azimuth (e),(f), of the light-flavoured jets used for the main kinematic fit of the top quark for the $N_{\text{jet}} = 3$ channel. The plots on the left column are referred to the The single top Wt, t, s-channel, $t\bar{t}$, Z+jets and diboson samples are normalised to their theory predictions; the W+jets and QCD multi-jet components of the background are normalised by means of data-driven techniques. The rightmost bin contains the sum of the events in that bin or higher.

6.3. Fitting of Leptonic Top Quark Decays

In this case the associated W decays hadronically into two light-flavoured jets. This allows the full reconstruction of the four-momentum vectors for both W bosons and the top quark. As displayed in Fig. 6.6, two simultaneous fits are done: on one hand all the possible combinations of light-flavoured jets are used to test the decay of the associated W boson in two quarks, constraining the system with the given invariant mass m_{W}; on the other hand, the fit tries to reconstruct the leptonic decay of the top quark using the invariant mass of the top quark and its daughter W boson as kinematic constraints. Since the number of b-jets per event is restricted to one, only one combination of input objects for the leptonically top quark (b-jet, lepton and $E_{\mathrm{T}}^{\mathrm{miss}}$) exists. At the same time the fit is performed for all possible pairs of light-flavoured jets (the number of possible combinations is one for $N_{\mathrm{jet}}=3$ and three for $N_{\mathrm{jet}}=4$) in order to reconstruct the hadronic decay of the associated W boson. The combination with the best (lowest) χ^2 is chosen as candidate. For the case of a leptonically decaying top quark the fitter is able to reconstruct the full four-momenta of the top quark, both the W bosons and the neutrino. In Fig. 6.10, B.1, 6.11 and B.2 the pseudorapidity of the neutrino as well as the invariant masses of the top quark and both W bosons are shown for each selection channel.

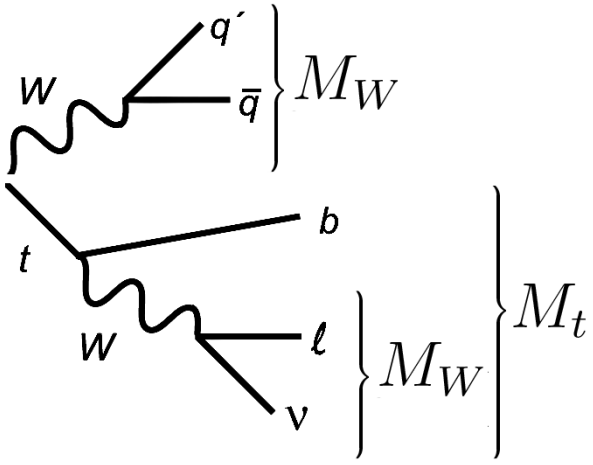

Figure 6.6.: Reconstruction of the Wt production events in the lepton+jets channel with the help of the KinFitter package. In the leptonic case the fitter uses three simultaneous constraints on the invariant mass of the heavy particles involvolved in the Wt decay process. The momentum vectors of the reconstructed lepton and the missing transverse energy are combined to reproduce a leptonically decaying W boson. The b-quark is then added, in order to reconstruct the top quark decay. At the same time, the two remaining light-flavoured jets are combined to reconstruct the hadronic decay of the associated W boson.

6.4. Fitting of Hadronic Top Quark Decays

Opposite to the leptonic top decay mode described above, in the hadronic decays of the top quark no constraint can be imposed on the leptonic decay of the associated W boson, because such a two-body decay does not provide enough information to reconstruct the neutrino p_z component unambiguously, and therefore the jets are the only available input to the kinematic fit in this case, as shown in Fig. 6.7. As in the previous case, all the available pairs of light-flavoured jets are used to fulfill the constraint on the invariant mass of the W boson coming from the top quark decay. Again, the combination with the best χ^2 is chosen as candidate. Since the leptonic part of the event does not enter the fit at any level, it is not possible to reconstruct the full four-momentum of the neutrino, nor the invariant mass of the associated W boson here. The observables reconstructed by the hadronic fit are presented in Fig. 6.12, where the invariant masses of the top quark and the W-boson daughter are shown, in the three-jet bin for the muon and electron selection.

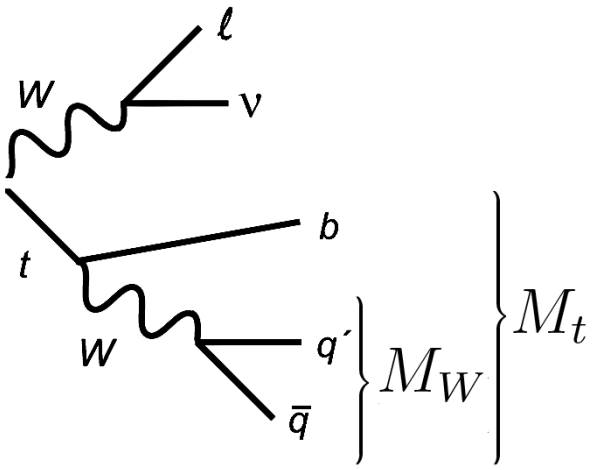

Figure 6.7.: Reconstruction of the Wt production events in the lepton+jets channel with the help of the KinFitter package. In the hadronic case the fitter can use only two simultaneous constraints on the invariant mass of the heavy particles involvolved in the t-quark decay process. The momentum vectors of the reconstructed light-flavoured jets are combined to reproduce an hadronically decaying W boson. The b-quark is then added, in order to reconstruct the fully hadronic top quark decay. No further constraints can be imposed on the event in regard to the associated part: being a two-body decay, the constraint on the invariant mass of the W boson is not sufficient to reconstruct univocally the longitudinal component of the neutrino momentum in the leptonic decay of the associated W boson.

6.5. Combination of Fit Results

Finally, the p-values from the leptonic top-decay hypothesis and the hadronic one are compared and the best hypothesis is selected. The distributions of the χ^2 and $\mathcal{P}(\chi^2)$ of the best event candidates for the selected three-jet bin are shown in Fig. 6.8. In the histogram shown in Fig. 6.8e the $\mathcal{P}(\chi^2)$ distributions for the signal and the background are normalised to the number of entries, in order to identify the shape differences and exploit the separation power of the observed quantity. At high values of $\mathcal{P}(\chi^2)$ the distributions take the form of a plateau, with a preferred accumulation of the background events for values around zero. In the minimisation process, the fitter also computes corrections to the momenta of the given final state objects which results in a smaller dependence on the energy scale uncertainty of the jets and of the missing transverse energy. A sensitive consistency test of the fitting procedure is provided by the pull distributions of the kinematic variables. The pull of a variable is its residual before and after the fit, normalised by the standard deviation of this residual, as defined in Eq. 5.7. If this quantity follows a standardised Gaussian distribution, the assumptions made for the covariance matrix elements entering the kinematic fit are correct, and it is safe to assume that the double mass constraint employed in the analysis model is fulfilled.

In App. A the pull plots of the physical objects entering the fit of Wt simulated events are presented. These plots show the residual distribution of the kinematic quantities before and after the kinematic fit for all the recontructed objects, fitted to a standardised Gaussian function. The histograms shown are filled only when either of the fit converges, and it can be assumed that the tested hypothesis is correct. The result is shown only for the simulated events of the signal channel (associated Wt production), where the selection acceptance associated to the fit convergence is expected to be highest. For all the kinematic variables, a correct agreement with standardised Gaussian distributions is seen, which confirms the goodness of the covariance matrices modelling. In the results of this study the residuals of the jet transverse momentum do not seem to be affected by the constant positive bias that was found in the application of the kinematic fit to the single top t-channel production [Her14]. Instead, the fitted mean of the pull distributions for the jet p_{t} fluctuates around the null value; consequently, no compensating shift is registered in the $E_{\mathrm{T}}^{\mathrm{miss}}$ magnitude pull distribution.

6.6. Background Veto Fits

The kinematic fitter described in Chap. 5, was originally developed for the identification of a number of final states, such as:

- hadronic decay W bosons [Her14];
- leptonic decay channel (e^+e^-, $\mu^+\mu^-$) of Z+jets [BBG+12];
- leptonic decay channel (e, μ) of single top quarks in the t-channel [Rie10, Her14];

- semileptonic decay channel (e, μ) of top-antitop pairs [BBG+12, Rie10].

As it is seen in Sec. 2.4, these types of events are found in the background to the Wt signal after the standard selection and, virtually, they could all be identified by dedicated instances of the kinematic fitter. In this sense, the fitter procedure can be used to place a veto on events identified as background, thus improving the signal purity in the final event yield. In practice, only events with a topology compatible with semi-leptonic $\mathrm{t\bar{t}}$ production can be successfully and meaningfully vetoed. In fact, for the case of the W+jets background, the fitter can be used to reconstruct the hadronically decaying W, but these events are not part of the final yield, since no highly energetic electron or muon populate the final states; in addition, hadronically decaying W bosons populate half of the final states of the semileptonic decay of the Wt production, thus preventing the option to set a veto on this identification. Furthermore, the fitter cannot reconstruct the leptonic decay of the W produced in association with jets, since n_d is null when only one constraint can be imposed, m_{T}^{W}, and only one free parameter, η_ν, is available. Furthermore, even though a good performance is given by the application of the fit to the production of single top quarks in the t-channel (*cf.*[Her14]), as well as the Z+jets events background (*cf.*[BBG+12]), it is not needed here. since these two backgrounds are sufficiently suppressed by the standard selection. On one hand, the fraction of t-channel events drops since the spectator jet is produced mainly in the forward region; while the veto on events containing a second lepton of signal quality is very effective at removing most of the Z+jets background events. The remaining contamination from these events is efficiently reduced exploiting the separation power of the $\mathcal{P}(\chi^2)$ distribution of the Wt fit, by means of a simple cut on the χ^2 probability. the jet multiplicity, and to the matrix element/showering models whose variations are available only for the MC@NLO generator that is used to simulate the $\mathrm{t\bar{t}}$ events. Therefore, since the combination of the four jet bin is not expected to lead to an improvement of the measurement significance, the full analysis chain is only applied to three jets events.

6.6.1. Background Veto Fit of Semi-Leptonic $\mathrm{t\bar{t}}$ Production

Since the $\mathrm{t\bar{t}}$ background consists of events where two top quarks populate the final state, a dedicated veto fit can be applied. The application of the fit for the identification of $\mathrm{t\bar{t}}$ was originally developed in the same framework used for this analysis, in [Rie10]. It includes two W mass constraints, a leptonic and a hadronic one, as well as a same-mass [2] requirement for the two particles decaying into a W and a b-jet. Analogously to the case of the Wt signal fits, the numerical value for the W mass is taken from [Nakon]. This veto fit can only be used if at least four jets are present and is thus only effective in the ≥ 4 jets bin. Again, all possible assignments of jets to the four required jets (two b-jets and two jets from the hadronic W decay) are considered. All four jets entering the fit are required to have

[2] This means the top-mass itself is a free parameter in the fit and only the masses of the t candidate and its counterpart must be equal.

$|\eta| < 2.5$. There must be at least one b-tagged jet among the four jets. Here, a minimum value of $\mathcal{P}(\chi^2) > 0.001$ for the fit is required to classify the event as $\mathrm{t\bar{t}}$ production. Despite the good performance of the fitting tool, we chose not to use the four jet bin for the final analysis, due to two main reasons. On one hand, the absolute number of signal events obtained with the complete selection in the four jet bin is too low to allow a clear distinction of the signal above the statistical fluctuations. On the other hand, the event kinematics of the Wt and $\mathrm{t\bar{t}}$ are extremely similar, and do not allow to build a physical observable quantity with sufficient resolution power to distinguish the two processes.

6.7. Final Event Selection

For all events passing the common preselection requirements the KinFitter-based algorithms test the compatibility of the kinematics of the input objects with the topology of the Wt events. The events are then selected exploiting the KinFitter response. After the fit procedure, the top quark and its W boson daughter are completely reconstructed for any successful hypothesis, while the longitudinal component of the momentum of the spectator W boson remains unknown. With such ingredients, the following cuts are applied to further reject the background events:

- **Convergence**: This cut demands that the reconstruction of a single top quark and a W boson by the KinFitter algorithm converged.

- **$\mathrm{t\bar{t}}$ Veto**: If the reconstruction of a semi-leptonically decaying top pair by the KinFitter with a same-mass constraint was successful, i.e. the KinFitter yields a $\mathcal{P}(\chi^2)$ *higher* than 0.001, the event is *rejected* as $\mathrm{t\bar{t}}$ background.

- **Signal Hypothesis Match**: In order to reduce the background rate in the final event count, the separation power of the $\mathcal{P}(\chi^2)$ distribution for the fit combination shown in Fig. 6.8e is exploited. The fitted events are *rejected* if they yield a probability score *lower* than 0.1 to match the Wt single top hypothesis.

- **W + t Balance**: For the events passing the selection operated by the kinematic fit (fully displayed in Fig. 6.1) a cut on the p_{t} of the system composed by the top quark and the associated W boson reconstructed by the fit is applied, in order to reduce the signal-to-background-ratio. The top and the associated W boson are the only physical objects produced in the Wt events, and their system is therefore expected to appear more balanced in the transverse plane of the signal events than in $\mathrm{t\bar{t}}$, where at least one more jet initiated by a b quark in the hard final state is present. This is shown in the comparison of the histogram shapes in Fig. 6.9c. The $(\vec{p}_{\mathrm{top}} + \vec{p}_{\mathrm{W_{ass}}})_{\mathrm{t}} = p_{\mathrm{t}}^{Wt} < 35\,\mathrm{GeV}$ selection cut is chosen, in order to reject the phase space region dominated by the

$t\bar{t}$ background. The rejection power of this kinematic observable able is not correlated with the one displayed by the $\mathcal{P}(\chi^2)$ in Fig. 6.8e, thus providing an independent criterion for the selection of the signal events.

	3 Jets Selection	
Process	**e**	***μ***
Wt Channel	143.92	196.04
t-Channel	35.91	49.60
s-Channel	1.86	3.17
$t\bar{t}$	601.37	860.47
W+LF Jets	55.53	94.73
W+HF Jets	233.13	450.27
Z+Jets/Diboson	29.55	34.87
QCD	18.59	33.12
S/B	0.147	0.128
Total expected	1119.87	1722.30
Total observed	1191.00	1705.00

Table 6.3.: Event yield after the final event selection. For all the events where the convergence of the Wt hypothesis fit occurs, the $\mathcal{P}(\chi^2) > 10\,\%$ and $p_T^{Wt} < 35\,\text{GeV}$ consecutive cuts are applied in the three-jet bin for the electron and muon channel separately. After the cuts the agreement between the number of expected and observed events is maintained. The numbers in the table are used as input rates for the signal extraction described in Sec. 7.2.4.

In Fig. 6.9 the stacked distribution of the transverse momentum p_t^{Wt} of the system composed by the single top quark and the associated W boson reconstructed by the kinematic fit is shown. As it is seen in the normalised shapes provided in Fig. 6.9c, the distribution of the p_t^{Wt} quantity provides a sizable discrimination power between Wt and $t\bar{t}$ events. The cut at 35 GeV is chosen at the point where the Wt and $t\bar{t}$ shape cross, selecting the region richer in Wt events. The number of events surviving the selection is presented in Tab. 6.3. A combined total of 340 ± 18 signal events and of 1502 ± 39 background events are expected, corresponding to a signal over background ratio of X% and a statistical significance of $S/\sqrt{B} = N$. The total expected event yield is 2842.2 ± 53.3, which is in agreement with the observed 2895 events.

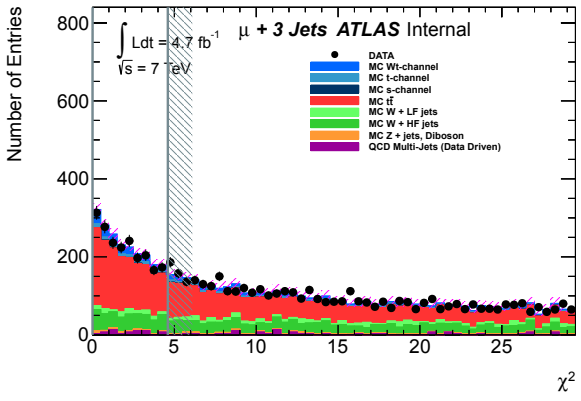

(a) μ+3 Jets.

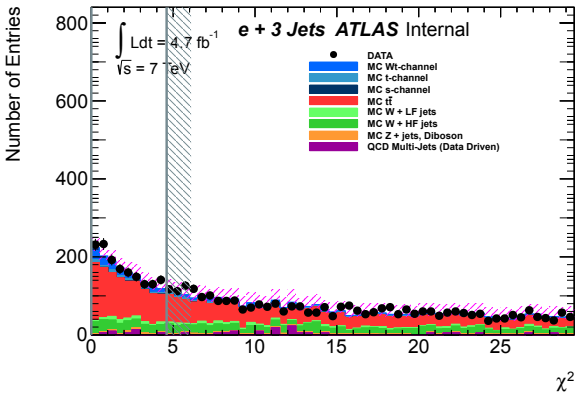

(b) e+3 Jets.

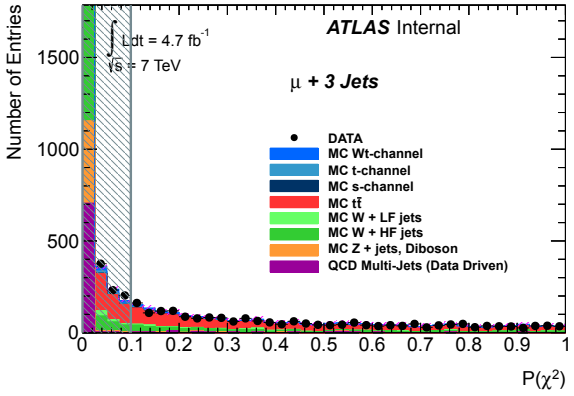

(c) $P(\chi^2)$ μ+3 Jets.

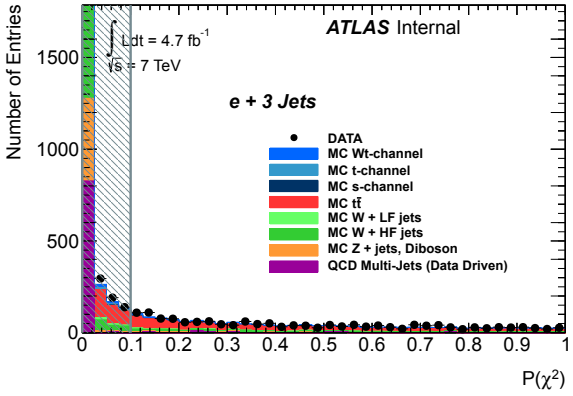

(d) $P(\chi^2)$ e+3 Jets.

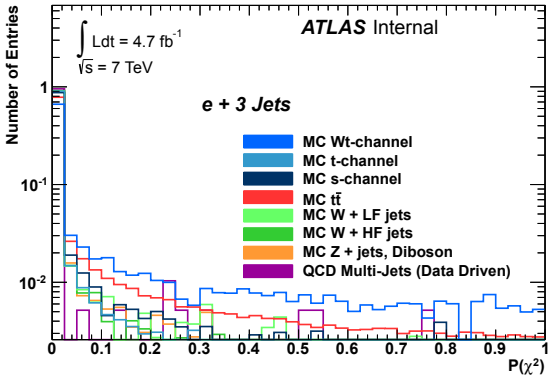

(e) $P(\chi^2)$ Shape.

Figure 6.8.: Distribution of the χ^2 and χ^2-probability of the Wt fit for the 3 jet bin in the muonic (c), (a) and electronic, (b), (d) channels after the decision explained in Sec. 6.3 and 6.4. The exclusion lines indicate the cut used for signal enrichment, $\mathcal{P}(\chi^2) > 0.1$. Histograms (c) and (d) are populated with the events for which the convergence of the kinematic fit is reached. The single top Wt, t, s-channel, $t\bar{t}$, Z+jets and diboson samples are normalised to their theory predictions; the W+jets and QCD multi-jet components of the background are normalised by means of data-driven techniques. The histogram in (e) are normalised to the number of entries, in order to identify the shape differences and exploit the separation power of the observed quantity.

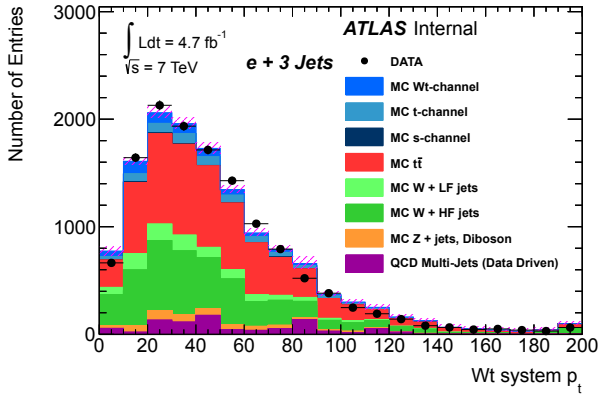

(a) e+3 jets: p_{t}^{Wt} stacked.

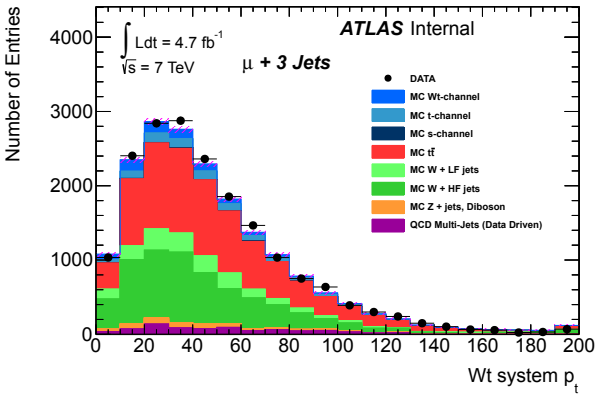

(b) μ+3 jets: p_{t}^{Wt} stacked.

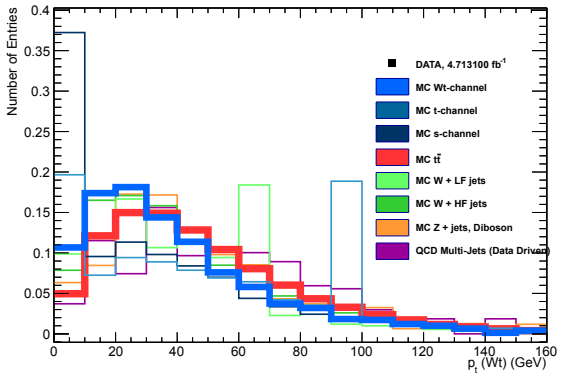

(c) p_{t}^{Wt} shapes.

Figure 6.9.: Compared distributions of p_{t}^{Wt}, defined as $(\vec{p}_{\mathrm{top}} + \vec{p}_{\mathrm{W_{ass}}})_{\mathrm{t}}$. The plots in (a) and (b) show the stacked distribution in the exemplary 3 jet bin. Histograms (a) and (b) are populated with the events for which the convergence of the kinematic fit is reached. In (c) the pure shape of the distribution is shown for each input sample. The histograms in (c) are normalised to the number of entries, in order to identify the shape differences and exploit the separation power of the observed quantity. The Wt and $\mathrm{t\bar{t}}$ shapes are put into evidence drawn in bold azure and red lines respectively. A cut at 35 GeV is chosen at the point where the Wt and $\mathrm{t\bar{t}}$ shapes cross, selecting the region richer in Wt events.

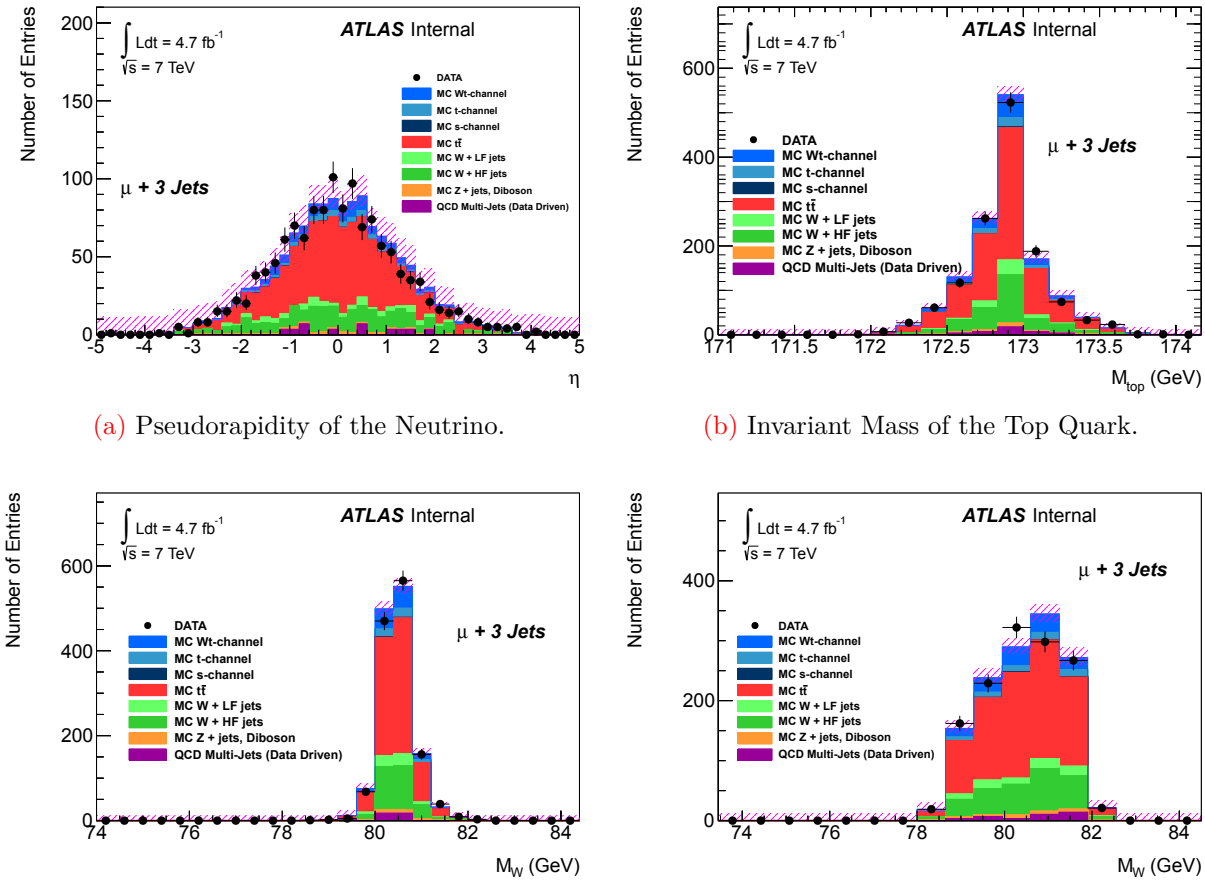

(a) Pseudorapidity of the Neutrino.

(b) Invariant Mass of the Top Quark.

(c) Invariant Mass of the W Boson (Top Decay).

(d) Invariant Mass of the W Boson (Associate).

Figure 6.10.: The plots represent, for the "leptonic top" case in the μ+3 jets channel, the distribution of the pseudorapidity of the neutrino (a) and of the invariant mass of the top quark (b), the leptonically decaying W boson (c) and the hadronically decaying associate W boson (d). All histograms are populated with the events for which the convergence of the kinematic fit is reached, and a p-value greater than 10% is found for the signal hypothesis.

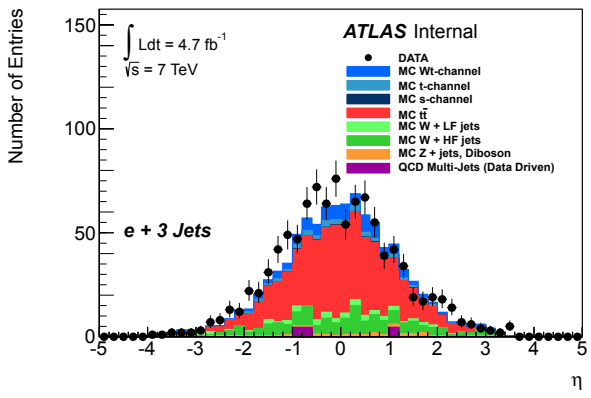

(a) Pseudorapidity of the Neutrino.

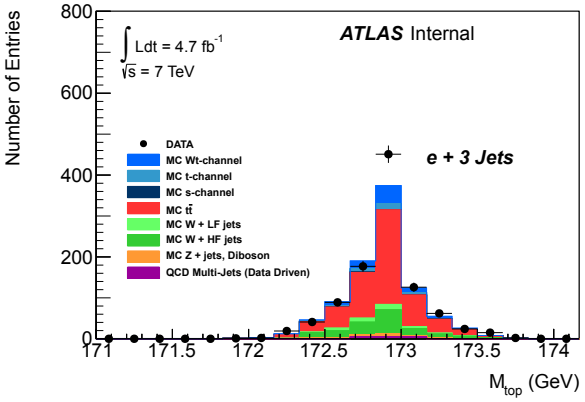

(b) Invariant Mass of the Top Quark.

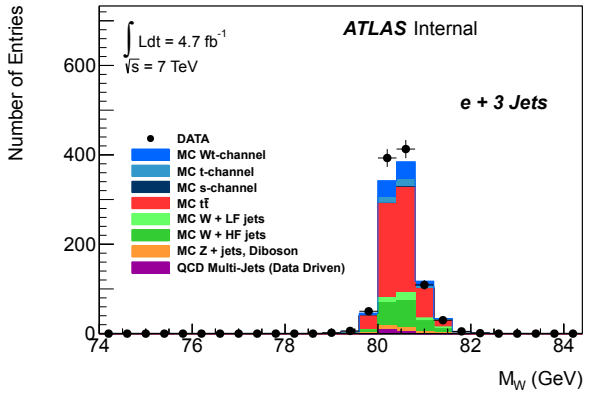

(c) Invariant Mass of the W Boson (Top Decay).

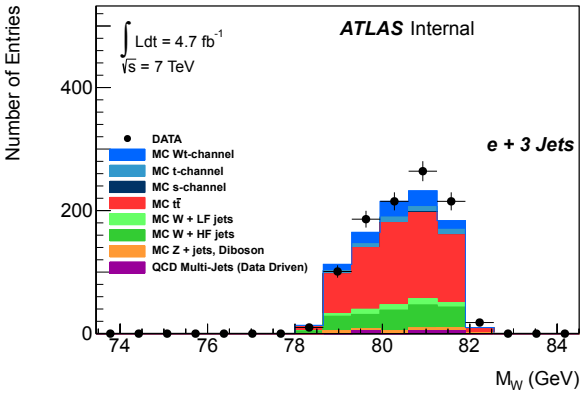

(d) Invariant Mass of the W Boson (Associate).

Figure 6.11.: The plots represent, for the "leptonic top" case in the e+3 jets channel, the distribution of the pseudorapidity of the neutrino (a) and of the invariant mass of the top quark (b), the leptonically decaying W boson (c) and the hadronically decaying associate W boson (d). All histograms are populated with the events for which the convergence of the kinematic fit is reached, and a p-value greater than 10% is found for the signal hypothesis.

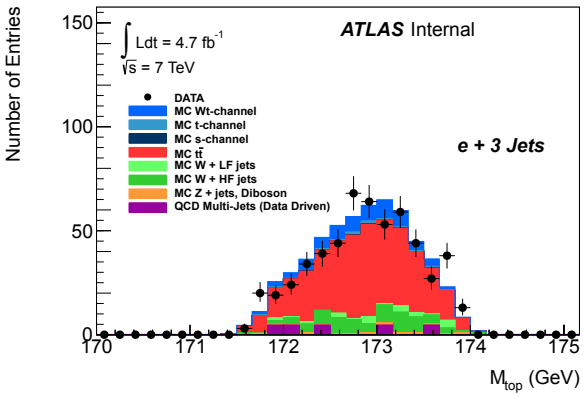

(a) Invariant Mass of the Top Quark.

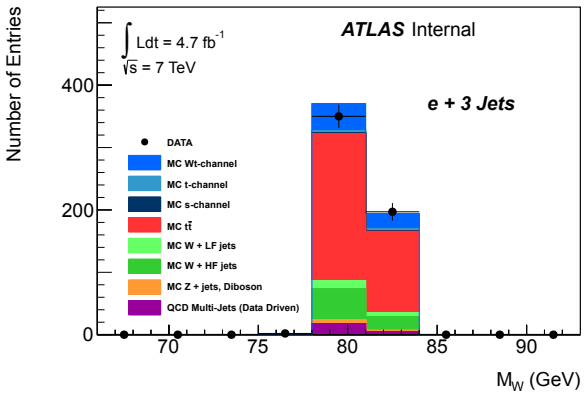

(b) Invariant Mass of the W Boson (hadronic).

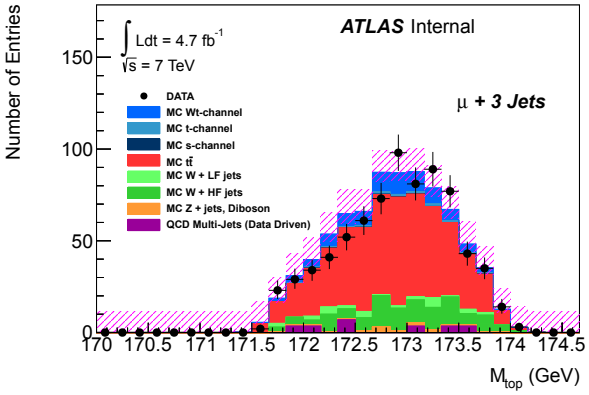

(c) Invariant Mass of the Top Quark.

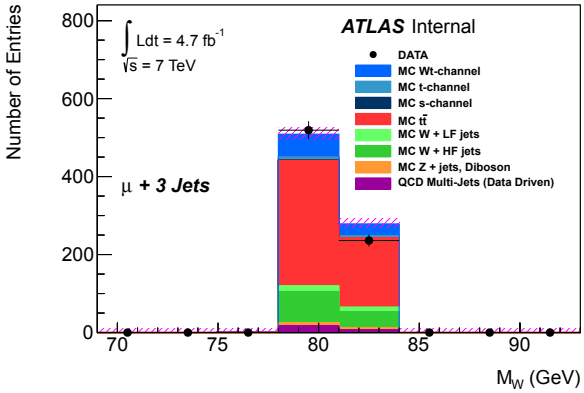

(d) Invariant Mass of the W Boson (hadronic).

Figure 6.12.: The plots represent the invariant masses reconstructed by the fit for the "hadronic top" hypothesis in the electron (above) and muon (below) channel. The distribution of the invariant masses of the top quark (a), (c)) and the hadronically decaying W boson originated from the top quark (b), (d) are shown for the analysis of the three-jet bin. All histograms are populated with the events for which the convergence of the kinematic fit is reached, and a p-value greater than 10% is found for the signal hypothesis.

7. Analysis Results

The purpose of the analysis is the measurement of the inclusive Wt production cross section. As mentioned in Chapter 3, this observable is directly related to the number of observed signal events, therefore it can be extracted directly from the results yielded by the selection obtained exploiting the discrimination power of the kinematic fit, after applying the quality requirements of the ATLAS common prescription for the preselection of top quark physics events.

The measurement of the cross section is affected by two types of uncertainties. On one hand, a first source of uncertainties is caused by the limited statistics of the data and MC samples utilised for the simulation of the events composing the signal and the background. Secondly, the measurement is affected by the systematic uncertainties associated to the reconstruction methods and to the modelling of the data. The different sources of systematic uncertainties are therefore discussed in Sec. 7.1.

In Sec. 7.2 the statistical treatment of the event yield is described, leading to the determination of an upper limit on the inclusive cross section σ_{Wt} for the production of single top quarks in association with W boson, presented in Sec. 7.2.4. In conclusion, a comparison of the result of this analysis with the latest measurements performed at the LHC is presented in Sec. 7.2.5; in Sec.7.3, the possible further developments of the current analysis are presented.

7.1. Systematic Uncertainties

Each source of systematic uncertainties has been taken into account in accordance with the standard prescriptions released by the top quark physics working group of the ATLAS experiment (*cf.* [A$^+$12k]). These prescriptions, in turn, were previously agreed upon with each one of the ATLAS physics performance teams. They can be divided into the two general classes of event mismodelling and experimental uncertainties. The systematic effects discussed in the following are provided in a two-sided fashion, unless stated otherwise. The various sources of systematic uncertainties give raise to variations on the selection acceptance that differ depending on the sample involved. Their quantitative impact to the event yield after the selection is presented in Tab. 7.3 and 7.4, where it is visualized for each of the signal and event yields in the two signal regions. These figures are used as input to the fit procedure, serving as strength parameters to generate the pseudo-experiments.

The use and implementation of pseudo-experiments to evaluate the final impact on the fit of each source of uncertainty is discussed in Sec. 7.2.2; for the combined fit, the results are

presented in Tab. 7.7, pooled in terms of their type and ranked in order of importance. The detailed records for the each lepton channel and jet bin are reported in Tab. 7.5 and 7.6.

7.1.1. Model Uncertainties

Generator Dependence

In order to quantify the uncertainty due to the Monte Carlo simulation of the physics process, the simulations obtained from different generators have been compared. To estimate only the uncertainty resulting from the generator model, the parton shower model is not varied.

In order to be consistent, it is decided to compare the predictions given by models treating the same level in perturbation theory. The $t\bar{t}$ and Wt events are generated at next-to-leading order precision level, therefore a POWHEG+JIMMY simulation has been used to estimate the deviation with respect to the results obtained from the nominal MC@NLO+JIMMY. The main difference between the two generators regards the different treatment of higher order terms[BBG+11]. The number of events collected from the MC@NLO simulation is then assigned an uncertainty:

$$N_{\text{MC@NLO}} \pm (N_{\text{MC@NLO}} - N_{\text{POWHEG}}) \,. \tag{7.1}$$

The yields obtained from the variation of the matrix element generator (upward and downward variation for each of the two leptonic channels separately) are passed to the likelihood fit as systematic variations.

A 7.1% uncertainty is assigned on the single top t-channel samples [A+10d, A+12g]. This uncertainty was estimated by comparing the distribution of the transverse momentum of the spectator b-quark as it is obtained in the gluon-splitting from the ACERMC generator with the result of the NLO calculation in a four-flavour scheme [CFMT09] using the MCFM tool. The uncertainties are studied in an uncorrelated manner, thus varying each of them up and down one at the time.

Wt - Diagram Subtraction

As discussed in Sec. 2.3.2, the matrix element amplitude for the production of top quarks in association with real top quarks is influenced, beyond the tree level, by a quantum interference with the $t\bar{t}$ production. The uncertainty connected to the numerical implementation in the event generation [WFLM09] is evaluated by symmetrising the difference between the nominal Wt sample, produced with the *diagram removal* scheme (DR), and an identically tuned sample differing only for the application of the *diagram subtraction* scheme (DS). The symmetrisation is implemented using the difference between the selection results form the two diagram treatment schemes as upward and downward variation:

$$N_{\text{Wt, DR}} \pm (N_{\text{Wt,DR}} - N_{\text{Wt, DS}}) \,. \tag{7.2}$$

Parton Shower Modelling

The dependence on the parton shower algorithms is evaluated by symmetrising the difference between the models used in the nominal simulation of each physics process and an alternative type. At the time of this work, variations of the $t\bar{t}$ MC sample alone were made available for a reliable comparison, while no realistic assessment can be performed with the single top samples. For the $t\bar{t}$ background simulation the difference between PowHeg+Jimmy and the PowHeg+Pythia variant is symmetrised with respect to the Mc@Nlo+Jimmy sample used for the nominal analysis, as shown in the following relation:

$$N_{t\bar{t}} \pm (N_{t\bar{t},\ \text{POWHEG+Jimmy}} - N_{t\bar{t},\ \text{POWHEG+Pythia}})\,. \tag{7.3}$$

The analysis results from the two variations are passed to the likelihood fit as systematic variations.

Initial and Final State Radiation

The impact of the uncertainty related to the modelling of the initial and final state radiation (ISR/FSR) emission is estimated in a correlated way for all the processes where the production of top quarks is involved. Given the current technical availability of the radiation emission parametrisation in the generators, the variation samples have been produced with the AcerMC+Pythia generator. The variations of the radiation emission are here obtained by varying by a factor two, upward and downward, the parameters which correspond to the invariant mass cut-off for photon emissions in parton showers. The events obtained by applying these variations contain, finally, "more" or "less" activity in the underlying event, and are therefore named in accordance with this characteristic. The variation of the event yield around each nominal sample - then used as systematic variations in the likelihood fit - is taken as:

$$N_{\text{nominal}} \pm \frac{1}{2}(N_{\text{moreIFSR}} - N_{\text{lessIFSR}}). \tag{7.4}$$

It is important to remark here that the difference between the ISR/FSR tunings in AcerMC+Pythia is interpreted and applied as the variation of nominal samples generated with a different generator, since the Mc@Nlo+Jimmy is used for the production of the top quark nominal samples in the present analysis (*cf.* Tab. 2.3). It is then assumed that the same variations would occur if one were able to implement an identical shift in the parametrisation of the nominal sample generated with Mc@Nlo+Jimmy.

Parton Distribution Functions

According to the factorisation theorem (Eq. 2.15), the parton distribution functions are used to define the composition of the initial states that are used for the computation of the quantum amplitudes. Given this central role in determining the flavour composition and the

kinematics of the final states, it is necessary to evaluate, to the fullest possible extent, the impact on this analysis of the propagation of their uncertainty. There are two fundamental types of uncertainty that proceed from the choice of PDF set:

- **Intra-PDF uncertainty:** this is the uncertainty strictly associated to a given PDF set measurement. A PDF is usually obtained from a fit of orthogonal functions ("eigenvectors") to collision data in dedicated experiments. The uncertainty of a PDF set is then assumed to be represented by the errors associated to the fits of the parameters for the eigenvectors. These "error PDF sets" can then be used instead of the central values, to generate the variation samples.

- **Inter-PDF uncertainty:** this is the variation that occurs when switching from one PDF set to another. The comparison is made using the central value obtained repeating the procedure for each PDF set and compare the variation on the observable.

The full uncertainty needs to be obtained by combining the inter and intra-PDF uncertainties.

Due to the limited availability of computing resources, a comparison between samples produced with every available PDF set is not feasible. A PDF re-weighting technique is therefore adopted in order to assess the global systematic uncertainty related to the choice of PDF sets. For the implementation of such technique, a procedure agreed among the four LHC experiments collaborations [Col12, A+12o] is used, which employs the software tool named LHAPDF [DFM+10, A+10a]. According to this procedure, each event generated with a given PDF set is re-weighted by a w_{PDF} value [A+10d] that embodies a mathematical relation with any new PDF set:

$$w_{PDF} = \frac{q_{new}(x_1, f_1, Q^2) \cdot q_{new}(x_2, f_2, Q^2)}{q_{nominal}(x_1, f_1, Q^2) \cdot q_{nominal}(x_2, f_2, Q^2)}, \tag{7.5}$$

where $x_{1,2}$ and $f_{1,2}$ are the momentum fraction and the flavour of the two partons. Following the definition given in Sec. 2.3, Q^2 represents the energy scale of the process. The quantities $q^{nominal}$ and q^{new} are the original and the new PDF; in this procedure, the latter can be both an error PDF and a new central value PDF. The outcome of this procedure is the so-called PDF envelope, which contains, in a two-sided definition, the global uncertainty proceeding from the choice and the use of a given PDF set. The extremes of the envelope are chosen as the maximum upward and downward variation with respect to the central value of the distribution obtained re-weighting the observable according to all the variations available. The excursions from the central value are then imposed as uncertainties on the central value obtained from the *nominal* samples.

The reweighting method that has been used for this analysis has been implemented in [Sta13b] and is well documented inside the ATLAS collaboration [Sta13a].

QCD Multi-jet Background Normalisation

The QCD background is normalised to data by means of the fitting method discussed in Sec. 4.3.1 for the electron and the muon channel. On the basis of previous comparisons with an alternative data driven estimate based on the *matrix method* described in [BCC13], a systematic uncertainty of 50% is assigned to the normalisation factors obtain from the fit[A+12g].

More recent studies [Sta13b] have questioned this estimate of the uncertainty of the QCD multi-jet background. It has been observed that the kinematic distributions of the observables, and therefore the shape of the template, is left unaltered by this type of variation. A second criticism can be raised, observing that the Jet-Electron model does not retain the information associated to the QCD cross section uncertainty – which in fact is never taken into account by the method – but the uncertainty which it provides is strictly connected to the Jet-Electron internal systematic variations, whose determination is based only on comparisons with MC samples, on the basis of histogram shape differences.

W+Jets Background Uncertainty

As shown in Sec. 4.3.2, the normalisation of the W+jets background sub-components is extracted from data itself using a fit procedure that involves the charge asymmetry and the count of events before and after the b-tagging cut selection. A minimal set of two uncorrelated uncertainties is associated to the method, in order to cover the internal systematics related to the model's assumptions. As previously discussed, the method relies on the computation of

- the relative amount of W+LF and W+HF expected events, and
- the relative amount of W+c and the combined W+cc/W+bb contribution expected inside the W+HF sample.

In this sense, the main source of systematic uncertainty strictly inherent to the method is the statistics of the MC events that are collected after the aforementioned selections. For each jet bin and lepton channel, the two sets of upward and downward variations are computed inside the tool implementing the model, and are used to constrain the normalisation with a better (smaller) variation than the one obtained from the theory predictions. The uncertainties obtained in this analysis for the normalisation of the light and heavy-flavoured components of the W+jets background, are shown in Tab. 7.1.

Theoretical Cross Section Normalisation

For each background sample, the production cross section prediction is used to compute the number of expected events presented in Tab. 6.3. For the $t\bar{t}$, Z+jets, diboson and single top backgrounds, the uncertainties from the theory computation are used to assign the uncertainty on the rate predictions that are presented in Tab. 7.1.

7.1.2. Detector Uncertainties

Lepton Energy Scale/Resolution

The effect of the lepton energy scale on the acceptance is taken into account by simply applying a 1-sigma variation on the lepton p_t on the Monte Carlo simulations, while resolution effects are included by smearing the central values. The variations are based on external studies of the resolution and scale of the Z mass. These variations are propagated through the full analysis chain in order to assess their impact on the selection acceptance. The momentum smearing is applied differently in the electron and muon case, due to the different reconstruction techniques.

In the electron case, it is shown in [A+12k] that the uncertainties originate principally from the dependence of the cluster energy scale s_{cluster} on the detector material and the presampler energy scale (see Sec. 3.5.5). Here, the total error is estimated to amount to about $\pm 1.5\,\%$ of the cluster energy. This figure is used to study the effect of the electron energy uncertainty on the final yield, smearing the calorimeter cluster energy. In contrast, since the muon momentum measurement combines the independent information from both the Inner Detector and the Muon System, uncorrelated smearings are applied separately on the two parts of the muon reconstruction. Furthermore, the uncertainty stemming from the muon p_t scale is estimated by the difference between the bare energy measurement and its application, setting this shift as a symmetrical error on the nominal scaled p_t value.

To assess the effect of these variations on the result of the selection acceptance, the analysis is repeated after the application of upward and downward variations of both the scale and the resolution. Each of the considered variations is applied in a uncorrelated way, before the new yields are passed to the signal extraction fit.

Lepton Trigger Efficiency Scale Factors

As discussed in Sec. 4.2.4, the efficiencies of the identification, reconstruction and trigger selection of the leptons show differences between data and the Monte Carlo simulation samples. These differences, which can amount up to a few percent, are used in order to correct for the data acceptance. To do so, each event in the simulated samples undergoes a reweighting procedure: each event weight is multiplied by a scale factor which, in turn, is obtained from the analysis of Z and W decays in data. To propagate the related uncertainty to the final result, a 1-sigma variation of the order of $3\,\%$ for electrons and $1.5\,\%$ for muons [1] is applied on the scale factor of the lepton in the selected events [A+12k]. The thus modified acceptance of the expected yields is passed to the signal extraction fit in an uncorrelated and exclusive way, so that the electron scale factor systematic is only applied in the electron channel and the muon scale factor systematic only in the muon channel.

[1] The tools used to generate the scale factor variations in this analysis are provided by ATLAS working groups which work as liaisons between the physics object reconstruction groups and the Top quark group.

Jet Energy Scale

The total uncertainty on the calibration of the electromagnetic energy scale of the jet (EM+JES) described in Sec. 3.5.6 consists of the combination of several different sources of uncertainties, of which a detailed reference is given in [A+12e]. These uncertainties proceed, in first stance, from both the detector and Monte Carlo model assumptions:

- Systematic effects arise from the fact that the *in situ* techniques used to calibrate the jet energy scale assume a balance, in the transverse momentum, between the jet and the respective reference object, while this requirement is only approximately fulfilled. Furthermore, systematic uncertainties are also associated to the very definition of the reference object. In total, there are 54 sources of uncertainty that have been associated to the *in-situ* calibration (*cf.* Tab. 10 of [A+12e]). These are related to the detector, the physics modelling, the available statistics of the input events and the analysis techniques. Interplays of these effects are also taken into account. The final number of independent sources of uncertainty is reduced to 6 [A+12k]. This is obtained by diagonalising a covariance matrix which contains the information regarding the correlations between the different sources. Restricting the energy range to $p_{\mathrm{t}}^{\mathrm{jet}} < 600\,\mathrm{GeV}$, the JES uncertainty related specifically to the *in-situ* calibration amounts to about 2.5 % for $p_{\mathrm{t}}^{\mathrm{jet}} = 25\,\mathrm{GeV}$, decreasing to below 1 % for $55\,\mathrm{GeV} \leq p_{\mathrm{t}}^{\mathrm{jet}} \leq 500\,\mathrm{GeV}$.

- The events used to derive the *in-situ* calibration, tend to be biased towards jets caused by high-p_{t} quarks, while the samples used for the analysis contain also gluonic jets. Jets labelled as originating from light quarks have significantly different response (p_t^{reco}/p_t^{truth}) from those labelled as originating from gluons in the MC simulation. This difference is a result of a difference in fragmentation that can be ascribed to differences in observable properties of the two types of jets. Gluon jets tend to have more particles, and as a result, those particles tend to have lower transverse momentum than in the case of light-quark jets. Additionally, gluon jets tend to have a wider angular energy profile before interacting with the detector. This flavour-dependent response difference is largest at low p_{t} (up to 8% for), and decreases to a few percent at high p_{t}. However, the impact of fragmentation differences of quark and gluon-induced jets is assessed by assigning a systematic error that is analysis-dependent.

- An additional p_{t}-dependent uncertainty is associated to the energy scale of jets initiated by b-quarks (b-JES). This uncertainty is applied to b-tagged jets, replacing the light jet flavour composition uncertainty. The magnitude of this uncertainty is determined in the MC simulation, and validated on data by a comparison of track jets and calorimeter b-jets. It is found to amount to up to 2.5% and 3% in the ranges $|\eta| < 1.2$ and $1.2 \leq |\eta| \leq 2.5$, respectively, for jets with transverse momentum lower than 400 GeV.

- The studies for the calibration of the jet energy scale use isolated jets from MC, initially neglecting the presence of close-by jets which might affect the calorimeter jet.

The occurrence of close-by jets must then be considered as an additional systematic uncertainty. Ratios involving isolated jets and their non-isolated counterparts are used, to quantify this effect. Both transverse momenta of calorimeter jets and track jets in data and MC are studied, yielding an uncertainty of about 2 % to 3.5 % for $p_{\mathrm{t}}^{\mathrm{jet}} < 100\,\mathrm{GeV}$, decreasing with the p_{t} of the jet.

- The total JES uncertainty is increased by the error associated to the pile-up offset correction of the calibration scheme described in Sec. 3.5.6. This contribution is studied as a function of the jet p_{t}, for different N_{PV} and μ in data samples from run periods characterised by different beam conditions. The JES uncertainty due to pile-up mismodelling amounts to a maximum of 3 % for $p_{\mathrm{t}}^{\mathrm{jet}} > 40\,\mathrm{GeV}$, in correspondence with the the direst pile-up conditions.

Two exemplary detailed shapes of the total JES uncertainty and its component as a function of the jet p_{t} are presented in Fig. 7.1a for light jets at $\eta = 2$, and in Fig. 7.1b for b-jets at $\eta = 0.5$; the distributions are extracted from the nominal semi-leptonic $\mathrm{t\bar{t}}$ sample, after applying the standard selection and the recommended corrections (Sec. 4.2).

A dedicated tool provided by the jet performance group is employed in order to combine the different contributions to the JES uncertainty, and thus generate 1-sigma variation samples. The analysis is rerun over these samples, thus propagating the effect of the JES uncertainty to the final acceptance. The two outcomes are then passed to the template fit as JES systematic templates. Analogously to the other jet-related systematics, the total impact of the JES uncertainty increases with respect to the jet bin number of the analysis.

Jet Energy Resolution

As referred in Sec. 4.2.4, no additional smearing procedure on the jet energy resolution is put in place in the MC samples, as a good agreement with data is apparently found. The possibility of a systematic effect arising from the calibration of the jet energy resolution (JER), however, is tested applying a smearing procedure based on a random 1-σ variation of the jet transverse momentum in the MC. The absolute magnitude of this variation is obtained from the uncertainties of the JER calibration procedure. As it is mentioned in Sec. 3.5.6, the transverse momenta of the reconstructed jets are calibrated with the aid of two *in-situ* techniques, which are used to correct the energy reconstruction in the MC and mirror the response obtained in data. The first of these techniques is the dijet balance method, where an asymmetry parameter

$$A(p_{\mathrm{t},1}, p_{\mathrm{t},2}) = \frac{p_{\mathrm{t},1} - p_{\mathrm{t},2}}{p_{\mathrm{t},1} + p_{\mathrm{t},2}} \tag{7.6}$$

is fitted with a Gaussian in events with two back-to-back jets in the same pseudorapidity region. For a perfectly balanced event, this quantity is expected to be null. The second is

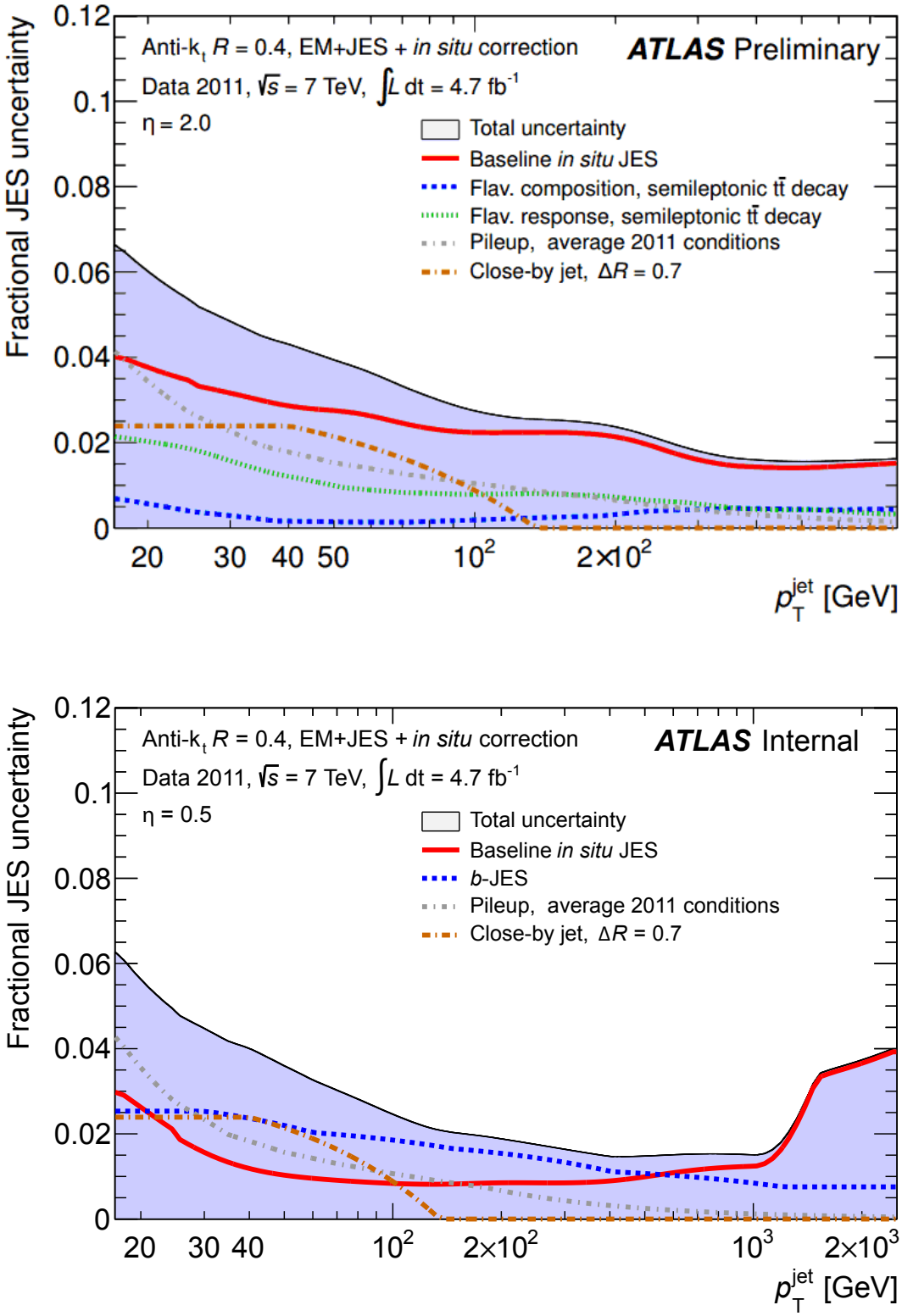

Figure 7.1.: Jet energy scale systematic uncertainties, shown as a function the jet transverse momentum, for anti-k_T ($R = 0.4$) light-flavoured jets with $\eta = 2$ (a), and b-jets with $\eta = 0.5$ (b), after the EM+JES calibration. The sample used are semi-leptonic $t\bar{t}$ events, after applying the standard selection and the corrections described in Sec. 4.2. The different contributions of the overall uncertainty are shown as well as the total resulting JES uncertainty [A+12e].

referred to as the bisector method. This method relies on an imbalance (transverse) vector, which is defined as the vector sum of the two leading jets in the dijet event. This vector is projected along an orthogonal coordinate system in the transverse plane, where one of the new axis is chosen in the direction that bisects the angle formed by the two jets. The vector sum is then decomposed in its projections on the two new axes; analogously to the dijet method, it is expected that these two projections fluctuate around a null value, and the variance of the two distributions is expected to be of the same intensity of the variation of the asymmetry $A(p_{\mathrm{t},1}, p_{\mathrm{t},2})$. The two methods provide independent measures of $\frac{\sigma_{p_\mathrm{t}}}{p_\mathrm{t}}$. At this point, the total JER uncertainty is extracted combining the uncertainties associated with both methods, which originate from the specific kinematic cuts used to define the test samples used as input for the two techniques. The final jet energy resolution uncertainty is found to amount to 10 % for $30\,\mathrm{GeV} < p_\mathrm{t}^{\mathrm{jet}} < 500\,\mathrm{GeV}$, for jets in the range $|y| < 2.8$ [RSP+11]. Only one variation template can be generated according to this procedure. Analogously to the other one-sided systematic cases, the template thus obtained is used as 1-σ *up* variation, while the *down* counterpart is obtained symmetrising with respect to the nominal acceptance. As in the JES case, the rate uncertainty caused by this variations increases according to the number of jets used by the analysis.

Jet Reconstruction Efficiency

As it described in Sec. 4.2.4, each jet in the simulated events is assigned a multiplicative scale factor, which accounts for the discrepancies of the jet reconstruction efficiencies between data and MC. These uncertainties are widely described in [ATL10], and they are associated to the kinematic cuts employed to select the samples of "tag" and "probe" jets used:

- Minimal p_t;
- Maximal ΔR used to match the track and the calorimeter jet;
- Minimal $\Delta\phi$ separation between the "tag" and "probe" jet.

The final systematic uncertainty associated to the weight of each jet is estimated by using a tool released by the ATLAS JetEtMiss performance group. The tool simulates the reconstruction inefficiency by means of a random-based algorithm that removes single jets from the event; the "tag" and "probe" efficiencies are used as input to drive the dropping algorithm. The results are compared in data and MC, and an uncertainty of 2 % is assigned to this systematic. Thus obtained, this systematic is one-sided only. The full analysis is then repeated on the varied sample, obtaining the *up* variation template. Its difference with the nominal acceptance is then symmetrised to extract the template of the *down* variation. Again, the rate uncertainty caused by this variations increases according to the number of jets used.

b-Tag, c-Tag and Mis-Tag Scale Factor Uncertainty

The uncertainties related to the scale factors associated to the b-tag cut working point are taken into account by applying a variation on the event weight according to the flavour of each jet (in MC samples). The implementation of the systematic variation follows the procedure suggested by the ATLAS flavour tagging group [A+12a].

Jet Vertex Fraction Scale Factor

As mentioned in Sec. 4.2.4 a scale factor is applied to the Monte Carlo simulated samples in order reproduce the efficiency on data of the jet vertex fraction cut. A 1-sigma variation is applied on each jet weight to evaluate the overall impact on the final result. This variation represents the uncertainty on the extraction of the scale factors, which takes into account two main sources of the uncertainties:

- the uncertainty related to the selection criteria used in the definition of hard-scatter jets, which is evaluated by varying both the minimal values of the the p_{t} of the Z boson in the reconstruction, and $\Delta\phi$ between the leading jet and the Z boson candidate;
- The quality of the fitted function extracted to parametrise the JVF scale factors in terms of the jet transverse momentum: this is assessed by augmenting the fit uncertainty by a factor of $\sqrt{\chi^2/n_d}$, where χ^2 and n_d are the squared residual and the number of degrees of freedom of the fit, respectively.

These variations are used to generate four new multiplicative scale factors (*cf.* [Gra12]) which take into account the effect of the (in)efficiency of selecting (rejecting) the hard scatter (pile up) jets. These new efficiency and inefficiency factors are then combined in order to obtain two new sets of JVF weights, which are then used to produce the upward and downward variation templates to pass to the final fit.

Pile-up

As mentioned in Sec. 3.4.1, the modelling of the pile-up is also done by applying a reweighting procedure to the events in all MC samples, in order to match the distribution of the average interactions per bunch crossing $\langle\mu\rangle$ that is seen in data. To assess its impact, a dedicated pile-up systematic that propagates the uncertainties of the event weight to the final acceptance is not made available for this analysis. However, the influence of the pile-up modelling has already been taken into account when quantifying the systematic uncertainty for the 4-momenta of the all the reconstructed physics objects (jets, e, μ). Besides these, the pile-up has a considerable impact on the low energy components of Eq. 3.9, thus affecting the refined measurement of the missing transverse energy, $E^{\mathrm{miss}}_{\mathrm{x,y,Ref}}$. This uncertainty is derived studying the data of Z$\rightarrow\ \mu\mu$ and Z$\rightarrow$ee events where no jets with $p_{\mathrm{t}} > 20\,\mathrm{GeV}$ are found[A+12k]. Using this data sample, the distribution of the "data/MC" ratio of the $\langle\sum E_{\mathrm{t}}\rangle$ observable

is compared to an expected flat profile, in three different pseudorapidity regions (central, end-cap, forward region). A total uncertainty of ±6.6 % is then obtained, combining the results. This variation is then used to scale each of the soft terms of Eq. 3.9 (Jets, SoftJets and CellOut) to generate systematic templates. Also in this case, the variations are applied in a uncorrelated way, intending them as independent from each other. The full analysis sequence is run again over the thus varied simulation samples, and the results passed to the fit to assess the final uncertainty.

$E_{\mathrm{T}}^{\mathrm{miss}}$ Computation

The computation of the components of the missing energy in the transverse plane is described in detail in Sec. 3.5.8. As it is expected, the systematic errors of the computation of the refined missing transverse energy $E_{\mathrm{x,y,Ref}}^{\mathrm{miss}}$ originate from the energy scale and the resolution of the components of Eq. 3.9, together with the effects related to the additional energy deposited in the calorimeter from soft pile-up events. Of these, all the uncertainties related to the misreconstruction of the leptons and the jets are already taken into account, since the effects of each of their respective systematic variation schemes are propagated to the final result through the re-computation of the missing transverse energy. Analogously, the effects due to the pile-up uncertainty are already covered by the pile-up systematic. The remaining effects are due to the underlying event component resulting in low energy jets and from calorimeter topoclusters that were not associated to any physical object reconstructed in the event. These two latter categories correspond to the "SoftJets" and "CellOut", respectively.

The influence of the soft terms is studied with a QCD multi-jet Monte Carlo sample generated with Pythia[A+12k]. In this sample, different parton shower models are tried out, the tunes varied. Furthermore, small variations of the model of the upstream dead material are applied, and the full simulation chain is rerun. The uncertainty on the "CellOut" term is quantified as 13 %, while the uncertainty on "SoftJet" term amount 10 %; being fully anti-correlated due to the common sample, the two effects are combined and treated as one single systematic. Again, to study the effect of this systematic, these upward and downward variations are applied in each event, shifting the recomputation of the $E_{\mathrm{x,y,Ref}}^{\mathrm{miss}}$ term and rerunning the complete analysis chain. The two results obtained are then passed to the fit as systematic fluctuations.

Luminosity

The measurement of the luminosity during the collision in ATLAS detector is described in detail in Sec. 3.4. There are several partial sources of uncertainty associated to it. The main contribution to the uncertainty proceeds from the error of the measurement of the bunch population product $n_{\mathrm{p1}}n_{\mathrm{p2}}$ in the method of the "van der Meer scan". Furthermore, the status of the LHC beams throughout the 2011 collision runs required the evaluation of the impact of the "afterglow" background [A+12d]. By this name is identified the tiny

diminishment of activity of the LUCID and BCM detectors for bunch-crossings without hard collisions. Thirdly, an additional source of uncertainty is associated to the time stability of the luminosity calibration in the BCM. Lastly, the parameters used for the calibration rely on both directly measured and computed quantities, that are generally assumed to be linearly dependent from the interaction rate μ. Therefore, collision run samples from the 2011 data have been used to quantify any deviation from such linearity, thus interpreting it as an additional source of systematic error. Finally, the combination of these principal (and other, non mentioned here) effects, allows the determination of the full systematic uncertainty of the total integrated luminosity of the 2011 data set. This is estimated to be $\delta\mathscr{L}/\mathscr{L} = \pm 1.8\,\%$ [A+12d, Lis12]. This systematic error is employed directly in the signal extraction fit as the uncertainty on the data counts.

7.2. Signal Extraction

For the extraction of the number of signal events in the final count, a template fit of the signal and background models to data is employed. In practice, the extraction of the Wt production events in data is performed using the BILL (**Bi**nned **L**og **L**ikelihood) fitter tool, which was already used for the t-channel single top cross section measurement [A+12h, Sar12a, Sar12b]. In the following sections the principles of the likelihood fit are described, together with the determination of its total uncertainty and the computation of the significance of the extracted signal. A more detailed study of the application of the BILL tool to the t-channel analysis was done in [Sta13b], where a comparison to another statistics approach as well as criticism of some of its techniques are found.

7.2.1. Extraction of the Signal Cross Section

The likelihood function for a number of independent processes is built as follows:

$$L(\beta_1, ..., \beta_{N_{\text{proc}}}) \;=\; \prod_{k\,\in\,\text{all bins}} \frac{e^{\mu_k} \cdot \mu_k^{N_k^{\text{obs}}}}{N_k^{\text{obs}}!} \;\cdot\; \prod_{j\,=\,2}^{N_{\text{proc}}} G(\beta_j, \Delta_j)\,. \tag{7.7}$$

In this representation, the index j denotes each of the N_{proc} processes used for modelling the data. These are eight in total: the single top Wt channel signal ($j = 1$), and the seven components of the background, listed in Tab. 7.1 ($j = 2, \ldots, 8$). The index k represents each one of the search channels, *i*. e. the electron and muon selections in the three-jet bin, in the present analysis. For each bin k the likelihood function includes a Poisson term with the number of observed events, N_k^{obs}. The expectation value μ_k of the Poisson distribution is then given by

$$\mu_k = \sum_{j=1}^{n} \nu_j \;\cdot\; \beta_j\, \alpha_{jk}\,, \tag{7.8}$$

where ν_j represents the number of expected events collected in the simulation of the j^{th} process. The terms denoted as α_{jk} are the relative fractions of events collected in the k^{th} bin for the j^{th} process; in this sense, they have to fulfill the normalization condition

$$\sum_{k \in \text{all bins}} \alpha_{jk} = 1\,. \tag{7.9}$$

The definition above allows to interpret the α_{jk} as shape parameters, thus extending the usage of the likelihood fit to the exploit a kinematical distribution where the signal takes a shape markedly different from its underlying background. The β parameters represent the ratio between the number of events observed and predicted, and can be seen as the relative observed cross section, for each process:

$$\beta_j = \frac{\sigma_j^{\text{obs}}}{\sigma_j^{\text{SM}}}. \tag{7.10}$$

These quantities constitute the actual parameters of the fit. Here, the number of expected background events can be constrained using the *a priori* knowledge of their production cross sections (*cf.* Tab. 2.3). In the likelihood function of Eq. 7.7 this constraint is represented by a Gaussian term:

$$G(\beta_j, \delta\sigma_j) = \frac{1}{\sqrt{2\pi(\delta\sigma_j)^2}} \exp\left(-\frac{1}{2}\left(\frac{\beta_j - 1}{\delta\sigma_j}\right)^2\right), \tag{7.11}$$

where the mean value and the width are the relative observed cross section of j^{th} process and its uncertainty.

The uncertainties on the background normalisation that are reported in Tab. 7.1 constitute the width parameters, Δ_j, of each Gaussian function. The contribution from QCD multi-jet events is fixed, since it has been estimated with the jet-electron model in advance (*cf.* Sec. 4.3.1), and is not allowed to vary in the fit: in practice, this is implemented by setting the uncertainty of the QCD Gaussian constraint to $\delta\sigma_{\text{QCD}} = 1 \times 10^{-7}$. A 50% systematic uncertainty is assigned to the QCD multi-jet model normalisation as a nuisance template instead.[2] The uncertainties on the W+jets normalisation are taken from the data-driven estimate outlined in Sec. 4.3.2, while for the remaining processes the uncertainty on the theory prediction has been used. The cross section is extracted from a simple counting procedure, due to the absence of a significant event statistics that would allow to exploit the shape of a kinematic distribution and identify a region of the phase space preferred by the Wt production channel. The numerical stability of the fit result is ensured by replacing the

[2] This is in accordance with both the current prescriptions [A+12k] and the t-channel analysis use case [A+12h].

Background Process	$\Delta\sigma$ [%]
t-channel single top	6.0
s-channel single top	6.0
$t\bar{t}$ (semi/dileptonic)	11.0
W+ light flavour jets	8.4
W+ heavy flavour jets	8.4
Z + jets and Diboson	60.0
QCD multi-jet	0.0

Table 7.1: Estimated relative errors on the MC sample cross sections used by the BILL tool to extract the Wt-channel single top signal from the KinFitter analysis [Kid12, A+10f, A+10b].

likelihood by its negative logarithmic function, corresponding to

$$-\ln L(\beta_1, ..., \beta_{N_{\text{proc}}}) = \sum_{k=1}^{N_{\text{bins}}} -(\mu_k + N^{\text{obs}} \cdot \ln \mu_k) + \sum_{j=2}^{N_{\text{proc}}} -\frac{1}{2}\left(\frac{\beta_j - 1}{\delta\sigma_j}\right)^2 . \quad (7.12)$$

This new quantity is now minimized using the program Minuit [**?**]. The maximum likelihood of Eq.(7.7) corresponds to a generic a single channel of the analysis. In this work, the likelihoods have been combined for the two leptonic channels of the three jet bin. Finally, by means of Eq. 7.10, the cross section is obtained from the fit parameter β relative to the Wt signal multiplying this value by the expected cross section.

7.2.2. Estimation of the Total Cross Section Uncertainty

The total error of the cross section result includes multiple sources of uncertainties. Each source of uncertainty is taken into account by producing, for each MC sample in Tab. 2.3, an equivalent template where the upward or downward variation is applied. The analysis chain is then run again, for each of these variation templates, thus obtaining a different result, whose excursion from the nominal result contains the information about the impact of that specific source of uncertainty. All the sources of systematic uncertainties described in Sec. 7.1 are treated in this manner. Additionally, also the statistical errors associated to data and to the MC production need to be computed, as well as error associated with the cross section uncertainties. Following a frequentist approach, pseudo-experiments are eventually employed in order extract the total uncertainty and the contributions of each systematic.

Data Statistical Uncertainty

The event yield resulting from running the analysis on the nominal templates is used in order to evaluate the impact of the statistical error associated to the limited number of events collected in data. In practice, this is determined by performing pseudo-experiments where a number is drawn from a Poisson distribution. The expectation value of this distribution

is given by the original number ν_j constituting the event yield of the analysis for the jth MC sample (*cf.* Eq. 7.8). The sum of the draws then constitutes a pseudo-data template, deviating from the nominal sum. To build the uncertainty distribution, 10,000 pseudo-experiments are performed.

MC Statistical Uncertainty

The impact of the statistical error associated to the limited number of MC events available to the analysis is also evaluated. For each MC sample j, a the number of events in each bin is reset in a pseudo-experiment, drawing a random number according to a Poisson distribution, with an expectation value given by the original event yield ν_j[3]. The resulting yields of all processes are added up and used as template for the evaluation of the uncertainty. Again, 10,000 dedicated pseudo-experiments are performed in total to simulate the impact of this uncertainty.

Cross Section Uncertainty

To model the background in the fit, the cross sections reported in Tab. 7.1 are used. The impact of the expected uncertainties on the final result is evaluated, again, by means of pseudo-experiments where the number of expected events in the analysis background is varied. In practice, this is done in three steps. In the first place, a random number x is drawn from a log-normal distribution[4] with a mean of one and a standard deviation equal to the corresponding (relative) cross section uncertainty $\delta\hat{\sigma}_j$ from :

$$\ln\mathcal{N}(x;\mu_j,\sigma_j) = \frac{1}{x\sqrt{2\pi\sigma_j^2}}\exp\left(-\frac{1}{2}\left(\frac{\ln x-\mu_j}{\sigma_j}\right)^2\right) \tag{7.13}$$

with

$$\mu_j = -\frac{1}{2}\sigma_j^2\,, \tag{7.14}$$

$$\sigma_j^2 = \ln[(\delta\hat{\sigma}_j)^2+1]\,. \tag{7.15}$$

In Equations (7.13), (7.14) and (7.15), μ_j and σ_j are the two parameters needed to build the log-normal distribution belonging to the $j-th$ process. Secondly, the expectation value of the nominal total number of events of the $j-th$ process is scaled by the multiplication factor x. Finally, the Poisson statistics is employed again to draw randomly a new number of events N_j^{xsec}, using the value previously scaled as mean of the distribution. Analogously to

[3] Since only the event yield is used to extract the signal in this analysis, without involving the comparison of distribution shapes, there is no need to consider the statistical uncertainty associated to the binning.
[4] A log-normal distribution is chosen to ensure that only positive numbers can be drawn.

the treatment of the data and MC statistics systematics, the sum of all the (independently) shifted templates serves as pseudo-data in the fit. In total, again, 10,000 pseudo-experiments are performed.

Systematic Uncertainties

The limited number of signal events available to the analysis after the event selection does not allow to use the shape of the distribution of the most discriminating observable, p_{t}^{Wt}, which is instead used to select the events by setting an upper threshold on its value. Therefore, since the cross section extraction is based on a simple event count, all the systematics can be treated as simple *rate uncertainties*. These are taken into account by varying, in each channel m, for each process j, the expected number of events ν_{mj} according to a quantity

$$\nu_{mj}^{\mathrm{syst}} = \nu_{mj} \cdot \left(1 + \sum_{i}^{N_{\mathrm{syst}}} \delta_i \cdot [\Theta(\delta_i) \cdot \epsilon_{imj+} + \Theta(-\delta_i) \cdot \epsilon_{imj-}]\right) . \tag{7.16}$$

Here, ν_{mj}^{syst} is the expectation value of the total yield, shifted according to the effect of each of the N_{syst} systematic uncertainties on the acceptance of the process. In practice, this is done by using the nuisance parameter, δ_i, which is drawn at random from a standardized Gaussian distribution (with mean at zero and standard deviation of one). This nuisance parameter is then used in each pseudo-experiment to define the strength and sign of the ith systematic excursion. The quantity $\Theta(\delta_i)$ is the Heavyside step function. In this framework, it is used to distinguish between the application of relative acceptance uncertainties resulting from the use of upward variation templates from the respective downward ones.

The uncertainty associated to the luminosity measurement, ν_{mj} is also varied at random according to Eq. (7.16), but in this particular case the efficiency shifts are given by $\epsilon_{imj\pm} = \pm(\delta\mathscr{L}/\mathscr{L})$.

The ν_{mj}^{syst} quantities built in Eq. 7.16 represent now the new expectation values obtained from applying a systematic variation. These quantities are, again, taken as the mean of a Poisson distributions from which the total number of observed events in the current pseudo-experiment, N_{mj}^{syst}, is randomly determined. At this point, the contributions from all of the j processes are summed up to produce a new template. This template is then used as pseudo-data, in the sense that is treated like the real data, in order to the extract the cross section from the fit described in Sec. 7.2.1. For each source of systematic uncertainty described in Sec. 7.1.1 and 7.1.2, 10,000 pseudo-experiments are performed. In an identical fashion, this procedure is applied to assess the systematic impact of the statistical uncertainty associated to the data and the MC, the one from the cross section uncertainty in the background fit, and the luminosity. In each iteration, the nominal analysis templates are then fitted to the pseudo-data using the likelihood shown in Eq. 7.7.

The distributions of the β_j parameters obtained from each pseudo-experiment are then further exploited to quantify the resulting uncertainty associated to each systematic. The

standard deviation $\sigma_i(\beta_{Wt\text{-channel}})$ of the distribution of the $\beta_{Wt\text{-channel}}$ extracted from the 10,000 fits on the pseudo-data can be used as the estimator of the error associated to the $i-th$ systematic on the measured cross section of the Wt-channel.

Finally, the effect of the correlations between the different sources of uncertainty is assessed using 10,000 pseudo-experiments where all sources of uncertainties are combined. A new distribution of $\beta_{Wt\text{-channel}}$ is thus obtained, and its standard deviation, which now contains the effect of the correlations of all the systematic error sources, is used as the error on the final cross section result.

7.2.3. Compatibility With Backgrond-Only Hypothesis

The cross section result obtained in this work needs to be evaluated in terms of the power of the analysis to discriminate between the signal hypothesis and the background and decide on which of these hypotheses is preferred by data when taking into full account the impact of the systematic uncertainties described in Sec. 7.1. A figure of merit referred to as significance can be defined to serve this purpose, while a procedure to define an upper limit on the value of the physical observable can be put into place, when the ability of the analysis to sort between the two hypotheses is not sufficient.

Computation of the Significance

According to the Neyman–Pearson lemma, the likelihood ratio is found to be the most powerful test to distinguish between two hypotheses. The statistic test quantity

$$Q = -2 \ln \frac{L\left(H_1\right)}{L\left(H_0\right)} \tag{7.17}$$

is then built, where the likelihood functions L are formulated according to Eq. 7.7. At the numerator, the likelihood implements the signal plus background hypothesis H_1, defined by setting $\beta_{\mathrm{Wt}} = 1$ in the likelihood formulation. At the denominator, instead, the likelihood of the background-only hypothesis H_0 is set, obtained by setting $\beta_{\mathrm{Wt}} = 0$. The distributions of the test statistic Q are then computed, using two new ensembles of pseudo-experiments which, in turn, are built from the nominal samples to represent the data compatible with the two hypotheses. The two distributions must now be normalized, in order to represent the probability density function of the two hypotheses to test. The overlap of these functions, denoted respectively as $\hat{q}_1$ and $\hat{q}_0$, contains now the information relative to the separation power of the analysis applied to the pure simulation, taking into account the given set of known systematic uncertainties. In this sense, the goodness of the analysis separation power can be visualized as a small overlap of the probability density function for the two hypotheses. To proceed with the quantification of goodness of the analysis separation power, in terms of

hypothesis probability, a p-value is built as

$$p_0(Q_1) = \int_{-\infty}^{Q_1} \hat{q}_0(Q)\,\mathrm{d}Q\,, \tag{7.18}$$

where the term on the left hand side corresponds to setting the upper integration limit to be the median value of the $\hat{q}_1$ distribution. The median value, Q_1, of the signal hypothesis distribution $\hat{q}_1$ is chosen as representative of its *e*xpected Q-value, in order for the p_0-value to represent a 50 % probability that the H_1 hypothesis is true, while rejecting the background with probability equal to the p-value. In this sense, the integration over the $\hat{q}_0$ probability density up to the median of $\hat{q}_1$ represents the probability of observing a (simulated) effect compatible with the signal hypothesis H_1 if the background hypothesis H_0 is valid.

Now, an ensemble built from real collision data can be used to replace the simulation in the fit of the nominal samples, and thus build the normalized test statistic distribution $\hat{q}_{obs}$ of the observed test value, Q_{obs}. This distribution must then be compared to $\hat{q}_1$ and $\hat{q}_0$, to decide which hypothesis is more compatible with the real data. Like in the above, the *o*bserved p-value, $p_{0,\mathrm{obs}}$, is obtained by replacing as upper integration bound the median value of $\hat{q}_{obs}$ in Eq. 7.18. In this construction, $p_{0,\mathrm{obs}}$ represents the probability of observing, in real data, a background fluctuation compatible with the signal hypothesis, when the background-only hypothesis is valid.

It is customary to convert the p-values in terms of the significance. This is done by finding the value corresponding to the lower bound x_p of the integration of the right hand side of a standardized unitary Gaussian function (with null mean and unitary standard deviation) using the positive infinity as upper bound, when the integration amounts to the p-value:

$$p(Q) = \frac{1}{\sqrt{2\pi}} \int_{x_p}^{\infty} e^{-\frac{(x^2)}{2}}\,\mathrm{d}x\,. \tag{7.19}$$

The value x_p is referred to as the significance, and interpreted as the number of standard deviations associated to the p-value yielded by the test. Simplifying, the p-value is an estimate of the error associated to the rejection of the background-only hypothesis. An analysis is then expected to yield both small $p_{0,\mathrm{exp}}$ and $p_{0,\mathrm{obs}}$-values – and, conversely, large significances – for being able to claim a significant result above the expected background. It is a standard procedure to claim an observation when the significance obtained is above a customary value of three standard deviations (3σ) corresponding to a value of p_0 lower than 1.35×10^{-3}, while a discovery can be claimed when a significance figure above five standard deviations (5σ)is found, which corresponds to a p-value lower than 2.87×10^{-7}.

Extraction of the Upper Limit

When the conversion of the p-value of the rejection of the background hypothesis is such that it does not exceed the threshold of 3σ, rather than claiming a 1-σ cross section interval

it is customary to set a confidence interval on the test statistic, leading to the definition of an upper limit on the value of the physical observable. Among the several procedures to extract frequentist upper limits that are agreed within the ATLAS collaboration, the CL_s method has been chosen [Jun99, Rea02]. The reasons behind this choice are manifold: it is the most conservative option, it leads to the same results of a Bayesian limit on the mean value of a Poissonian or Gaussian distribution, and, given its wide use in the literature, it allows for comparisons with other experiments. Due to these reasons, the method has also been employed by ATLAS to set upper limits on the production cross section for single top quarks in the s-channel at both 7 and 8 TeV centre-of-mass energy [A$^+$11f, A$^+$14c].

In this case, the "target" value of confidence level (C.L.) is usually chosen to 95 %, corresponding to a coverage equal to two standard deviations. An integration of the probability density function of the fit of the signal hypothesis $\hat{q}_{\text{obs}}$ is then performed up to infinity starting from a value Q_0, where it yields a value of p_{s+b}:

$$\int_{Q_0}^{\infty} \hat{q}_1(Q)\,\mathrm{d}Q = p_{s+b}\,. \tag{7.20}$$

In the equation above, Q_0 represents now the *e*xpected Q-value of the probability density function $\hat{q}_0(Q)$, and defined again by its median value.

In the sense of the confidence level formulated in Eq. 7.20, the upper limit represents the threshold value of the test distribution above which the signal hypothesis is rejected with a confidence level p_{s+b} on the test sample[5]. In other words, p_{s+b} can be interpreted as the probability of drawing a Q-value greater or equal to Q_0, and then compatible with the background-only hypothesis, under the assumption that the signal+background hypothesis is valid. According to the CL_s procedure, the signal model is regarded as excluded at a confidence level of $1-\alpha = 95\,\%$ if:

$$\frac{p_{s+b}}{1-p_b} < \alpha \tag{7.21}$$

where p_b is intended as the p-value associated to the rejection of the background hypothesis, p_0, as defined in Eq. 7.18. The exclusion limit *e*xpected by the analysis separation power of is found when the value Q_0, the integration bound in Eq. 7.20, is the median of the probability density function $\hat{q}_0(Q)$; in an analogous way, the corresponding *o*bserved limit is determined by using $\hat{q}_{\text{obs}}(Q)$ instead of $\hat{q}_0(Q)$. As a result, the *e*xpected and the *o*bserved upper limits can be obtained by rescaling the predicted value of the physical observable under study up to reach the CL_s exclusion values at 95 % confidence level [6].

[5] The definition of confidence level adopted here is to be taken neither as a "degree of belief" of the limit obtained with the described procedure, nor as a statement on the probability of the range real value, which remains always unknown, but simply with respect to the coverage of the test sample used

[6] In practice, this is done extracting the value of the physical observable generated in the pseudo-experiment which yields a figure close to the Q-value used in the integration of Eq. 7.20

A suitable number of pseudo-experiments needs to be done to ensure a reliable computation of the significance. Ensembles with a population greater than 10 millions are needed to obtain a result of the signal hypothesis test which allows to safely claim a significance above 3σ. Since the measurement performed in this work is affected by systematic uncertainty of about 100% though, a much lower value of the significance is to be expected, and a number of 100,000 pseudo-experiments is sufficient to estimate the limit.

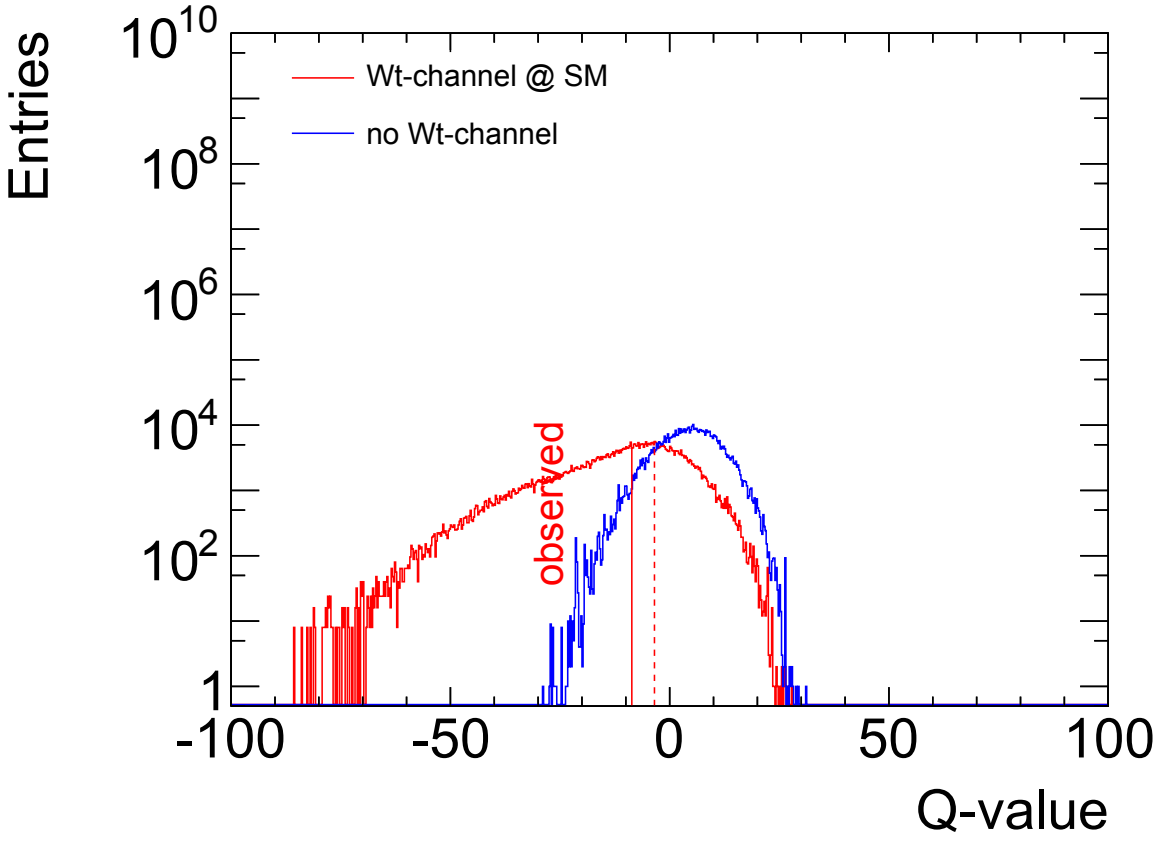

Figure 7.2.: Distributions of the Q-value given the background-only hypothesis H_0 (in blue), and $\hat{q}_1 1$, representing the probability to observe a Q-value given the signal-plus-background hypothesis H_1 (in red). The continuous and dashed lines represent the expected and the observed Q-values respectively.

7.2.4. Cross Section Measurement Result

By using the statistical framework illustrated in Sec. 7.2, the expected and observed results of the Wt production cross section measurement are presented. The outcome of the simultaneous maximum likelihood fit of the number of events which are counted after requiring

	Process	e		μ		Comb.	
		β	$\Delta\beta$	β	$\Delta\beta$	β	$\Delta\beta$
S	Wt Production	1.15	0.38	1.10	0.39	1.12	0.35
B	t-channel single top	1.09	0.06	1.05	0.06	1.06	0.06
	s-channel single top	1.06	0.06	1.03	0.06	1.04	0.06
	$t\bar{t}$ (semi/dileptonic)	1.05	0.06	1.04	0.06	1.05	0.06
	W+ light flavour jets	1.02	0.08	1.01	0.08	1.01	0.08
	W+ heavy flavour jets	1.03	0.08	1.02	0.08	1.02	0.08
	Z + jets and Diboson	1.02	0.06	1.01	0.06	1.01	0.06
	QCD multi-jet	1.00	0.02	1.00	0.02	1.00	0.02

Table 7.2.: The fit values by process and lepton channel for the chosen three-jet bin. A good agreement between the electron and muon channel is seen in the result of the Wt signal fit. The background parameters and their uncertainties are in agreement with the input values provided to the maximum likelihood fit, shown in Tab. 7.1

the standard quality selection, the convergence of the kinematic fit yielding an adequate p-value, and a balance of the transverse momentum of the system composed by the top quark and the associated W boson reconstructed in the events signal region defined by the presence of three high energy jets and one unique highly energetic lepton is summarized in Tab. 7.2. The fit parameters β, defined in Eq. 7.10, represent, for each physics process, the ratio of the contributions preferred by data in the selected phase space, to the ones predicted by the Standard Model. The measurement is performed combining the fit of the event yields in the electron and muon selection channels, since the combination allows for a more statistically precise result than the one obtained fitting the event counts from single lepton bins separately. As mentioned, all the β parameters are allowed to vary within their normalisation uncertainty, with the exception of the QCD multi-jet fraction of which a 50% uncertainty on the model normalisation is taken into account as a systematic variation. The fitted normalisation ratios of each component of the background are compatible with unity, thus showing a good agreement with the starting values. In Tab. 7.2 uncertainty associated to each parameter in the fit is shown, and a good agreement is found with the input values presented in Tab. 7.1. This signifies that the background is well modelled in all its SM components, and upholds the trust in the overall analysis procedure. The fit of the signal fraction yields similar results, not distant from unity, in the electron and muon channel, thus confirming the goodness of the global Monte Carlo model in use. Even if all the central values preferred by the fit are very close to the theoretical expectation, the result is not very instructive, since it is characterized by a striking lack of sensitivity, when considering the large fit uncertainty associated to the β parameter of the Wt component. This large figure arises from the total expected uncertainty affecting the measurement: from the fit results,

we observe in fact a Wt production cross section of

$$\sigma_{\text{obs}}^{\text{Wt}} = 17.63^{+2.92}_{-2.92}\,(\text{stat})\,^{+17.3}_{-17.6}(\text{syst})\,[\text{pb}] \tag{7.22}$$

for the combination of the two lepton channels, whereas the theoretical value

$$\sigma_{\text{th}}^{\text{Wt}} = 15.74^{+1.17}_{-1.22}\,[\text{pb}] \tag{7.23}$$

is expected [Kid10b]. Since the needed sensitivity level allowing to quote a measurement has not been achieved by this study, we prefer to express the result in terms of a limit on the cross section value.

However, it is instructive to investigate the reasons behind such a large total uncertainty, identifying the quantitative impact of the relative contributions to the total uncertainty on the Wt-channel cross section, which can be done by generating separate ensembles of pseudoexperiments, where each source of systematic uncertainty is considered alone. The result of this study on the combined fit is illustrated in Tab. 7.7, where the systematic breakdown of the relative contributions to the total uncertainty are pooled by the type in which they are described in Sec. 7.1 and ranked by their importance. The detailed records for the each lepton channel and jet bin are reported in Tab. 7.5 and 7.6.

The analysis is highly affected by systematics related both to the object reconstruction and the background modelling. The uncertainty on the jet energy resolution and B-tagging have the highest impact, followed by the missing transverse energy. Concerning the modelling-related uncertainties, all the sources that have been considered in this study present and quite large impact, except for the modelling of the signal events. As anticipiated in Sec. 6, the main issue for the identification of Wt events lies in their similarity with the kinematics of top pairs, which constitute the main background due to its large cross section magnitude. As a direct result, all the variations of the $\text{t}\bar{\text{t}}$ modelling (ISR/FSR, parton shower, matrix element model, cross section magnitude) have a disruptive effect which prevents the clear isolation of the Wt signal.

Significance and Limit

The measured cross section measurement corresponds to an expected significance of 1.87 standard deviations, while a value of 1.31 standard deviation is found for the observed significance, which are determined in following the procedure described in Sec. 7.2.3. The slightly higher value of the expected significance is due to an expected median value of the test statistic ($Q_{\text{exp}} = -8.6$) lower than its observation ($Q_{\text{obs}} = -3.5$) and therefore to a smaller probability that the signal contribution arises just from a background fluctuation (the expected p-value is equal to 0.03, compared to 0.13 for the observed p-value).

The distributions of the test statistic Q obtained for the signal-plus-background and background-only ensembles tests is shown in Fig. 7.2, where the expected and observed Q-values are indicated. With the CL_s method, the observed (expected) limit set at 95 %

C.L is found to be $\sigma_{\mathrm{Wt}} < 32.51\,\mathrm{pb}$ (30.03 pb).

7.2.5. Conclusion

We presented in this chapter the challenging analysis of the production of single top quarks in association to a W boson arising from proton-proton collisions at a centre-of-mass energy of 7 TeV. This process arises via quark-gluon interactions and is therefore favoured at the LHC in comparison with the Tevatron, since its approximate NNLO cross section is predicted to be low, but visible. The predicted fraction of signal events collected after the common event preselection is negligible compared to the main sources of background, while no observable kinematic quantities allows a powerful discrimination. For this reason, the implementation of an alternative analysis technique based on a kinematic fit was set into place. This fit procedure allows the possibility to rank each event by the χ^2-probability to match the physical constraints associated to the signal hypothesis, and opened up the possibility to apply further event requirements, in order to obtain a higher signal purity. Events where the fit has converged with a high probability value were selected, and the physical objects reconstructed by the ATLAS algorithms (electrons, muons, jets, missing transverse energy) were further corrected according to the fit best parameters, in order to improve the reconstruction. By this procedure, the system composed solely by one top quark and a W boson was built, and required to carry a total transverse momentum compatible with zero. A signal purity higher than 10 % in both the electron and muon channel was achieved. Finally, in order to extract the signal, a maximum likelihood fit was performed using the number of selected events as a template. The uncertainty affecting the cross section measurement was estimated via the generation of pseudo-experiments according to the rate variations associated to different systematic and statistical uncertainties. Unfortunately, the strong impact of the uncertainties jeopardised the sensitivity of the analysis, which does not reach the significance necessary to reliably claim an observation and quote a central measurement. Two classes of uncertainty dominate the systematics that affect the analysis of the Wt production channel. The first has its source in the modelling of the multiple levels of the Monte Carlo tools used for the simulation. Among these the modelling of the $\mathrm{t\bar{t}}$ background events has a major impact on the analysis, which is in accordance with the results in the dilepton channel. In decreasing order of importance, the sources of background modelling uncertainties are the initial and final state radiation models, the parton shower model and the generator of the "hard" events. On account of the physics reconstruction, the principal uncertainties arise from the presence of the three jets in the chosen final state. The high multiplicity increases in fact the uncertainty related to the jet reconstruction and energy calibration, that are far less precise than the leptons.

Following the CL_s method, value of 32.51 pb (30.03 pb) is found as an observed (expected) upper limit at 95 % C.L. on the cross section value for the Wt production, which is considerably worse than the latest results of the searches for the Wt associated production in the dileptonic channel, where the cross section could be measured and an evidence of 3.3 and

4.0 standard deviations was found by ATLAS and CMS [A+12c, C+13]. Similar results have been obtained by the other two analyses that have been carried out in parallel, exploiting other methods than the kinematic fit, in the single lepton plus jets channel [BLM+11, Ta12], confirming the difficult challenge offered by the analysis target.

The different performance of the analysis with respect to the dilepton channel results can be imputed to the different jet multiplicity where the search insists upon, for two main reasons. On one hand the ratio of signal events with respect to the background is considerably larger in the selection performed by the dilepton analysis, and the overall contribution related to the mismodelling of the background is considerably reduced. The low jet multiplicity required by the dilepton analysis is very useful to reject the $t\bar{t}$ component of the background, which has a large cross section uncertainty, and for which the discrepancy yielded by the application of the parton shower models, the generator model and initial and final state radiation effects, – all of them not very uniformly and coherently modelled by the generators available – become less influent. On the other hand, the dileptonic channel analyses consider an additional lepton in the place of two light-flavoured jets required in the final states of the lepton+jets case, which allows to replace the large impact of the jet-related systematics, whose impacts increase monotonically with the number of jets, with the much better known lepton reconstruction uncertainty.

e+3 jets	$\Delta N_{Up/Down}/N[\%]$							
Source	Wt-Channel	t-Channel	s-Channel	$t\bar{t}$	W+HF Jets	W+LF Jets	Z/Diboson	QCD
Electron Energy Scale	-0.66/0.07	-0.79/-1.01	0.19/0.66	0.02/-0.08	-0.16/1.35	-3.53/-2.41	-1.67/-0.27	0.00/0.00
Electron Energy Res	-0.74/-0.66	-0.19/-0.80	-0.66/1.82	-0.17/0.05	0.57/0.45	-0.56/-1.89	-1.07/-3.00	0.00/0.00
Lepton Reconstr. Eff.	2.46/-2.46	2.45/-2.45	2.44/-2.44	2.47/-2.47	-2.15/2.14	3.83/-3.91	2.47/-2.47	0.00/0.00
Muon p_t Res. (ID)	-0.06/0.00	0.17/0.00	0.51/0.51	-0.02/-0.03	0.01/0.02	-0.04/-1.06	0.00/0.00	0.00/0.00
Muon p_t Res. (MS)	-0.06/0.00	0.19/0.17	0.00/0.51	-0.01/-0.04	0.28/0.02	-0.02/-0.03	0.00/-0.41	0.00/0.00
Muon p_t Scale	-0.07/0.00	0.08/0.00	0.51/0.00	-0.06/0.00	0.29/0.00	-0.02/0.00	-0.41/0.00	0.00/0.00
Jet Reconstruction Eff.	0.17/0.00	-2.31/0.00	-0.88/0.00	1.39/0.00	-4.86/0.00	6.06/0.00	-3.34/0.00	0.00/0.00
Jet Energy Scale	-0.99/-10.15	1.78/-6.12	12.28/-12.15	-10.46/2.56	7.80/-10.94	27.03/19.14	10.00/-2.59	0.00/0.00
Jet energy Resolution	-8.19/0.00	3.24/0.00	-1.27/0.00	-8.16/0.00	1.65/0.00	184.47/0.00	8.62/0.00	0.00/0.00
B-Tagging Eff.	6.42/-6.45	2.87/-3.24	-3.06/1.83	3.17/-3.65	-9.46/-6.29	4.94/2.07	0.64/-0.66	0.00/0.00
C-Tagging Eff.	-1.57/1.57	-0.36/0.36	-0.26/0.26	-1.48/1.48	-10.35/-5.27	6.47/0.66	7.45/-7.63	0.00/0.00
Mistagging Eff.	-0.32/0.33	-0.12/0.12	-0.27/0.27	-0.24/0.24	-17.67/0.65	32.93/-23.08	7.38/-7.44	0.00/0.00
Jet Vertex Fraction	2.66/-2.38	2.70/-2.73	2.38/-2.33	3.29/-2.92	-12.93/-3.33	9.81/-4.58	3.48/-3.80	0.00/0.00
E_T^{miss} CellOut+SoftJet	-2.59/0.91	-2.29/-0.33	-3.30/1.90	-1.78/1.56	1.28/2.92	-2.33/2.40	-1.65/0.02	0.00/0.00
E_T^{miss} Pile-Up	-2.29/0.76	-2.61/0.31	-1.80/1.64	-1.39/0.95	0.51/1.01	-3.08/-0.22	-2.75/-1.08	0.00/0.00
QCD Norm.	0.00/0.00	0.00/0.00	0.00/0.00	0.00/0.00	-9.58/9.61	-0.84/0.86	0.00/0.00	50.00/-50.00
Ratio Wc/(Wc$\bar{c}$+Wb$\bar{b}$)	0.00/0.00	0.00/0.00	0.00/0.00	0.00/0.00	-5.45/6.45	0.00/0.00	0.00/0.00	0.00/0.00
Ratio W+LF/W+HF	0.00/0.00	0.00/0.00	0.00/0.00	0.00/0.00	10.29/-12.35	-21.15/25.38	0.00/0.00	0.00/0.00

Table 7.3.: Percentual rate variations due to all the instrumental and theoretical uncertainties considered are shown for each sample used to model the data yield. The results are relative to the nominal yield in the e+3 jets search mode. The values in the table constitute the strength of the nuisance parameters used as input to generate the correlated pseudo-experiments in the fit procedure. The effects due to the jet reconstruction efficiency, the jet energy smearing and the muon unscaling are asymmetric, and therefore considered one-sided only in the table.

μ+3 jets	$\Delta N_{Up/Down}/N$[%]							
Source	Wt-Channel	t-Channel	s-Channel	$t\bar{t}$	W+HF Jets	W+LF Jets	Z/Diboson	QCD
Electron Energy Scale	0.00/0.00	-0.09/-0.09	0.00/0.00	0.01/-0.02	0.01/0.00	0.01/0.00	0.00/0.00	0.00/0.00
Electron Energy Res.	0.00/0.00	-0.15/-0.09	0.00/0.00	0.01/0.01	0.00/0.00	0.01/0.00	0.00/0.00	0.00/0.00
Lepton Reconstr. Eff.	1.50/-1.50	1.50/-1.50	1.48/-1.48	1.51/-1.51	-1.17/1.15	2.36/-2.35	1.48/-1.48	0.00/0.00
Muon p_t Res. (ID)	0.07/0.05	0.09/0.34	-0.00/0.38	0.04/0.01	-0.00/0.54	-0.00/-1.43	0.27/-0.66	0.00/0.00
Muon p_t Res. (MS)	0.02/0.00	0.21/-0.13	0.44/0.22	-0.04/0.04	0.34/0.12	0.17/-2.26	-0.27/-0.18	0.00/0.00
Muon p_t Scale	0.14/0.00	-0.20/0.00	0.45/0.00	0.12/0.00	-0.29/0.00	-2.98/0.00	-0.13/0.00	0.00/0.00
Jet Reconstruction Eff.	-0.65/0.00	-1.07/0.00	-0.69/0.00	1.78/0.00	-1.65/0.00	0.54/0.00	-7.97/0.00	0.00/0.00
Jet Energy Scale	1.68/-11.41	1.20/-6.50	1.95/-7.64	-11.86/3.05	-7.49/-5.34	7.50/56.05	31.71/-15.69	0.00/0.00
Jet Energy Resolution	-11.01/0.00	-1.13/0.00	-6.68/0.00	-9.76/0.00	-11.02/0.00	-8.51/0.00	-1.78/0.00	0.00/0.00
B-Tagging Eff.	6.43/-6.47	2.83/-3.25	-3.54/2.20	2.91/-3.47	-10.77/-7.14	6.25/2.93	0.80/-0.82	0.00/0.00
C-Tagging Eff.	-1.54/1.54	-0.40/0.40	-0.10/0.10	-1.44/1.44	-10.17/-7.96	6.53/2.87	7.04/-7.17	0.00/0.00
Mistagging Eff.	-0.21/0.21	-0.30/0.30	-0.28/0.28	-0.20/0.20	-20.27/0.82	34.77/-22.14	6.65/-6.71	0.00/0.00
Jet Vertex Fraction	2.72/-2.51	2.95/-2.73	2.81/-2.97	3.36/-2.99	-13.16/-4.38	11.38/-2.05	3.87/-4.34	0.00/0.00
E_T^{miss} CellOut+SoftJet	-0.51/1.02	-1.28/1.82	-0.36/2.09	-1.67/1.34	-0.53/3.50	-2.88/3.28	-4.32/0.35	0.00/0.00
E_T^{miss} Pile-Up	-0.20/1.02	-1.08/1.75	-0.85/0.68	-1.10/0.85	-0.17/2.17	-2.05/1.29	-2.76/0.26	0.00/0.00
QCD Norm.	0.00/0.00	0.00/0.00	0.00/0.00	0.00/0.00	-5.54/5.54	-0.69/0.70	0.00/0.00	50.00/-50.00
Ratio Wc/(Wc$\bar{c}$+Wb$\bar{b}$)	0.00/0.00	0.00/0.00	0.00/0.00	0.00/0.00	-3.13/3.65	0.00/0.00	0.00/0.00	0.00/0.00
Ratio W+LF/W+HF	0.00/0.00	0.00/0.00	0.00/0.00	0.00/0.00	8.90/-10.44	-19.54/22.91	0.00/0.00	0.00/0.00

Table 7.4.: Percentual rate variations due to all the instrumental and theoretical uncertainties considered are shown for each sample used to model the data yield. The results are relative to the nominal yield in the μ+3 jets search mode. The values in the table constitute the strength of the nuisance parameters used as input to generate the correlated pseudo-experiments in the fit procedure. The effects due to the jet reconstruction efficiency, the jet energy smearing and the muon unscaling are asymmetric, and therefore considered one-sided only in the table.

3 Jet Bin, Electron Channel

Systematic	$\delta\sigma_{t\text{-channel}}$ Up[%]	Down[%]	Bias[%]
Data Statistics	24.01	-24.01	0
Luminosity	10.88	-10.88	3
MC Statistics	2.68	-2.68	-0.17
QCD Normalization	5.97	-5.97	-0.16
Ratio W+LF/W+HF	4.49	-4.50	-0.39
Ratio W+c/(W+c$\bar{c}$+W+b$\bar{b}$)	9.64	-9.61	0.75
Background Cross Sections	45.96	-45.96	-0.22
Matrix Element Generator (Wt-channel)	5.55	-5.55	-0.15
Matrix Element Generator t$\bar{t}$	13.27	-13.27	-0.20
Parton Shower Generator t$\bar{t}$	16.62	-16.62	-0.56
PDFs	33.00	-33.00	0.34
ISR/FSR	65.47	-65.47	-0.80
Lepton Reconstruction Efficiency	12.90	-12.90	9
Electron Energy Scale	4.74	-4.75	-0.35
Electron Energy Resolution	5.64	-5.64	0.14
Muon p_{t} Resolution (ID)	3.01	-3.01	0.23
Muon p_{t} Resolution (MS)	3.19	-3.19	9
Muon p_{t} Scale	4.82	-4.82	0.10
Jet Reconstruction Efficiency	3.44	-3.44	0.17
Jet Energy Scale	8.32	-7.50	3.62
Jet Energy Resolution	14.00	-14.01	-0.60
Mistagging Efficiency	2.44	-2.44	9
C-Tagging Efficiency	8.32	-8.32	3
B-Tagging Efficiency	26	-26	-0.60
JVF	6.64	-6.64	-0.27
$E_{\mathrm{T}}^{\mathrm{miss}}$ Pile-Up	14.50	-14.56	-1.32
$E_{\mathrm{T}}^{\mathrm{miss}}$ CellOut+SoftJet	21.09	-21.24	-2.48
Total(sys)	98.39	-98.39	-1.33
Total(sys+stat)	101.28	-101.28	-1.33

Table 7.5.: The systematic table for the cut & count experiment after the p-value cut and $p_T^{Wt} < 35\,\mathrm{GeV}$ consecutive cut are shown in the three-jet bin for the electron selection channel. The effects due to the jet reconstruction efficiency, the jet energy smearing and the muon unscaling are one-sided only, and their impact is therefore symmetrised.

3 Jet Bin, Muon Channel

Systematic	$\delta\sigma_{t\text{-channel}}$ Up[%]	Down[%]	Bias[%]
Data Statistics	22.04	-22.04	0
Luminosity	10.92	-10.92	-0.26
MC Statistics	3.44	-3.46	-0.33
QCD Normalization	3.94	-3.94	0.11
Ratio W+LF/W+HF	2.82	-2.87	-0.55
Ratio W+c/(W+c$\bar{c}$+W+b$\bar{b}$)	5.88	-5.85	0.61
Background Cross Sections	47.83	-47.83	-0.15
Matrix Element Generator (Wt-channel)	2.89	-2.89	4
Matrix Element Generator t$\bar{t}$	22.78	-22.78	0.14
Parton Shower Generator t$\bar{t}$	24.17	-24.17	-0.11
PDFs	31.65	-31.65	1
ISR/FSR	56.51	-56.51	0.48
Lepton Reconstruction Efficiency	8.02	-8.02	0.18
Electron Energy Scale	0.59	-0.59	2
Electron Energy Resolution	1.56	-1.53	0.29
Muon p_{t} Resolution (MS)	2.43	-1.94	1.47
Muon p_{t} Resolution (ID)	2.27	-2.18	0.64
Muon p_{t} Scale	2.40	-2.36	0.47
Jet Reconstruction Efficiency	2.03	-2.01	0.28
Jet Energy Scale	13.38	-15.01	-6.79
Jet Energy Resolution	37.79	-37.79	0.49
Mistagging Efficiency	3.25	-3.25	6
C-Tagging Efficiency	8.59	-8.59	7
B-Tagging Efficiency	18.70	-18.70	-0.57
JVF	3.31	-3.37	-0.63
$E_{\mathrm{T}}^{\mathrm{miss}}$ Pile-Up	11.36	-11.33	0.77
$E_{\mathrm{T}}^{\mathrm{miss}}$ CellOut+SoftJet	18.94	-18.94	0.18
Total(sys)	100.80	-101.06	-7.16
Total(sys+stat)	103.18	-103.43	-7.16

Table 7.6.: The systematic table for the cut & count experiment after the p-value cut and $p_T^{Wt} < 35\,\mathrm{GeV}$ consecutive cut are shown in the three-jet bin for the muon selection channel. The effects due to the jet reconstruction efficiency, the jet energy smearing and the muon unscaling are one-sided only, and their impact is therefore symmetrised.

3 Jet Bin, Electron and Muon Channel Combination

Systematic	$\delta\sigma_{t\text{-channel}}$ Up[%]	Down[%]	Bias[%]
Data Statistics	16.59	-16.59	0
Luminosity	10.83	-10.83	5
MC Statistics	1.94	-1.92	0.28
QCD Normalization	4.88	-4.88	0.31
Ratio W+LF/W+HF	3.06	-3.06	7
Ratio W+c/(W+c$\bar{\text{c}}$+W+b$\bar{\text{b}}$)	7.88	-7.85	0.69
Background Cross Sections	46.50	-46.50	-0.23
Matrix Element Generator (Wt-channel)	3.21	-3.21	-0.18
Matrix Element Generator t$\bar{\text{t}}$	16.99	-16.99	0.23
Parton Shower Generator t$\bar{\text{t}}$	19.87	-19.87	-0.51
PDFs	32.38	-32.38	-0.52
ISR/FSR	62.05	-62.05	-0.37
Lepton Reconstruction Efficiency	10.79	-10.79	3
Electron Energy Resolution	1.56	-1.56	8
Electron Energy Scale	2.08	-2.12	-0.40
Muon p_{t} Scale	1.18	-1.18	-0.10
Muon p_{t} Resolution (MS)	1.30	-1.27	0.29
Muon p_{t} Resolution (ID)	2.24	-2.24	0.21
Jet Reconstruction Efficiency	0.68	-0.65	0.23
Jet Energy Scale	3.23	-3.38	-1.02
Jet Energy Resolution	23.64	-23.67	-1.27
Mistagging Efficiency	3.07	-3.07	2
C-Tagging Efficiency	7.98	-7.98	0.28
B-Tagging Efficiency	19.21	-19.21	-0.36
JVF	4.37	-4.38	-0.31
$E_{\text{T}}^{\text{miss}}$ Pile-Up	12.89	-12.89	-0.38
$E_{\text{T}}^{\text{miss}}$ CellOut+SoftJet	19.92	-19.98	-1.60
Total(sys)	98.18	-98.35	-5.83
Total(sys+stat)	99.57	-99.74	-5.83

Table 7.7.: The systematic table for the cut & count experiment after the p-value cut and $p_T^{Wt} < 35\,\text{GeV}$ consecutive cut are shown in the three-jet bin for the lepton combination. The effects due to the jet reconstruction efficiency, the jet energy smearing and the muon unscaling are one-sided only, and their impact is therefore symmetrised.

7.3. Further Developments

Analysis Improvement

The difficulties met by the analysis at hand are common to all the current attempts made at the measurement of the Wt production cross section in the lepton+jets channel, since in spite of all the different tools that they developed, none of them managed to construct a classifier able to effectively reject the $t\bar{t}$ background component. As a result, the similarities with the $t\bar{t}$ background are such that the uncertainties associated to it, together with the common reconstruction systematics, affect the clear identification of the Wt signal in a seemingly incurable manner – at the current stage of the reconstruction and modelling performances. A new attempt is currently under study, where the NeuroBayes neural network classifier [FKK+11] is used, after the positive results obtained in the case of various t-channel analyses [A+12h, A+12g]. In the light of the analysis performed in this work, it is clear that the kinematic fit developed by this and other analyses of single top quark channel constitutes a valid tool to help identifying the Wt events. For this reason, it would be a natural option – already taken into account during the time of this work – to append the p-value of the signal hypothesis as an additional and independent discriminant input to a multivariate analysis, to combine its separation power with the one of other observables. Since a further advantage of the kinematic fit is the possibility to unambiguously reconstruct the longitudinal component of the neutrino momentum, the full four-momentum of the top quark can be in principle reconstructed. Even if this can be actually performed only in 50% of the events, when the W boson from the decay of the single top quark decays leptonically. Once the event is reconstructed and re-fitted in its entirety also on the longitudinal plane, the fit-corrected observables can be used as input to multivariate schemes.

Furthermore, attempts are currently being developed at ATLAS with very promising initial results, exploiting the matrix element method, which has been applied by the Tevatron experiments for the measurement of the single top production cross section, and allowed a precise measurement of the top quark mass measurement from single top event, with a relative uncertainty lower than 0.9 % [A+11i]. Another option to be investigated is the profiling of the most important sources of uncertainty, that would result in constraining *in situ* some of the systematic errors.

Measurement Combinations at 7 TeV

The cross section of the Wt associated production has been measured by ATLAS using $2.05\,\mathrm{fb}^{-1}$ of collision data by requiring two leptons in the final state, a selection which allows a significant drop of the total uncertainty, enough to determine the signal evidence at $3.3\,\sigma$ level. Combinations of this result with the analysis performed on the single lepton channel can in principle be performed, with the purpose of producing one single measurement result which combines all the efforts done on the hunt for the Wt signal events at ATLAS,

characterised by the smallest possible total uncertainty. In this respect, a positive aspect is given by the fact the a better statistical precision can be reached, since the samples selected by the dilepton and lepton+jets analyses are built to be orthogonal. On the other hand, many of the sources of systematic uncertainties are expected to be correlated between the channels, and it is not necessarily true that the combination would lead to an improvement in terms of the total uncertainty, which might turn out to increase affecting the final significance. The potential of a combination of the cross section measurement in the two channels is currently being evaluated, by means of the *best linear unbiased estimate* (BLUE) method which has been successfully used to combine the t-channel analyses results [A$^+$11c].

Measurement at 8 TeV

The kinematic fit analysis of collisions data at the centre-of-mass energy of 8 TeV collected by ATLAS in 2012 has not been performed yet and is therefore not part of this thesis.

As shown by the results of this work, the analyses of top physics events are fully dominated by the uncertainties on the hadronic radiation models (I/FSR, Parton Shower) and on the procedures adopted for the scale calibration and the resolution of the jet energy. Following the experience with the 7 TeV data, several improvements were put into place. In this respect, triggered by the higher pile-up rate conditions, refined calibrations schemes have been adopted. These new calibrations are based on local calorimeter clusters, and appear to possess the potential to further reduce the jet-related uncertainties and therefore improve, partially, the precision of the Wt production cross section measurement. Also, promising results showing an improvement of the I/FSR model uncertainty have been obtained from the latest tunings of the $\mathrm{t\bar{t}}$ generator in use for the 8 TeV analyses. Thirdly, with respect to the 2011 data at 7 TeV, several improvements have been obtained by the LHC in terms of luminosity and beam stability.

The larger data available and the improved understanding of the systematics allow the analyses performed by ATLAS and CMS, using 20.3 and 12.2 fb^{-1} of collision data, to register an excess of events consistent with the signal hypothesis in the dilepton channel. These measurements [A$^+$13b, C$^+$14c], later combined in [Top14a], show a significance corresponding to to 4.2 and 6.1 standard deviations above a background-only hypothesis, respectively, thus consenting to identify the signal with a certainty sufficient for the claim of a discovery (*cf.* Sec. 7.2.3).

Prospects of Top Physics Measurements at 13/14 TeV (2015)

In the year 2015 the physics programme of the LHC will restart after that the accelerator and all the experiments have been upgraded. Proton beams with a initial energy of 6.5 TeV will collide at an expected instantaneous luminosity of about $2\,10^{34}\,\mathrm{cm}^{-2}\mathrm{s}^{-1}$, thus opening a breach to access a promising era of further precision measurements and potential discoveries of new phenomena. The analysis scenario for the so called “Phase 1” operations is manifold.

While the same standard issues are expected to affect the precise measurement of physics observables related to the production of single top quarks after the energy upgrade, it is clear that the trigger model based on the single lepton that has been so far in use for the analysis top physics will no longer stand. In fact, while a lower pile-up is expected with the planned bunch spacing of 25 ns, the high luminosity will sensibly increase the trigger rates of physics events, leading to the necessity to prescale the simplest triggers in favour of more complex ones. For this reason, trigger algorithms that make use of multiple reconstructed objects are being developed. The impact of the trigger selection model is in fact different for the top physics branches. For the analysis of $t\bar{t}$ production, the use of dilepton and combined triggers with acceptable rates can be used, thus keeping both the lepton+jets and the dilepton channel in the physics menu. On the other hand, in spite of the raise of the cross section values for all the production mechanisms of single top quarks (*cf.* Fig. 2.6), no easy solution is foreseen for the analysis of events where one single lepton and a low jet multiplicity is expected, which is the case of single top final states searches. For such analyses, a new trigger model needs to be developed, based on a partial physics reconstruction already at the LVL1. The current studies in this sense aim in the direction of dedicated LVL1 topological triggers exploiting the lepton+jets signatures in combination with angular differences in the transverse plane between the lepton and the missing energy, which is a type of selection which, might be able to produce a significant sample of single top quark events. On a different level of the discussion, the option of a whole new LVL4 trigger layer collecting RAW data to be stored, reprocessed and analysed at a later stage is under investigation.

8. Summary and Conclusion

In the first period of operation at a centre-of-mass energy of $\sqrt{s} = 7\,\text{TeV}$, the ATLAS experiment at CERN collected sufficient data from proton-proton collisions delivered by the LHC accelerator to perform statistically precise measurements of several parameters of the Standard Model. In this respect, an accurate knowledge of the production of single top quark through the electroweak interaction represents a building block for tests of the Standard Model. The measurement of the cross section for the production of a single top quark in association with a real W boson, commonly referred to as Wt channel, is presented in this thesis. A detailed understanding the top quark production modes allows to proceed to precision measurements of its properties. In this view, the Wt production provides an optimal framework to study the W-t-b vertex and the CKM matrix element involved. Also, the knowledge of Wt production is expected to help isolating the signal from charged Higgs bosons, to which the Wt events constitute one of the main backgrounds.

The entire dataset collected during the year 2011 by the ATLAS experiment has been used in the analysis, for a total amount of $4.7\,\text{fb}^{-1}$ of data recorded with optimal detector conditions. The analysis has been conducted in the "lepton+jets" search mode, limited to events containing three jets exclusively and exactly one highly energetic electron or muon.

A standard event selection developed and optimised in common with all the analyses that investigate the top quark within the ATLAS collaboration is applied. After the standard selection a weighting procedure is applied to the Monte Carlo simulated samples on an event basis. This is found necessary to account for the response to many of the selection cuts, which differs slightly between the real and the simulated data. After this procedure, a good agreement between the observed and predicted yields is obtained for all the kinematic distributions used for controlling the input to the specific analysis.

The signal has been selected implementing a χ^2-based kinematic fit procedure that is able to exploit the signature of Wt signal events by constraining the physical objects (single lepton, jets, missing transverse energy) to reconstruct the invariant mass of the top quark and the associate W boson present in the event, thus allowing to resolve univocally the longitudinal component of the neutrino momentum. To enrich the fraction of Wt signal events, two consecutive cuts are applied in the chosen search channels. In a first stance, events are discarded if the kinematic fit does not converge, and then rejected if the associated χ^2 probability is below 10%. Secondly, expecting that the top quark and the associated W boson reconstructed by the fit are the only particles populating the final state, the transverse momentum of their combined system is computed and events are removed from the final count if this quantity exceeds the value of 35 GeV.

The cross section has been extracted by means of a simple event counting procedure, using a maximum likelihood fit. For the combination of the electron and muon search channels in the three jet bin the final result yields a result characterised by a total systematic uncertainty of about 100 %, jeopardising the sensitivity of the analysis, which does not reach the significance necessary to reliably claim an observation and quote a central measurement. Following the CL_s method, a value of 32.51 pb (30.03 pb) is found as an observed (expected) upper limit on the cross section value for the Wt production at at 95 % C.L.. This is not an improvement with respect to the analyses conducted in parallel in the dileptonic channel, where the impact of the jet-related systematics and from the top pair production model is considerably lower, and a signal evidence above three standard deviations has been detected. The statistical uncertainty is not found to be the limiting factor to the cross section measurement, in agreement with all the single top analyses performed insofar at the LHC. Among the several sources of systematic uncertainties that can in principle degrade the measurement, the dominating are those that affect the energy scale and the reconstruction of jets, together with the correct modelling of the kinematics and the normalisation cross section of the top quark pair production component of the background.

Parallel results from the analyses published by the ATLAS and CMS collaborations of the other single top production modes support the conclusion that an improvement of the physics simulation models is needed, together with a better resolution of the physics object reconstruction, to allow for precision tests of the electroweak theory in the top quark sector to take place.

The kinematic fit developed for the analysis proves to be a robust method to isolate a wide class of events, and constitutes a valid alternative to all the tools currently available for the analysis of high energy physics events. Despite the fit performance, a major improvement is necessary to refine the analysis power and increase the rejection of the top pair background.

In fact, the intrinsic vicinity of the Wt and $\mathrm{t\bar{t}}$ final states makes it very hard to identify a phase space region where the fraction of signal events can dominate in the single lepton signature mode. This task is yet necessary, since the theoretical uncertainty on the top pair production rate amounts, roughly, to the predicted value of the Wt production cross section.

A. Performance and Pull Plots

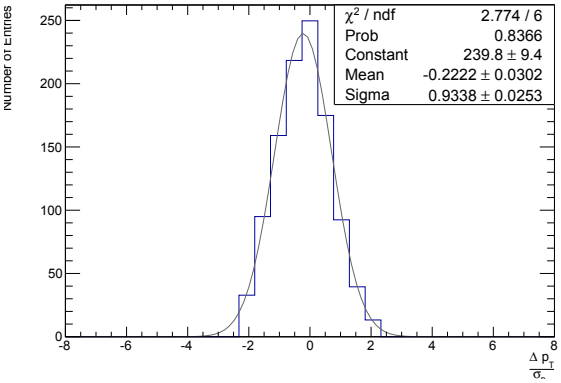

(a) Electron Transverse Momentum

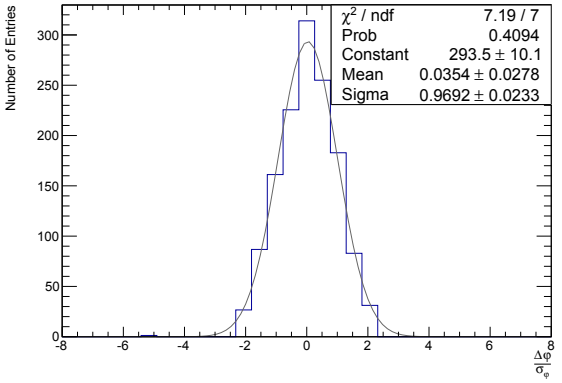

(b) Muon Transverse Momentum

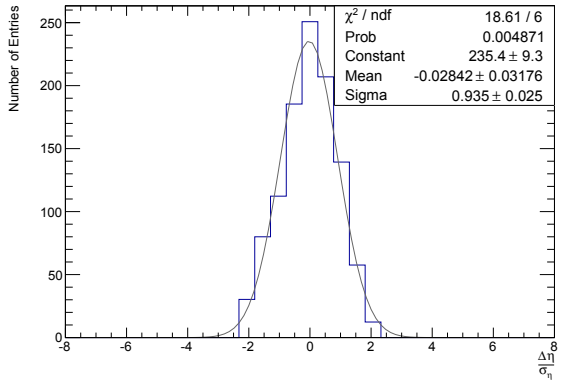

(c) Electron Pseudorapidity

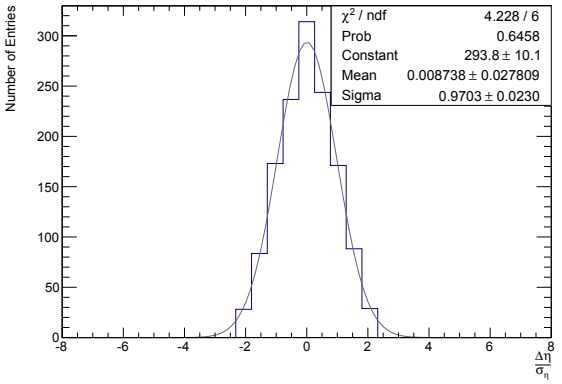

(d) Muon Pseudorapidity

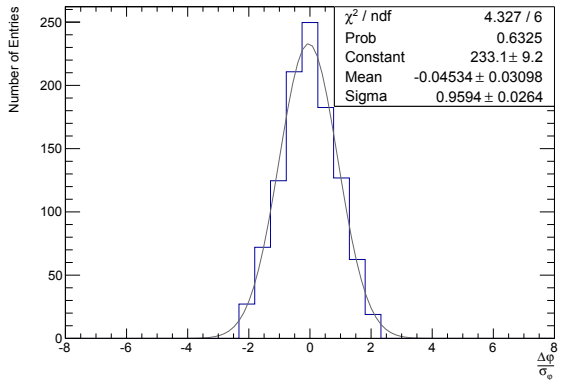

(e) Electron Azimuth

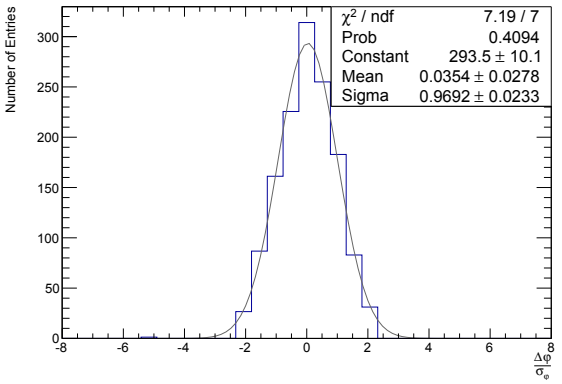

(f) Muon Azimuth

Figure A.1.: The plots show the pull distributions of the lepton kinematic variables after the leptonic top fit procedure described in Sec. 6.3. The Δ quantities at the numerator contain the (signed) variation between each kinematic component of the lepton entering the fit and its value after the correction obtained by the fit. The σ used at the denominator is exactly the uncertainty extracted from the track fit from the lepton reconstruction (*cf.* 3.5.2, 5.2.2).

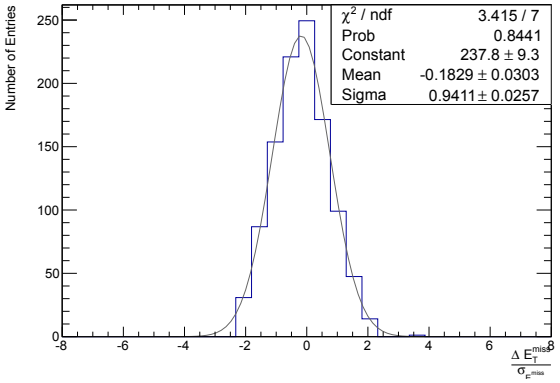

(a) Missing Transverse Energy (muon channel)

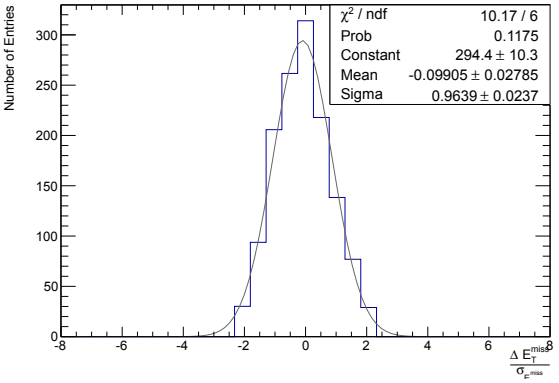

(b) Missing Transverse Energy (electron channel)

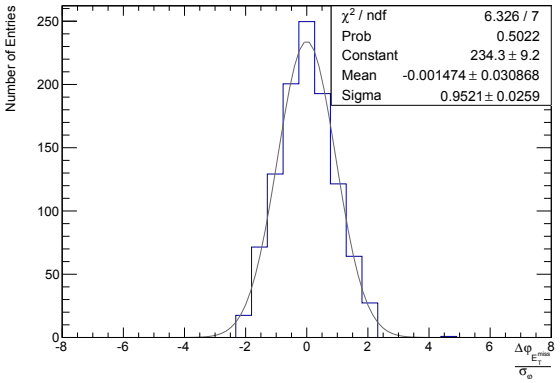

(e) Missing Energy Azimuth (muon channel)

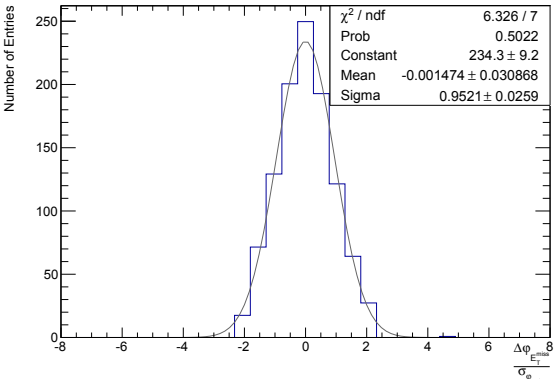

(f) Missing Energy Azimuth (electron channel)

Figure A.2.: The plots show the pull distributions of the lepton kinematic variables after the leptonic top fit procedure described in Sec. 6.3. The Δ quantities at the numerator contain the (signed) variation between each kinematic component of the missing energy entering the fit and its value after the correction obtained by the fit. The σ used at the denominator is exactly the uncertainty extracted from the covariance matrices plots in Fig. 5.5.

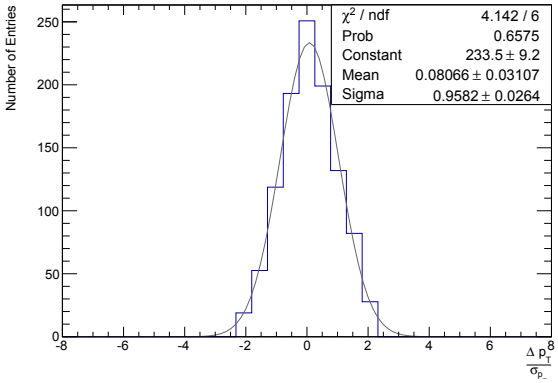

(a) b-Jet Transverse Momentum (electron channel)

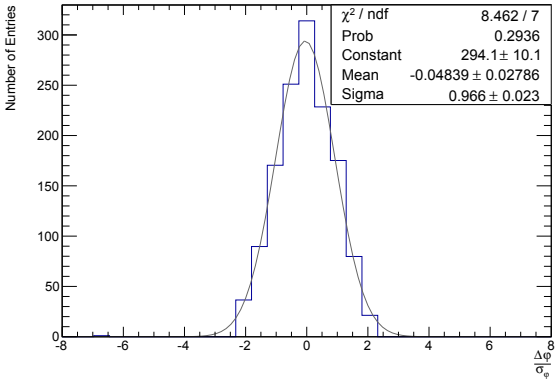

(b) b-Jet Transverse Momentum (muon channel)

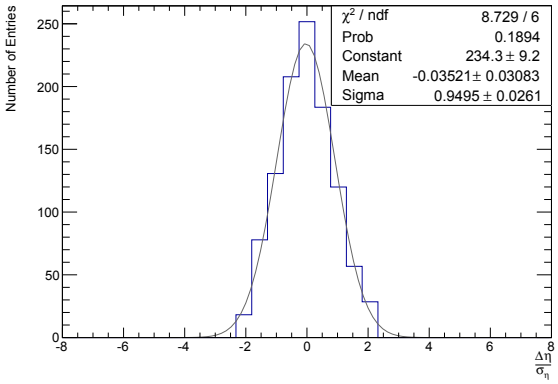

(c) b-Jet Pseudorapidity (electron channel)

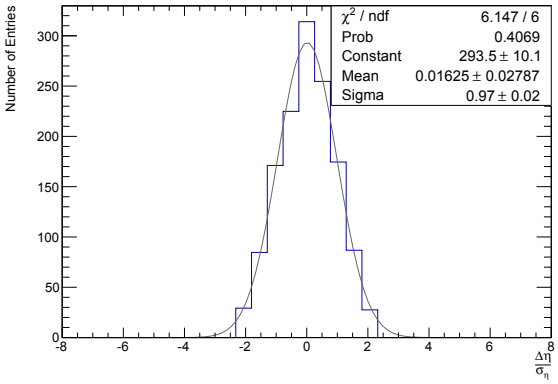

(d) b-Jet Pseudorapidity (muon channel)

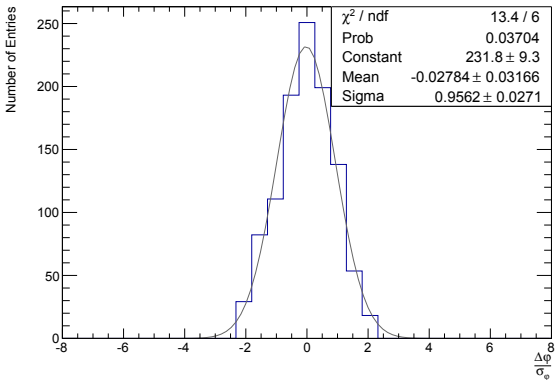

(e) b-Jet Azimuth (electron channel)

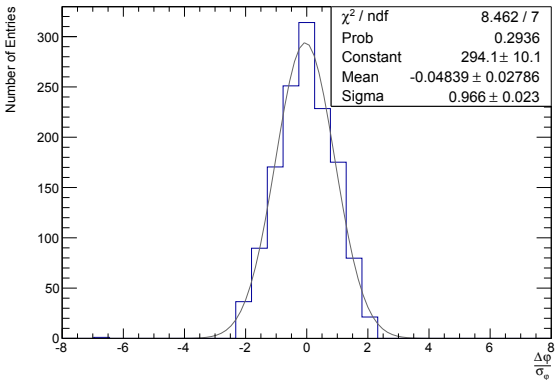

(f) b-Jet Azimuth (muon channel)

Figure A.3.: The plots show the pull distributions of the b-jet kinematic variables after the leptonic top fit procedure described in Sec. 6.3. The Δ quantities at the numerator contain the (signed) variation between each kinematic component of the jet entering the fit and its value after the correction obtained by the fit. The σ used at the denominator is exactly the uncertainty extracted from the covariance matrices plots in Fig. 5.4.

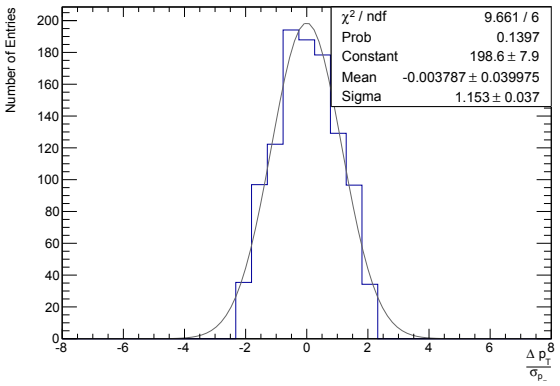

(a) 1st light-Jet Transverse Momentum (electron channel)

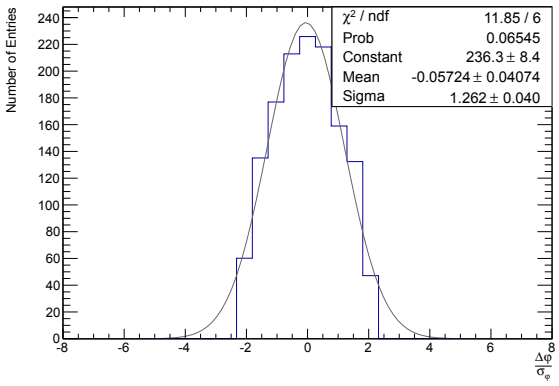

(b) 1st light-Jet Transverse Momentum (muon channel)

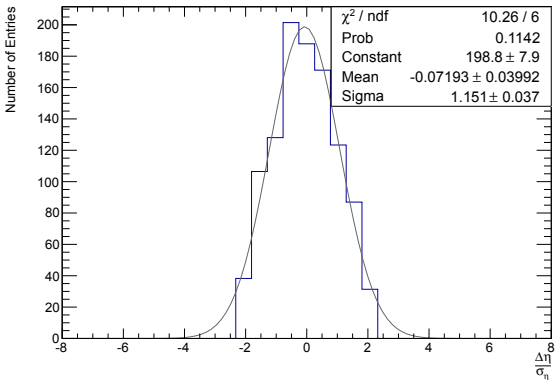

(c) 1st light-Jet Pseudorapidity (electron channel)

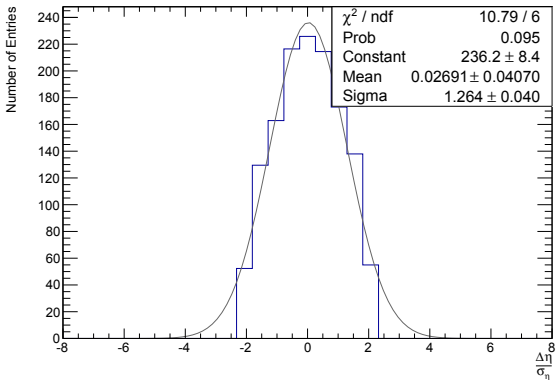

(d) 1st light-Jet Pseudorapidity (muon channel)

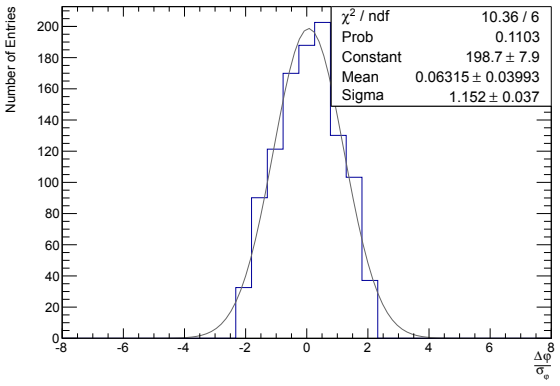

(e) 1st light-Jet Azimuth (electron channel)

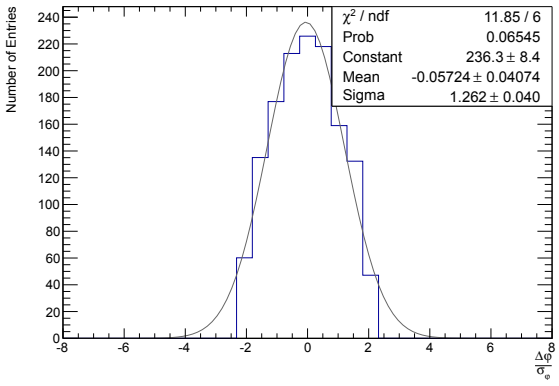

(f) 1st light-Jet Azimuth (muon channel)

Figure A.4.: The plots show the pull distributions of the first (p_t-ordered) light-flavoured jet kinematic variables after the hadronic fit of the associate W boson in the leptonic top fit procedure described in Sec. 6.3. The Δ quantities at the numerator contain the (signed) variation between each kinematic component of the jet entering the fit and its value after the correction obtained by the fit. The σ used at the denominator is exactly the uncertainty extracted from the covariance matrices plots in Fig. 5.4.

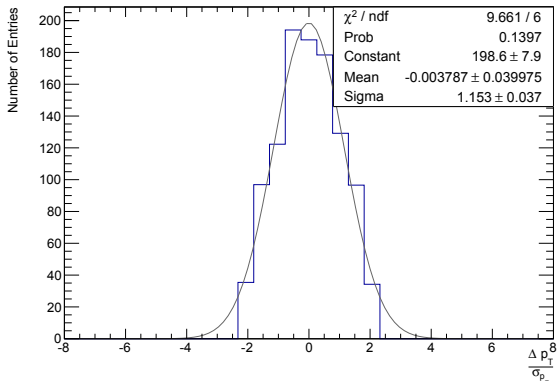

(a) 2nd light-Jet Transverse Momentum (electron channel)

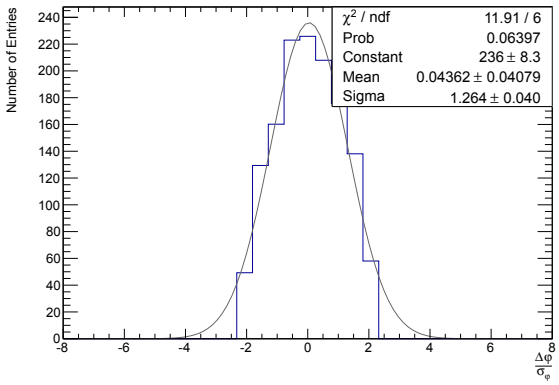

(b) 2nd light-Jet Transverse Momentum (muon channel)

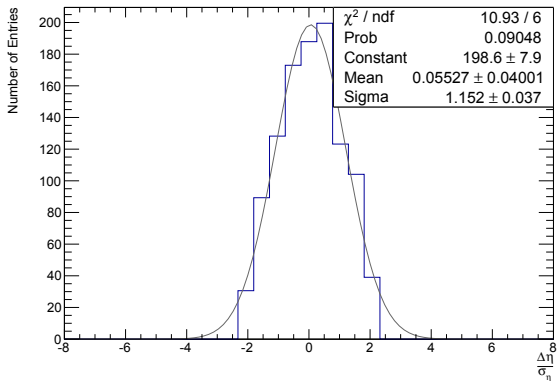

(c) 2nd light-Jet Pseudorapidity (electron channel)

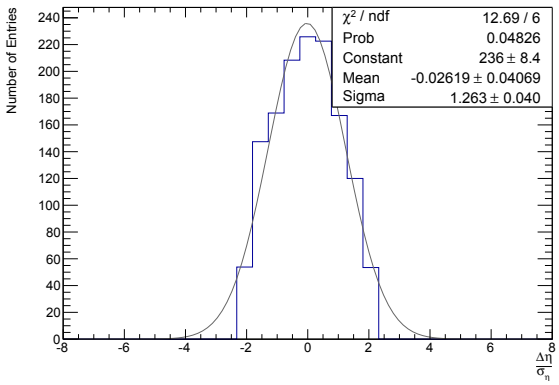

(d) 2nd light-Jet Pseudorapidity (muon channel)

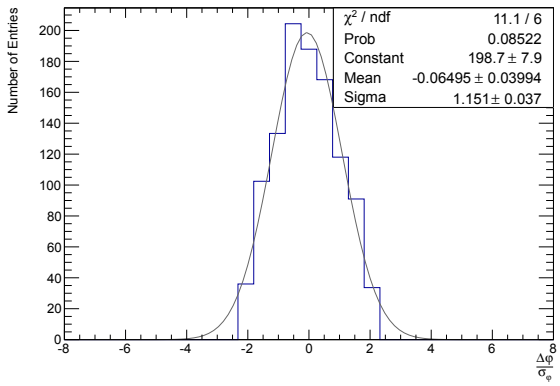

(e) 2nd light-Jet Azimuth (electron channel)

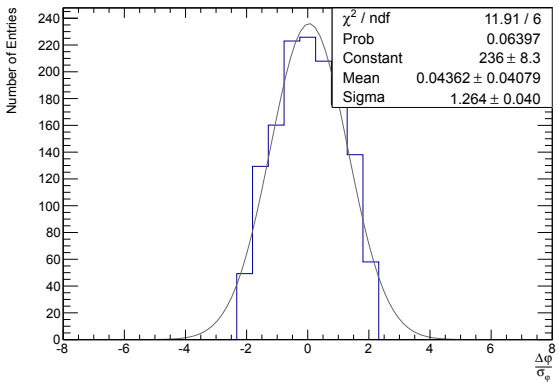

(f) 2nd light-Jet Azimuth (muon channel)

Figure A.5.: The plots show the pull distributions of the second (p_t-ordered) light-flavoured jet kinematic variables after the hadronic fit of the associate W boson in the leptonic top fit procedure described in Sec. 6.3. The Δ quantities at the numerator contain the (signed) variation between each kinematic component of the jet entering the fit and its value after the correction obtained by the fit. The σ used at the denominator is exactly the uncertainty extracted from the covariance matrices plots in Fig. 5.4.

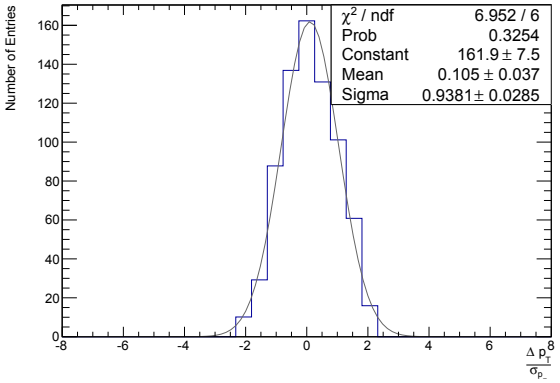

(a) b-Jet Transverse Momentum

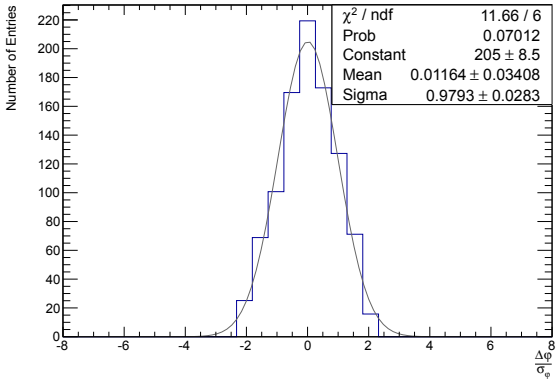

(b) b-Jet Transverse Momentum

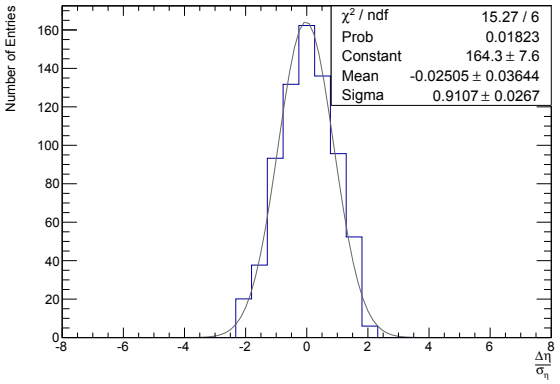

(c) b-Jet Pseudorapidity

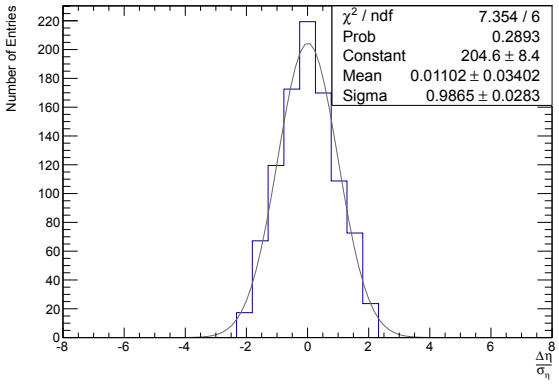

(d) b-Jet Pseudorapidity

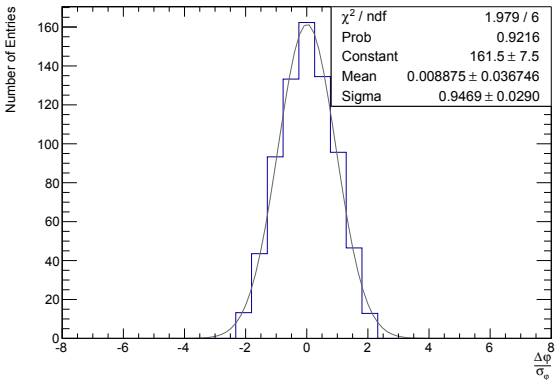

(e) b-Jet Azimuth

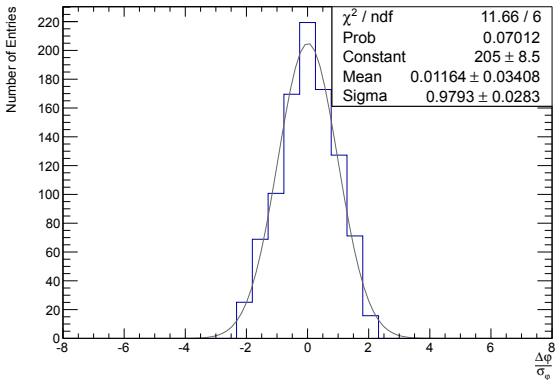

(f) b-Jet Azimuth

Figure A.6.: The plots show the pull distributions of the b-jet kinematic variables after the hadronic top fit procedure described in Sec. 6.4. The Δ quantities at the numerator contain the (signed) variation between each kinematic component of the jet entering the fit and its value after the correction obtained by the fit. The σ used at the denominator is exactly the uncertainty extracted from the covariance matrices plots in Fig. 5.4.

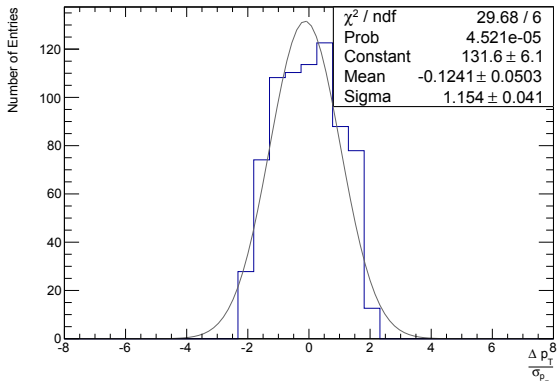

(a) 1st light-Jet Transverse Momentum

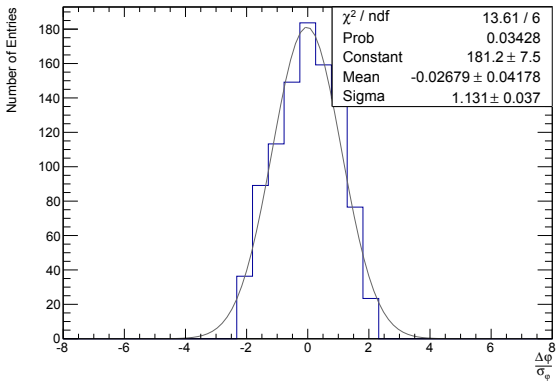

(b) 1st light-Jet Transverse Momentum

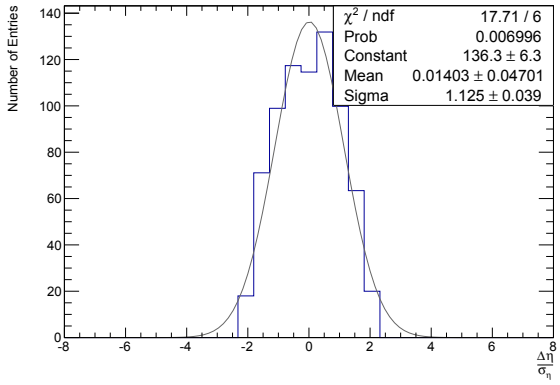

(c) 1st light-Jet Pseudorapidity

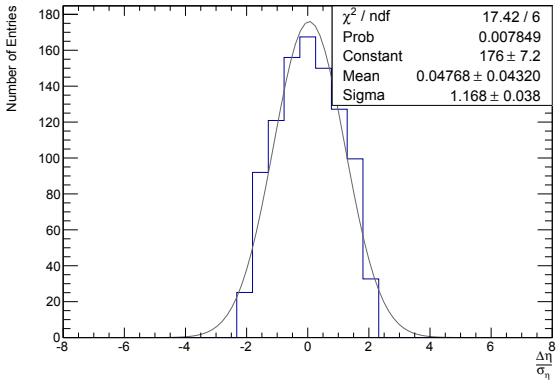

(d) 1st light-Jet Pseudorapidity

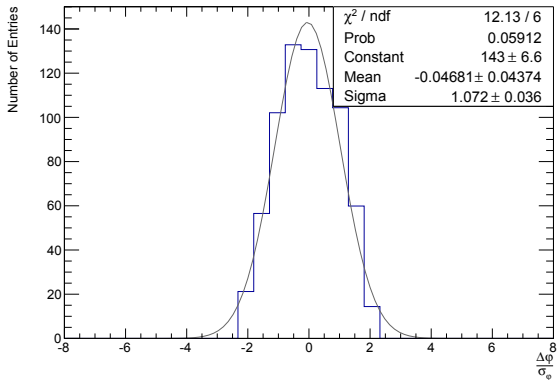

(e) 1st light-Jet Azimuth

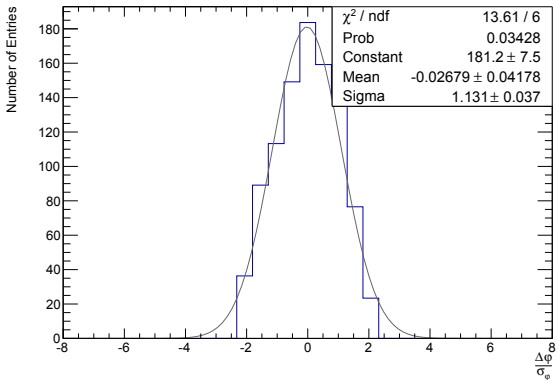

(f) 1st light-Jet Azimuth

Figure A.7.: The plots show the pull distributions of the first (p_t-ordered) light-flavoured jet kinematic variables after the hadronic fit of the W boson in the hadronic top fit procedure described in Sec. 6.4. The Δ quantities at the numerator contain the (signed) variation between each kinematic component of the jet entering the fit and its value after the correction obtained by the fit. The σ used at the denominator is exactly the uncertainty extracted from the covariance matrices plots in Fig. 5.4.

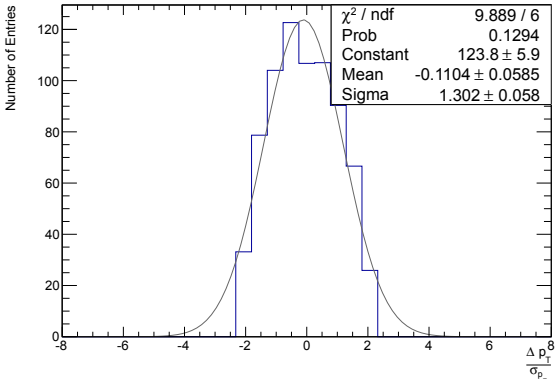

(a) 2nd light-Jet Transverse Momentum

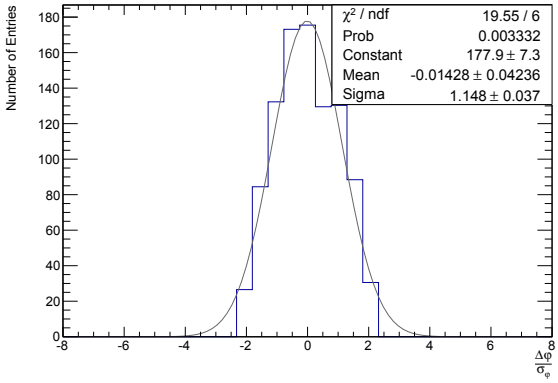

(b) 2nd light-Jet Transverse Momentum

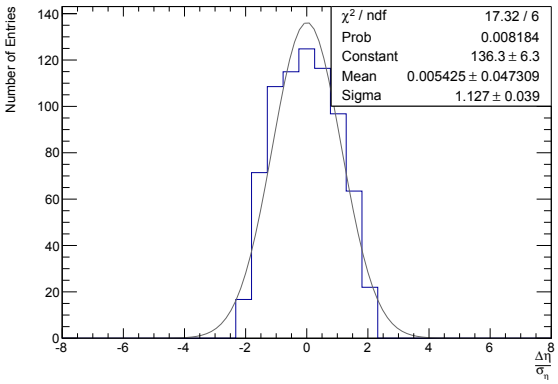

(c) 2nd light-Jet Pseudorapidity

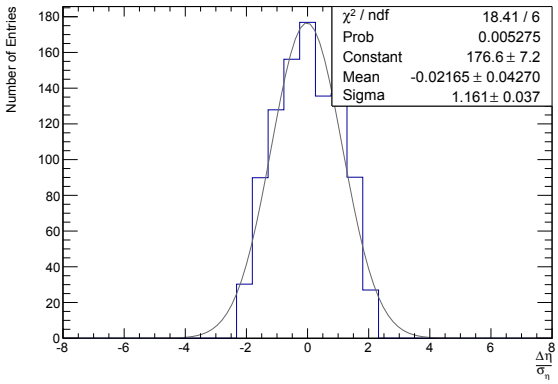

(d) 2nd light-Jet Pseudorapidity

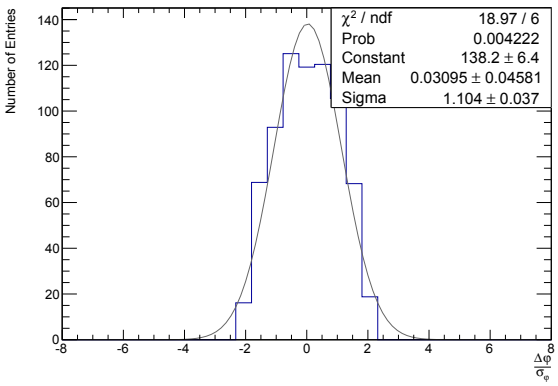

(e) 2nd light-Jet Azimuth

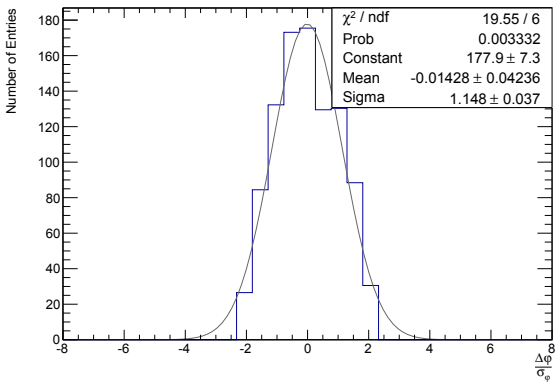

(f) 2nd light-Jet Azimuth

Figure A.8.: The plots show the pull distributions of the second (p_t-ordered) light-flavoured jet kinematic variables after the hadronic fit of the W boson in the hadronic top fit procedure described in Sec. 6.4. The Δ quantities at the numerator contain the (signed) variation between each kinematic component of the jet entering the fit and its value after the correction obtained by the fit. The σ used at the denominator is exactly the uncertainty extracted from the covariance matrices plots in Fig. 5.4.

B. Mass Plots in the Four Jet Bin

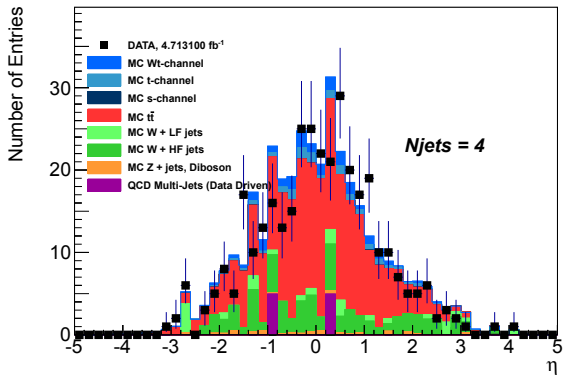

(a) Pseudorapidity of the Neutrino.

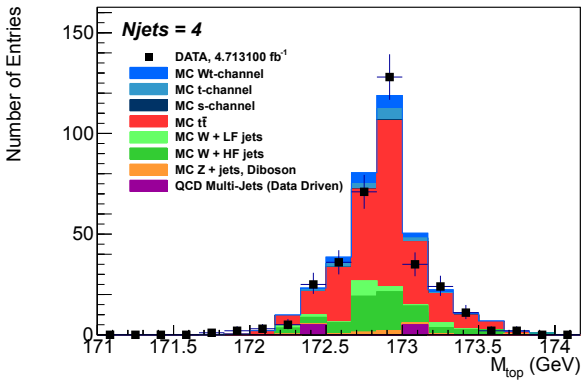

(b) Invariant Mass of the Top Quark.

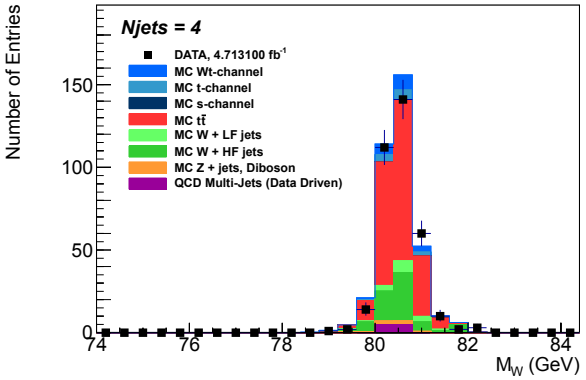

(c) Invariant Mass of the W Boson (from Top Quark Decay).

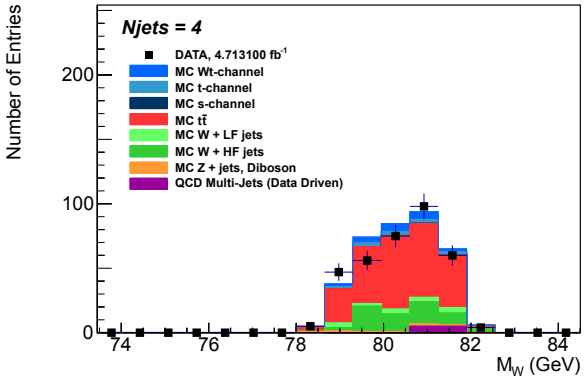

(d) Invariant mass of the W boson (Associate).

Figure B.1.: The plots represent, for the μ+4 jets channel, the distribution of the pseudorapidity of the neutrino (a) and of the invariant mass of the top quark (b), the leptonically decaying W boson (c) and the hadronically decaying associate W boson (d).

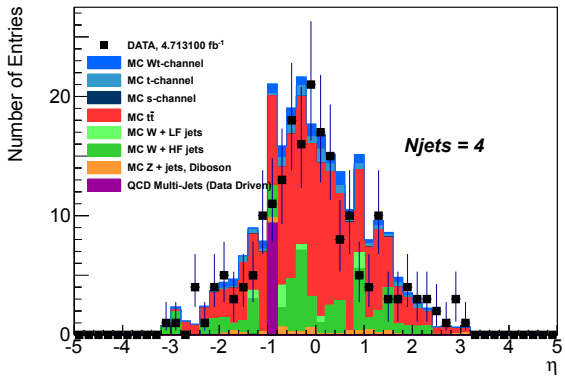

(a) Pseudorapidity of the Neutrino.

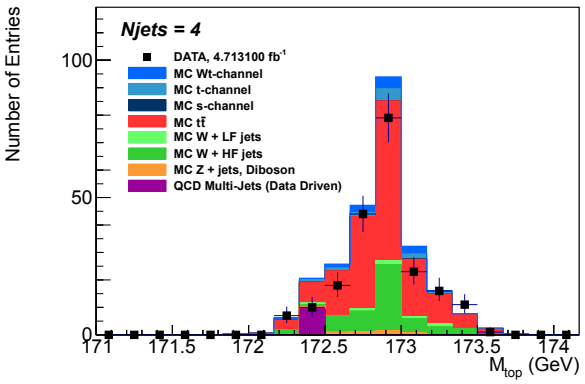

(b) Invariant Mass of the Top Quark.

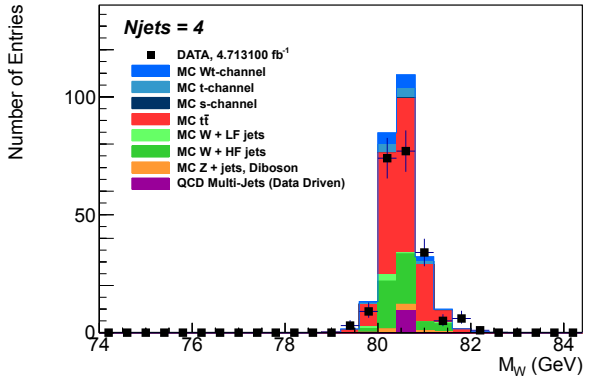

(c) Invariant Mass of the W Boson (from Top Quark Decay).

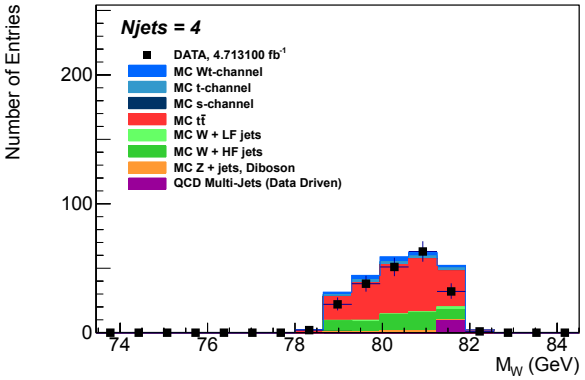

(d) Invariant Mass of the W Boson (Associate).

Figure B.2.: The plots represent, for the "leptonic top" case in the e+4 jets channel, the distribution of the pseudorapidity of the neutrino (a) and of the invariant mass of the top quark (b), the leptonically decaying W boson (c) and the hadronically decaying associate W boson (d).

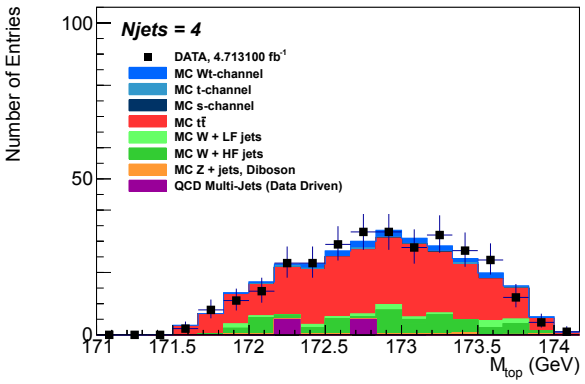

(a) Invariant Mass of the Top Quark.

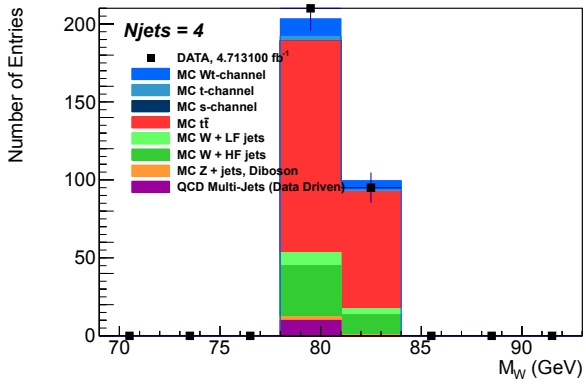

(b) Invariant Mass of the W Boson (hadronic).

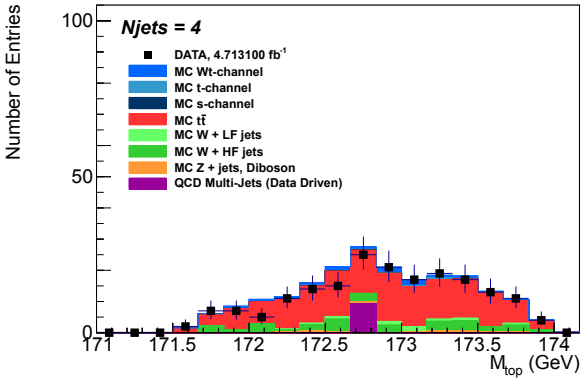

(c) Invariant Mass of the Top Quark.

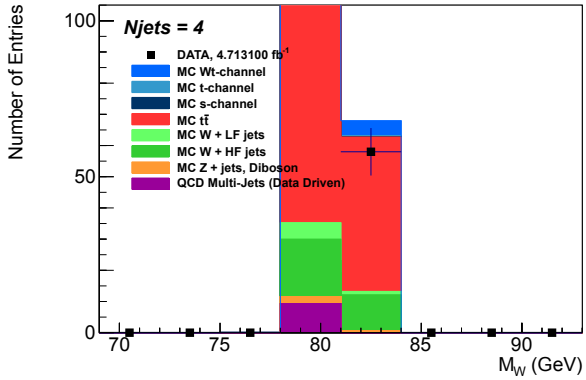

(d) Invariant Mass of the W Boson (hadronic).

Figure B.3.: The plots represent the invariant masses reconstructed by the fit for the "hadronic top" hypothesis in the electron channel. The distribution of the invariant masses of the top quark ((a), (c)) and the hadronically decaying W boson originated from the top quark ((b),(d)) are shown for the analysis of the three and four jet bin.

Bibliography

[A+83] Arnison, G.; et al.: Experimental observation of isolated large transverse energy electrons with associated missing energy at s=540 gev. In: *Physics Letters B*, volume 122(1):pp. 103 – 116, 1983.

[A+03a] Aad, Georges; et al. (ATLAS Collaboration): A Muon Identification and Combined Reconstruction Procedure for the ATLAS Detector at the LHC at CERN. Technical report, CERN, Oct 2003.

[A+03b] Agostinelli, S.; et al. (GEANT4 Collaboration): GEANT4: A Simulation toolkit. In: *Nucl.Instrum.Meth.*, volume A506:pp. 250–303, 2003.

[A+05] Aad, Georges; et al. (ATLAS Collaboration): *Atlas Computing: Technical Design Report*. CERN, Geneva, 2005.

[A+07a] Aad, Georges; et al. (ATLAS Collaboration): Concepts, Design and Implementation of the ATLAS New Tracking (NEWT). Technical Report ATL-SOFT-PUB-2007-007. ATL-COM-SOFT-2007-002, CERN, Geneva, Mar 2007.

[A+07b] Alwall, J.; et al.: Is Vtb=1 ? In: *Eur.Phys.J.*, volume C49:pp. 791–801, 2007.

[A+08] Aad, Georges; et al. (ATLAS Collaboration): The ATLAS Experiment at the CERN Large Hadron Collider. In: *Journal of Instrumentation*, volume 3(08):p. S08003, 2008.

[A+09a] Aad, Georges; et al. (ATLAS Collaboration): Pile-up jet energy scale corrections using the jet-vertex fraction method. Technical Report ATL-COM-PHYS-2009-180, CERN, Geneva, Apr 2009.

[A+09b] Aaltonen, T.; et al. (CDF Collaboration): First Observation of Electroweak Single Top Quark Production. In: *Phys.Rev.Lett.*, volume 103, 2009.

[A+09c] Abazov, V. M.; et al. (D0 Collaboration): Observation of Single Top Quark Production. In: *Phys.Rev.Lett.*, volume 103, 2009.

[A+09d] Antcheva, I.; et al.: ROOT – A C++ framework for petabyte data storage, statistical analysis and visualization. In: *Computer Physics Communications*, volume 180(12):pp. 2499 – 2512, 2009.

[A+10a] Aad, Georges; et al. (ATLAS Collaboration): ATLAS Top Quark Working Group PDF Uncertainty Twiki Page. Technical report, CERN, 2010.

[A+10b] Aad, Georges; et al. (ATLAS Collaboration): Estimation of the W+Jets Background for Top Quark Re-Discovery in the Single Lepton+Jets Channel. Technical Report ATL-COM-PHYS-2010-834, CERN, Geneva, Oct 2010. Supporting document for top paper.

[A+10c] Aad, Georges; et al. (ATLAS Collaboration): Missing Transverse Energy for Top Physics analyses with early ATLAS data at $\sqrt{s}$=7 TeV. Technical Report ATL-COM-PHYS-2010-821, CERN, Geneva, Oct 2010.

[A+10d] Aad, Georges; et al. (ATLAS Collaboration): Monte Carlo samples used for top physics. Technical Report ATL-PHYS-INT-2010-132, CERN, Geneva, Dec 2010.

[A+10e] Aad, Georges; et al. (ATLAS Collaboration): Performance of primary vertex reconstruction in proton-proton collisions at $\sqrt{s}$ =7 TeV in the ATLAS experiment. Technical Report ATLAS-CONF-2010-069, CERN, Geneva, Jul 2010.

[A+10f] Aad, Georges; et al. (ATLAS Collaboration): Single Boson and Diboson Production Cross Sections in Collisions at sqrts=7 TeV. Technical Report ATL-COM-PHYS-2010-695, CERN, Geneva, Aug 2010.

[A+11a] Aad, Georges; et al. (ATLAS Collaboration): ATLAS Muon Combined Performance Guidelines for Analyses of 2011 Data in Release 17. Technical report, CERN, 2011.

[A+11b] Aad, Georges; et al. (ATLAS Collaboration): ATLAS tunes of PYTHIA 6 and Pythia 8 for MC11. Technical Report ATL-PHYS-PUB-2011-009, CERN, Geneva, Jul 2011.

[A+11c] Aad, Georges; et al. (ATLAS Collaboration): Combination of t-Channel Single Top-Quark Production Cross-section Measurements Using the BLUE Method. Technical Report ATL-COM-PHYS-2011-1407, CERN, Geneva, Oct 2011.

[A+11d] Aad, Georges; et al. (ATLAS Collaboration): Commissioning of the ATLAS high-performance b-tagging algorithms in the 7 TeV collision data. Technical Report ATLAS-COM-CONF-2011-110, CERN, Geneva, Jun 2011.

[A+11e] Aad, Georges; et al. (ATLAS Collaboration): Pile-up Reweighting Tool Twiki Page. Technical report, CERN, 2011.

[A+11f] Aad, Georges; et al. (ATLAS Collaboration): Search for s-Channel Single Top-Quark Production in pp Collisions at $\sqrt{s}$ = 7 TeV. Technical Report ATLAS-CONF-2011-118, CERN, Geneva, Aug 2011.

[A+11g] Aaltonen, T.; et al. (CDF Collaboration): Measurement of Single Top Quark Production in 7.5 fb^{-1} of CDF Data Using Neural Network. Technical Report CDF/PUB/TOP/PUBLIC/10793, Tevatron, Apr 2011.

[A+11h] Abazov, V. M.; et al. (The D0 Collaboration): Measurements of single top quark production cross sections and $|V_{tb}|$ in $p\overline{p}$ collisions at $\sqrt{s} = 1.96$ TeV. In: *Phys. Rev. D*, volume 84:p. 112001, Dec 2011.

[A+11i] Abazov, Victor Mukhamedovich; et al. (D0 Collaboration): Precise measurement of the top-quark mass from lepton+jets events at D0. In: *Phys.Rev.*, volume D84:p. 032004, 2011.

[A+12a] Aad, Georges; et al. (ATLAS Collaboration): B-jet tagging calibration on c-jets containing D^{*+} mesons. Technical Report ATLAS-CONF-2012-039, CERN, Geneva, Mar 2012.

[A+12b] Aad, Georges; et al.: Electron performances measurements using the 2011 LHC proton-proton collisions. Technical Report ATL-COM-PHYS-2012-1024, CERN, Geneva, Jul 2012.

[A+12c] Aad, Georges; et al. (ATLAS Collaboration): Evidence for the associated production of a W boson and a top quark in ATLAS at 7 $\sqrt{s} = 7$ TeV. In: *Physics Letters B*, volume 716(1):pp. 142 – 159, 2012.

[A+12d] Aad, Georges; et al. (ATLAS Collaboration): Improved Luminosity Determination in pp Collisions at $\sqrt{s} = 7$ TeV using the ATLAS Detector at the LHC. In: *ATLAS-COM-CONF-2012-180*, 2012.

[A+12e] Aad, Georges; et al. (ATLAS Collaboration): Jet energy scale and its systematic uncertainty in proton-proton collisions at $\sqrt{s}$=7 TeV with ATLAS 2011 data. Technical Report ATLAS-COM-CONF-2012-171, CERN, Geneva, Aug 2012.

[A+12f] Aad, Georges; et al. (ATLAS Collaboration): Measurement of inclusive jet and dijet production in pp collisions at $\sqrt{s} = 7$ TeV using the ATLAS detector. In: *Phys. Rev.*, volume D86:p. 014022, 2012.

[A+12g] Aad, Georges; et al. (ATLAS Collaboration): Measurement of the t-channel single top-quark and top-antiquark production cross-sections and their ratio in pp collisions at $\sqrt{s} = 7$ TeV. Technical Report ATLAS-COM-CONF-2012-028, CERN, Geneva, Feb 2012.

[A+12h] Aad, Georges; et al. (ATLAS Collaboration): Measurement of the t-channel single top-quark production cross section in pp collisions at $\sqrt{s} = 7$ TeV with the ATLAS detector. In: *Phys.Lett.*, volume B717:pp. 330–350, 2012.

[A+12i] Aad, Georges; et al. (ATLAS Collaboration): Measurement of the top quark mass with the template method in the $t\bar{t} \rightarrow$ lepton+jets channel using ATLAS data. In: *The European Physical Journal C - Particles and Fields*, volume 72:pp. 1–30, 2012.

[A+12j] Aad, Georges; et al. (ATLAS Collaboration): Measurement of the W boson polarization in top quark decays with the ATLAS detector. In: *Journal of High Energy Physics*, volume 2012, 2012.

[A+12k] Aad, Georges; et al. (ATLAS Collaboration): Object selection and calibration, background estimations and MC samples for the Autumn 2012 Top Quark analyses with 2011 data. Technical Report ATL-COM-PHYS-2012-1197, CERN, Geneva, Aug 2012.

[A+12l] Aad, Georges; et al. (ATLAS Collaboration): Object selection and calibration, background estimations and MC samples for the Winter 2012 Top Quark analyses with 2011 data. Technical Report ATL-COM-PHYS-2012-224, CERN, Geneva, Feb 2012.

[A+12m] Aad, Georges; et al. (ATLAS Collaboration): Performance of Missing Transverse Momentum Reconstruction in Proton-Proton Collisions at 7 TeV with ATLAS. In: *Eur.Phys.J.*, volume C72:p. 1844, 2012.

[A+12n] Aad, Georges; et al. (ATLAS Collaboration): Performance of the ATLAS Inner Detector Track and Vertex Reconstruction in the High Pile-Up LHC Environment. Technical Report ATLAS-CONF-2012-042, CERN, Geneva, Mar 2012.

[A+12o] Aad, Georges; et al. (ATLAS Collaboration): Practical implementation of the PDF4LHC recipe. Technical report, CERN, 2012.

[A+12p] Aad, Georges; et al. (ATLAS Collaboration): Selection of jets produced in proton-proton collisions with the ATLAS detector using 2011 data. Technical Report ATLAS-CONF-2012-020, CERN, Geneva, Mar 2012.

[A+12q] Aad, Georges; et al. (ATLAS Collaboration): Supporting document on electron performance measurements using the 2011 LHC proton-proton collisions. Technical Report ATL-COM-PHYS-2012-1023, CERN, Geneva, Jul 2012.

[A+13a] Aad, Georges; et al. (ATLAS Collaboration): Combined coupling measurements of the Higgs-like boson with the ATLAS detector using up to 25 fb^{-1} of proton-proton collision data. In: , 2013.

[A+13b] Aad, Georges; et al.: Measurement of the cross-section for associated production of a top quark and a W boson at $\sqrt{s} = 8$ TeV with the ATLAS detector. Technical Report ATLAS-CONF-2013-100, CERN, Geneva, Sep 2013.

[A+13c] Aad, Georges; et al. (ATLAS): Measurement of the top quark charge in pp collisions at $\sqrt{s} = 7$ TeV with the ATLAS detector. In: *JHEP*, volume 11:p. 031, 2013.

[A+13d] Aad, Georges; et al. (ATLAS Collaboration): Study of the spin of the Higgs-like boson in the two photon decay channel using 20.7 fb-1 of pp collisions collected at $\sqrt{s} = 8$ TeV with the ATLAS detector. In: , 2013.

[A+14a] Aad, Georges; et al. (ATLAS Collaboration): Comprehensive measurements of t-channel single top-quark production cross sections at $\sqrt{s} = 7$ TeV with the atlas detector. In: *Phys. Rev. D*, volume 90:p. 112006, Dec 2014.

[A+14b] Aad, Georges; et al.: Measurement of the Inclusive and Fiducial Cross-Section of Single Top-Quark t-Channel Events in pp Collisions at $\sqrt{s} = 8$ TeV. Technical Report ATLAS-CONF-2014-007, CERN, Geneva, Mar 2014.

[A+14c] Aad, Georges; et al. (ATLAS Collaboration): Search for s-channel single top-quark production in proton - proton collisions at $\sqrt{s} = 8$ TeV with the ATLAS detector. In: *Phys.Lett.*, volume B740:pp. 118–136, 2014.

[A+16] Aad, Georges; et al.: Measurement of the production cross-section of a single top quark in association with a w boson at 8 tev with the atlas experiment. In: *Journal of High Energy Physics*, volume 2016(1):p. 64, 2016.

[ALL+11] Aliev, M.; Lacker, H.; Langenfeld, U.; Moch, S.; Uwer, P.; et al.: HATHOR: HAdronic Top and Heavy quarks crOss section calculatoR. In: *Comput.Phys.Commun.*, volume 182:pp. 1034–1046, 2011.

[ATL10] ATLAS Collaboration: Jet energy resolution and selection efficiency relative to track jets from in-situ techniques with the atlas detector using proton-proton collisions at a center of mass energy $\sqrt{s} = 7$ tev. Conference Note ATLAS-CONF-2010-054, CERN, Geneva, 7 2010.

[ATL12] ATLAS Collaboration (ATLAS Collaboration): Observation of a new particle in the search for the Standard Model Higgs boson with the ATLAS detector at the LHC. In: *Phys.Lett.*, volume B716:pp. 1–29, 2012. 1207.7214.

[B+83] Banner, M.; et al.: Observation of single isolated electrons of high transverse momentum in events with missing transverse energy at the cern pp collider. In: *Physics Letters B*, volume 122(5 - 6):pp. 476 – 485, 1983.

[BBG+11] Buckley, Andy; Butterworth, Jonathan; Gieseke, Stefan; Grellscheid, David; Hoche, Stefan; et al.: General-purpose event generators for LHC physics. In: *Phys. Rept.*, volume 504:pp. 145–233, 2011.

[BBG+12] Beumler, S; Bilski, S; Giorgi, FM; Heinrich, L; Herrberg, R; Kendziorra, C; Kind, OM; Kintscher, T; Prosperi Porta, U; Rieck, P; Schade, AS; Thomas, F: Kinematic Fitting of ATLAS Data Using the KinFitter Package. Technical report, CERN, Geneva, Oct 2012.

[BCC13] Boudreau, Joseph; CDF, ATLAS CMS; Collaborations, D0: Instrumental backgrounds to $t\bar{t}$ and single top production at hadron colliders. In: *Journal of Physics: Conference Series*, volume 452(1):p. 012013, 2013.

[BEM+00] Beneke, M.; Efthymiopoulos, I.; Mangano, Michelangelo L.; Womersley, J.; Ahmadov, A.; et al.: Top quark physics. In: *Report of the "1999 CERN Workshop on SM physics (and more) at the LHC"*, 2000.

[BFS96] Butterworth, J.M.; Forshaw, Jeffrey R.; Seymour, M.H.: Multiparton interactions in photoproduction at HERA. In: *Z.Phys.*, volume C72:pp. 637–646, 1996.

[Bil12] Bilski, S.: Studien zur elektroschwachen Produktion von Top-Quarks in Proton-Proton-Stößen bei ATLAS, 2012. Masterarbeit, Humboldt-Universität zu Berlin.

[BL98] Blobel, V.; Lohrmann, E.: *Statistische und numerische Methoden der Datenanalyse*. Teubner Verlag, 1st edition, 1998.

[BLM+11] Brock, I C; Loddenkoetter, T; Mergelmeyer, S; Seema, P; Stillings, J A: Measurement of the Wt production in the lepton+jets channel using neural networks. Technical Report ATL-COM-PHYS-2011-1706, CERN, Geneva, Dec 2011.

[C+01] Corcella, G.; et al.: HERWIG 6: An event generator for hadron emission reactions with interfering gluons (including supersymmetric processes). In: *JHEP*, volume 0101:p. 010, 2001.

[C+12a] Chatrchyan, S.; et al. (CMS Collaboration): Measurement of the single-top-quark t-channel cross section in pp collisions at $\sqrt{s} = 7$ tev. In: *Journal of High Energy Physics*, volume 2012(12):35, 2012.

[C+12b] Chatrchyan, S.; et al. (CMS Collaboration): Measurement of the top-quark mass in $t\bar{t}$ events with dilepton final states in pp collisions at $\sqrt{s}$=7 TeV. Technical report, CERN, Geneva, Sep 2012.

[C+12c] Chatrchyan, S.; et al. (CMS Collaboration): Measurement of the top-quark mass in $t\bar{t}$ events with lepton+jets final states in pp collisions at $\sqrt{s}$=7 TeV. Technical report, CERN, Geneva, Sep 2012.

[C+13] Chatrchyan, S.; et al. (CMS Collaboration): Evidence for associated production of a single top quark and W boson in pp collisions at 7 TeV. In: *Phys. Rev. Lett.*, volume 110:p. 022003, Jan 2013.

[C+14a] Chatrchyan, S.; et al. (CMS Collaboration): Measurement of the t-channel single-top-quark production cross section and of the |v tb| ckm matrix element in pp collisions at $\sqrt{s} = 8$ tev. In: *Journal of High Energy Physics*, volume 2014(6):90, 2014.

[C+14b] Chatrchyan, S.; et al. (CMS Collaboration): Observation of the associated production of a single top quark and a w boson in pp collisions at $\sqrt{s} = 8$ TeV. In: *Phys. Rev. Lett.*, volume 112:p. 231802, Jun 2014.

[C+14c] Chatrchyan, S.; et al. (CMS Collaboration): Observation of the associated production of a single top quark and a w boson in pp collisions at $\sqrt{s} = 8$ TeV. In: *Phys. Rev. Lett.*, volume 112:p. 231802, Jun 2014.

[Cab63] Cabibbo, N.: Unitary Symmetry and Leptonic Decays. In: *Phys. Rev. Lett.*, volume 10:pp. 531–533, Jun 1963.

[Cat00] Catani, S.: Aspects of QCD, from the Tevatron to the LHC. In: *Proceedings of the Workshop on Physics at TeV Colliders. Les Houches, France*, Jun 2000.

[CFMT09] Campbell, John M.; Frederix, Rikkert; Maltoni, Fabio; Tramontano, Francesco: NLO predictions for t-channel production of single top and fourth generation quarks at hadron colliders. In: *JHEP*, volume 0910:p. 042, 2009.

[Cha09] Chanowitz, Michael S.: Bounding CKM Mixing with a Fourth Family. In: *Phys. Rev. D*, volume 79:p. 113008, Jun 2009.

[Cha12] Chatrchyan, Serguei and others (CMS Collaboration): Observation of a new boson at a mass of 125 GeV with the CMS experiment at the LHC. In: *Phys.Lett.*, volume B716:pp. 30–61, 2012. 1207.7235.

[Cha13] Chatrchyan, S. and others (CMS Collaboration): Evidence for associated production of a single top quark and w boson in pp collisions at $\sqrt{s} = 7$ TeV. In: *Phys. Rev. Lett.*, volume 110:p. 022003, Jan 2013.

[CKR03] Chakraborty, Dhiman; Konigsberg, Jacobo; Rainwater, David L.: Review of top quark physics. In: *Ann.Rev.Nucl.Part.Sci.*, volume 53:pp. 301–351, 2003.

[Col12] Collaborations, LHC (LHC Collaborations): Higgs Cross Section Calculation at 7, 8 and 14 TeV. Technical report, CERN, 2012.

[CS06] Cacciari, Matteo; Salam, Gavin P.: Dispelling the N^3 myth for the k_t jet-finder. In: *Phys.Lett.*, volume B641:pp. 57–61, 2006.

[CSS08] Cacciari, Matteo; Salam, Gavin P.; Soyez, Gregory: The Anti-k(t) jet clustering algorithm. In: *JHEP*, volume 0804:p. 063, 2008.

[CSS12] Cacciari, Matteo; Salam, Gavin P.; Soyez, Gregory: FastJet User Manual. In: *Eur.Phys.J.*, volume C72:p. 1896, 2012.

[CT05] Campbell, John M..; Tramontano, F.: Next-to-leading order corrections to Wt production and decay. In: *Nucl.Phys.*, volume B726:pp. 109–130, 2005.

[DFM+10] Demartin, Federico; Forte, Stefano; Mariani, Elisa; Rojo, Juan; Vicini, Alessandro: The impact of PDF and alphas uncertainties on Higgs Production in gluon fusion at hadron colliders. In: *Phys.Rev.*, volume D82:p. 014002, 2010.

[FC98] Feldman, Gary J.; Cousins, Robert D.: Unified approach to the classical statistical analysis of small signals. In: *Phys. Rev. D*, volume 57:pp. 3873–3889, Apr 1998.

[FGH+09] Flacher, Henning; Goebel, Martin; Haller, Johannes; Hocker, Andreas; Monig, Klaus; et al.: Revisiting the Global Electroweak Fit of the Standard Model and Beyond with Gfitter. In: *Eur. Phys. J.*, volume C60:pp. 543–583, 2009.

[FKK+11] Feindt, Michael; Keller, Fabian; Kreps, Michal; Kuhr, Thomas; Neubauer, Sebastian; et al.: A Hierarchical NeuroBayes-based Algorithm for Full Reconstruction of B Mesons at B Factories. In: *Nucl.Instrum.Meth.*, volume A654:pp. 432–440, 2011. 1102.3876.

[FLM+08] Frixione, S.; Laenen, E.; Motylinski, P.; Webber, B.; White, C. D.: Single-top hadroproduction in association with a W boson. In: *Journal of High Energy Physics*, volume 2008(07):p. 029, 2008.

[FNO07] Frixione, Stefano; Nason, Paolo; Oleari, Carlo: Matching NLO QCD computations with Parton Shower simulations: the POWHEG method. In: *JHEP*, volume 0711:p. 070, 2007.

[FW02] Frixione, Stefano; Webber, Bryan R.: Matching NLO QCD computations and parton shower simulations. In: *JHEP*, volume 0206:p. 029, 2002.

[FW08] Frixione, Stefano; Webber, Bryan R.: The MC@NLO 3.4 Event Generator, 2008. 0812.0770.

[Gav97] Gavrilenko, I: Description of Global Pattern Recognition Program (XKalman). Technical Report ATL-INDET-97-165. ATL-I-PN-165, CERN, Geneva, Apr 1997.

[Gho12] Ghodbane, Nabil: Atlas twiki: Top jet reconstruction efficiency, 1 2012. URL https://twiki.cern.ch/twiki/bin/viewauth/AtlasProtected/TopJetReconstructionEfficiency.

[Gol61] Goldstone, J.: Field Theories with Superconductor Solutions. In: *Nuovo Cim.*, volume 19:pp. 154–164, 1961.

[Gra12] Grahn, Karl Johan: Atlas twiki: Jet recommendations for r17 analyses, 10 2012. URL https://twiki.cern.ch/twiki/bin/viewauth/AtlasProtected/TopJetLiaisonR17Recommendations.

[GSW62] Goldstone, Jeffrey; Salam, Abdus; Weinberg, Steven: Broken Symmetries. In: *Phys. Rev.*, volume 127:pp. 965–970, 1962.

[Her14] Herrberg, R.: Cross-Section Measurement of Single-Top t-Channel Production at ATLAS, April 2014.

[HH+09] Holdom, B; Hou, W. S.; et al.: Four Statements about the Fourth Generation. In: *PMC Phys.*, volume A3:p. 4, 2009.

[Hol90] Hollik, W. F. L.: Radiative Corrections in the Standard Model and their Role for Precision Tests of the Electroweak Theory. In: *Fortschr. Phys.*, volume 38:pp. 165–260, 1990.

[Jun99] Junk, Thomas: Confidence level computation for combining searches with small statistics. In: *Nucl.Instrum.Meth.*, volume A434:pp. 435–443, 1999.

[Kid10a] Kidonakis, Nikolaos: NNLL resummation for s-channel single top quark production. In: *Phys.Rev.*, volume D81:p. 054028, 2010.

[Kid10b] Kidonakis, Nikolaos: Two-loop soft anomalous dimensions for single top quark associated production with a W- or H-. In: *Phys.Rev.*, volume D82:p. 054018, 2010.

[Kid11] Kidonakis, Nikolaos: Next-to-next-to-leading-order collinear and soft gluon corrections for t-channel single top quark production. In: *Phys.Rev.*, volume D83:p. 091503, 2011.

[Kid12] Kidonakis, Nikolaos: Differential and total cross sections for top pair and single top production. In: *20th International Workshop on Deep-Inelastic Scattering and Related Subjects (DIS 2012)*. 2012. 1205.3453.

[KM73] Kobayashi, M.; Maskawa, T.: CP-Violation in the Renormalizable Theory of Weak Interaction. In: *Progress of Theoretical Physics*, volume 49(2):pp. 652–657, 1973.

[KP+07] Kribs, Graham D.; Plehn, T.; et al.: Four Generations and Higgs Physics. In: *Phys. Rev. D*, volume 76:p. 075016, Oct 2007.

[KRW04] Kersevan, B. P.; Richter-Was, E.: The Monte Carlo event generator AcerMC version 2.0 with interfaces to PYTHIA 6.2 and HERWIG 6.5, 2004.

[Lan89] Langacker, P.: Implications of recent M_Z, W and neutral-current measurements for the top-quark mass. In: *Phys. Rev. Lett.*, volume 63:pp. 1920–1921, Oct 1989.

[LGH+10] Lai, Hung-Liang; Guzzi, Marco; Huston, Joey; Li, Zhao; Nadolsky, Pavel M.; et al.: New parton distributions for collider physics. In: *Phys.Rev.*, volume D82:p. 074024, 2010.

[Lis12] Lister, Alison: Atlas twiki: Top systematic uncertainties, 8 2012. URL https://twiki.cern.ch/twiki/bin/viewauth/AtlasProtected/TopSystematicUncertainties2011.

[Luk12] Lukas, W: Fast Simulation for ATLAS: Atlfast-II and ISF. Technical Report ATL-COM-SOFT-2012-137, CERN, Geneva, May 2012.

[MMP+03] Mangano, Michelangelo L.; Moretti, Mauro; Piccinini, Fulvio; Pittau, Roberto; Polosa, Antonio D.: ALPGEN, a generator for hard multipartonic processes in hadronic collisions. In: *JHEP*, volume 0307:p. 001, 2003.

[MSTW09] Martin, A.D.; Stirling, W.J.; Thorne, R.S.; Watt, G.: Parton distributions for the LHC. In: *Eur.Phys.J.*, volume C63:pp. 189–285, 2009.

[Nakon] Nakamura, K. *et. al.*: Review of Particle Physics. In: *J. Phys. G*, volume 37:pp. 1+, (2010) and 2011 partial update for the 2012 edition.

[Nas04] Nason, Paolo: A New method for combining NLO QCD with shower Monte Carlo algorithms. In: *JHEP*, volume 0411:p. 040, 2004.

[PP12] Prosperi Porta, U.: Studien zur Abschätzung des QCD-Untergrundes elektroschwacher Top-Produktion bei ATLAS, 2012. Masterarbeit, Humboldt-Universität zu Berlin.

[PS95] Peskin, Michael E.; Schroeder, Dan V.: *An Introduction To Quantum Field Theory (Frontiers in Physics)*. Westview Press, 1995.

[Rea02] Read, A L: Presentation of search results: the cl s technique. In: *Journal of Physics G: Nuclear and Particle Physics*, volume 28(10):p. 2693, 2002.

[Rie10] Rieck, P.: Entwicklung eines kinematischen Fits zur Untersuchung elektroschwacher Top-Quark-Produktion bei ATLAS, 2010. Masterarbeit, Humboldt-Universität zu Berlin.

[RSP+11] Romeo, G; Schwartzman, A; Piegaia, R; Carli, T; Teuscher, R: Jet energy resolution from in-situ techniques with the atlas detector using proton-proton collisions at a center of mass energy $\sqrt{s} = 7$ tev. Internal Note ATLAS-COM-PHYS-2011-240, CERN, Geneva, 3 2011.

[Rub77] Rubbia, C.: Measurement of the Luminosity of $p\bar{p}$ Collider with a (generalized) Van der Meer Method. In: *CERN-$p\bar{p}$-Note-38*, 1977.

[S+10] Soni, A.; et al.: The fourth family: a simple explanation for the observed pattern of anomalies in B-CP asymmetries. In: *Phys.Lett.*, volume B683:pp. 302–305, 2010.

[Sar12a] Sartisohn, G.: ATLAS TWiki: The BILL Tool, July 2012. (cit. on p. 152), URL url:https://twiki.cern.ch/twiki/bin/viewauth/AtlasProtected/BillTool.

[Sar12b] Sartisohn, G.: Higgs Boson Search in the H $\rightarrow$ WW(*) $\rightarrow$ $\nu\nu$ Channel using Neural Networks with the ATLAS Detector at 7 TeV, March 2012. PhD thesis. Berg. Univ. Wuppertal.

[SG09] Sundermann, J.E.; Goepfert, Th.: KinFitter – A Kinematic Fit with Constraints. Technical Report ATLAS-COM-SOFT-2009-014, CERN, Geneva, Sep 2009.

[SMS06] Sjostrand, T.; Mrenna, S.; Skands, P. Z.: PYTHIA 6.4 Physics and Manual. In: *JHEP*, volume 0605:p. 026, 2006.

[Sta13a] Stamm, Sören: PdfReweightingTool Reference Guide, 12 2013. URL https://ms2.physik.hu-berlin.de/~stamm/PdfReweightingTool/htmldoc/index.html.

[Sta13b] Stamm, Sören: Studien zur Signalextraktion elektroschwacher Top-Quark-Produktion bei ATLAS, 2013.

[Str12] Strandberg, S: Tracking, vertexing and b-tagging performance at ATLAS. Technical Report ATL-COM-PHYS-2012-1278, CERN, Geneva, Aug 2012. Proceedings of the PLHC Conference 2012 in Vancouver.

[Ta12] Ta, D B: Search for the Wt production in the lepton+jets channel with ATLAS. Technical Report ATLAS-COM-CONF-2012-061, CERN, Geneva, Mar 2012.

[Tai00] Tait, Timothy M.P.: The tW^- mode of single top production. In: *Phys.Rev.*, volume D61:p. 034001, 2000.

[TEW11] TEWWG (Tevatron Electroweak Working Group, for the CDF and D0 Collaborations): Combination of CDF and D0 results on the mass of the top quark using up to 5.8 fb-1 of data, 2011.

[Top13] Top Physics LHC working group (TOP-LHC-WG) (ATLAS and CMS Collaborations): Combination of single top-quark cross-sections measurements in the t-channel at $\sqrt{s} = 8$ TeV with the ATLAS and CMS experiments. Technical Report CMS-PAS-TOP-12-002. ATLAS-CONF-2013-098, CERN, Geneva, Sep 2013.

[Top14a] Top Physics LHC working group (TOP-LHC-WG): Combination of cross-section measurements for associated production of a single top-quark and a W boson at $\sqrt{s} = 8$ TeV with the ATLAS and CMS experiments. Technical Report ATLAS-CONF-2014-052, CERN, Geneva, Sep 2014. http://twiki.cern.ch/twiki/bin/view/LHCPhysics/TopLHCWG.

[Top14b] Top Physics LHC working group (TOP-LHC-WG) (ATLAS and CMS Collaborations): Summary of LHC and Tevatron measurements of the top-pair production cross-section. Technical report, CERN, Geneva, Sep 2014.

[vdM68] van der Meer, S.: Calibration of the effective beam height in the ISR. In: *CERN-ISR-PO-68-31*, 1968.

[Vre13] Vreeswijk, Marcel: Charge dependence of the heavy flavour fractions of w+jets. Private Communication, 1 2013.

[WD86] Willenbrock, Scott S. D.; Dicus, Duane A.: Production of heavy quarks from W -gluon fusion. In: *Phys. Rev. D*, volume 34:pp. 155–161, Jul 1986.

[WFLM09] White, Chris D.; Frixione, Stefano; Laenen, Eric; Maltoni, Fabio: Isolating Wt production at the LHC. In: *JHEP*, volume 0911:p. 074, 2009.

[WS08] Wicke, Daniel; Skands, Peter Z.: Non-perturbative QCD Effects and the Top Mass at the Tevatron. In: *Nuovo Cim.*, volume B123:p. S1, 2008.

[Zhu02] Zhu, S.: Next-to-leading order QCD corrections to b g $\rightarrow$ t W- at the CERN Large Hadron Collider. In: *Phys. Lett.*, volume B524:pp. 283–288, 2002.

List of Figures

List of Tables